BOSTON UNIVERSITY

GRADUATE SCHOOL OF ARTS AND SCIENCES

Dissertation

INTERSTELLAR CARBON UNDER THE INFLUENCE OF HII REGIONS

by

MAOHAI HUANG

B.Sc., Peking University, 1991
M.A., Boston University, 1999

Submitted in partial fulfillment of the

requirements for the degree of

Doctor of Philosophy

2001

Approved by

First Reader ____

Thomas M. Bania, Ph.D.
Professor of Astronomy

Second Reader ____

James M. Jackson, Ph.D.
Associate Professor of Astronomy

Acknowledgement

I am indebted to my parents for bringing me up and trusting my decisions. I thank my advisor Professor Tom Bania for his scientific advice: not only because of his astrophysical and intellectual guidance, but also because (as in AST/RO insiders' version of "scientific advice") ploughing through my manuscripts was labor intensive!

I thank the AST/RO project for offering me wonderful academic, social, and personal experiences. I thank Tony Stark for showing me the "It should just work." attitude. I thank Professor Jim Jackson, Alberto Bolatto, and Kathleen Kraemer for academic discussions, Professor Ken Janes for his generous support at some of the more difficult times, Professor Ken Brecher for putting up with my delays and letting me pass AS751, Xiaolei Zhang for taking the data for my thesis, Bob Wilson for his inspiration, and David Mann for assuring me that "There *is* an end."

I thank John Travis for picking me up from Logan Airport when I first arrived in Boston as a total stranger, in a midnight more than eight years ago; I treasure the friendship from Anders Jørgensen, Markos Georganopoulos, Jim Ingalls, Alberto Bolatto, Thanasis Boudouridis, Mohamed Alothman, and my other fellow graduate students. I deeply appreciate Sha Ma for her love and help. She was there with me when the thesis-writing became frustrating and arduous. I thank many of my climbing partners. I cannot finish this dissertation without the "hang in there and pull it off" dogged spirit that was sharpened in difficult climbs.

I am grateful for the graduate study opportunity that people in the US generously provide me. This research is partly supported by the United States National Science Foundation grant DPP88-18384, and by the Center for Astrophysical Research in Antarctica and the NSF under Cooperative Agreement OPP89-20223.

INTERSTELLAR CARBON UNDER THE INFLUENCE OF HII REGIONS

(Order No.   )

MAOHAI HUANG

Boston University, Graduate School of Arts and Sciences, 2001

Major Professor: Thomas M. Bania, Professor of Astronomy

ABSTRACT

The photodissociation region (PDR) is an area in the interstellar medium where far-ultraviolet radiation from OB stars dominates the physical and chemical processes and conditions. I study properties of the PDRs near the ionized hydrogen (H II) regions, which surround massive, hot stars. Carbon is one of the most abundant species after hydrogen and helium. I concentrate my study on the properties of carbon in its various forms to further our understanding of PDR physics.

PDRs have been studied in detail in only a small number of classic "test bed" sources with a limited range of physical and geometrical conditions. I study a much larger sample of H II regions with a large range of radiative excitation conditions, selected from H II region radio-recombination line surveys. I observe these sources in emissions from ionized (C II), neutral (C I), and molecular carbon (CO; the carbon monoxide molecule) to obtain carbon properties in a broad range of PDR conditions. To observe my sources I use the ISO satellite and the AST/RO telescope which I helped to build. In addition I use published data from the IRAS satellite and other sources. I compare these observations with theoretical predictions of existing PDR models.

My major conclusions include: the C I intensity is due mainly to local heating; the correlation between C I and CO observations and H II radio observations strongly supports a spherically-structured PDR model; PDR linewidths and H II region excitation parameters are positively correlated. Using the combined data I derive the density and the incident far-ultraviolet emission flux in my sample of PDRs.

I have identified a number of problems in applying the current homogeneous slab PDR models to the observational results. When these problems are addressed the PDR models can explain the infrared observational results within error limits, however the models do not explain the neutral and molecular observations. I find that spherical and clumpy PDR models can help to interpret these results.

Based on my study I suggest that current PDR models should include a range of gas turbulent velocities and address the geometry and clumpiness of the PDRs.

Contents

List of Tables

List of Figures

Chapter 1

Introduction

1.1. Focus of this Thesis

I study the properties of ionic (C^+), atomic (C I), and molecular (CO) carbon in photodissociation regions (PDRs; see 1.2.2) near H II regions, the fully ionized zones surrounding massive, hot stars. The goal of my thesis is to use these properties to further understanding of PDR physics.

Our Galaxy is a collection of stars and tenuous interstellar matter that pervades the space between stars. The physical and chemical conditions of the interstellar medium (ISM) are strongly influenced by the stars. On the other hand the stars are formed in the ISM. The interactions between the stars and the ISM are fundamental processes in the evolution of the Galaxy.

My study concentrates on the understanding of how young OB stars and the H II regions they create (see the next section) influence the properties of the PDR. To do this I study a large sample of H II regions with a large range of radiative excitation conditions. These observations are compared with PDR theoretical predictions about the properties of carbon in the vicinity of H II regions.

In this chapter I first explain the basic physics of H II regions and the PDRs, with an emphasis on the importance of studying carbon species in the ISM. Then I describe the H II region source sample selected for the purpose of this study. Finally I describe the Antarctic Submillimeter Telescope and Remote Observatory (AST/RO), which I have helped to build in order to acquire data for this thesis.

1.2. H II Regions and Photodissociation Regions

1.2.1. H II Regions

Studying the physical properties of the ISM around H II regions will provide evidence to help us better understand the conditions of the ISM in the Galaxy and the star formation process. Only O and early B stars are hot enough to form H II regions. Since these stars have typical lifetimes between 10^6 and 10^7 years, H II regions are indicators of recent star formation. These luminous young stars are the major heating and ionizing sources of their interstellar environs.

The Excitation Parameter

The most basic physical consideration in an H II region is the ionization and recombination balance. The photons in the UV radiation field from the OB stars totally ionize hydrogen in the nearby ISM. The ionized region is separated from the neutral ISM by a sharp boundary (Strömgren 1939), and is called the Strömgren sphere. The photons with energy greater than 13.6 eV ionize hydrogen atoms and produce free electrons. This photoionization process is balanced by the recombination process. The recombination happens when a free electron is captured by a hydrogen ion. (I ignore here other less abundant elements for simplicity.) Part of the kinetic energy of the electron-H^+ system is taken away by the photons radiated when the electron recombines into a bound state, and then cascades down from higher excitation states to lower ones. Since the excitation states of hydrogen atoms in the ISM are mostly populated by this recombination process, the spectral line emission radiated during de-excitation is called recombination line radiation. The free-free continuum radiation and the recombination line radiation at radio frequencies have historically been used together to identify H II regions in the ISM.

The mathematical description of the balance of ionization and recombination processes can be found in many papers (e.g. Mezger & Henderson 1967; Mezger & Hoglund 1967; Hjellming 1968; Mezger & Ellis 1968; Dupree & Goldberg 1970). The ionization and recombination equilibrium in a pure hydrogen cloud is expressed as:

$$\frac{dS_u(r)}{dr} = -4\pi r^2 n_H^2 \alpha_{(2)}, \tag{1.1}$$

where n_H is the hydrogen number density. The quantity $S_u(r)$ is defined as the number of UV photons more energetic than 13.6 eV flowing through a shell at distance r from the surface of the exciting star. The partial recombination coefficient, $\alpha_{(2)}$, is defined as the total hydrogen recombination rate coefficient to all states minus the recombination rate to the H ground state. The photons generated by recombinations to the H ground state are absorbed elsewhere in the H II region and ionize the absorbing H atom. Therefore this rate does not contribute to any net recombination.

Assuming constant density, the above equation can be integrated from the surface of the star ($r = 0$) to the surface of the Strömgren sphere ($r = r_s$ and $S_u(r) = 0$) to obtain:

$$S_u(0) = \frac{4\pi}{3} r_s^3 n_H^2 \alpha_{(2)}. \tag{1.2}$$

By definition $S_u(0)$ equals the Lyman continuum photon flux, L_c, produced by the exciting star.

Based on the above equation, L_c can be related to the *excitation parameter*, U. Using the notion of Hjellming (1968), the excitation parameter is defined as:

$$U \equiv \left[\frac{3}{4\pi} \int_{\mathrm{HII\ region}} \mathrm{n_e}^2 dV \right]^{1/3} , \tag{1.3}$$

where n_e is the electron volume number density. If the H II region is spherically symmetric and is comprised of a pure uniform hydrogen gas, U takes the form:

$$U = r_s \langle {n_e}^2 \rangle^{1/3} = r_s n_H^{2/3}. \tag{1.4}$$

Note that $\langle {n_e}^2 \rangle^{1/2}$ is the rms electron density of the H II region. Since $\alpha_{(2)}$ in Equation 1.2 is a slow function of the electron temperature ($\alpha_{(2)} = 2.59 \times 10^{-13} \sim 2.52 \times 10^{-13}$ when the electron temperature $T_e = 10,000$ K $\sim 20,000$ K, Osterbrock 1989), Equations 1.2 and 1.4 imply that $L_c \propto U^3$. Therefore the excitation parameter, U, *is a measure of the strength of the OB star's H-ionizing radiation field.* Note that the above statement is true even if the H II regions are not spherically symmetric or do not have a uniform density, as I have assumed in the derivation of U. This is because the interpretation of the excitation parameter is independent of any geometrical assumption even though the interpretation of r_s and $\langle {n_e}^2 \rangle^{1/3}$ are not (Hjellming 1968). As will be shown below, another significance of U is that it is measurable by radio wavelength observations.

Basic Observables

The electron temperature, T_e, density, n_e, emission measure, EM, and excitation parameter, U, of an H II region can be obtained from observing radio continuum emission and radio recombination line (RRL) emission. The formalism discussed here is used to calculate these parameters for the H II region sample.

The free electrons in the H II region mostly have a Maxwellian velocity distribution due to their large free-free collision cross section. The electron temperature is used to characterize this property of the free electrons, and can be derived from the relation (see derivations in Mezger & Ellis 1968):

$$\frac{T_L}{T_C} \cdot \left[\frac{\Delta\nu_L}{\mathrm{KHz}}\right] = \frac{2.33 \times 10^4}{a(\nu_L, \mathrm{T_e})} \left[\frac{\nu_L}{\mathrm{GHz}}\right]^{2.1} \mathrm{T_e}^{-1.15} \left[1 + \frac{n_{\mathrm{He^+}}}{n_{\mathrm{H^+}}}\right]^{-1}, \tag{1.5}$$

where T_L and T_C are the brightness temperatures of the RRL line and radio continuum, respectively, $\Delta\nu_L$ the full width half maximum (FWHM) of the RRL, $\mathrm{T_e}$ the electron temperature, and ν_L the RRL frequency. The dimensionless quantity $a(\nu_L, \mathrm{T_e})$ is a slowly varying function with a value that is close to 1. Its values are tabulated in Mezger and Ellis (1968). The ratio $(n_{\mathrm{He^+}}/n_{\mathrm{H^+}})$, the effective abundance ratio of singly ionized helium and hydrogen, is assumed to be 0.1. Adopting a spherical H II region model with a uniform density distribution, the electron density is given by (see Mezger & Henderson 1967; Reifenstein *et al.* 1970):

$$\left[\frac{\mathrm{n_e}}{\mathrm{cm^{-3}}}\right] = 98.2a(\nu_L, \mathrm{T_e})^{-0.5} \left[\frac{\nu_L}{\mathrm{GHz}}\right]^{0.05} \left[\frac{\mathrm{T_e}}{K}\right]^{0.175} \left[\frac{S_\nu}{Jy}\right]^{0.5} \left[\frac{d}{\mathrm{kpc}}\right]^{-0.5} \left[\frac{\theta_G}{\mathrm{arcmin}}\right]^{-1.5} \tag{1.6}$$

where $\mathrm{n_e}$, $a(\nu_L, \mathrm{T_e})$, ν_L, and $\mathrm{T_e}$ are as defined previously, S_ν is the radio flux density at frequency ν_L, and d is the distance to the H II region. The angular FWHM, θ_G, is obtained by a Gaussian fit to a map of the H II region's radio continuum emission.

The emission measure is defined as $EM \equiv \int \mathrm{n_e}^2 \mathrm{d}l$ integrated through the source along the line of sight. In the above model:

$$\left[\frac{EM}{\mathrm{pc\,cm^{-6}}}\right] = 2r_s\mathrm{n_e}^2 = 0.428 \left[\frac{d}{\mathrm{kpc}}\right] \left[\frac{\theta_G}{\mathrm{arcmin}}\right] \left[\frac{\mathrm{n_e}}{\mathrm{cm^{-3}}}\right]^2 \tag{1.7}$$

where the Strömgren sphere radius, r_s, is simply taken as the size of the RRL emitting region.

From Equation 1.4 the excitation parameter is

$$\left[\frac{U}{\mathrm{pc\,cm^{-2}}}\right] = r_s\mathrm{n_e}^{2/3} = 0.214 \left[\frac{\theta_G}{\mathrm{arcmin}}\right] \left[\frac{\mathrm{n_e}}{\mathrm{cm^{-3}}}\right]^{2/3}. \tag{1.8}$$

In Equations 1.5, 1.6, 1.7, and 1.8 all quantities are either known, or can be reasonably assumed, measured, or derived from the RRL and radio continuum observations.

U and G_0

The excitation parameter and the intensity of the far ultraviolet ($6\,\mathrm{eV} < h\nu < 13.6\,\mathrm{eV}$; FUV) radiation field outside the H II region are closely related. But this relationship is not straight forward. My observational results can be used to find correlations between the FUV field intensity, G_0, and U. In turn this will aid in the understanding of the relationship between the ISM's properties and those of the H II region's exciting stars.

Outside the Strömgren sphere the hydrogen in the ISM is neutral. The energies of the UV photons escaping from the H II region are less than the hydrogen ionization potential energy. At the zero extinction ($A_v = 0$) position, the intensity of the incident FUV field onto the neutral hydrogen ISM is the source of the photodissociation process in the PDR as discussed in § 1.2.2.

Customarily G_0 is expressed in units of $1.6 \times 10^{-3}\,\mathrm{erg\,cm^{-2}\,sec^{-1}}$, which is the average interstellar flux between $6\,\mathrm{eV} < h\nu < 13.6\,\mathrm{eV}$ determined by Habing (1968). The FUV intensity can be approximated by assuming that the only source is the central exciting star which has a blackbody energy distribution characteristic of its stellar effective temperature, T_*. Then G_0 can be written as:

$$\mathrm{G}_0 = \left[\frac{R_*}{r_s}\right]^2 \int_{h\nu=6\,\mathrm{eV}}^{h\nu=13.6\,\mathrm{eV}} B(T_*,\nu)d\nu \frac{1}{1.6 \times 10^{-3}\,\mathrm{erg\,cm^{-2}\,sec^{-1}}}, \tag{1.9}$$

where R_* and r_s are the star and Strömgren sphere radius, respectively. The value of R_* depends on a stellar atmosphere model and is related to the excitation parameter, as shown below.

The U parameter is related to the Lyman continuum flux of the exciting star. The relation between L_c and T_* has been the subject of extensive studies (e.g. Panagia 1973; Georgelin, Lortet-Zuckermann, & Monnet 1975; Vacca, Garmany, & Shull 1996). It is far beyond the scope of this thesis to discuss the details of these studies.

In this thesis I look for a correlation between U and G_0 using a two-step process. First based on the study of L_c and OB star parameters by Vacca *et al*. (1996), I derive T_* and R_* from U. Then from Equation 1.9, I derive a G_0 value from T_* and R_*. This G_0 value can be compared with the G_0 value derived from the observational data. There are two ways to derive G_0 using the observational data, both independent of U: 1) assuming that the FUV radiation from an H II region is totally absorbed by the dust and re-radiated in the form of FIR continuum radiation, one can calculate G_0 from the observed FIR continuum of the H II regions as shown in §2; 2) using adopted PDR models, one can derive G_0 from spectral line intensities and the intensity ratios of carbon species in the PDR as shown in §5. The reliability of the determinations of U and G_0 are discussed in §5.

1.2.2. Photodissociation Region Theories

The photodissociation region is an area outside the H II region where the far-ultraviolet radiation from OB stars dominates the structure, chemistry, thermal balance, chemical composition, and the evolution of these properties in the region. Characterizing the physical and chemical conditions in the PDR is important to understanding the ISM in the Galaxy.

Basic Considerations of the PDRs

The photodissociation regions are the interface regions between young OB stars and the dense, dark interiors of molecular clouds, where far ultraviolet photons cannot penetrate. The PDRs were first studied when people discovered the "diffuse clouds" in the 1920's. Modeling the observational results from the *Copernicus* telescope in the 1970's (Glassgold & Langer 1976; Black & Dalgarno 1977) and studying the fine structure lines of [CII] and [OI] at the turn of the 1980's started to reveal properties of the IR-rich, predominantly neutral regions outside H II regions (Melnick, Gull, & Harwit 1979; Storey, Watson, & Townes 1979; Russell *et al*. 1980; Russell *et al*. 1981). Observations of the neutral atomic carbon (C I) ground state ($^3P_1 \rightarrow {}^3P_0$) transition emission showed that in the PDRs C I has a greater abundance (up to several times 10^{18} cm^{-2} in column density and $0.1 \sim 1$ in abundance ratio over CO) and a more extensive distribution than theoretical models had previously predicted (Phillips & Huggins 1981; Keene *et al*. 1985). Observational results of C I have motivated a wealth of theoretical modeling of the PDRs (Tielens & Hollenbach 1985a; Tielens & Hollenbach 1985b; Stutzki 1990; Genzel 1991; Kaufman *et al*. 1999).

Figure 1.1 shows a schematic diagram of a homogeneous, plane-parallel ("Slab") PDR illuminated from the left. As the incident FUV radiation penetrates the ISM, the visual extinction, A_v, increases. Starting from the left where $A_v = 0$, the FUV radiation dissociates molecules and dominates the chemistry and physical processes until A_v increases to about 10, where O_2 becomes shielded from photodissociation. This range, $0 < A_v < 10$, defines the photodissociation region. It is believed that PDRs comprise all of the atomic and at least 90% of the molecular gas in the Galaxy (Hollenbach & Tielens 1999).

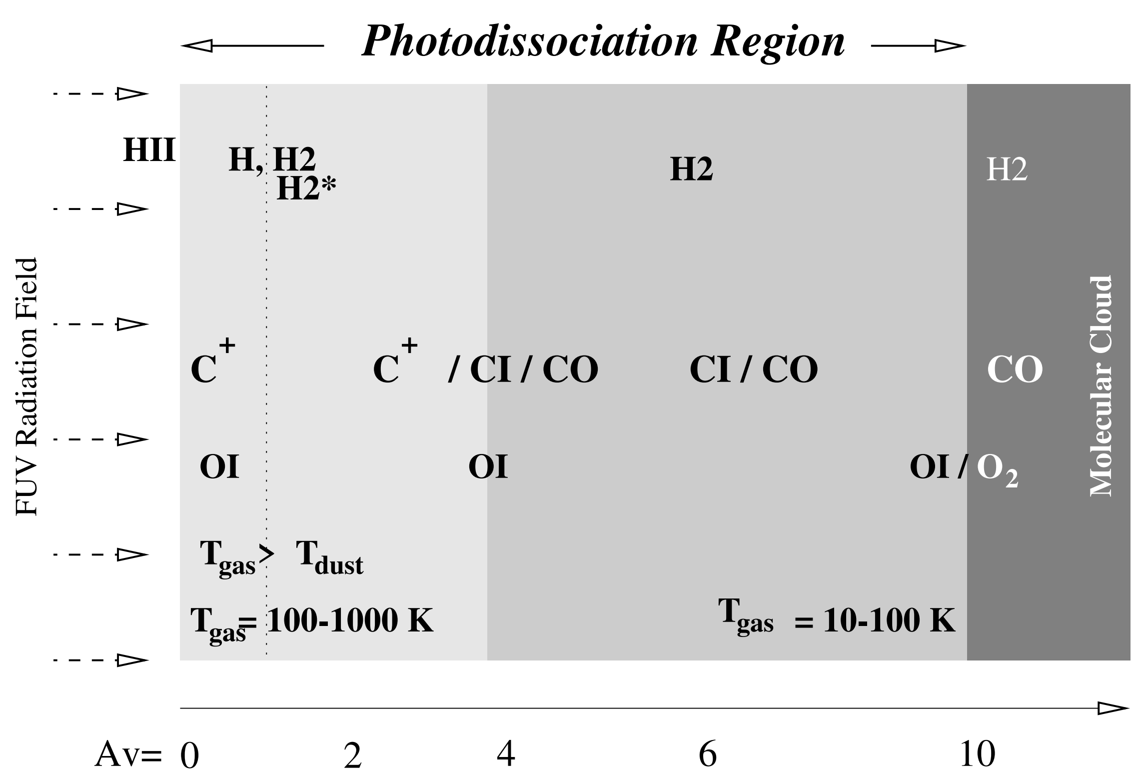

Fig. 1.1.— This is a schematic plot of a homogeneous Photodissociation Region. UV radiation penetrates the ISM from the left and causes gas temperature and composition changes in the photodissociation region. The changes happen in zones that are parallel to each other.

According to the standard steady state slab PDR model (Tielens & Hollenbach 1985b), along the direction of incident FUV radiation, the species' abundances, the heating and cooling rates of dust and gas, and the ISM composition are functions only of A_v. Detailed calculations are given by Hollenbach and Tielens (1985b). Here I only briefly describe the distribution of gas and dust temperatures, and the abundance distributions of several important hydrogen, carbon, and oxygen species at different A_v.

According to a typical model ($n = 2.3 \times 10^5\,\mathrm{cm}^{-3}, \mathrm{G}_0 = 10^5$), starting from $A_v = 0$, hydrogen becomes neutral after A_v reaches about 0.1. Hydrogen will become molecular and remain so after A_v exceeds 2. Both carbon and oxygen have ionization potentials lower than hydrogen. The singly-ionized carbon (C^+ or C II) exists in abundance from the close environs of the star to where A_v surpasses $4 \sim 5$. In the transition zone between C^+ and CO where $A_v > 2$, abundant neutral carbon is created. C I reaches its maximum abundance at $A_v = 4$, and turns molecular (CO) at deeper places into the PDR. Atomic oxygen is found in abundance at $A_v = 5 \sim 10$. The transition from O to O_2 defines the boundary of the PDR on the molecular cloud side.

The basic energetics of the PDR is that most of the FUV energy are absorbed by the dust grains. UV pumping of H_2 molecules and photoelectric heating by dust and large robust organic molecules (polycyclic aromatic hydrocarbons or PAHs) are the major heating processes of the gas. The bulk of the radiative cooling of the PDR is through IR continuum emission from heated dust. But cooling of the gas components occurs mainly through far-infrared (FIR) fine structure lines of [CII], [OI], and [C I]. About 1% of the total FUV radiation is converted to FIR fine structure line radiation. The gas temperature is about 10^2 K to 10^3 K where $A_v < 2 \sim 3$, and falls below 10^2 K after A_v increases to about 4. Overall the dust temperature falls monotonically from the star side of the PDR (110 K) to the molecular cloud side (~ 80 K).

Carbon in PDRs is an important species to study. It will help us to understand the physical properties of the various forms of carbon (C^+, C I, CO) and the PDR properties in general. Carbon has the lowest first ionization potential (11.3 eV) of the C, N, O elements which are the most abundant species in the ISM after H and He. A "C II" region exists outside of the Strömgren sphere of an H II region, extending

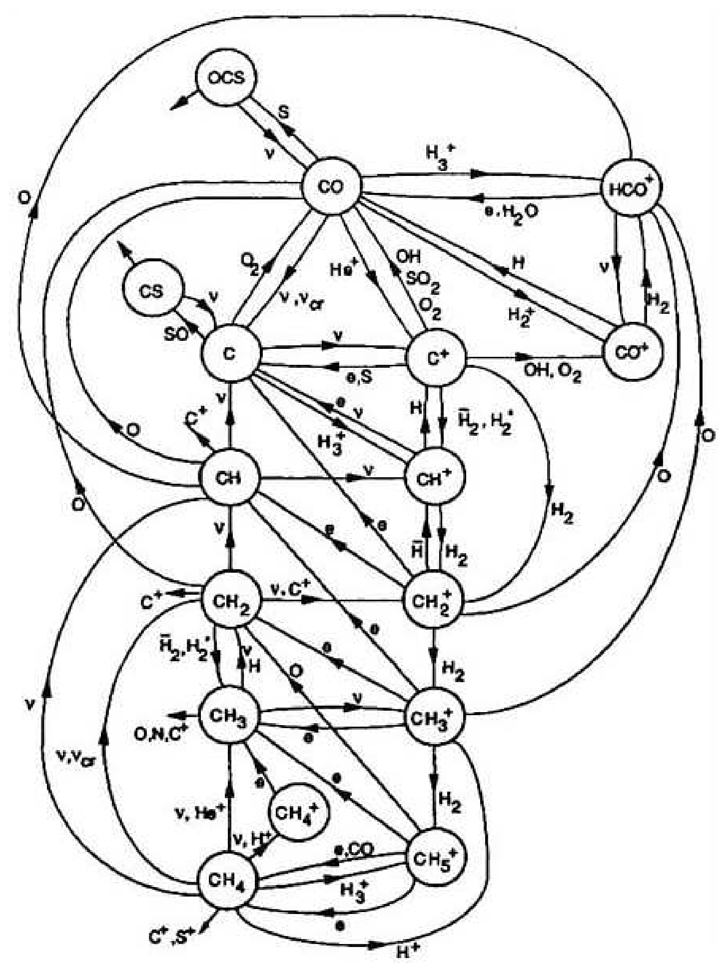

Fig. 1.2.— The carbon chemistry network in a PDR. The Tielens and Hollenbach (1985b) models were based on the important reactions in this network. Figure is reproduced from Sternberg and Dalgarno (1995).

to $A_v \approx 4$ in the PDR. Neutral carbon is created in the photodissociation process of carbon molecules: CO, CH, and CS etc., and in the recombination of the C^+ ion. A carbon chemistry network for the ISM proposed by Sternberg and Dalgarno (1995) is shown in Figure 1.2. The importance of the C I fine structure emission is that it is a major coolant of the PDR gas. The excitation energies of C I are $h\nu/k =$

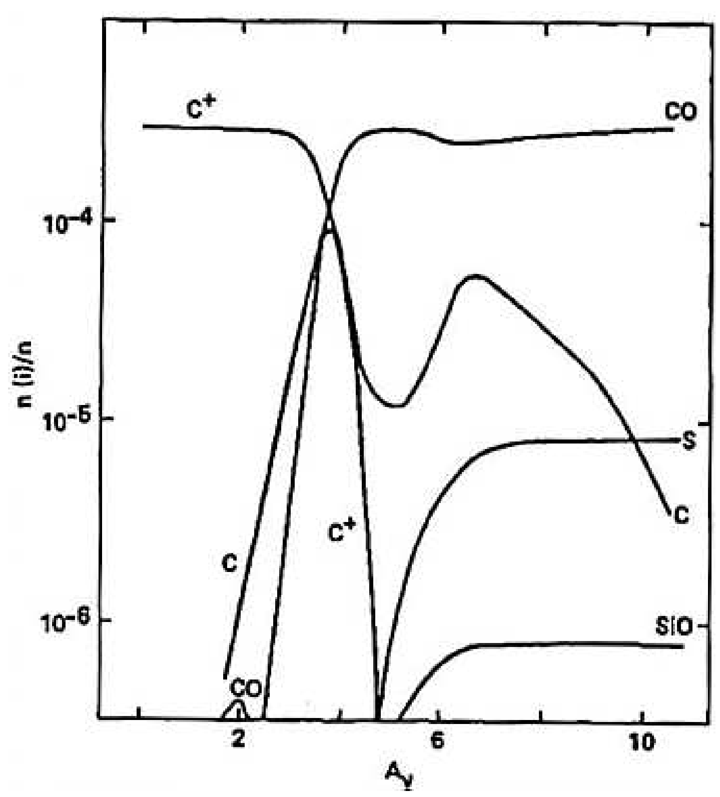

Fig. 1.3.— Carbon species abundances (fractions of the number density of hydrogen nuclei) as functions of the visual extinction, A_v, into the PDR. The calculation and figure are made using the Standard Model ($n = 2.3 \times 10^5\,\mathrm{cm}^{-3}, \mathrm{G}_0 = 10^5$) by Tielens and Hollenbach (1985b).

23.5 K and 62.5 K for the (J=1→0) transition at 492 GHz and (J=2→1) transition at 810 GHz, respectively. These temperatures are close to the gas temperature in many PDRs. One major success of the Tielens and Hollenbach (1985b) model of the PDR is that it explains the key observational result that neutral carbon is found far into the PDR, instead of being concentrated at the surface as previous models had predicted (Phillips & Huggins 1981; Keene *et al.* 1985, as indicated in Figure 1.3). This success is due to Tielens and Hollenbach's inclusion in their models of full gas chemistry and heat balance, more recent rate coefficients, and dust shielding of C^+ as well as C^+ self-shielding in the C^+/C/CO transition region.

Existing Models and Tests of PDRs

Here I show model calculations of the physical conditions of the carbon species in PDRs. The PDR models are stationary, one-dimensional "slab" models. In later chapters I use these results in conjunction with my observational data to answer the question: *Can these models consistently explain PDR conditions found for a large sample of H* II *regions that has a wide range of excitation conditions?*

Figures 1.4 to 1.11 show homogeneous slab PDR models: these figures give the intensities and intensity ratios of C I, C^+, CO(1-0), CO(4-3), and [OI] as functions of the incident FUV intensity, G_0 , and the volume number density of hydrogen nuclei, n. The calculations are made using the "standard model" of Kaufman *et al.* (1999). Kaufman *et al.* (1999) re-calculate the Tielens and Hollenbach (1985b) models using the most up-to-date values of atomic and molecular data, the most current chemical rate coefficients, and the newest grain photoelectric rates. They also broaden the density and G_0 ranges to $n = 10^1 \sim 10^7\,\mathrm{cm}^{-3}$ and $G_0 = 10^{-0.5} \sim 10^{6.5}$, as compared to $n = 10^3 \sim 10^6\,\mathrm{cm}^{-3}$ and $G_0 = 10^3 \sim 10^6$ in the original models of Tielens and Hollenbach (1985b).

After clumpiness was found in PDRs (Stutzki *et al.* 1988; Howe, *et al.* 1991) clumpy PDR models have been developed to explain the observational results. Meixner and Tielens (1993) investigated clumpy PDRs using simplified bi-component models. In their models dense clumps (the clump density $n_c = 5 \times 10^5$, 10^6, or $10^7\,\mathrm{cm}^{-3}$) are embedded in a less dense interclump medium ($n_i = 300$ or $3000\ cm^{-3}$). The average density of the gas is chosen to be constant at $10^5\,\mathrm{cm}^{-3}$. Therefore the clump density, n_c, and the clump volume filling factor, p_c, have the relation: $n_c \times p_c = 10^5\,\mathrm{cm}^{-3}$. The inter-clump gas is insignificant in mass but important in determining UV field penetration into the PDR. The C^+, C I, and CO emission intensities as functions of clump densities are shown in Figure 1.12.

Detailed comparisons of these PDR models with observational results have been successfully made (e.g., Phillips & Huggins 1981; Keene *et al*. 1985; Zmuidzinas *et al*. 1988; Tauber *et al*. 1995; Bergin, Snell, & Goldsmith 1996; van der Werf *et al*. 1996; Spaans & van Dishoeck 1997), but these authors limited their investigations to several well studied optically visible sources. Observing carbon species in a large sample of H II regions that has a wide range of excitation conditions will help to overcome this limitation. It is the main point of my thesis to study a large sample of H II regions in order to increase the limited number of sources that have been used to test the models.

In this thesis I shall use the following strategy to compare my new observations of carbon species in a sample of H II regions with PDR model predictions:

1. As described in § 1.3, I select a sample of H II regions.

2. In §2 for this same sample I observe the IR 158μm C^+ and [OI] emission line fluxes as well as the IR continuum flux using the ISO satellite for the same sample. The [OI] 145μm / [CII] 158μm line ratios and the line-to-continuum ratios of ([OI] 145μm + [CII] 158μm) / $I_{continuum}$ are derived. From the FIR luminosity G_0 is estimated.

3. In §3 for the sample sources I map C I emission intensity, derive the size of the C I region around the H II regions, and calculate the gas density and temperature assuming C I is optically thin.

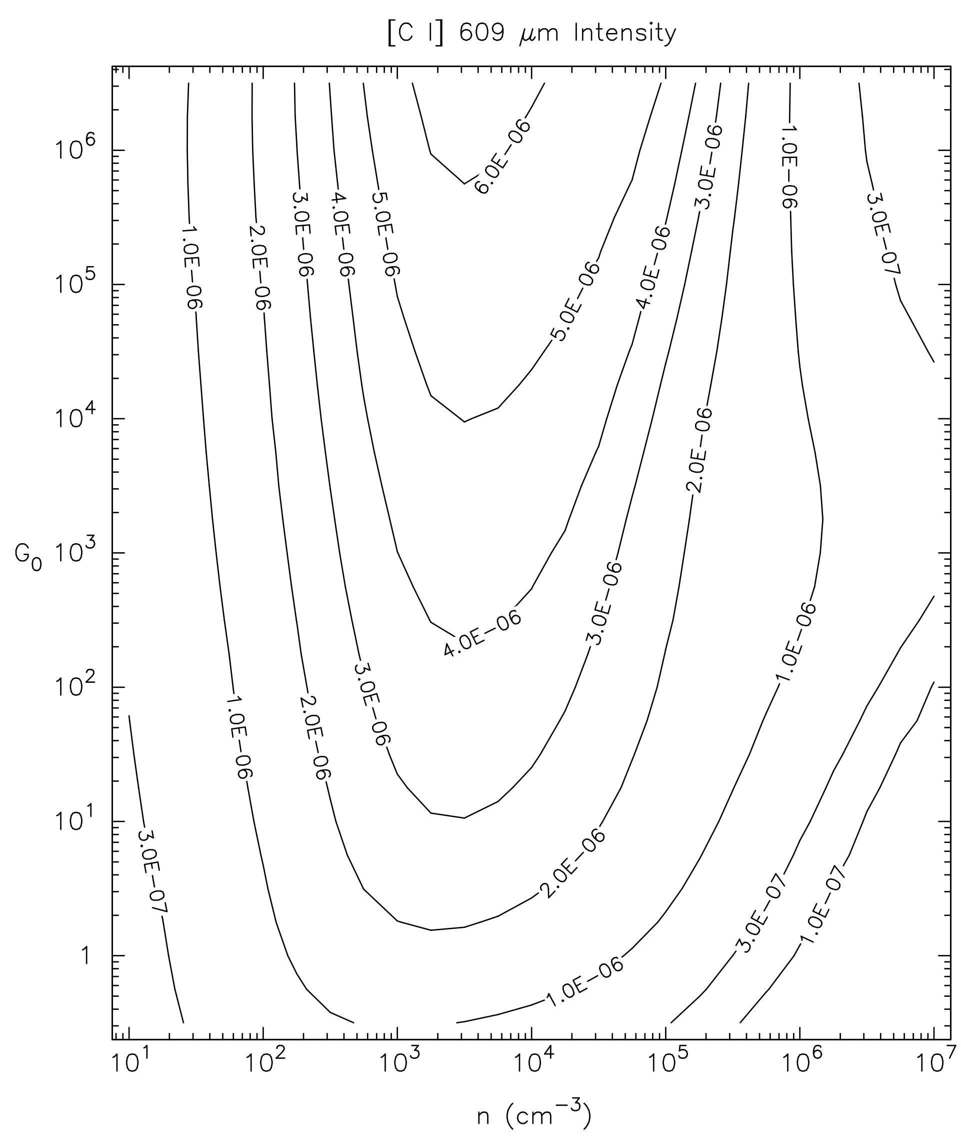

Fig. 1.4.— Emergent line intensity (in units of erg $\mathrm{cm}^{-2}\ \mathrm{sec}^{-1}\ \mathrm{sr}^{-1}$) of the 609$\mu$m C I transition emission as a function of incident FUV intensity (in units of $1.6 \times 10^{-3}\,\mathrm{erg\,cm^{-2}\,sec^{-1}}$) and hydrogen density. Calculation is made by Kaufman *et al.* (1999) using their standard homogeneous slab PDR model. See text for explanation of the model.

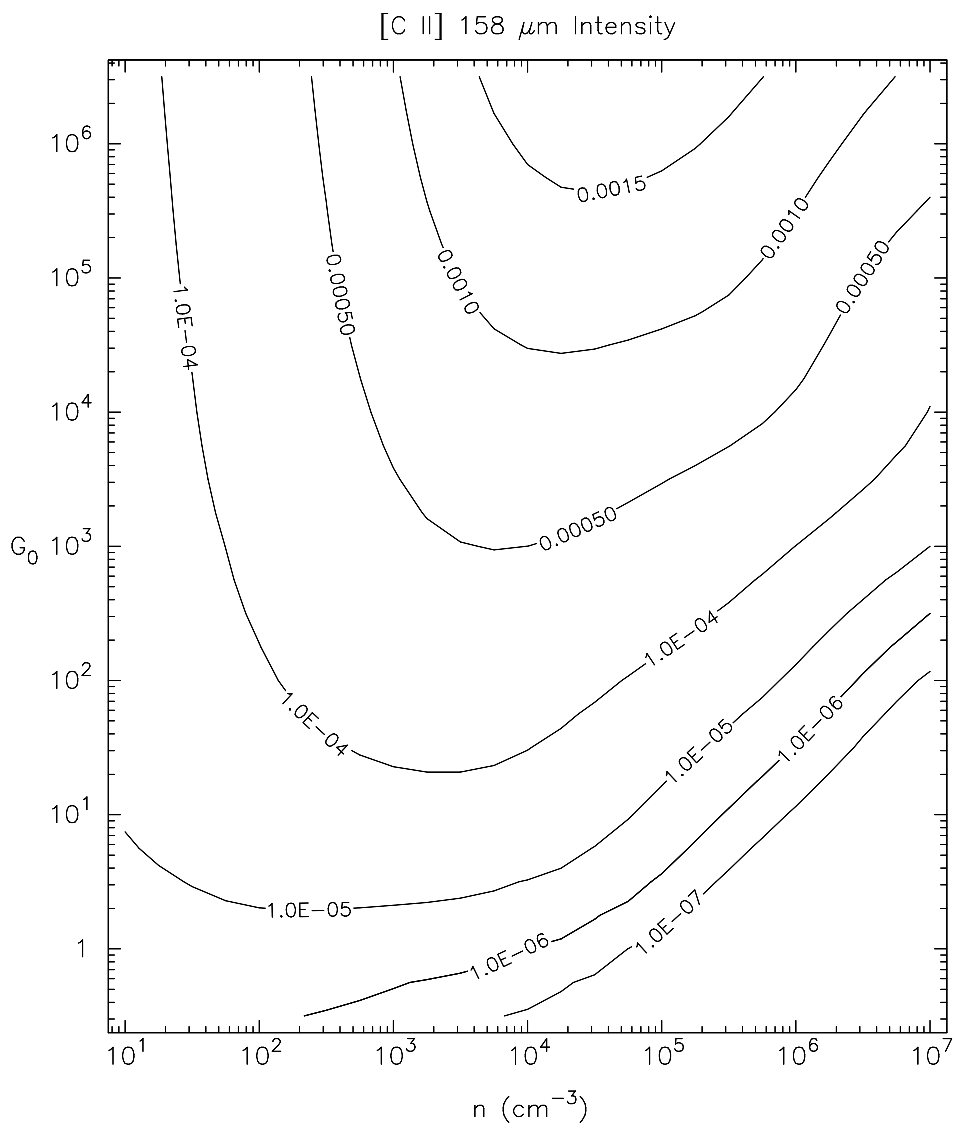

Fig. 1.5.— Emergent line intensity (in units of erg cm^{-2} sec^{-1} sr^{-1}) of the 158μm C^+ transition emission. See Figure 1.4 caption and text.

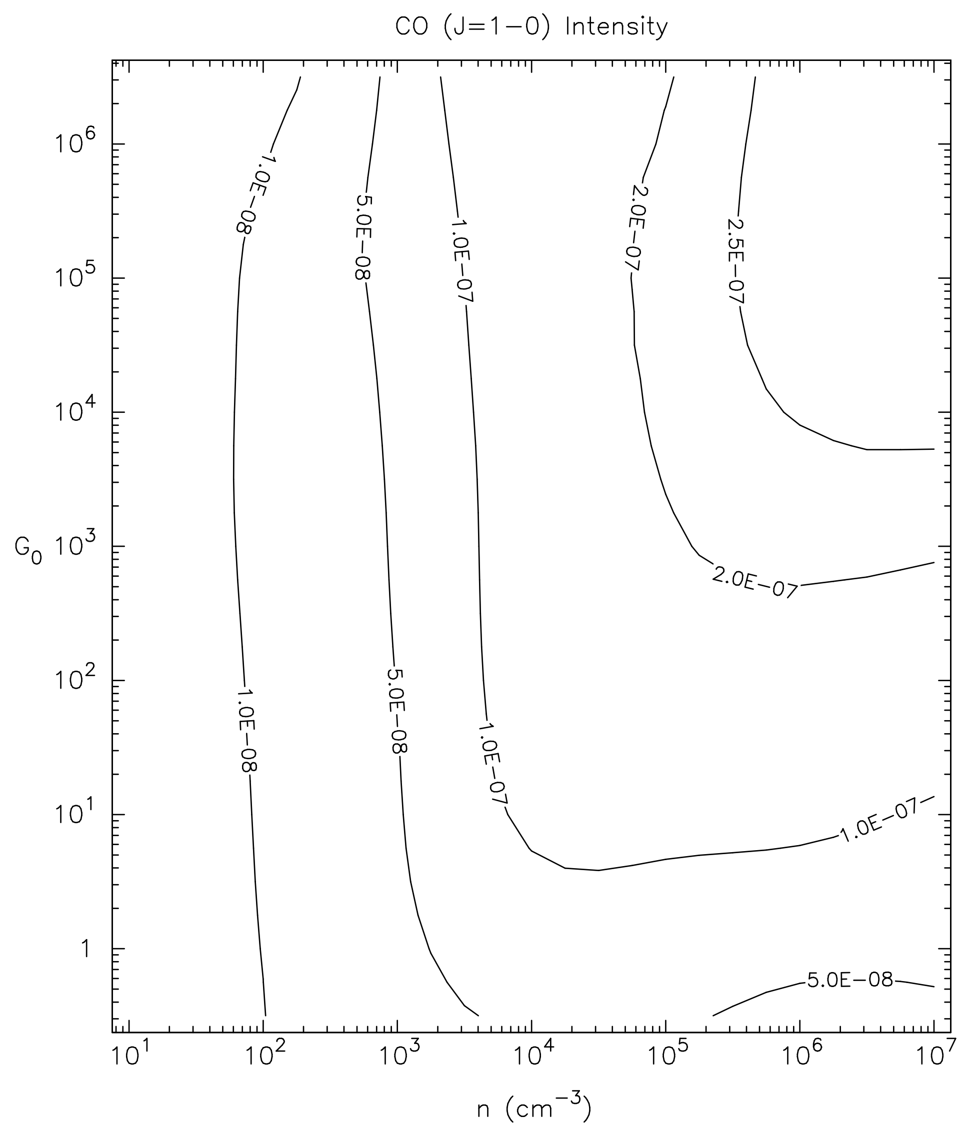

Fig. 1.6.— Emergent line intensity (in units of erg cm^{-2} sec^{-1} sr^{-1}) of the 115 GHz CO(J = 1 → 0) transition emission. See Figure 1.4 caption and text.

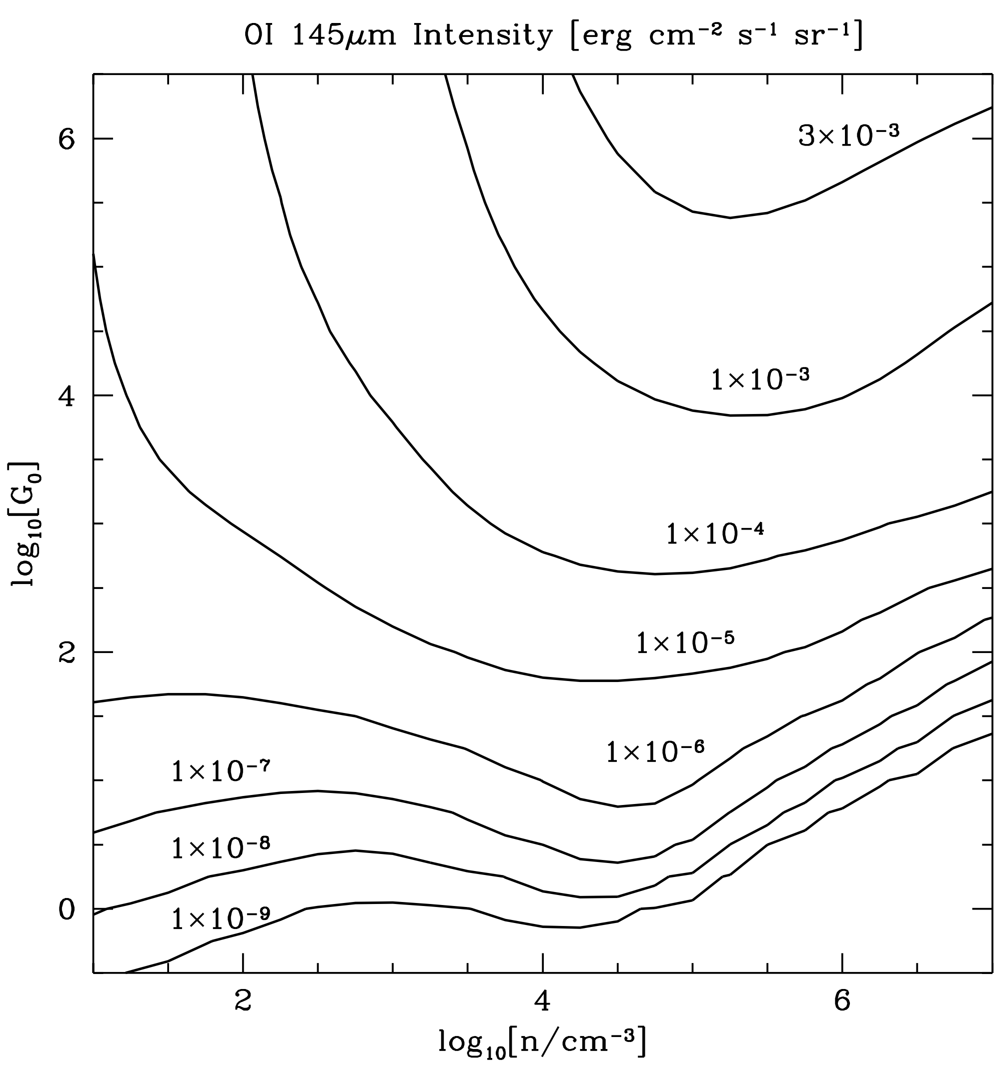

Fig. 1.7.— Emergent line intensity (in units of erg cm^{-2} sec^{-1} sr^{-1}) of the 145μm [OI] transition emission. See Figure 1.4 caption and text.

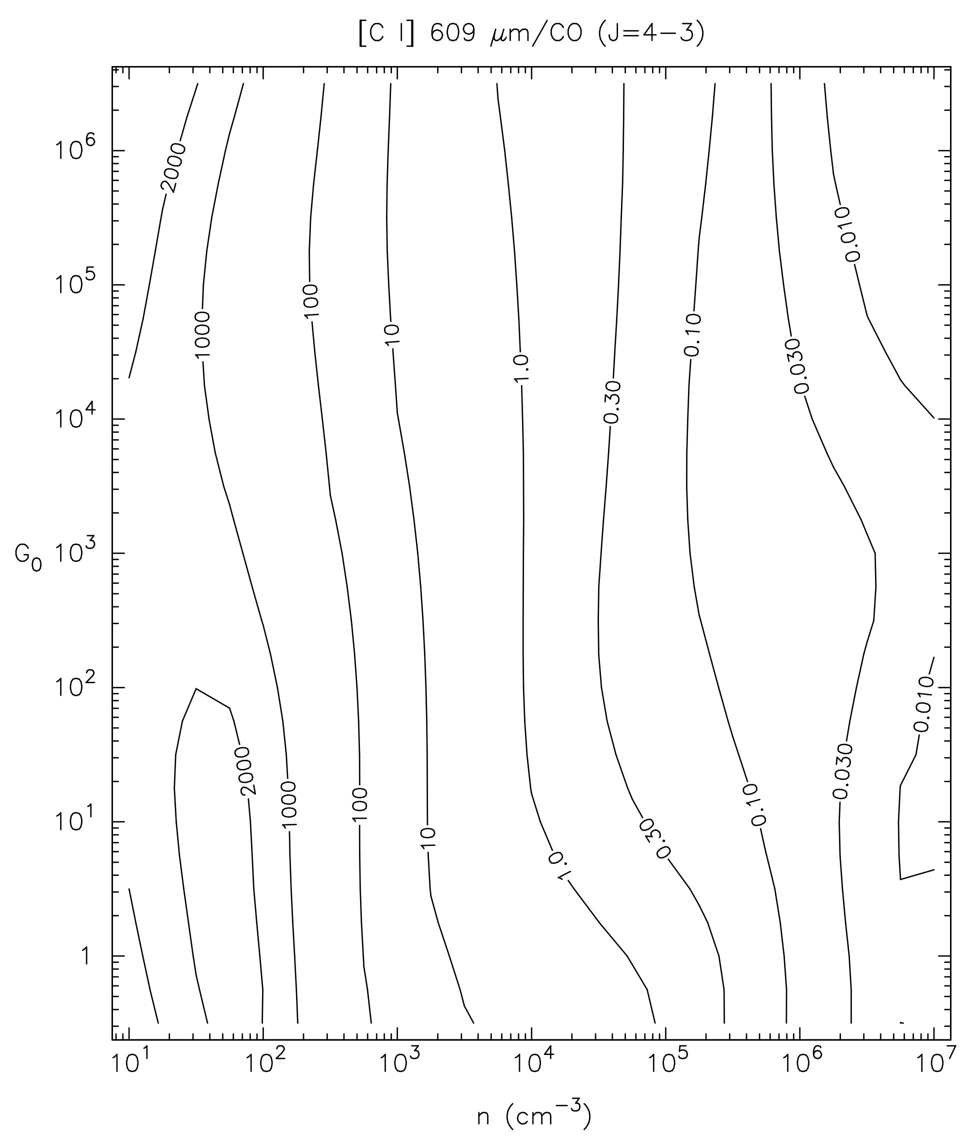

Fig. 1.8.— Emergent Intensity ratio of [C I] 609μm / CO(4-3) as a function of incident FUV intensity. See Figure 1.4 caption and text.

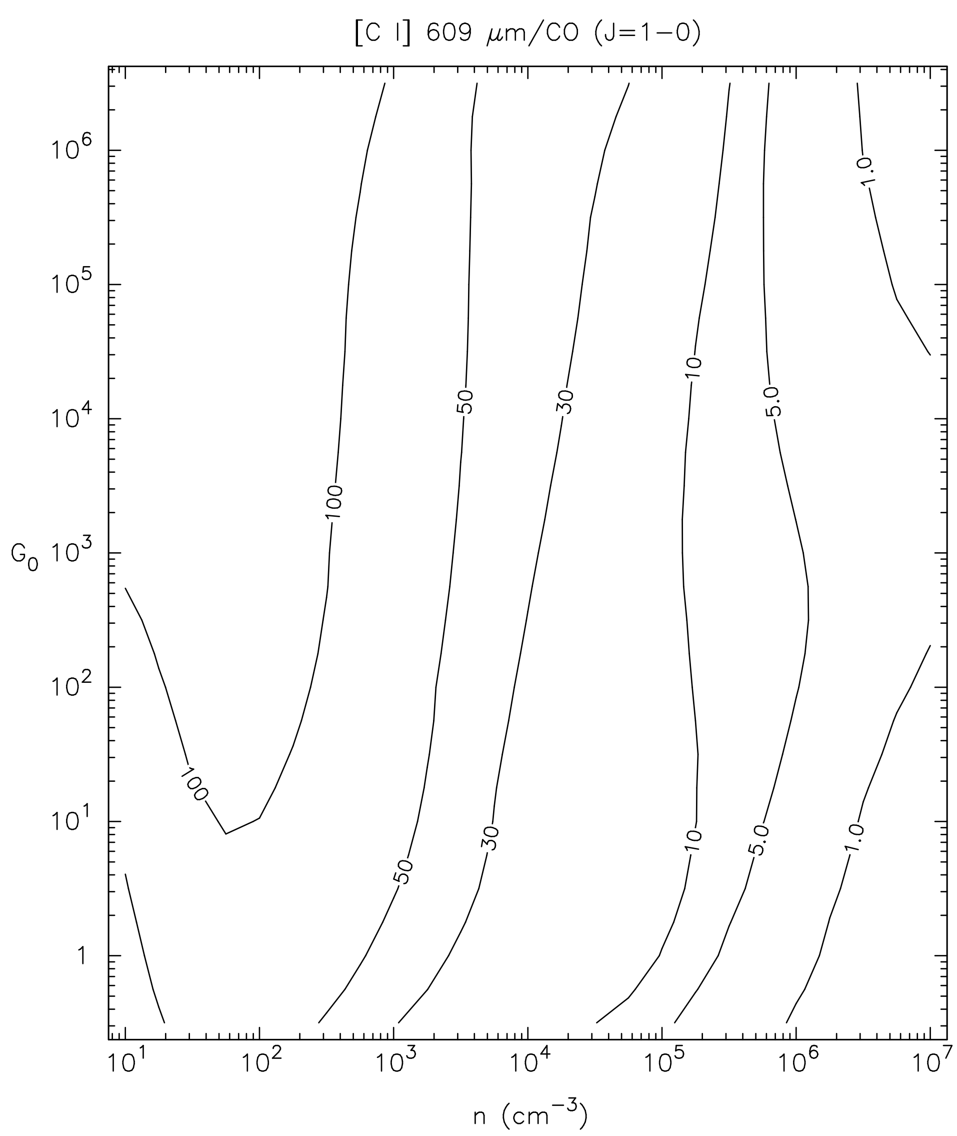

Fig. 1.9.— Emergent Intensity ratio of [C I] 609μm / CO(J = 1 → 0) as a function of incident FUV intensity. See Figure 1.4 caption and text.

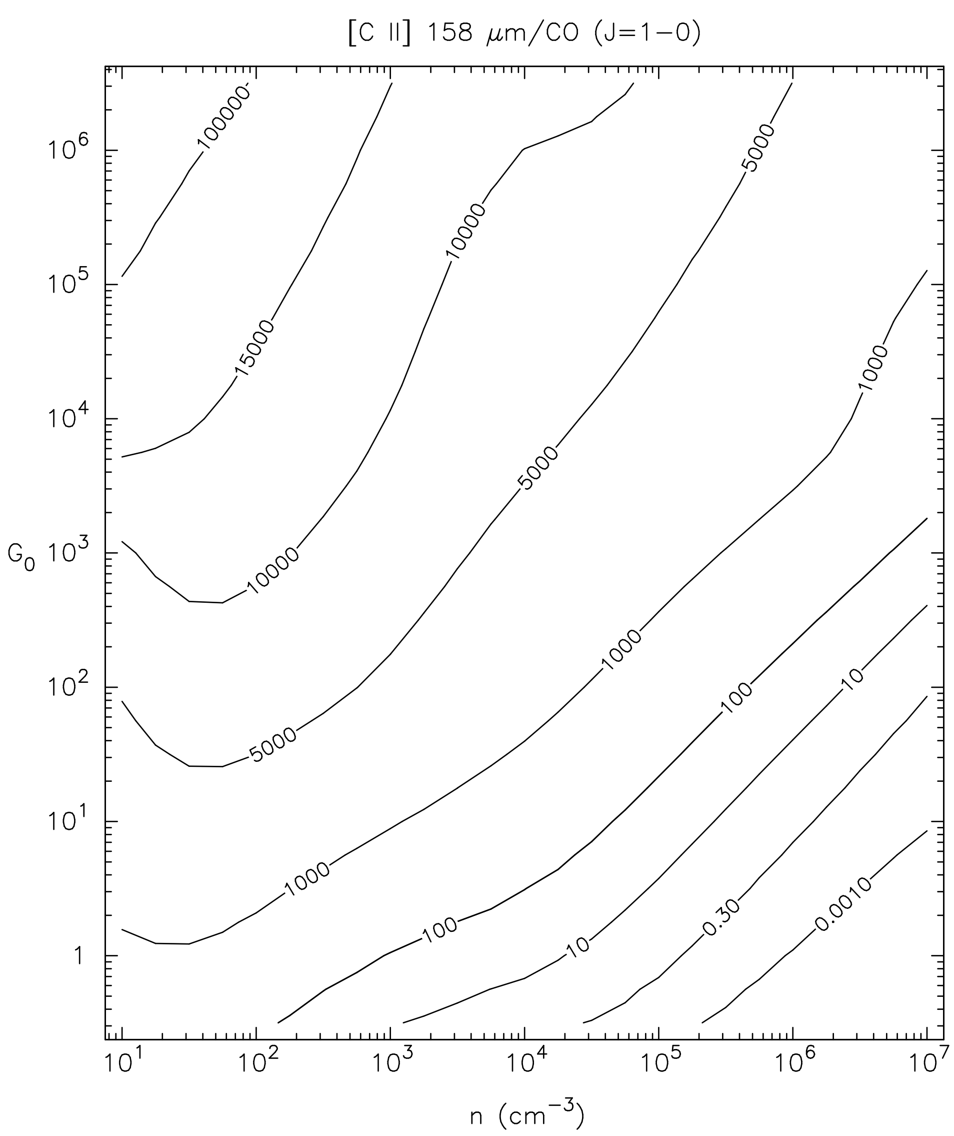

Fig. 1.10.— Emergent Intensity ratio of [CII] 158μm / CO(J $= 1 \rightarrow 0$) as a function of incident FUV intensity. See Figure 1.4 caption and text.

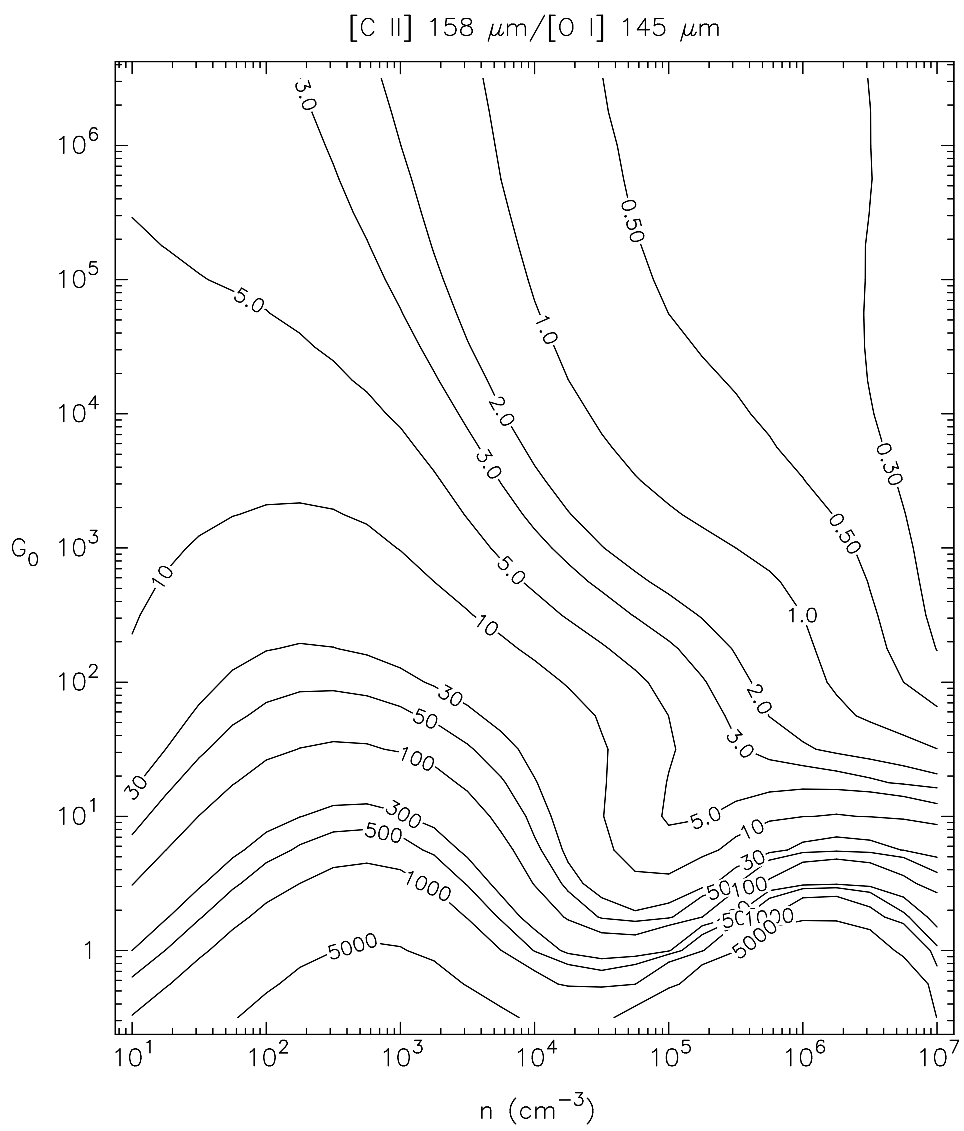

Fig. 1.11.— Emergent Intensity ratio of [CII] 158μm / [OI] 145μm as a function of incident FUV intensity. See Figure 1.4 caption and text.

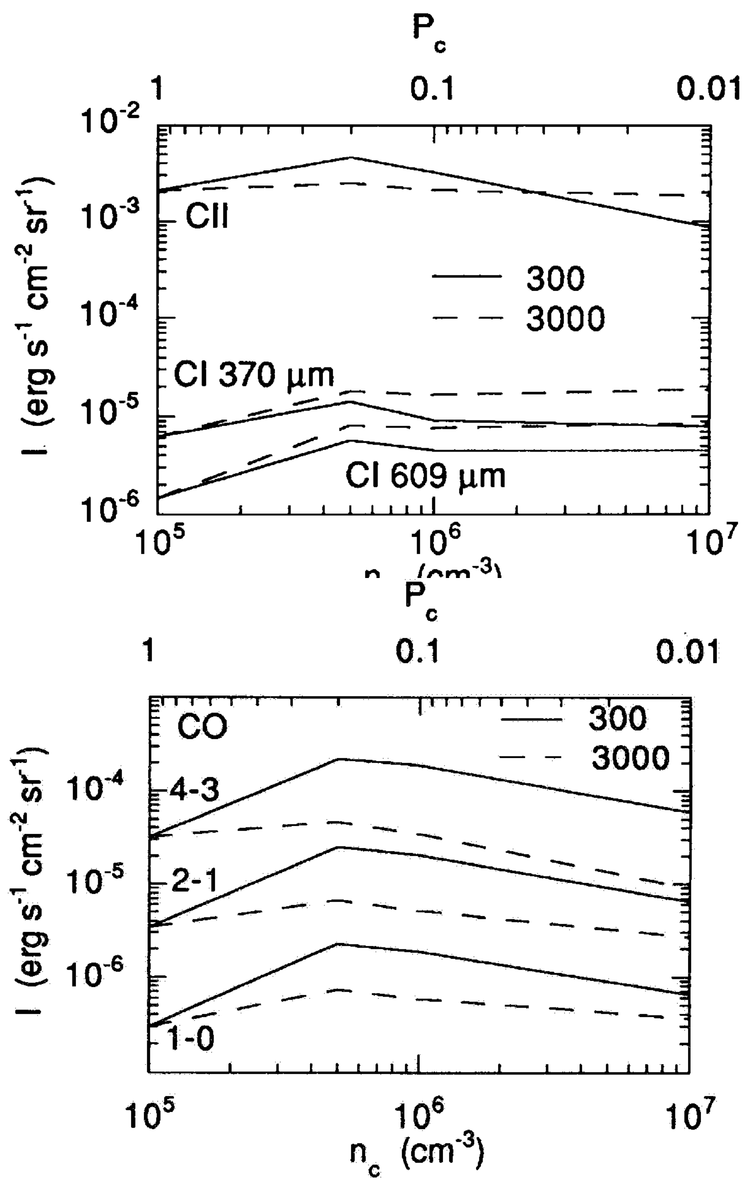

Fig. 1.12.— Intensities of C^+, C I, and CO emission as a function of hydrogen density in the clumps, n_c, calculated using clumpy PDR models (Figure reproduced from Meixner & Tielens 1993). Models with two inter-clump densities are shown. Solid lines refer to inter-clump density of $300\,\mathrm{cm}^{-3}$; dashed lines denote an interclump density of $3000\,\mathrm{cm}^{-3}$. The clump filling factor, P_c, is marked at the top of each panel. See text for details of the models.

4. In §4 for the sample sources I map the CO(4-3) emission intensity and gather the CO(1-0) observational results from the literature. The gas temperature and the lower limits to the density can be calculated using the CO intensities assuming that the line emission regions are well-mixed. After deriving the emergent line intensity of the CO transitions, I calculate the line ratios of [C I] 609μm / CO(4-3), [C I] 609μm / CO(1-0), and [CII] 158μm / CO(1-0).

5. In §5 I use these line intensities and intensity ratios to constrain G_0 and n using the PDR models described here. To do so, the plots in Figures 1.4 to 1.11 are used to obtain a set of G_0 and n consistent with each *individual* PDR observational diagnostic. These are the PDR theoretical predictions. Then I evaluate the consistency of these results by finding out whether these G_0 and n pairs are compatible with each other. The G_0 values derived from the observed FIR luminosities are compared with those gotten from PDR models.

6. In order to make direct comparison between PDR density and temperature with observations, volume (cm^{-3}) parameters need to be derived from observed column (cm^{-2}) parameters. This requires a geometrical assumption. The size of the C I emitting region is used as the size of the PDR region to convert tracer column densities to volume densities. A face-on geometry will be assumed, optical depth and self-absorption effects will be discussed. With this assumption of geometry, I compare the gas densities and temperatures obtained through observations (§2 to §4) with those predicted by PDR theory for the relevant G_0 and n pair.

Although the homogeneous and the clumpy PDR models have different predictions for PDR properties, the test methods for them are the same using the above steps because they all have slab global structures. Comparison of these models and my data and discussion of the results are presented in §5.1 and §5.3.

1.2.3. Confronting Models with Observations: PDR Geometry

PDR Geometry Considerations

Currently most PDR models are slab models. The FUV radiation fields are simplified to comprise only parallel incident rays illuminating the ISM. The PDR properties therefore change in plane parallel zones that are perpendicular to the direction of illumination. Even in the models of clumpy PDRs, the global change of the inter-clump medium characteristics still has a slab structure. In this slab PDR configuration, it is possible for an observer to view the PDRs from any direction. Traditionally the model calculations have been mostly tested in PDRs that have the simplest geometry: face-on or edge-on. In Figure 1.1, a face-on view of the PDR is when the observer sees the PDR from left, from the direction of the star that emits the FUV radiation. This geometry is what I assume to test the slab PDR model discussed in the previous section. An edge-on view is when the line of sight of the observer is parallel to the transition zones in the PDR. There is also the situation where the source star of the FUV field is behind the molecular cloud, therefore the PDR is between the observer and the star.

When an H II region forms inside a homogeneous molecular cloud the natural geometry of the photodissociation region developed around the central OB star should be spherical with layered structures. The gas temperature and species composition are functions of the visual extinction according to current one-dimensional PDR models. Figure 1.3 shows the Tielens and Hollenbach (1985b) calculation of the relative abundance of carbon species as a function of A_v. In an idealized homogeneous ISM, at the same distance from an OB star the visual extinction toward the star is the same. Identical photodissociation processes should take place at the same distance from the star. Therefore everywhere on a sphere centered on the star, the PDR gas properties should be identical. Figure 1.13 illustrates the concept of a spherical PDR.

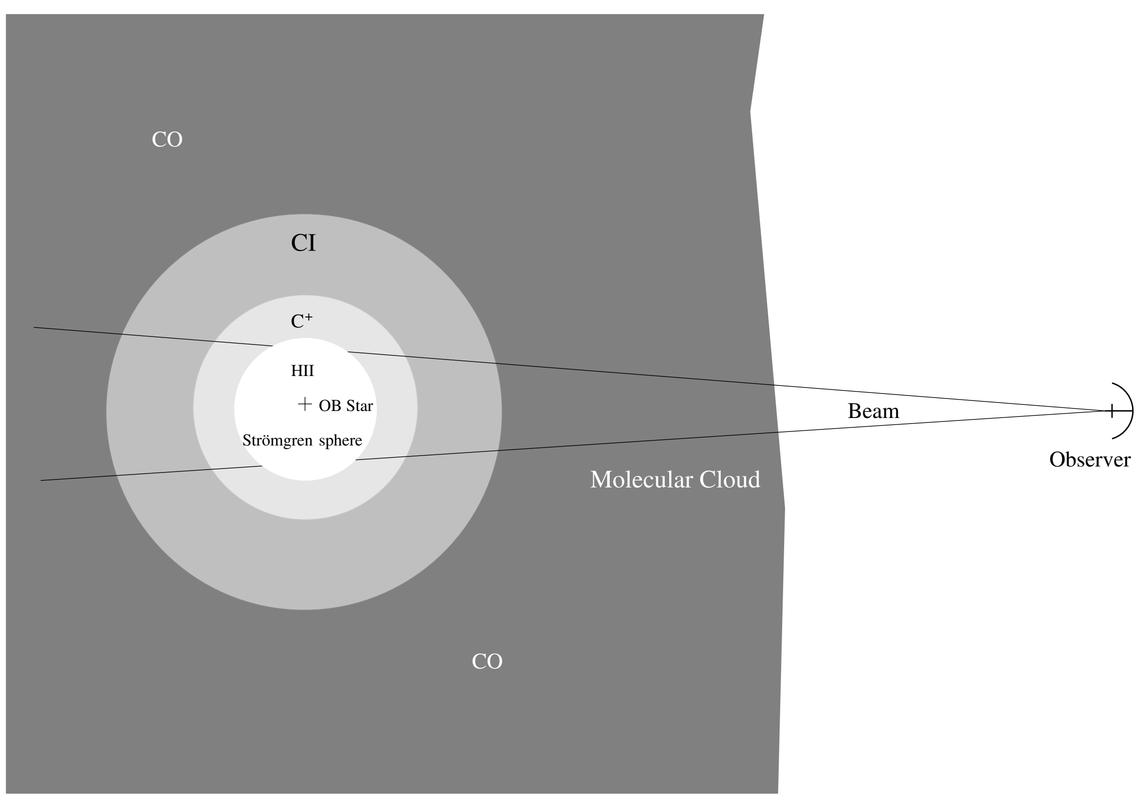

Fig. 1.13.— Schematics of a spherical PDR created around an H II region that has formed inside a homogeneous molecular cloud.

In this thesis I will investigate whether the spherical geometry PDR exists around my sample of H II regions, use my data to test PDR predictions in a spherical PDR with a geometric dilution effect, and estimate how common spherical PDRs are in the Galaxy (§5.2).

Predicted Characteristics of a Spherical PDR

A spherical PDR geometry implies specific, observable morphological and kinematic properties. First the morphology of a spherical PDR should have a single symmetric peak when seen in emission tracing the photodissociation effect of the central OB star. The peak of any PDR tracer should also spatially coincide with the H II region Strömgren sphere around the OB star, which is delineated by the RRL and free-free continuum emission. Assuming the movement of the ISM around the OB star is also spherically symmetric with respect to the star, similarities in kinematic properties should be found in the ionized gas and the PDR gas. In this thesis I will test these predictions by mapping PDR tracer emission around H II regions (see §3 and §4).

Emission line properties for carbon species can be predicted based on the spherical geometry and the homogeneous slab PDR models. The effect of geometrical dilution of the FUV field on the PDR structure is to accelerate the transition from the ionized ISM component to the molecular component as the radial distance from the star (therefore the visual extinction) increases.

The geometrical dilution effect around H II regions can be observed from the emission line ratios of carbon species. The effective attenuation caused by geometrical dilution at a distance, R, from the central star, when expressed in magnitudes, is:

$$A_d = 2.5 \log(\frac{R^2}{r_s^2}) \tag{1.10}$$

where r_s is the Strömgren sphere radius, measured from mapping the H II region in the radio continuum. Since the size of the PDR can be measured by mapping the PDR in C I emission, the effective extinction caused by dilution in a spherical PDR can be estimated. For a C I region 4 times the size of the H II region (a typical value as shown in §3), at the outer border of the C I region the geometrical dilution is $A_d \approx 3^{\mathrm{mag}}$. This is significant since according to the homogeneous PDR model the C^+ to CO transition happens within $A_v \approx 4 \sim 5$ mag.

In §5.2 I compare observations with the spherical PDR model. Because of the unexpectedly large AST/RO telescope beam (see §3 and §4), the observational data in this thesis can unfortunately only weakly test the predictions of the spherical PDR model.

I make the investigation in three steps: (1) I first calculate G_0 and n based on the emission intensity of I_{CI} and I_{CII}; (2) I then apply A_d to the resultant G_0 to predict an I_{CO}/I_{CII} value; and (3) I compare the predicted I_{CO}/I_{CII} value with the observed one. The A_d used is calculated using Equation 1.10 and the PDR size measured with C I mapping.

1.3. H II Region Sample with Large G_0 Range

The source selection criteria for this thesis define a sample of H II regions spanning a wide range of G_0 (U). With such a sample the extremes of PDR theory can be probed. Ideally one would want to map the sources to get spatial and kinematic distributions of all carbon species in ionized (C^+), neutral (C I), and molecular (CO) states. Here I have done this for C I and CO, but not for C^+ due to the unavailability of the necessary instrumentation.

Here I attempt to overcome limitations of past studies of the ISM near H II regions. As has been noted, one of these limitations is that the most detailed studies have been performed on a handful of well-studied, nearby "test-bed" sources. Another limitation is more subtle. It is that the sources selected for previous detailed PDR studies have historically been biased toward optical H II regions that are generally large, old, and of low density. Mine is a large sample of sources selected from a radio H II region catalog, with an emphasis on compact H II regions. Consequently my study will have a larger statistical base and a focus shifted to the more compact H II regions.

1.3.1. The Mapped Survey Sample

A sample of H II regions was chosen to be observed with the Long Wavelength Spectrometer (LWS) on the Infrared Space Observatory (ISO) satellite. The details of the LWS instrument on-board the ISO satellite are described in §2 as are the ISO observing proposals. The goal of these observations is to obtain C^+ and O line ratios, as well as line-to-continuum flux ratios. The sources were selected from the Caswell and Haynes (1987) RRL catalog. The source selection criteria, in the order of descending importance, include:

1. Not in the ISO reserved source list
2. Position in the visibility window of the ISO satellite
3. The IR continuum strong enough to be observed in the LWS LW01 AOT observing mode
4. The IR continuum not strong enough to saturate the LWS
5. Visible by AST/RO
6. Small size in radio continuum to fit into ISO LWS aperture
7. Covering as wide a range as possible in the U parameter

8. Covering as wide a range as possible in Galactocentric distance

9. Isolated morphology to make estimating the UV field easy

A total of 64 sources and 6 reference positions were proposed for ISO observations for the initial observing period. The sources in this sample are listed in Table 1.1.

Unfortunately the scheduling of ISO observations was beyond my control. Only 11 sources and 2 reference positions were observed before ISO exhausted its supply of liquid He cryogen. I will refer to these observed sources as "ISO sources" hereafter. ISO detected C^+ emission in every one of the 11 sources with good signal to noise ratios. In addition, the IR continuum in the full 42μm to 195μm wavelength range of the LWS and a series of O lines and N ion lines were observed.

As discussed in §3, these ISO sources plus an extra source G291.28−0.72 were mapped in C I emission to obtain spatial information about the C I distribution, the C I gas column density, and the C I mass. For this reason this sample of H II regions is also called "the mapped survey sample". I have also mapped this sample in CO(4-3) to study the mid-J CO transition emission properties of the PDRs (see §4). Because of equipment problems the CO(4-3) map quality is not good. Chapter 4 also compiles results of single-point observations in the J=1-0 transition of CO from the literature for this H II region sample. Since CO(1-0) traces colder molecular gas, these data help to probe the CO over larger spatial scales in the ISM, although at the expense of many complications such as different calibration, optical depth, beam sizes, etc.

Table 1.2 lists the mapped source name, position in Right Ascension and Declination (J2000.0), Galactic coordinates, velocity given in the RRL catalog, and

TABLE 1.1

Proposed ISO Sources

name	OSN[a]	α (2000.0) (h m s)	δ (2000.0) (° ′ ″)	name	OSN[a]	α (2000.0) (h m s)	δ (2000.0) (° ′ ″)
G307.62−00.32	01	13 32 39.6	−62 48 57.0	G342.08+00.42	55	16 52 37.8	−43 22 28.0
G308.65+00.58	03	13 40 01.2	−61 45 08.9	G334.71−00.67	56	16 28 58.6	−49 37 17.7
G311.49+00.37	05	14 03 37.9	−61 17 54.7	G344.44+00.05	57	17 02 11.5	−41 46 02.0
G316.81−00.04	07	14 45 21.0	−59 48 14.0	G338.41−00.24	58	16 42 01.4	−46 36 27.3
G317.04+00.30	09	14 45 51.3	−59 24 05.0	G342.30+00.31	59	16 53 50.5	−43 16 38.0
G300.96+01.16	10	12 34 47.2	−61 38 48.7	G345.03+01.54	61	16 57 53.9	−40 22 51.0
G317.29+00.27	11	14 47 45.8	−59 19 17.0	G345.21−00.75	63	17 08 06.4	−41 37 55.0
G308.09−00.43	12	13 36 54.0	−62 50 50.6	G345.43−00.94	64	17 09 35.8	−41 34 39.1
G317.99−00.76	13	14 56 19.7	−59 55 42.0	G345.31+01.47	65	16 59 05.0	−40 12 23.0
G311.63+00.27	14	14 04 57.8	−61 21 15.4	G345.40+01.41	67	16 59 39.7	−40 10 16.0
G319.16−00.42	15	15 03 11.7	−59 04 47.0	G345.50+00.33	69	17 04 26.6	−40 45 38.0
G321.71+01.16	17	15 13 49.4	−56 25 57.0	G346.54+00.10	70	17 08 42.4	−40 03 53.8
G322.15+00.61	19	15 18 38.0	−56 39 45.0	G345.56−00.04	71	17 06 11.1	−40 56 07.0
G322R	20	15 09 26.9	−54 31 31.4	G345.6R	72	17 16 59.5	−42 24 42.0
G326.96+00.03	23	15 48 42.9	−54 21 12.0	G347.39+00.27	73	17 10 37.2	−39 17 01.0
G318.06−00.46	24	14 55 43.4	−59 37 48.1	G347R	74	17 00 25.9	−37 46 23.9
G327.83+00.11	25	15 53 00.3	−53 44 24.0	G348.23−00.98	75	17 18 24.5	−39 19 37.0
G328.59−00.52	27	15 59 40.8	−53 44 09.0	G336.5R1	76	16 40 03.2	−48 51 15.1
G331.52−00.07	29	16 12 02.5	−51 26 56.0	G348.71−01.03	77	17 20 02.8	−38 57 31.0
G332.66−00.61	31	16 19 42.0	−51 02 37.0	G336.5R2	78	16 40 00.0	−48 51 45.1
G332.79−00.56	33	16 20 05.0	−50 55 26.0	G349.84−00.54	79	17 21 15.2	−37 45 11.0
G333.04+02.02	35	16 10 07.3	−48 52 56.0	G291.61−00.53	80	11 15 05.0	−61 15 41.0
G333.17−00.08	37	16 19 38.7	−50 18 50.0	G350.52+00.96	81	17 17 04.6	−36 20 01.0
G326.44−00.40	38	15 47 44.3	−55 00 34.6	G351.62+00.17	83	17 23 22.6	−35 53 17.0
G333.29−00.37	39	16 21 28.7	−50 25 57.0	G336.73+00.07	84	16 34 05.0	−47 38 44.2
G336.51−01.48	41	16 40 06.1	−48 50 47.0	G351.64−01.24	85	17 29 13.9	−36 39 15.0
G336.84+00.05	43	16 34 37.5	−47 34 59.0	G339.09−00.22	86	16 44 31.2	−46 04 43.1
G337.15−00.18	45	16 36 51.0	−47 30 36.0	G351.69−01.17	87	17 29 05.0	−36 34 15.0
G337.95−00.48	47	16 41 18.0	−47 06 31.0	G353.03+00.88	89	17 24 24.9	−34 19 03.0
G337.9R	48	16 52 40.6	−48 43 36.7	G353.14+00.66	91	17 25 34.7	−34 21 26.0
G338.09+00.01	49	16 39 43.1	−46 41 06.0	G353.21+00.91	93	17 24 47.2	−34 09 42.0
G327.31−00.54	50	15 53 03.7	−54 34 20.8	G353.43−00.37	95	17 30 31.3	−34 41 00.0
G338.45+00.06	51	16 40 53.0	−46 22 39.0	G349.14+00.02	96	17 16 54.3	−38 00 23.0
G333.61−00.21	52	16 22 09.8	−50 05 33.4	G353.56−00.01	97	17 29 25.6	−34 22 56.0
G340.78−01.01	53	16 54 12.2	−45 17 34.0	G356.23+00.67	98	17 33 41.4	−31 46 09.8

[a]Observation Sequence Number.

TABLE 1.2

OBSERVED ISO SOURCES [a]

name	α (2000.0) (h m s)	δ (2000.0) (° ′ ″)	l (°)	b (°)	RRL $V_{\rm LSR}$ (km sec^{-1})	Ref. Pos.[b] (′,′)
G291.28−0.72 [c,1]	11 11 53.1	−61 18 56	291.277	−0.717	−25	±30,0
G316.81−0.04 [2]	14 45 21.0	−59 48 14	316.808	−0.037	−36	−30,0
G322.15+0.61 [3]	15 18 38.0	−56 39 45	322.153	+0.613	−52	−36,0
G332.66−0.61 [4]	16 19 42.0	−51 02 37	332.662	−0.607	−48	+40,0
G333.29−0.37 [5]	16 21 28.7	−50 25 57	333.292	−0.371	−50	+42,0
G336.84+0.05 [6]	16 34 37.5	−47 34 59	336.840	+0.047	−79	+45,0
G337.15−0.18 [7]	16 36 51.0	−47 30 36	337.147	−0.181	−73	+46,0
G337.95−0.48 [8]	16 41 18.0	−47 06 31	337.949	−0.476	−40	+41,0
G340.78−1.01 [9]	16 54 12.2	−45 17 34	340.777	−1.008	−25	+46,0
G345.31+1.47 [10]	16 59 05.0	−40 12 23	345.308	+1.471	−15	−50,0
G348.71−1.03 [11]	17 20 02.8	−38 57 31	348.715	−1.031	−13	+36,0
G353.21+0.91 [12]	17 24 47.2	−34 09 42	353.206	+0.905	−4	+46,0
G322R	15 09 26.9	−54 31 31	...	...	...	−30,0
G337.9R	16 52 40.6	−48 43 36	...	...	...	+30,0

[a] The source optical identifications listed below include: 1) the sources found within 4' radius using the SIMBAD database; and 2) nebular identifications found in the SIMBAD database. Keys: IR, IRAS, IRSV: Infrared sources found in previous observations and surveys; Masers: maser sources; NGC: nebula; RCW: Rodgers et al. (1959), a catalog of H_α emission; *X: star of X spectral type.

[b]Reference Position for position switched AST/RO C I and CO observations. Positions are $d\alpha$ and $d\delta$ relative to the source position. The reference positions are relatively emission-free nearby positions on the 100μm IRAS maps.

[c]This source was not observed by ISO.

[1] NGC3576, RCW57A, *B, nebula in Visible and red

[2] Maser, IRAS, thin weak red nebula

[3] Maser, IRSV, weak red clouds separated by dark bands

[4] Maser, IRAS, fragmented cloud in short-red. invisible in IR

[5] Maser, IRAS, invisible

[6] Maser, IRAS, very faint large cloud in red

[7] Maser, IRAS, *K7, faint IR cloud in background; dark in blue, cirrus-like in short-red

[8] Maser, IRAS, very faint sign of background clouds

[9] IRAS, RCW110, Gum, *O+, Invisible in IR, nebula 4' north in red, short-red, J

[10] IRAS, *O+, nebula visible in IR, bright in red

[11] IR, RCW112A, Maser, blobs of nebula in red around within 1'

[12] IR, IR reflection+dark nebulae, strong red 3~4' size, NGC6357, dark to the East

the relative position(s) of the reference positions used for the AST/RO mapping observations. Below the table are listed identifications of the sources that lie within $4'$ of the H II region. Also given are the optical identifications based on my visual examination of the scanned photographic plates of the source. The plate data base is provided by SIMBAD, and consists of the *Space Telescopes Science Institute Digital Sky Survey (DSS-I)* in blue (J), and visible (V) bands (image size $14.1' \times 14.1'$), the AAO survey in red, and the *Centre d'Analyse des Images (CAI) ESO sky survey* in "short-red", red, and infrared (image size $11.8' \times 11.8'$) bands. The optical identification information is an indicator of the relative position between the H II region and the nearby molecular cloud. This information will be used in later chapters to help resolve the PDR geometry.

1.3.2. The Pointed Survey Sample

In order to find out the basic properties of C I emission around H II regions in general, I need to observe a large sample of H II regions that has a wide span of excitation conditions. The 12 mapped survey sources do not span a broad excitation parameter range with good coverage. For this sample the H II region U parameter distribution is only $47\ \mathrm{pc\,cm^{-2}} \leq \mathrm{U} \leq 131\ \mathrm{pc\,cm^{-2}}$.

In order to study a broader range of H II region excitation, I use the data from a Southern H II region survey made by AST/RO in 1995 Austral winter to complement the mapped survey sample. The observations were made on a sample of 49 Southern Hemisphere H II regions that cover a large range of excitation conditions ($46\ \mathrm{pc\,cm^{-2}} \leq \mathrm{U} \leq 295\ \mathrm{pc\,cm^{-2}}$). The source sample criteria are described in §3. Because long integrations were made for the pointed observations, this sample complements the mapped observations which were made with limited observing time.

TABLE 1.3

POINTED SURVEY SOURCES

name	α (2000.0) (h m s)	δ (2000.0) (° ′ ″)	l (°)	b (°)	RRL V_{LSR} (km sec^{-1})	Notes[a]
G6.528+0.076	17 57 05.04	−23 16 29.4	6.528	0.076	14.1	...
G265.144+1.450	8 57 37.92	−43 33 34.9	265.144	1.450	2.8	RCW36,op
G268.034−0.984	8 58 04.95	−47 20 13.6	268.034	−0.984	1.8	RCW38,*B
G285.261−0.048	10 29 36.17	−57 46 40.9	285.261	−0.048	−1.6	inv
G287.259−0.883	10 39 49.75	−59 29 12.0	287.259	−0.883	−17.0	...
G287.718−0.646	10 43 53.91	−59 29 30.5	287.718	−0.646	−26.0	*A,inv
G287.906−0.939	10 44 09.08	−59 50 18.5	287.906	−0.939	−20.7	eCar.*A0.*B
G291.276−0.717	11 09 44.77	−61 02 35.2	291.276	−0.717	−23.4	NGC3576,*B0V,RCW57
G291.610−0.528	11 12 53.00	−60 59 23.7	291.610	−0.528	9.4	NGC3603,RCW57B,*A0,*B7III
G298.227−0.340	12 07 23.83	−62 33 17.2	298.227	−0.340	30.6	inv v. faint small red neb
G298.837−0.347	12 12 37.84	−62 39 12.2	298.837	−0.347	25.0	inv *B+
G298.862−0.438	12 12 44.12	−62 44 49.2	298.862	−0.438	24.2	inv
G305.096+0.150	13 07 05.82	−62 22 35.4	305.096	0.150	−37.9	inv
G305.198+0.032	13 08 02.97	−62 29 12.7	305.198	0.032	−40.0	inv
G305.251+0.224	13 08 22.95	−62 17 29.3	305.251	0.224	−39.1	inv
G305.359+0.194	13 09 19.74	−62 18 47.1	305.359	0.194	−39.1	inv
G305.550+0.009	13 11 06.21	−62 28 54.4	305.550	0.009	−44.7	inv
G316.796−0.055	14 41 30.85	−59 36 53.2	316.796	−0.055	−36.1	inv
G322.164+0.625	15 14 48.96	−56 27 52.8	322.164	0.625	−51.8	RCW92?
G326.654+0.578	15 40 56.10	−53 57 13.3	326.654	0.578	−44.5	inv, RCW95?
G327.304−0.552	15 49 11.99	−54 26 31.6	327.304	−0.552	−48.8	RCW97, slight hint of Red neb
G328.312+0.433	15 50 17.95	−53 02 31.8	328.312	0.433	−96.2	inv
G331.529−0.084	16 08 21.88	−51 19 24.6	331.529	−0.084	−88.7	inv even in IR
G332.663−0.621	16 15 57.90	−50 55 59.2	332.663	−0.621	−47.0	inv
G332.815−0.567	16 16 24.98	−50 47 18.2	332.815	−0.567	−57.2	inv
G333.028−0.447	16 16 50.92	−50 33 13.4	333.028	−0.447	−53.8	inv *A2V
G333.122−0.446	16 17 16.01	−50 29 14.0	333.122	−0.446	−55.8	inv
G333.167−0.095	16 15 55.89	−50 12 16.8	333.167	−0.095	−90.8	*B6/*B7IV/V no neb
G333.293−0.382	16 17 45.05	−50 19 18.2	333.293	−0.382	−50.1	inv
G333.605−0.095	16 17 52.90	−49 53 54.0	333.605	−0.095	−53.7	inv
G333.610−0.217	16 18 26.18	−49 58 54.0	333.610	−0.217	−48.3	inv?, SNR ?
G336.427−0.251	16 30 33.20	−47 59 05.9	336.427	−0.251	−93.1	inv
G336.532−0.168	16 30 37.15	−47 51 05.7	336.532	−0.168	−88.6	? RCW108, NGC6193A
G336.807+0.043	16 30 49.05	−47 30 23.7	336.807	0.043	−78.9	inv
G336.934−0.146	16 32 08.99	−47 32 31.7	336.934	−0.146	−73.1	SNR?
G337.122−0.172	16 33 01.03	−47 25 17.6	337.122	−0.172	−72.7	inv
G337.753+0.126	16 34 13.82	−46 45 17.9	337.753	0.126	−52.5	...
G337.920−0.464	16 37 26.90	−47 01 35.4	337.920	−0.464	−40.4	inv
G338.425+0.053	16 37 09.92	−46 18 19.5	338.425	0.053	−36.9	inv
G340.793−1.014	16 50 38.97	−45 12 12.2	340.793	−1.014	−24.8	RCW110...11
G343.475−0.036	16 55 48.03	−42 30 14.1	343.475	−0.036	−30.3	inv
G345.210+1.020	16 57 08.90	−40 29 19.1	345.210	1.020	−9.4	inv
G345.385+1.398	16 56 09.93	−40 06 59.9	345.385	1.398	−14.6	inv
G347.611+0.205	17 08 06.93	−39 04 40.7	347.611	0.205	−96.2	inv
G348.719−1.040	17 16 38.98	−38 54 37.3	348.719	−1.040	−12.8	RCW122B
G351.347+0.663	17 17 16.07	−35 46 52.7	351.347	0.663	−3.2	inv
G351.419+0.644	17 17 32.91	−35 44 00.1	351.419	0.644	−5.0	inv
G353.191+0.890	17 21 29.88	−34 08 17.2	353.191	0.890	−3.8	inv
G353.122+0.642	17 22 17.91	−34 20 07.1	353.122	0.642	−4.1	inv

[a]The sources within 4' and nebular identification found in the SIMBAD database. Keys: IR, red, Red: Infrared sources or red ("red" for AAO survey, "Red" for ESO survey) nebula found at the source.; inv: no nebula found in visible or IR. NGC: nebula; RCW: Rodgers et al. (1959), a catalog of H_{α} emission; SNR: supernova remnent; *X: star of X spectral type; ?: questionable identification.

The properties of the H II regions in the pointed survey sample are listed in Table 1.3. The source name, position, and identification are listed, together with associated source identifications described in the same format as in Table 1.2.

TABLE 1.4

COMPARISON OF IMPORTANT OBSERVATIONAL PARAMETERS OF RRL CATALOGS

	Wilson et al. (1970)	Caswell & Hynes (1987)
System noise temperature (K)	110	70
Half Power Beam Width (′)	4.0	4.25
Position uncertainty (′)	1[a]	0.5
Spectrometer resolution (km sec^{-1})	6	2.3
Velocity uncertainty (km sec^{-1})	1.5[b]	1

[a]Implied by uncertainty of H II region angular size measurements.
[b]Wilson et al. catalog lists the uncertainty of V_{LSR} for each individual source. The value in the table is the average of the 11 sources that are in the Mapped Survey sample.

Sources in the mapped and pointed H II region samples were selected from different but related RRL catalogs. Both catalogs were based on observations made using the Australian Parkes 64m telescope at the same frequency, and using the same calibration techniques. Because of instrument changes, the catalog survey parameters were slightly different. Table 1.4 compares important parameters of the two catalogs (Wilson *et al*. 1970; Reifenstein *et al*. 1970; Caswell & Haynes 1987; Haynes Caswell & Simons 1978).

The data sample of my thesis provides a unique opportunity to confront PDR theories with observations. No previous PDR study has an H II region U parameter coverage as large as my sample. This is the first time that such a large sample of H II regions has been observed in all three forms of ISM carbon: ionized (C^+), atomic (C I), and molecular (CO).

1.4. The Antarctic Submillimeter Telescope and Remote Observatory (AST/RO)

In order to observe the ($^3P_1 \rightarrow {}^3P_0$) transition of C I, I need to use a telescope that can observe at 500 GHz frequency. Accurate C I measurements also require a stable submillimeter sky. The Antarctic Submillimeter Telescope and Remote Observatory (AST/RO) is unique in its ability to satisfy these requirements[1] . AST/RO is essential for collecting the data I need for my research in this thesis. Helping with the construction, installation, debugging, and routine observations has been my job in the project and has become an integral part of my research.

Here I give an overview of the AST/RO hardware system, and discuss the complexity of the integrated system. The software system of AST/RO is described. I use telescope tracking as an example of system complexity and integration.

1.4.1. AST/RO System Overview

In this section I give an overview on the AST/RO hardware system, so that the reader can understand the basics of the telescope. Detailed discussion of the specifications, design, fabrication, and maintenance can be found in the referenced technical documents.

The mechanical structure of the AST/RO antenna is shown in Figure 1.15. The telescope has an azimuth mount. Taking advantage of observing at the Geographic South Pole, the azimuth mount is equivalently an equatorial one. As a result Right Ascention position switched observations always switch between positions that do

[1] I

Fig. 1.14.— AST/RO was deployed at the Amundsen-Scott South Pole Station in the Austral summer of 1994-1995. The antenna is installed on an elevated steel structure directly on the Polar Ice Cap to avoid accumulation of snowdrifts at the building base. The antenna is exposed to the environment (shown here) most of the time. There is also a cover which provides a shielded environment so that people who are working on the telescope are not exposed to the elements. The 1.7 meter primary dish and its supporting truss can be seen in this photograph. Also shown is the cylinder shaped optical guide telescope installed for star pointing. The main South Pole base is the Geodesic Dome, located about 1 kilometer away from AST/RO. Shown here an LC130 Hercules cargo plane similar to the one that flew AST/RO to the Pole.

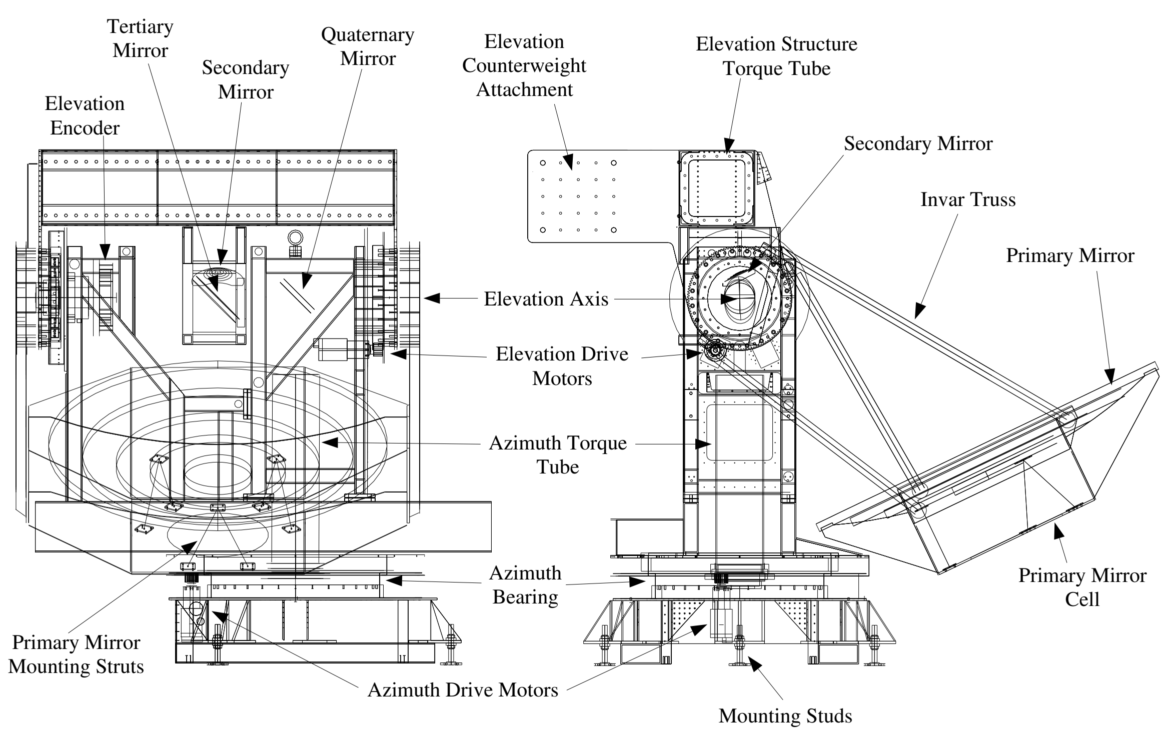

Fig. 1.15.— The AST/RO antenna has an azimuth mount, which simplified the design and construction of the telescope. At the Geographic South Pole, it is also an equatorial mount. This figure shows that the telescope is offset both in azimuth and elevation. The primary mirror cell is connected to the elevation torque tube using an Invar truss. The azimuth and elevation encoders are mounted outside their respective axial torque tubes. Two drive motors that exert torque in opposite directions serve each axis to eliminate any blacklash. (Figure from Stark *et al*. 1997)

not change their elevations when the telescope tracks. This has contributed to the high sensitivity and stability of the system. The AST/RO telescope is installed on top of a steel building constructed on the Polar ice-cap at the Geographic South Pole at an elevation of 2850 meters above mean sea level. The tower which the telescope resides on is decoupled from vibrations generated inside the AST/RO building (and vice versa).

The optical design of the telescope helps to minimize the baseline problems caused by stray radiation in the optical path. AST/RO employs an off-axis configuration that keeps the secondary mirror and its supporting structure out of the sky radiation collected by the primary mirror (figure 1.15 and figure 1.16). This helps to reduce the reflection of stray radiation by the mirrors, the secondary mirror mount, and the supporting structures of the telescope. Such stray radiation can come from the celestial source, the sky, the thermal radiation from the ground, and also it includes forwardly leaked radiation from the receiver LO system.

The telescope has a parabolic primary mirror made of carbon-fiber. The surface accuracy is better than 10μm RMS which surpasses the optical imaging requirement at 810 GHz (1/20 of 370μm wavelength). This highly accurate surface allows AST/RO to operate at frequencies as high as 1.5 THz, making it suitable for observations at wavelengths ranging from 200μm to 2000μm.

The receivers on AST/RO use state-of-the-art heterodyne SIS-junctions cooled to liquid helium (LHe) temperatures. These receivers achieve a sensitivity that approaches the quantum limit. There is a 230 GHz receiver and a quasi-optical receiver working at 492 GHz (Zmuidzinas *et al.* 1993; Engargiola, Zmuidzinas, & Lo 1994). A dual-junction receiver designed to observe at 490 GHz and 810 GHz (Walker *et al.*) was installed in 1997. This receiver can also be tuned to 460 GHz

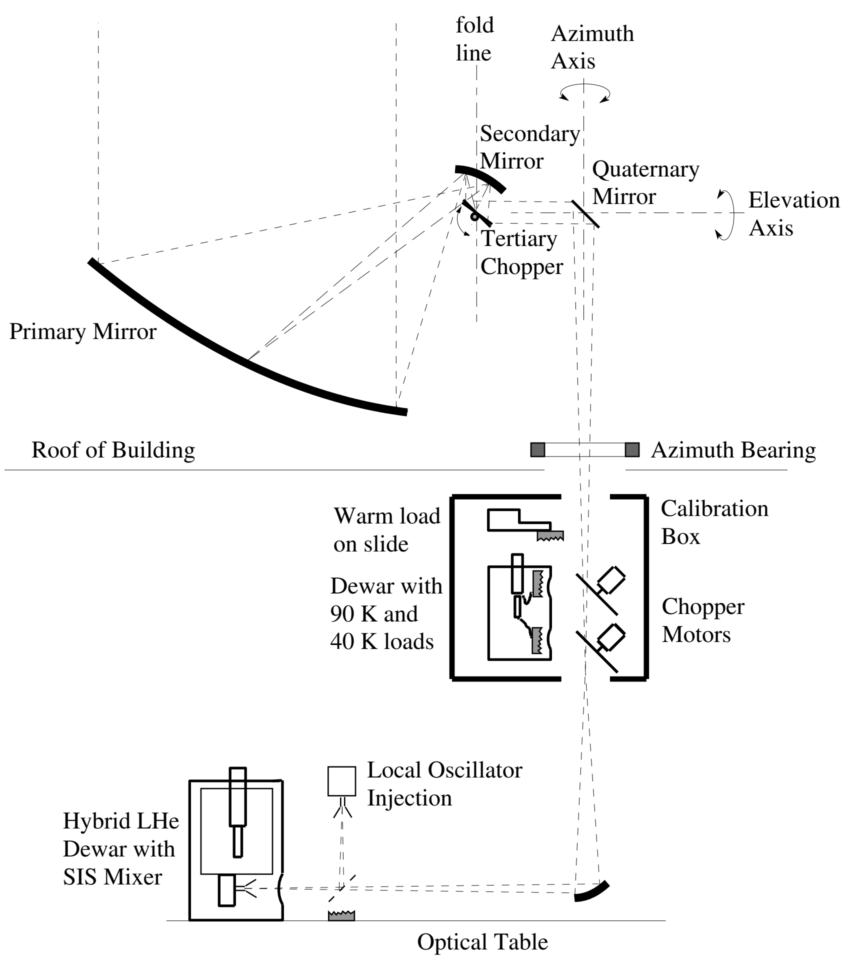

Fig. 1.16.— AST/RO has an offset optics system. As shown in this figure (also see Figure 1.15) the secondary mirror and tertiary chopper assemblies are out of the path of the celestial radiation that falls onto the primary mirror. The beam path is projected onto 2-dimensions at the "fold line" in this schematic presentation. The tertiary mirror is at the exit pupil so that when it chops, the illumination on the primary stays constant. The calibration box hosts two refrigerated calibration loads and a room temperature load. By means of rotational choppers and linear load-slides, various loads can be switched into the receiver beam. The receivers and alignment mirrors are installed on a optical bench suspended below the base of the antenna. (Figure from Stark *et al*. 1997)

to observe the CO(4-3) transition.

There are a set of mirrors used to feed radiation collected by the antenna to the receivers. Different receivers can be switched in and out of the telescope beam by means of a linear slider under computer control as schematically shown in Figure 1.17 (Described as the “Beam Switching Mirror Motor”). The size and shape of each receiver's beam is affected by the alignment of the mirrors in the optical path. Under-illuminating the primary mirror can cause the beam to be too big. This unfortunately was the case in the 1998 and 1999 seasons which adversely affected the C I and CO(4-3) beam.

After celestial radiation at a given sky frequency is mixed, amplified, and down converted, the intermediate frequency (IF) signal from a receiver is fed into an Acousto-optical Spectrometer (AOS) to obtain spectra. The AOSes are designed and fabricated by the University of Cologne (Schieder *et al*. 1989). For AST/RO, there are two 2048-channel low resolution AOSes with a channel spacing of 0.674 MHz, and a 2048-channel high resolution AOS with a channel spacing of 0.033 MHz. The FWHP channel width is about 1.5 times the channel spacing of these AOSes.

The AST/RO control computer runs the Lynx Realtime Operating System (LynxOS hereafter) on a rack-mounted Intel x86 CPU PC. This computer not only controls the hardware of the system but also serves as a data collection computer. Data collected by the AOSes are transfered to the AST/RO control computer. These data are then calibrated and stored to the hard-disks.

There are several aspects of the system that need to be calibrated: the intensity calibration for received celestial radiation, the frequency calibration, and the mechanical pointing calibration. From here on, the word “calibration” is used to refer to the intensity calibration unless otherwise specified.

The calibration system measures the power from blackbody loads of different temperatures, and calculates the system gains and the receiver temperature. As shown in Figure 1.16, two blackbody loads are kept in refrigerated dewars at radiometric temperatures of 80 K and 150 K; another blackbody load is kept at room temperature, ~290 K. These loads can be switched into the beam path by rotating choppers or a motorized linear slider.

The calibration procedure, which includes the measurement of the zenith opacity and the system efficiency, is discussed in detail by Ingalls (1998). Every spectral measurement of AST/RO is calibrated using a combination of blackbody load calibration and skydips. Periodic skydips are made to calculate the zenith opacity and sky slab temperature. This calibration process is done off-line in the data processing software COMB. The calibration of my data is described in more detail in subsequent chapters.

Frequency calibration of the system requires the determination of two properties of the spectrometer: the center channel location and the channel frequency spacing. The center channel is where a spectral line at the system center frequency appears in the spectrometer channel space. In order to find out the center channel of the spectrometer, a signal at the nominal IF frequency is generated by a frequency synthesizer and fed into the spectrometer. The center channel of the spectrometer is determined by fitting the line profile with a Gaussian. The center of the Gaussian is the center channel. The channel spacing of the spectrometer is calibrated by feeding a set of frequencies at 100 KHz interval to the spectrometer. Gaussian fits to the line profiles of these frequencies yield a set of corresponding channel numbers. The frequency spacing is derived by a linear regression analysis of these data.

The procedure to obtain accurate pointing has been under investigation with great effort throughout the development period and the first several operating seasons of AST/RO. An optical guide telescope is used to make a pointing model that takes care of telescope tilt, skew, wobble, and sag effects. Maps of H II regions, together with Sun and Moon observations have been used to obtain radio beam precession and pointing.

1.4.2. The Complexity of the Integrated System of AST/RO

My major duty in the AST/RO project is to develop, maintain, and debug the software system. In order to do so efficiently, I find it is necessary to view the system as a layered structure. Although AST/RO is an antenna with a relatively small aperture, it is nonetheless a general purpose observatory so it possesses a great deal of complexity. AST/RO could not function without this complexity. The layered view of the system helps to manage its complexity.

The system is composed of three layers of complexity: the *Task Layer*, the *Command Layer*, and the *Macro Layer*. These three layers of complexity are implemented for the most part through the software program *OBS*. Although these layers are hierarchical, they are also relatively independent, so one can work on a problem at a certain layer without being bothered by the details of the underlying layer.

The Task Layer

The Task Layer is the fundamental level of the system. It provides basic functions such as tracking, command parsing, time keeping, etc. This layer co-ordinates the operation of various hardware devices in order to achieve these basic tasks. The Task Layer is implemented by low-level software routines as illustrated in Figure 1.17. All these tasks are essential to the proper operation of AST/RO. They include: (1) user command input and parsing; (2) time keeping and system synchronization (timing); (3) source position and frequency acquisition; (4) telescope motion control: tracking and pointing; (5) receiver tuning parameters initialization; (6) frequency tracking; (7) data acquisition and calibration; (8) data storage and record-keeping; and (9) system status monitoring and display.

Each of the tasks requires a particular set of hardware to be interfaced and controlled. Various AST/RO technical memoranda discuss in detail how these tasks are implemented. An example of the complexity in this layer is the telescope's pointing and tracking task (the motion control; see 1.4.3).

The Command Layer

The Command Layer combines a variety of tasks in order to perform a meaningful observational operation, such as a position-switched integration on a source. This layer is built on top of the Task Layer. It shields the underlying tasks from the operations belonging to this layer. This layer of complexity enables an observer to perform an observation by issuing simple computer commands.

Once the vital parameters for such basic operations are specified, an observer should not need to be concerned with the details of executing routine sequences of hardware tasks. To execute these procedures, the system provides computer *commands* that take parameters from the user and execute the low level tasks required. To do this the system usually needs to carry out several different tasks, some simultaneously, and others sequentially with precise timing. An example of complexity at this level is a position switched observation that integrates 30 seconds

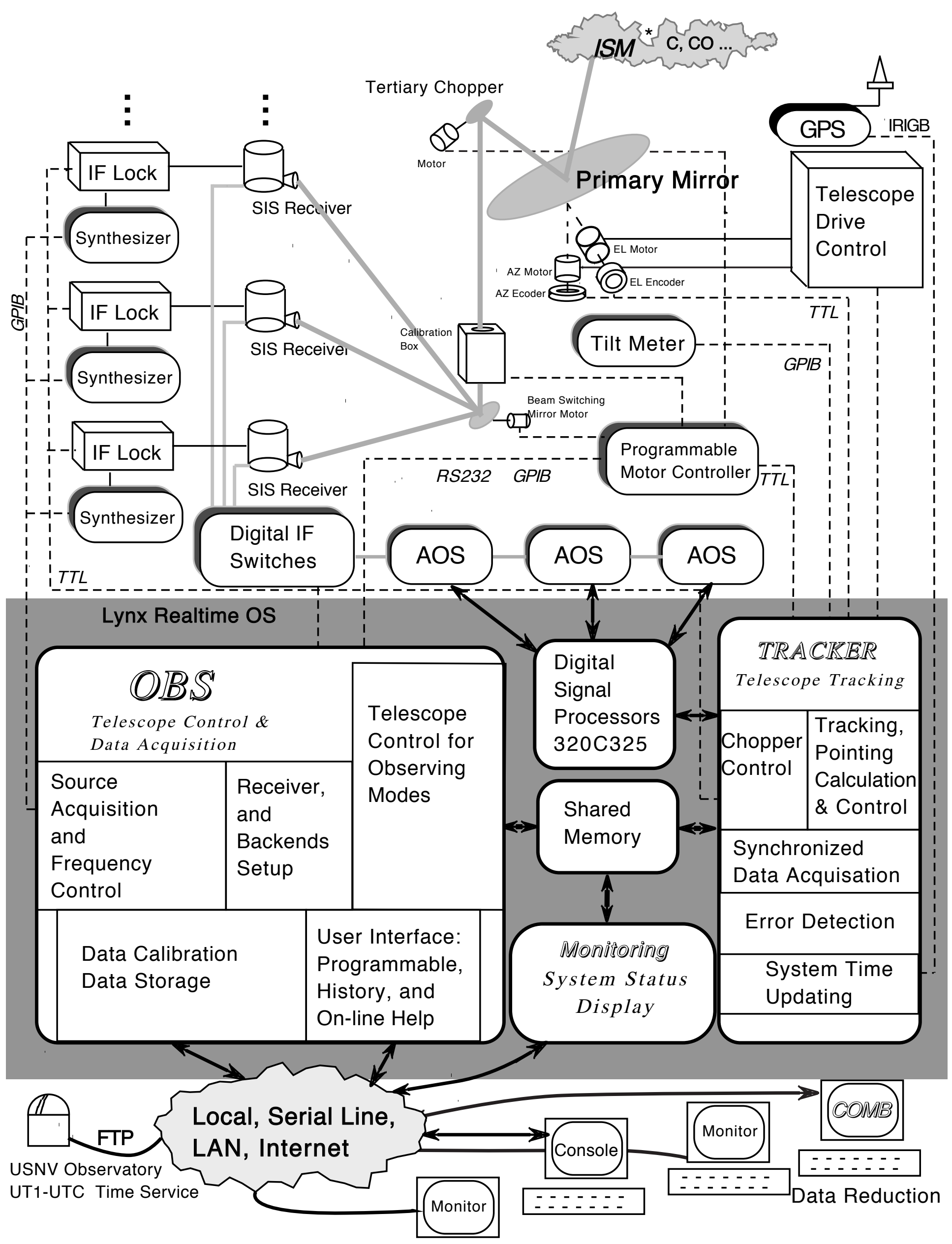

Fig. 1.17.— This block diagram shows the complexity of the integrated AST/RO system on the Task Layer. Using a variety of interfaces and protocols, the computer monitors and controls the hardware to fulfill an array of tasks that are the building blocks of a radioastronomical observation. The Shaded area shows the computer and software system.

on-source for each source-reference cycle, and executes 5 such cycles. The AST/RO *OBS* command for this observation is:

```
-> ps 30,5
```

The Macro Layer

The Macro Layer of complexity results from the requirement that AST/RO be a general purpose observatory where a variety of observations need to be made by one winterover scientist. The Macro Layer of complexity helps the observer to oversee many kinds of observational routines simultaneously. The observational requirements of AST/RO often need different hardware configurations, calibration sequences, switching modes, and mapping schemes. Some observations may need to perform a set of observing commands repeatedly, while others may need to execute different commands depending on the current state of the system and the weather. The observer needs to plan the observations based on the nature of the particular observation, the environmental conditions, the instrument's status, and the observer's own experience.

AST/RO provides a programmable user interface to facilitate the design and implementation of an astronomical observing program. The user interface allows basic observational commands to be scripted and executed. These scripts, called *macros*, can be stored and recalled as needed.

In addition to providing a programmable user interface, the system keeps the observer informed of the status of important parameters during the observation. It provides information about individual tasks (such as the scan counts and the tracking errors), as well as high level information about the progress of the astronomical observation.

1.4.3. AST/RO Software System

The software system is essential to operate AST/RO and to collect the type of data I need. Developing these vital software tools has been my contribution to the AST/RO project and this effort comprises an important part of this thesis. As just discussed, by using Task Layer software the computer manages the routine control of most of the system. Thus the higher levels of telescope monitor and control are entirely solved by carefully programmed computer software. The *OBS* software package (*OBS* hereafter) communicates with the observer, controls the telescope, and collects data. *OBS* resides on the AST/RO control computer.

Overview of the Software System OBS

OBS was originally written for the 7-meter radiotelescope at Bell Laboratories. Many people have contributed to its development. During its evolution, *OBS* has undergone many changes in commands, features, the language it is written in, and in the computer hardware platforms it runs on. During the past 20 years *OBS* has been evolving with new developments in telescope, receiver, and spectrometer technologies. The progress in observational techniques and the revolution of information technology symbolized by micro-controllers, personal computers, and the Internet have also changed the way *OBS* operates.

The skeletal structure of Bell Labs *OBS* is preserved in the AST/RO reincarnation, mostly due to the fact that both the 7-meter telescope and AST/RO are single dish telescopes that have similar control and observational requirements.

This similarity can be best seen in that the Bell Labs *OBS* and AST/RO *OBS* share a similar set of user commands. I have been working mostly on solving the Task Layer and Macro Layer complexities that are associated with the peculiarities of AST/RO.

OBS provides the underlying mechanism to solve all three layers of complexity. Part of *OBS* monitors and communicates with actuators and hardware controllers through a variety of I/O interfaces (TTL, RS232, GPIB, SCSI, etc.). *OBS* provides a command line based user interface that takes command language instructions from the observer and executes these commands according to the options given.

The user interface of *OBS* enables the user to write sophisticated script programs (*macros*) to control the telescope. The parser of *OBS* allows the user to compound commands to create structured macros. The command line parser supports conditional change of executing sequences, provides pre-defined variables that reflect current system conditions (e.g., time, system parameters, statistics, error conditions, etc.), allows the user to define mnemonic variables, and supports macro nesting.

OBS can be remotely accessed from with either an RS232 serial line, or, more commonly, from a network. Both the observing and monitoring programs can be started remotely when the operator logs on the telescope-control computer from another host. In principle the observer can find out the current operational status of the telescope from any host on the Internet. This feature has eliminated the need for the AST/RO telescope operator to remain in the control building at all times. This makes it possible for a single winterover scientist to make observing schedules efficiently, and to integrate observing duties into daily life in the Station.

Example Task: Telescope Tracking

The tracking control of AST/RO is an example of how a typical task is accomplished by carefully integrating and coordinating many parts of the system. Most of the details of the software motion control are given in the *AST/RO Technical Memorandum #32 "Software for AST/RO Telescope Servo System*" in Appendix I.

In order to point to an object and track it, the system: (1) obtains the source position from the terminal through the parser; (2) acquires current time from the time-keeping circuit board in the computer (which needs to be initialized and synchronized with the GPS receiver); (3) calculates the precession and nutation corrections to convert the source position to the current epoch; (4) converts this coordinate system to azimuth-elevation; (5) applies pointing corrections to the coordinates to calculate the commanded telescope position (a pointing correction model needs to be prepared and installed in the system in advance); (6) finds out the current telescope position and velocity from reading the telescope axis encoders; (7) calculates an angular velocity command to move the telescope when the commanded position is different from the telescope position; and (8) iterates this procedure until the position difference is within a pre-set error margin.

Many hardware instruments are involved in order for the telescope to point and track correctly. In order to function on this level, the system requires that devices be initialized and kept in constant contact with the computer via a variety of interfaces. The computer is at the center of the stage in coordinating and fulfilling these telescope tasks.

1.5. Summary and Structure of Thesis

In this chapter I describe the goal of my thesis: to determine the physical conditions of interstellar carbon around H II regions, and to compare the theoretical models of PDRs with my observational results.

First I describe the basic physics of an idealized H II region. I explain ionization and recombination equilibrium, the Strömgren sphere, and the radio recombination lines (RRLs). I derive the Strömgren sphere radius and the excitation parameter, U, for an H II region created by the OB star in a simplified homogeneous hydrogen cloud. I summarize equations that allow the electron temperature, density, and the excitation parameter of an H II region to be derived from radio observations of the RRL and continuum emission.

Next PDR theories are introduced and the connections between PDRs and H II regions are summarized. I review a simplified model of a PDR: the homogeneous slab PDR model of Tielens and Hollenbach (1985b), and emphasize the importance of carbon species as a probe of the PDR. I show the results of the Kaufman *et al.* (1999) calculation of the slab PDR model as well as the clumpy models of Meixner and Tielens (1993). I describe my plan to test these models in this thesis.

Comparison between observations and PDR models requires that the source geometry be known. I discuss several possible PDR geometries and introduce the concept of a spherical PDR. Predictions of observable morphological and kinematic properties of spherical PDRs are made. I show the significance of the geometric dilution effect for spherical PDRs and outline how I will test this effect using my data.

Limitations of current PDR studies are identified: the observational support has mostly come from a limited number of well studied optical sources. It will help to overcome this limitation to observe carbon species in a large sample of H II regions that are selected from a RRL catalog and have a wide range of excitation condition.

I describe the selection criteria for the sources used in my thesis. According to the goal of my study I proposed a total of 64 sources to be observed by the ISO satellite. Only 11 sources were observed. I mapped these 11 sources in C I and CO(4-3), and gathered IR line and continuum data as well as CO(1-0) data from the literature. To complement the mapped sources I analyzed a pointed survey of 49 Southern H II regions observed on AST/RO. These sources have a wide range of U ($46\ \mathrm{pc\,cm^{-2}} \leq \mathrm{U} \leq 295\ \mathrm{pc\,cm^{-2}}$) and Galactic longitude distribution, and are observed with excellent signal to noise ratio C I spectra. I tabulate the names and positions of the mapped and pointed survey sample sources, as well as indicate any identifications with visible nebulae. This is the first complete data set of C^+, C I, and CO properties compiled for a sample of H II regions that is both large and has such a large U parameter coverage. This is a unique contribution to the study of PDRs.

At last I give an overview of the AST/RO system which enabled me to make the essential C I observations for this thesis. I give an overview of the hardware and software system, introduce the three layers of complexity, and explain how the *OBS* program overcomes these complexities to achieve structured control of the system. The telescope motion control is described (Appendix I) to illustrate how one single task is accomplished by carefully integrating and coordinating many parts of the system.

Structure of Thesis

In Chapter 2 after describing briefly the ISO satellite and its LWS instrument, I present the observational results for the ISO sources. Line intensities of CII, OI, and NIII emission and parameters of FIR continuum emission are listed for the ISO source sample. IRAS data are used to complement the ISO continuum data taken with the small LWS aperture. I derive line ratios and line-to-continuum ratios and estimate G_0 using the FIR continuum luminosity.

Chapter 3 presents AST/RO C I observations of H II regions, the pointed survey and the mapped (ISO) samples. The pointed survey sample observation and analyses are given in the first part. The second part discusses the mapped survey observations and analyses, and compares these results with the pointed survey. Here I develop a method to establish physical associations between C I components and the H II region, and derive the C I mass and density using Gaussian fits to the C I maps.

Chapter 4 discusses observations and analyses of CO(4-3) data for the mapped survey sample. Previous observational results of CO(1-0) emission from the literature are summarized. Here I estimate CO gas properties, and investigate the kinematics of C I and CO using their line parameters.

In Chapter 5 I first compare observational results for all the carbon species C^+, C I, CO with homogeneous PDR models (see §1.2.2). These models are also compared with PDR kinematic information found in §3 and §4. The geometric dilution effect of the spherical PDR models described in §1.2.3 is tested. I discuss how common spherical PDRs are in the Galaxy. The last part of this chapter examines the clumpy PDR models using the line intensity data (see §1.2.2) and line velocity information. At the end I summarize and compare the relative successes of these PDR models in explaining my observations, summarizes this thesis, and suggests future research directions.

Chapter 2

Observations of C^+ and the Infrared Continuum

2.1. Introduction

Ionized carbon, C^+, is an important component in the ISM environment of H II regions and a critical tracer for examining PDR models. A C^+ region is formed beyond the Strömgren sphere of the H II region because carbon has a lower ionization potential energy (11.3eV) than hydrogen does. Extending from regions close to the ionizing star to $A_v \approx 4 \sim 5$, C^+ is predicted by PDR theories to exist in abundance.

Studying the properties of the far-infrared [C II] fine structure line at 157.741μm ($^2P_{3/2} \rightarrow {}^2P_{1/2}$; Cooksy *et al*. 1986; referred to as 158μm hereafter) around H II regions can directly contribute to the understanding of the energy balance of the warm ISM in star forming regions (Stacey *et al*. 1991). The C^+ ion is easily excited from its ground level to the first fine-structure level due to the relatively small excitation energy (ΔE / $h\nu$ = 91 K). The critical density for the excitation is also small (3000 cm^{-3}). Because of this, 158μm C^+ line emission dominates the line-cooling of the interstellar gas. The observed luminosity ratio of the L(C II)/L(FIR) is about 3×10^{-3} over the Galaxy (Hollenbach & Tielens 1999) and about 2×10^{-3} in active star forming regions (Nakagawa *et al*. 1998).

The [CII] fine structure line and the [OI] fine structure lines ($^3P_1 \rightarrow {}^3P_0$ at 63.184μm and $^3P_2 \rightarrow {}^3P_1$ at 145.525μm) are important diagnostics for PDRs. PDR theories predict the intensities and intensity ratios of these lines given the physical conditions of the region. These line intensities and intensity ratios can be used to probe the physical conditions of unknown PDRs based on PDR theories, or conversely, to examine the PDR theories in PDRs with known physical conditions.

The far-infrared continuum radiation around H II regions is also a useful probe of the PDR. From studying the FIR continuum the dust temperature can be derived and the FUV field intensity (G_0) in the PDR outside the H II region can be estimated.

Because PDR theories have specific predictions of the line to continuum ratios as functions of G_0 and n (see §1), these ratios are also important PDR diagnostics.

Using the Infrared Space Observatory (ISO) satellite I observed H II regions in the ISO source sample described in §1. All sources except G291.28−0.72 were observed. For detailed discussion of source selection see §1.3.1 and Table 1.2. A number of neutral and ionic spectral lines in the IR as well as the FIR continuum were detected and are available for study.

The major goals of this chapter are to report the observational results of the ISO source sample and to derive IR emission properties. After describing the Infrared Space Observatory (ISO) satellite and its Long Wavelength Spectrometer (LWS) instrument with an emphasis on the calibration, I present the observational results for the ISO sources. Then the IR emission properties that are important to the PDR study in §5 are derived. The important line properties include: 1) the fluxes and intensities of the 158μm [CII] line and the [OI] lines at 63μm and 145μm; and 2) the parameters of the FIR continuum emission including dust temperatures and intensities of the total FIR continuum emission. The fluxes of [OIII] and [NIII] lines generated in the ionized region are derived as by-products. Although these lines can be used to determine the properties of the ionizing star of the H II region (Rubin *et al*. 1994) and to derive G_0 and U, they are not used in my PDR study. IRAS data are used to complement the ISO continuum data taken with the small LWS aperture. I derive dust temperatures, fine-structure emission line ratios and line-to-continuum ratios. Finally I estimate G_0 using the FIR continuum luminosity.

2.2. The 158μm Infrared Transition of C^+

2.2.1. The ISO and the LWS

The Infrared Space Observatory is an astronomical satellite constructed and operated by a multinational team and the European Space Agency. The satellite essentially consists of a large liquid helium cryostat, a telescope with a 60 cm diameter primary mirror, four scientific instruments, and a service module. The scientific instruments are the Infrared Camera, the Photo-Polarimeter, the Short Wavelength Spectrometer, and the Long Wavelength Spectrometer. Detailed technical description and scientific overview of ISO can be found in Eggel *et al.* (1990), Kessler *et al.* (1991, 1996), Clegg *et al.* (1996), and references therein.

ISO was operational between November 1995 and May 1998 until it exhausted its liquid helium supply. Free from the obstruction of Earth's atmosphere, ISO made infrared observations between wavelengths from 2.5μm to 240μm. About one thousand proposals were accepted, each one consisting on average of 50 observations. Over 500 principal investigators have made observations with ISO.

The LWS is described here in greater detail because it is the instrument I used to observe a sample of H II regions. I describe the major aspects of the LWS including the optics structure, the grating operation, and the detector array block. For complete details of LWS see Clegg *et al.* (1996), Swinyard *et al.* (1996), Gry (2000), and references therein.

The structure of the LWS is shown schematically in Figure 2.1. Seven mirrors comprise the input/collimating optics. The Fabry-Perot (FP) etalon assemblies, the diffraction grating, and the detector array can be seen in Figure 2.1. The first five mirrors define the field of view and produce a parallel beam. After having been

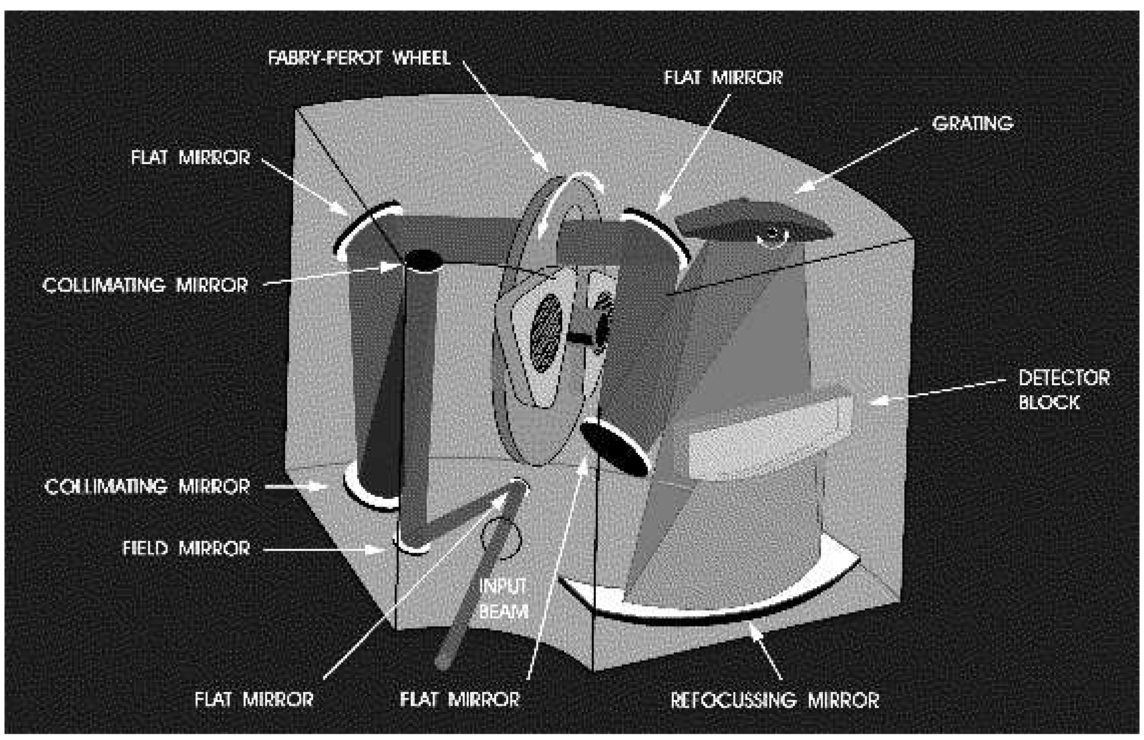

Fig. 2.1.— A schematic diagram of the optical components of the Long Wave Spectrometer. Figure from Eggel *et al*. (1990).

deflected by the first five mirrors, the radiation passes through the FP exchange wheel which carries a clear aperture. The theoretical field of view of LWS is $1.65'$, which matches the diffraction limit of the telescope at 118μm. From this point on, the radiation is received in different ways depending on the observing mode. The LWS observes between 43μm and 197μm and operates in two modes: Medium and High Resolution. The Medium Resolution Mode is also known as the grating mode and the LW01 Astronomical Observation Template (AOT). In this mode the LWS uses a reflection grating with a resolving power between about 140 and 330 (resolution of 1500 $\mathrm{km\,s^{-1}}$). In the high resolution mode, an FP Interferometer is used to give a resolution of about 10,000.

The LW01 AOT was used to observe my H II region sample. In the following text, "LWS" means LWS used in this Medium Resolution mode. In this mode the beam illuminates the diffraction grating directly, via the 5th and the 6th mirrors. The grating is used in second order to disperse the wavelength range from 43 to 94.6μm and in first order for the wavelength range from 94.6 to 196.9μm. The dispersed radiation is refocused by the 8th mirror onto the detector array block. Figure 2.2 shows the structure of the detector array block. In the block, 10 detectors are used to cover the full wavelength range, with a wavelength overlap between adjacent detectors to provide redundancy in the event of a detector failure. Some of the spectral lines, notably the [C II] line, are in the overlap areas. This redundancy also helps to examine instrument calibration across detectors. There are five short wavelength detectors named SW1 to SW5, and five long wavelength detectors named LW1 to LW5. During observation, a servo mechanism drives the diffraction grating to scan back and forth so that each detector is illuminated with radiation at different wavelengths as a function of the scan angle. The bandpass filters mounted in front of the detectors guarantee that the detectors only see radiation in the correct diffraction order and wavelength range.

The electronic read-out circuits measure the photocurrent from the detectors and record the scan angle in order to construct raw spectra. The photocurrent readings from each of the detectors are roughly converted to flux by the instrumental response profile that is known as the Relative Spectral Response Function (RSRF) of the detector. As described in the next section, refined LWS calibration is achieved by observing Uranus and using internal illuminators.

Note that the terms such as "flux" and "intensity" are used interchangeably

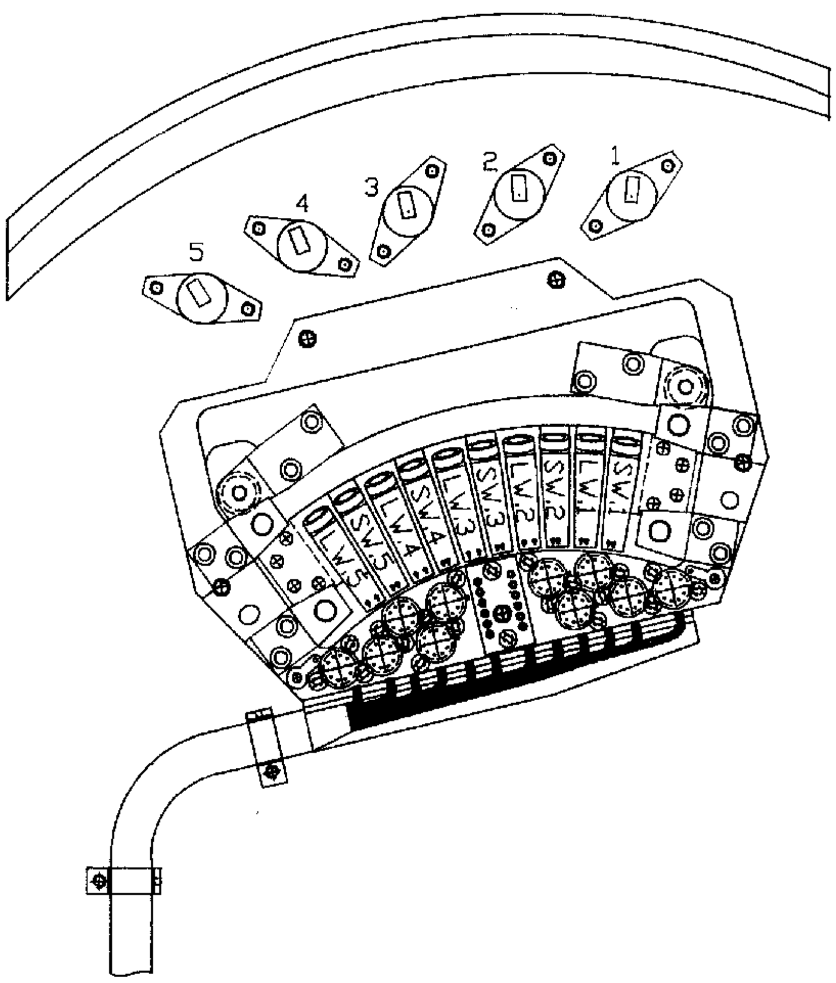

Fig. 2.2.— This drawing shows the detector block of the LWS. The short wavelength detectors SW1 to SW5 and the long wavelength detectors LW1 to LW5 are alternately mounted on the cryostats. The numbers 1 to 5 mark the calibration illuminators (see text). Figure reproduced from Clegg *et al.* (1996).

in much of ISO technical literature. In this thesis "total flux" or "integrated flux" is defined to be the amount of radiation energy flowing through unit area in unit time over a certain wavelength range (W cm^{-2}). For the integrated flux of spectral lines, I simply use the term "flux". The term "flux density" stands for flux per unit wavelength or frequency interval (W cm$^{-2}\mu$m^{-1} or Jansky: 10^{-30} W cm^{-2} Hz^{-1}). When there is no ambiguity "flux" can be used instead of flux density. The term "intensity" is used for integrated flux per unit solid angle (W cm$^{-2}\mu$m^{-1} sr^{-1} or Jy sr^{-1}).

2.2.2. LWS Calibration

It is critical to understand how ISO data are calibrated in order to be certain of the quality of the data and to be able to recognize peculiar problems and remove residual errors. Data are extensively processed before they are made available to the users through the ISO data archives. A great deal of detailed error analyses and data processing hides behind the automatic data processing pipeline. The ISO data processing is mostly based on models of the instrument behavior and assumptions that simplify the calibration procedures. After receiving a particular set of data, the user often needs to remove errors caused by instrumental errors not corrected in the automatic processing routines or caused by peculiarities of the sources in question.

Wavelength and Spectral Resolution

In order to use LWS data one needs both to calibrate the wavelength scale and to determine instrumental spectral resolution. The wavelength calibration and spectral resolution determinations are made using strong oxygen, nitrogen, and carbon IR emission lines of planetary nebulae and bright H II regions. In the LW01 AOT the spectral resolution of the LWS is nominally 0.29μm for detectors SW1 to SW5 and 0.60μm for LW1 to LW5. The RMS wavelength accuracy has been determined to be $2.6 \times 10^{-2}\mu$m (Swinyard *et al*. 1996). The equivalent velocity resolution of LWS is greater than 1500 $\mathrm{km\,s^{-1}}$. In the context of the studies of this thesis the spectral line features of the sample of H II regions have linewidths on the order of ~ 10 $\mathrm{km\,s^{-1}}$ (e.g., Caswell & Haynes 1987; Felli *et al*. 1990). Therefore the spectral lines of these H II regions are not resolved. Other than being used as line identifications, the LWS wavelength data provide no useful astrophysical information. I conclude that current calibration in wavelength and spectral resolution are more than sufficient for this purpose.

Flux

The flux calibration of the LWS needs to be addressed in more detail. There are three stages in calibrating LWS data: 1) measuring the flux calibration sources to establish the RSRF and ARC (see below); 2) measuring the calibration sources during each observation; and 3) analyzing errors and making further corrections in the Off-Line Processing (OLP) stage.

RSRF and ARC Factors

The overall absolute LWS flux calibration is based on Uranus as the primary calibrator. The spectral characteristics of Uranus are determined based on observations and modeling of the planet's emission properties. All LWS observations are ultimately calibrated based on the Uranus emission models and observations. The RSRF of the LWS is derived from 36 full-scan observations of Uranus interleaved with dark current measurements made on the 28th of September 1996, during revolution 317.

Since Uranus is not available during every user observation, five illuminators (see Figure 2.2) are used as secondary calibrators. The illuminators are calibrated using Uranus in revolution 317, and are compared with a series of astronomical sources weekly throughout the mission to monitor changes of the illuminator powers.

During each observation these illuminators are used to establish the detector sensitivity baseline and to correct for any detector responsivity drift. The photocurrent readings from these illuminators are compared with those recorded after the Uranus measurement. An Absolute Responsivity Correction (ARC) factor is derived for each detector for each observation. After the spectra from the astronomical source are made using the RSRF as described in the previous section, they are re-scaled using the ARC factors to correct for detector responsivity drift. Additionally, when all illuminators are off and the optical path of LWS is blocked by the FP Wheel, the dark current of each detector is measured.

The OLP, Outstanding Problems, and Error Budget

The detailed error analyses and calibration of ISO data are made in the OLP (often referred to as pipeline processing) stage. The OLP makes the correction for the Dark Current, the Grating Positions, the Time Responsivity Drift, detector glitches caused by energetic particles hitting the detectors, and the ARC factors. Extensive cross-calibrations are made to compare among different ISO instruments, to compare between ISO and external instruments such as KAO, IRAS, and COBE, and to ensure that the ISO data are homogeneously processed. The line profiles, photometric calibration, polarization, and transient effects of the instrument are studied. The cross-calibration report by Gry (2000) gives details of the OLP cross-calibration.

The normal flux calibration procedure has several outstanding problems that are necessary to address for my ISO data:

1. After ISO was launched, severe fringes were found in the continuum of some of the ISO grating data. All my ISO source data were affected by severe fringing. The problem is caused by the interference between the off-axis radiation rays reflected from mirror 2 and from its mounting plate. Any source that is not a point source located at the center of the field of view will be affected by this problem. The current software can *defringe* the spectra by fitting sinusoidal functions in wave-number space to the fringes in the continuum. How this defringing process affects the spectral lines depends on the spatial structure of the object in the field of view. If the line emitting area is extended, the line flux should be divided by the fitted sinusoidal functions; if the line emitting area is a point source, the function should be subtracted from the spectra; if the source size is comparable to the LWS beam size, currently there is no precise treatment available. Since the line emission areas of my H II regions are generally comparable to the LWS beam size based on IRAS observations (the accurate distributions are unknown) the precise fringe correction to the emission line data is not possible to determine. This problem can cause errors in line flux measurement up to 20% to 30% based on my experience using the defringing software.

2. The nominal beam size of the LWS is a function of the spatial structure of the source and the wavelength. It has been found that the LWS beam is 20% narrower than the theoretical diffraction limit ($87''$ compared with $113''$).

Extended sources need to have an extra correction factor applied to the flux. This correction also depends on the spatial structure of the source, and, among all LWS errors, is the most difficult to evaluate accurately. The details can be found in Swinyard *et al*. (1996), Salama (2000), and García-Lario (2000).

3. Bright sources cause the LWS detectors to become non-linear. The detector responsivities are affected by photon curing of the detectors. The H II regions I have observed usually are strong enough to cause this effect. An empirical method has been used in the OLP to identify non-linear effects in the photocurrent readings and to attempt to remove them. According to the error budget analysis (see below) the non-linearity caused by the strong H II region fluxes may be one of the biggest error contributors.

4. There are Time Constant Effect and Poor Order Sorting problems associated with some of LWS data. So far these effects on my H II region data have not been found to be significant. Therefore no corrections have been specifically applied.

5. Since the RSRF and ARC factors are derived separately for each detector, the consistencies of the calibration applied to the entire LWS bandwidth cannot be checked until the final calibrated spectrum is produced by the OLP. The calibration errors among the detectors result in disconnected sub-spectra, as discussed in §2.2.3.

The LWS Interactive Analysis (LIA) tools are used to help the user to understand and to correct the above problems. Thus improvements on data quality for individual sources can be manually made with LIA.

In spite of the data correction tools provided by ISAP and LIA, the two most serious adverse effects listed above still remain: the detector responses to strong sources in general are poorly known and the current data processing tools cannot handle sources that have finite source sizes (i.e., the source size is comparable to the aperture size). Overcoming these obstacles remains a goal of future ISO data processing and is beyond the scope of this thesis. The current (OLPv8.7) overall error budget of the absolute calibration for LW01 AOT is believed to be 50% for a bright extended source and 30% for a point source (García-Lario 2000 and references therein). This implies that the finite size of the sources is a major contributor to calibration uncertainty. Relative calibration accuracy of the LWS is better. The photometric accuracy for LWS Medium Resolution mode is 10% between repeated scans on the same detector and 30% between adjacent detectors (§5.4.1.1 of Trams 1998).

Although these uncertainties are large compared with the measurements made by many well understood instruments, the ISO data are still very useful for PDR theory studies within their error margins. I will discuss the measurement errors and future improvements in §5.

2.2.3. Observations and Line Intensities

Observation

I proposed a total of 64 H II regions and 6 reference positions to be observed using the LWS with the LW01 AOT. Unfortunately the ISO scheduling and observation sequences were beyond my control. Only 11 sources and 2 reference positions were observed on May 29, 1997. The proposed and observed source names and positions

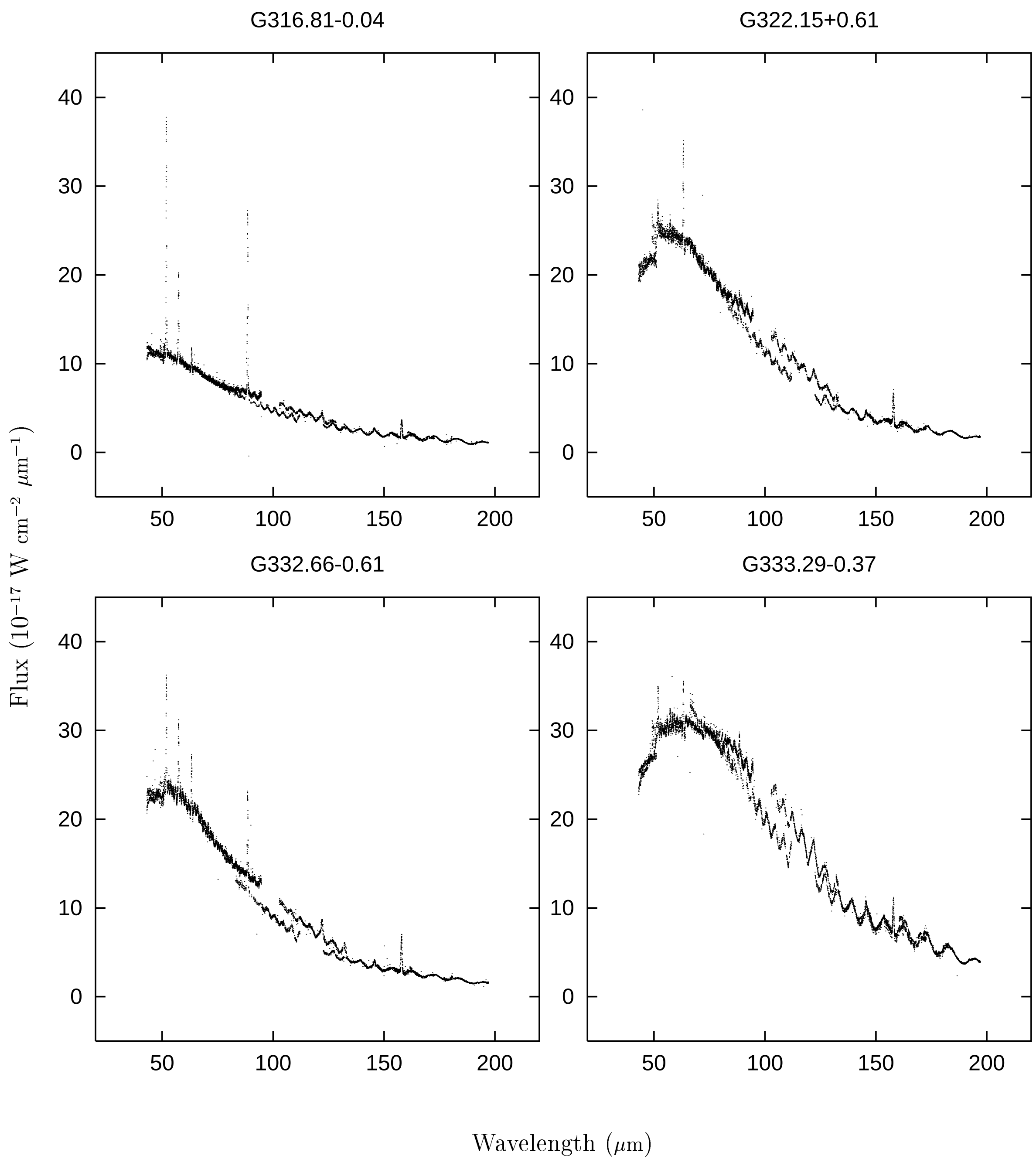

Fig. 2.3.— ISO Medium-Resolution Mode (LW01 AOT) spectra of H II regions and a reference position. The wavelength coverage spans the full range from 43μm to 197μm. The spurious fringe effect and disconnected sub-spectra are apparent in the continuum. (continuing to the next page)

1

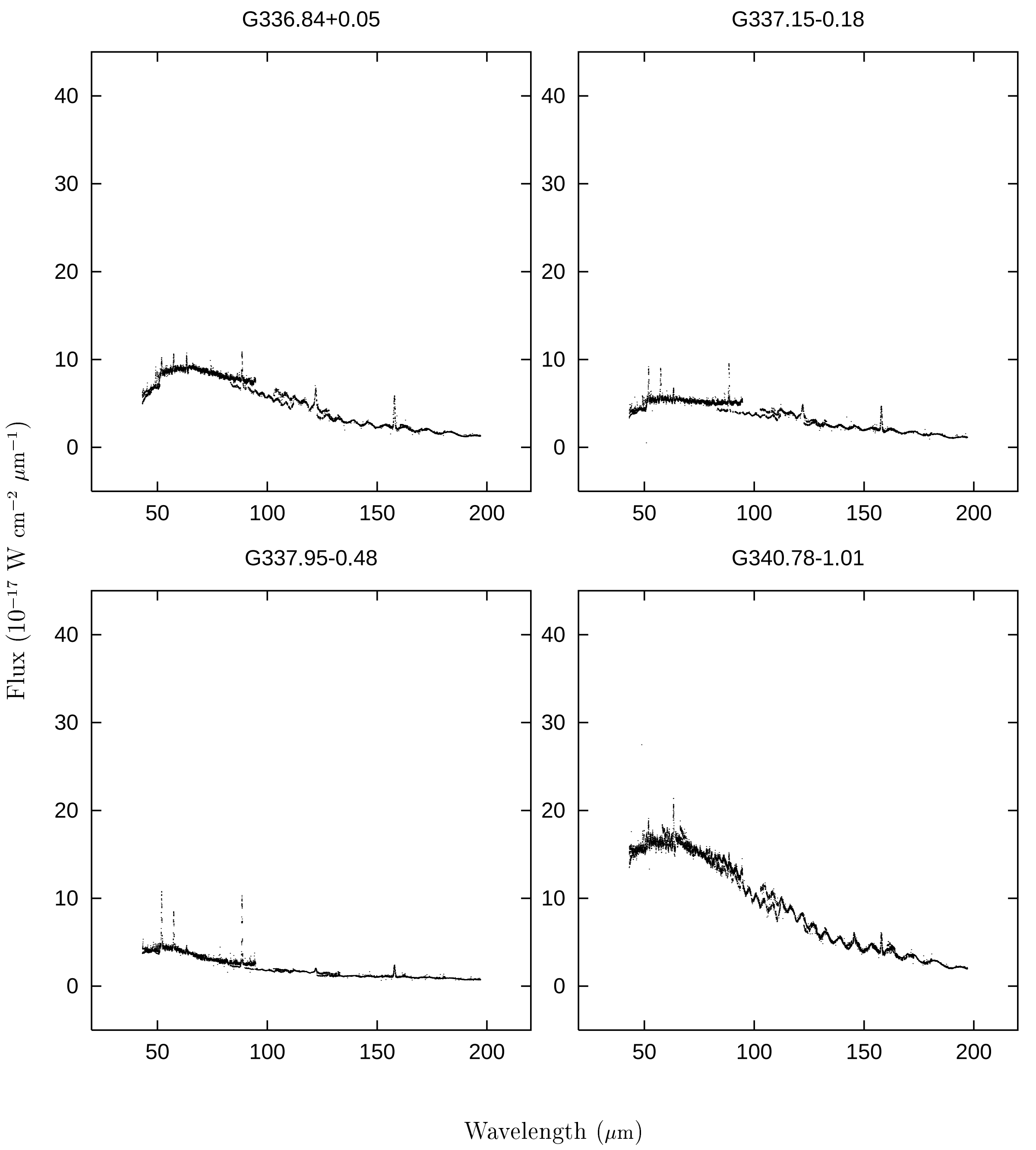

Fig. 2.3.— (continued)

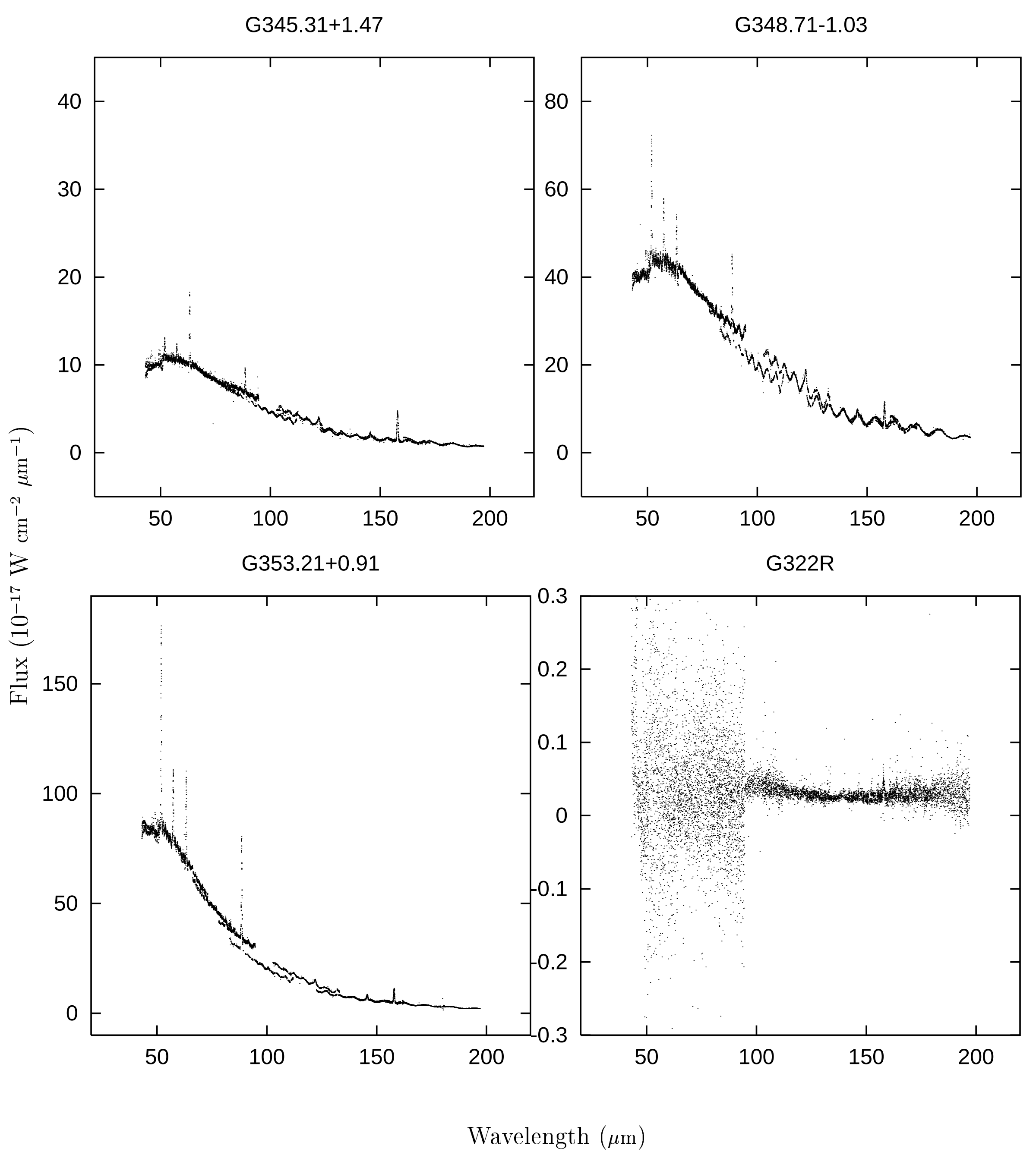

Fig. 2.3.— (continued) The source G322R is a reference position located off the Galactic Plane. A weak C^+ line is shown even in this reference position.

are listed in §1. The 11 observed sources are referred to as the ISO sources.

The ISO sources were observed in single point "stare" mode. The on-target observing time was 1145 seconds for every source except G340.78−1.01, which was 1373 seconds. The Fast Ramp technique was used to minimize the impact of glitches on detector sensitivity. Each source was observed in 7 scans at the same position. During each scan the LWS read all ten detectors and constructed one spectrum. After the observation a number of versions of re-processed data have been released when new OLP versions were developed. The data presented here are reduced from the OLPv6.1 release.

Figure 2.3 shows spectra of all the sources and a reference position as released by OLP6.1. Strong IR emission lines and continua are detected. The fine structure lines of [OI] at 63μm and 145μm, and [CII] line at 158μm are detected in all sources with a good signal to noise ratio. Also detected are an array of neutral and ionic emission lines of oxygen and nitrogen. Strong fringes can be seen in the continuum. The sub-spectra generated by different detectors are not connected, indicating errors in cross calibration among detectors. The reference position G322R is also shown in Figure 2.3. With the low emission level the G322R plot not only shows that there is very low residue emission when an H II region is absent from the field of view but also demonstrates that the LWS dark current is negligible for these H II region observations.

Post-OLP Data Reduction

During the post-OLP manual processing of the ISO source data, I made further reductions interactively using the LIA and the ISO Spectral Analysis Package

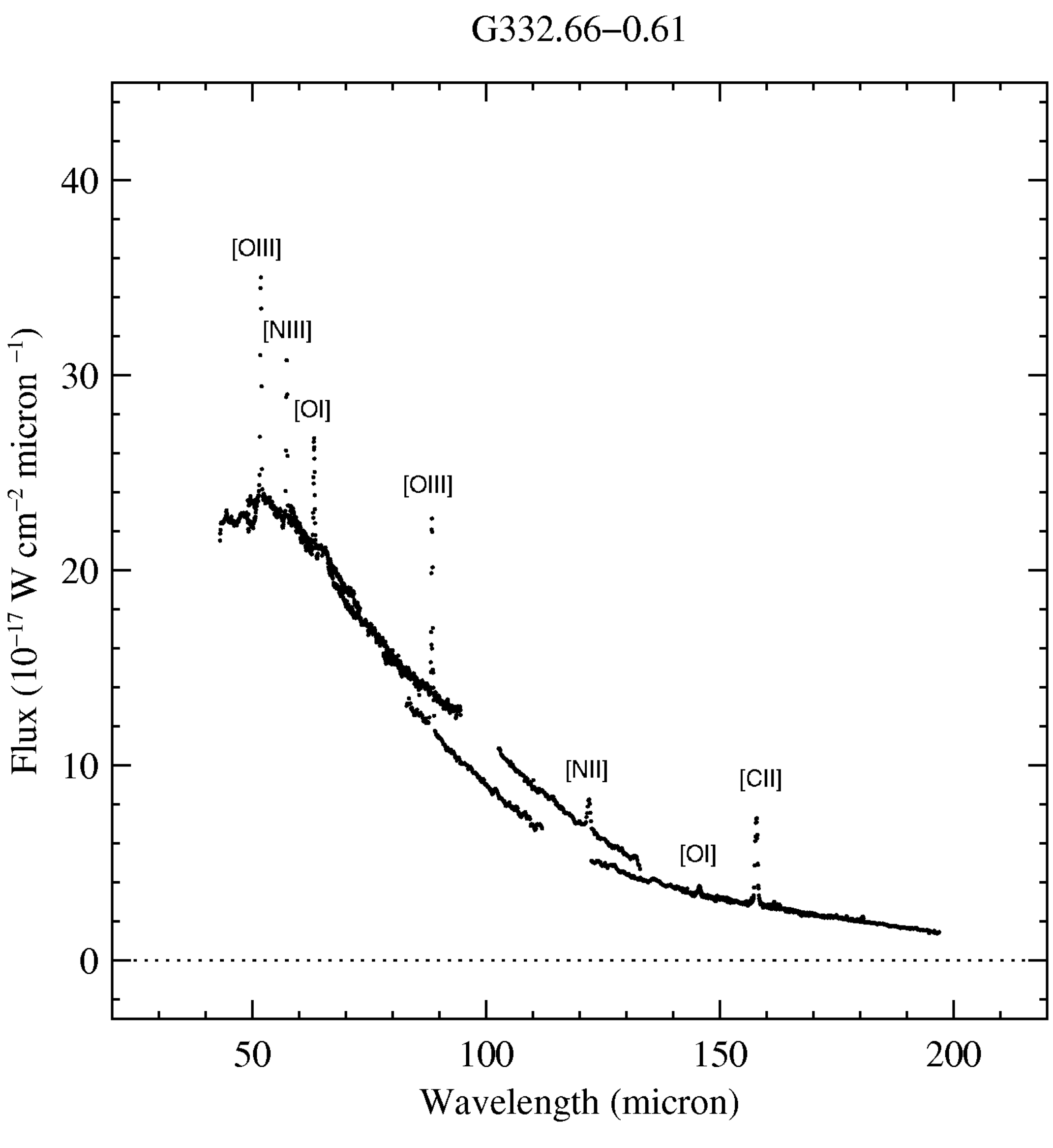

Fig. 2.4.— Example spectrum of G332.66−0.61 after the post-OLP processing. The glitches and fringes have been removed. The data from different scans and two scan directions have been averaged. Sub-spectra from different detectors are decidedly not connected. See text for data reduction details. The weak features in the spectrum (e.g., at 50μm, 70μm, 135μm, and 180μm) are due to a combination of glitches, fringes, and responsivity errors.

(ISAP[1]). ISAP is the major software tool to assist the user to process post-pipeline LWS data. Detailed information about ISAP can be found on the World Wide Web at the Infrared Processing and Analysis Center (IPAC).

To begin the post-pipeline processing the ISO LWS data are first obtained from the ISO archive. These data include the automatically processed LWS scan file and calibration related files in FITS format. Then ISAP is used to process the scan files and to derive infrared emission line properties in the following manner:

1. Sporadic, out-lying data points are usually the result of incomplete glitch removal during the OLP. They have the characteristic profile of a fast rise followed by a slow tapering off in flux. These data points are removed ("zapped"). Because every source has multiple scans in its spectra which overlap in wavelength, removing some bad data points in one scan does not significantly affect the final averaged spectra.

2. Data in different scans and data in different scan directions are averaged so that at one wavelength there is only one flux value for each detector.

3. The fringes are removed using the ISAP defringe routine, assuming the sources are extended (larger than $20''$). An example of the result of this processing is shown in Figure 2.4.

4. The Extended Source Correction to the intensity scale is applied. The ISO calibration pipeline assumes that all objects are point-sources. (See the paragraph above for LWS point-source definition.) Since none of the ISO sources is a point source, this step is therefore necessary.

[1]ISAP is a joint development by the LWS and SWS Instrument Teams and Data Centers, with contributing institutes of CESR, IAS, IPAC, MPE, RAL and SRON.

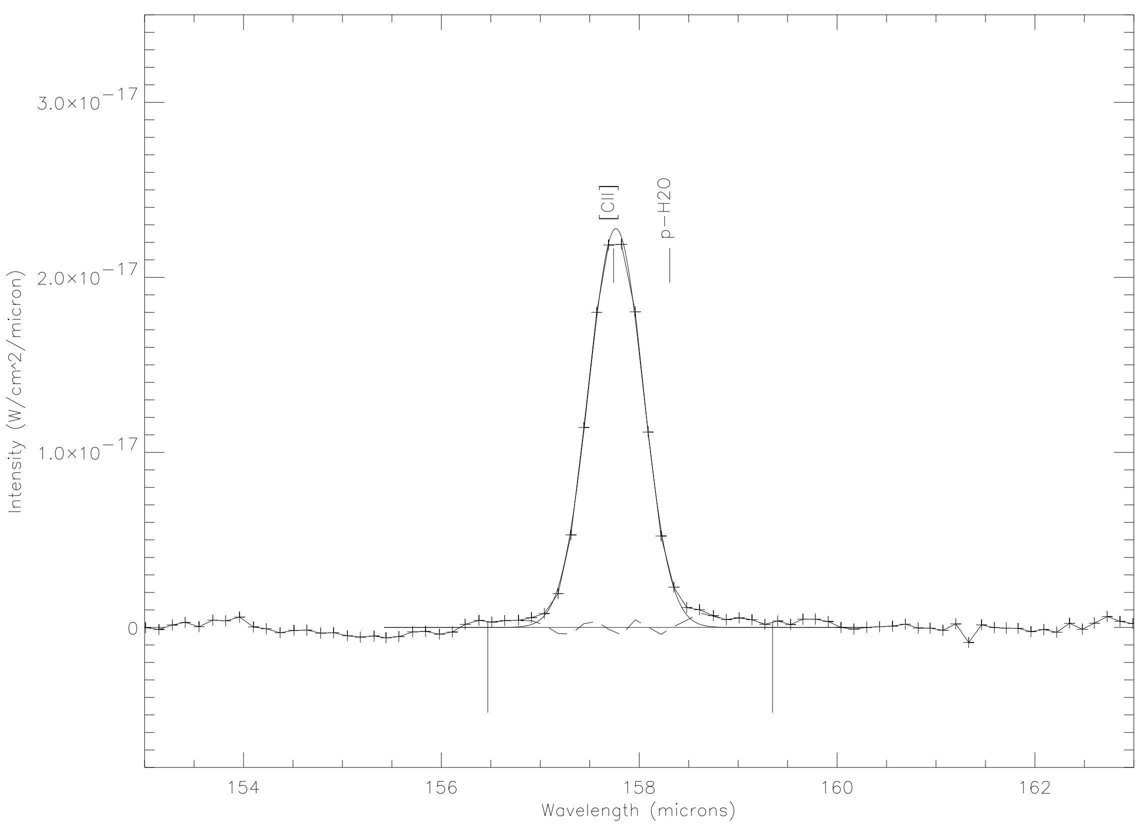

Fig. 2.5.— Example of the Gaussian fit to the 158μm C^+ line in the spectrum of G316.81−0.04. A first order baseline is removed before the fit. The two vertical lines below the baseline denote the range in wavelength used for the fit. The residual after the fit is plotted as a dashed line. The two labels ("`[CII]`" and "`p-H2O`") and short vertical lines are line identifications for the entire wavelength range displayed. They are provided by the ISO spectral line database. The possibility of confusing the spectral lines in Table 2.1 with other transitions is minimal because the intensities of the former are usually orders of magnitudes stronger.

5. Spectral lines are identified. The spectral lines chosen for study (see § 2.1) include the three important PDR diagnostic lines: 63.184μm [OI], 145.525μm [OI], and 157.741μm [CII]. Also included are ionic lines: 51.814μm [OIII], 57.330μm [NIII], 88.356μm [OIII], and 121.898μm[NII]. These seven spectral lines can usually be easily identified because of their high signal to noise ratios. These include all three PDR diagnostic lines. A few weak ionic lines can also be identified by inspecting their known wavelength ranges, but analysis of these transitions is beyond the scope of this thesis.

6. A Gaussian fit is made to the selected transitions to yield the line flux. Usually a first order baseline is removed, but when the fringe is not completely removed a higher order baseline is fitted to the continuum and subsequently removed. An example Gaussian fit result is shown in Figure 2.5.

I made no attempt to connect the sub-spectra of individual detectors by re-scaling and shifting. The discontinuous spectra caused by unconnected sub-spectra are apparent in Figure 2.3 and Figure 2.4. Although empirically connecting the sub-spectra was recommended in the past by the ISO team, it is now strongly recommended that the problem be left for OLP to solve systematically. The reason is that in order to connect the sub-spectra, one "good" detector has to be chosen so that other sub-spectra can be aligned to it. This is, however, an arbitrary operation since it is known that the misalignment is mostly due to problems currently unsolvable (see §2.2.2), so it is impossible to determine which detector is "good" *a priori*. Manually aligning the sub-spectra is very likely to disturb the overall flux calibration made by the OLP. The ISO team plans to address some of these problems in OLPv10, which is expected to be released after mid-2001. Note that the discontinuities between the sub-spectra are already reflected in the LWS error budget discussed in §2.2.2. It does not affect the estimation of total FIR flux significantly in §2.3.

IR Line Fluxes

The spectral line fluxes from the Gaussian fits to the seven atomic and ionic carbon, oxygen, and nitrogen transition lines are listed in Table 2.1. The source names are the same as shown in Table 1.2. The transitions are identified in the column heads by their nominal wavelengths, e.g., "$F_{158\mu\mathrm{m}}$" denotes the C[II] line. The average fluxes and RMS flux dispersions are also listed. The errors given are derived from the RMS errors in the baselines. The major contribution to the baseline RMS error is a residual fringe that cannot be removed by the defringe routine of ISAP. The systematic errors cited in the error budget analysis (described in §2.2.2) are not included in Table 2.1. Therefore the error shown in Table 2.1 should be regarded as a lower limit to the line intensity errors, and as an indicator of the confidence level in the Gaussian fit.

All the seven atomic and ionic fine structure lines of [CII], [OI], [OIII], [NII], and [NIII] are detected in every one of the 11 ISO sources. The signal to noise ratios of all detections are above 3 except for the 122μm line of [NII] in G348.71−1.03. This shows that neutral and ionic carbon, oxygen, and nitrogen species are ubiquitous in the H II regions. Their transition lines are easily observable probes of the physical conditions of the regions. The [CII] fine structure emission is even detected in the two reference positions selected to lie 2.5 degrees off the Galactic Plane. The line flux in these zones of "blank" sky is ~1% of the average H II region [CII] flux ($1.4 \pm 0.5 \times 10^{-17}$W cm^{-2}).

TABLE 2.1

ISO LWS SPECTRAL LINE FLUXES FOR THE H II REGION SAMPLE[a]

Source	$t_{\rm obs}$ (sec)	$F_{52\mu m}$ [OIII]	$F_{57\mu m}$ [NIII]	$F_{63\mu m}$ [OI]	$F_{88\mu m}$ [OIII]	$F_{122\mu m}$ [NII]	$F_{146\mu m} \times 10$ [OI]	$F_{158\mu m}$ [CII]
G316.81−0.04	1145	7.30 ± 0.09	2.83 ± 0.09	0.55 ± 0.01	4.19 ± 0.31	0.22 ± 0.03	1.39 ± 0.10	0.90 ± 0.01
G322.15+0.61	1145	0.79 ± 0.07	0.33 ± 0.04	2.78 ± 0.03	0.27 ± 0.05	0.36 ± 0.03	1.79 ± 0.12	1.40 ± 0.01
G322R	1145	...	...	...	...	...	...	0.01 ± 0.00
G332.66−0.61	1145	3.52 ± 0.16	2.29 ± 0.05	1.44 ± 0.02	2.19 ± 0.13	0.71 ± 0.05	1.92 ± 0.10	1.70 ± 0.01
G333.29−0.37	1145	1.72 ± 0.17	0.44 ± 0.09	1.34 ± 0.02	0.34 ± 0.03	0.40 ± 0.04	4.20 ± 0.10	1.54 ± 0.02
G336.84+0.05	1145	0.43 ± 0.04	0.47 ± 0.03	0.34 ± 0.01	0.68 ± 0.03	1.10 ± 0.06	0.65 ± 0.05	1.55 ± 0.01
G337.15−0.18	1145	0.93 ± 0.04	0.94 ± 0.02	0.26 ± 0.01	0.92 ± 0.06	0.66 ± 0.05	0.56 ± 0.03	1.22 ± 0.01
G337.95−0.48	1145	1.64 ± 0.05	1.10 ± 0.03	0.12 ± 0.00	1.72 ± 0.10	0.21 ± 0.01	0.33 ± 0.02	0.56 ± 0.00
G337.9R	1145	...	...	...	...	...	...	0.04 ± 0.00
G340.78−1.01	1373	0.49 ± 0.06	0.17 ± 0.03	1.44 ± 0.02	0.18 ± 0.03	0.11 ± 0.02	3.16 ± 0.10	0.97 ± 0.01
G345.31+1.47	1145	0.55 ± 0.05	0.43 ± 0.02	2.20 ± 0.01	0.48 ± 0.03	0.37 ± 0.03	1.66 ± 0.13	1.48 ± 0.01
G348.71−1.03	1145	7.63 ± 0.29	3.98 ± 0.03	3.29 ± 0.07	3.35 ± 0.24	0.64 ± 0.22	4.08 ± 1.34	2.21 ± 0.03
G353.21+0.91	1145	24.41 ± 0.35	9.40 ± 0.13	9.55 ± 0.17	11.08 ± 0.73	0.88 ± 0.06	8.08 ± 0.26	2.12 ± 0.02
Average	...	4.49 ± 6.78	2.03 ± 2.61	2.12 ± 2.55	2.31 ± 3.05	0.51 ± 0.29	0.25 ± 0.22	1.42 ± 0.47

[a] Fluxes are in units of 10^{-17} W cm^{-2}. Data reduction is made using ISAP v2.0 based on the ISO pipeline OLPv6.1 data assuming extended sources.

IR Line Intensities and Intensity Ratios

PDR theories predict IR line intensities and intensity ratios based on model calculations. Emission line intensities and their ratios of [CII] and [OI] are calculated in this section so that they can be compared with PDR theories in §5. The line intensity I is derived from the line flux F and the ISO LWS beam size Φ:

$$I = \frac{F}{\Phi}. \tag{2.1}$$

The beam radii for the 65μm and the 145μm lines of [OI] and the 158μm line of [CII] are 42$''$, 35$''$, and 30$''$, respectively (Gry 2000). Table 2.2 lists $I_{63\mu\mathrm{m}}$, $I_{145\mu\mathrm{m}}$, and $I_{158\mu\mathrm{m}}$, the intensities of the abovementioned [OI] and [CII] fine structure transitions. The line intensity ratios of $I_{63\mu\mathrm{m}}/I_{158\mu\mathrm{m}}$, $I_{145\mu\mathrm{m}}/I_{63\mu\mathrm{m}}$, and $I_{145\mu\mathrm{m}}/I_{158\mu\mathrm{m}}$ are also given. The errors for intensities quoted in Table 2.2 are calculated as 50% of the intensity, based on the LWS error budget discussion in §2.2.2. The relative intensity errors between adjacent detectors are estimated to be 30% based on ISO crosss calibration results (see §2.2.2). I adopt 30% as the error of these line ratios. The last line in Table 2.2 gives the line intensities and intensity ratios averaged over all 11 sources. The RMS dispersions of these average values are also listed. Table 2.2 shows that the average values of $I_{63\mu\mathrm{m}}$, $I_{145\mu\mathrm{m}}$, and $I_{158\mu\mathrm{m}}$ are $1.6 \pm 2.0 \times 10^{-10}$W cm^{-2}sr^{-1}, $2.8 \pm 2.4 \times 10^{-11}$W cm^{-2}sr^{-1}, and $2.1 \pm 0.7 \times 10^{-10}$W cm^{-2}sr^{-1}, respectively. The average C[II] line intensity is only 30% stronger than the 63μm [OI] line.

In the extended ISM of the Galaxy the [CII] emission is the dominant cooling line. The high [OI]/[CII] ratios found for the H II region sample indicate that the H II region gas is warmer than the general Galactic ISM. The relative RMS dispersions of the [OI] line intensities (120% and 86%) are greater than that of [CII] (33%). This shows that the [CII] intensity in the H II region sample is more uniformly distributed. This can be qualitatively explained by the easier excitation condition of [CII] than

TABLE 2.2

PDR Diagnostic IR Line Intensities and Ratios of the ISO Sources[a]

Source	$I_{63\mu m}$ (10^{-11}W cm^{-2}sr^{-1})	$I_{145\mu m}$ (10^{-11}W cm^{-2}sr^{-1})	$I_{158\mu m}$ (10^{-11}W cm^{-2}sr^{-1})	$\frac{I_{63\mu m}}{I_{158\mu m}}$	$\frac{I_{145\mu m}}{I_{63\mu m}}$	$\frac{I_{145\mu m}}{I_{158\mu m}}$
G316.81−0.04	4.2 ± 02.1	1.5 ± 0.8	14 ± 07	0.31 ± 0.09	0.37 ± 0.11	0.11 ± 0.03
G322.15+0.61	21.3 ± 10.7	2.0 ± 1.0	21 ± 11	1.01 ± 0.30	0.09 ± 0.03	0.09 ± 0.03
G332.66−0.61	11.1 ± 05.5	2.1 ± 1.1	26 ± 13	0.43 ± 0.13	0.19 ± 0.06	0.08 ± 0.02
G333.29−0.37	10.3 ± 05.1	4.6 ± 2.3	23 ± 12	0.44 ± 0.13	0.45 ± 0.14	0.20 ± 0.06
G336.84+0.05	2.6 ± 01.3	0.7 ± 0.4	23 ± 12	0.11 ± 0.03	0.27 ± 0.08	0.03 ± 0.01
G337.15−0.18	2.0 ± 01.0	0.6 ± 0.3	18 ± 09	0.11 ± 0.03	0.31 ± 0.09	0.03 ± 0.01
G337.95−0.48	0.9 ± 00.5	0.4 ± 0.2	8 ± 04	0.11 ± 0.03	0.39 ± 0.12	0.04 ± 0.01
G340.78−1.01	11.1 ± 05.5	3.5 ± 1.7	15 ± 07	0.76 ± 0.23	0.32 ± 0.09	0.24 ± 0.07
G345.31+1.47	16.9 ± 08.4	1.8 ± 0.9	22 ± 11	0.76 ± 0.23	0.11 ± 0.03	0.08 ± 0.02
G348.71−1.03	25.3 ± 12.6	4.5 ± 2.3	33 ± 17	0.76 ± 0.23	0.18 ± 0.05	0.14 ± 0.04
G353.21+0.91	73.3 ± 36.7	8.9 ± 4.5	32 ± 16	2.30 ± 0.69	0.12 ± 0.04	0.28 ± 0.08
Average	16.3 ± 19.6	2.8 ± 2.4	21.4 ± 7.1	0.65 ± 0.60	0.25 ± 0.12	0.12 ± 0.08

[a]Line intensities and intensity ratios have errors of 50% and 30%, respectively. See text.

[OI] in the ISM around H II regions. The critical density of [CII] is $3000\,\mathrm{cm}^{-3}$, about two orders of magnitude lower than that of the two [OI] lines. Furthermore the upper energy level of [CII] is less than half that of the [OI] transition energies. Therefore the range of density and temperature that can excite [CII] is greater than [OI]. The permitted density and temperature ranges in the PDR are $10 \sim 10^6\,\mathrm{cm}^{-3}$ and $10 \sim 1000$ K, respectively. These excitation conditions cause the [OI] emission to be concentrated in the dense and warm regions that are relatively compact and associated with the exciting stars of the H II regions.

Figure 2.6 shows a correlation between the 63μm and the 145μm [OI] line intensities of the sample. A linear regression fit to the logarithmic intensities gives: $\log(I_{145}\mu\mathrm{m}) = (0.69 \pm 0.10)\log(I_{63}\mu\mathrm{m}) - (3.7 \pm 1.0)$. with a correlation coefficient of 0.91. The error of the fit is greater for sources that have $I_{63}\mu\mathrm{m} > 10^{-10}$ W cm^{-2} sr^{-1}. Figure 2.7 shows a weaker correlation of the 63μm [OI] line intensity and the 158μm [CII] line intensity. A linear fit to the data gives: $I_{158}\mu\mathrm{m} = (1.0 \pm 0.5) \times 10^{-10}\log(I_{63}\mu\mathrm{m}) + (1.2 \pm 0.5) \times 10^{-9}$ (W cm^{-2} sr^{-1}). These correlations will be used in § 5 to discuss why the 63μm [OI] line could be a problematic tracer for studying PDRs (Kraemer, Jackson & Lane 1998).

The average line intensity ratios for $I_{63\mu m}/I_{158\mu m}$, $I_{145\mu m}/I_{63\mu m}$, and $I_{145\mu m}/I_{158\mu m}$ are 0.65 ± 0.60, 0.25 ± 0.12, and 0.12 ± 0.08, respectively. Besides the correlations discussed above, I have examined correlations among other line intensities and line ratios. Not all correlations speak to issues of testing PDR theory. The relations among these quantities will be discussed in §5 in the frame of PDR theories. The column densities of C^+ will also be estimated and compared with the results of other tracers in §5.

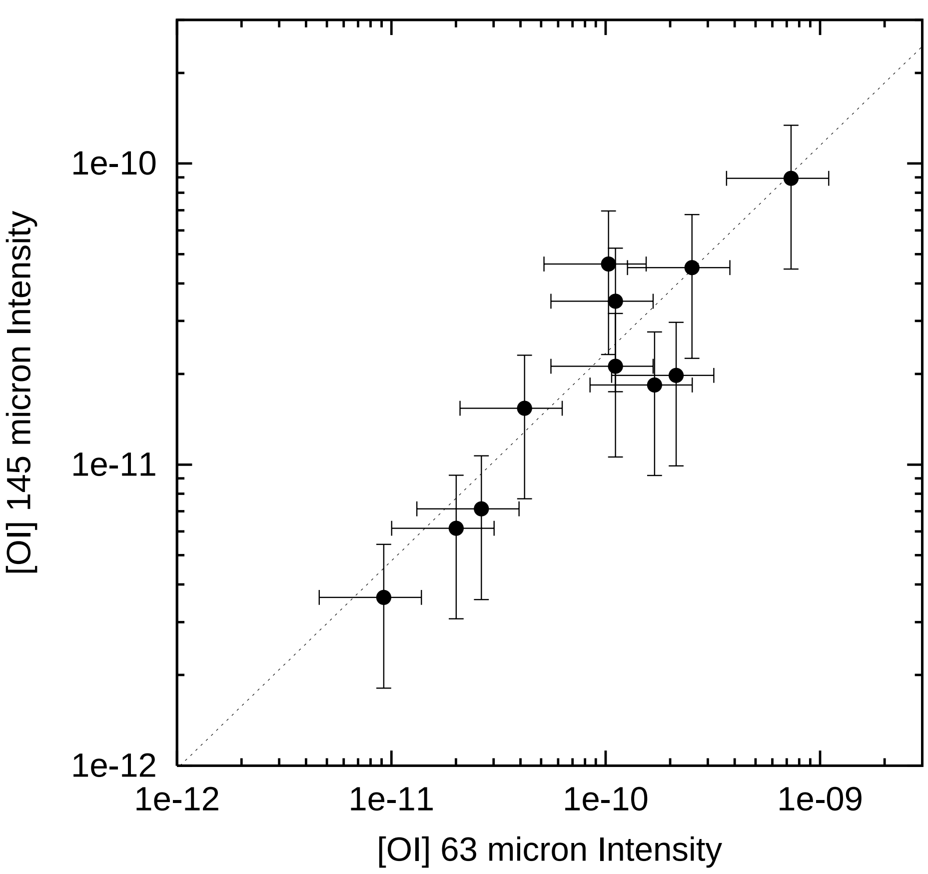

Fig. 2.6.— The 63μm and the 145μm [OI] line intensities of the ISO sources. The units are W cm^{-2} sr^{-1}. The errors in the intensities are the 50% overall error of ISO LWS. The dashed line shows a fit to the intensities: $\log(I_{145\mu}\text{m}) = (0.69 \pm 0.10)\log(I_{63\mu}\text{m}) - (3.7 \pm 1.0)$.

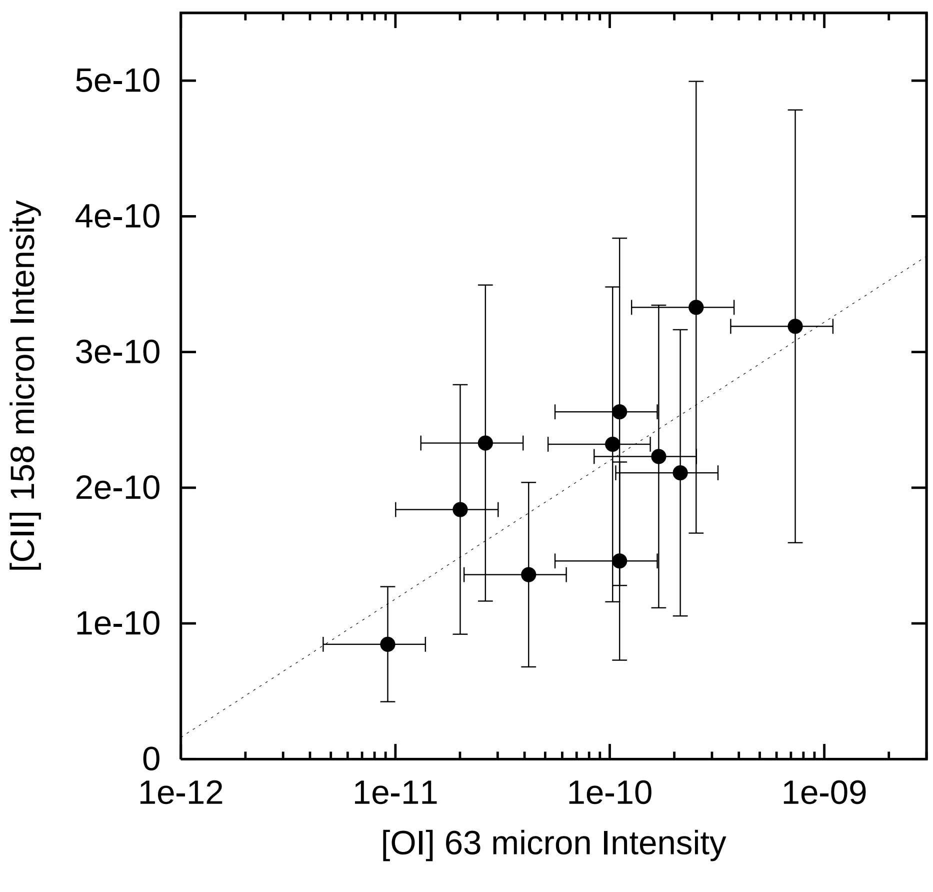

Fig. 2.7.— The 63μm [QI] and the 158μm [CII] line intensities of the ISO sources. The units are W cm^{-2} sr^{-1}. The errors in the intensities are the 50% overall error of ISO LWS. The dashed line shows a fit to the intensities: $I_{158\mu\mathrm{m}} = (1.0 \pm 0.5) \times 10^{-10} \log(I_{63\mu\mathrm{m}}) + (1.2 \pm 0.5) \times 10^{-9}$.

2.3. Infrared Continuum Data

The infrared continuum from the ISM around H II regions comes mainly from the dust components. The blackbody tail of the central star's emission and the free-free continuum emission from the H II region are several orders of magnitude weaker than the detected IR continuum level in the LWS wavelength range. The observed IR continuum is emitted from the dust in the H II region that is predominantly heated by photoelectric heating in the PDR. Only a small part of the IR emission is from dust absorbing photons inside the Strömgren sphere (e.g., Harper 1974; Tielens & de Jong 1979; Tielens & Hollenbach 1985a).

In this section I analyze infrared continuum data for the ISO sources obtained from my ISO observations and the IRAS data product. The goals of the analysis are: 1) to determine the dust temperatures by fitting the ISO source continua with blackbody distributions; 2) to derive the integrated far-infrared continuum emission flux, F_{LWS}, from the LWS spectra; and 3) to estimate the total FIR luminosity of the H II regions based on IRAS 60μm and 100 μm maps. This information is then used to derive line-to-continuum ratios and to estimate the FUV incident flux, G_0, for the ISO H II regions. Note that the dust temperature is not quantitatively used in the study of PDR theory in this thesis. Its measurement is for completeness and for comparison with past studies of H II regions in FIR wavelengths in § 2.3.2.

2.3.1. Data Acquisition and Reduction

The first source of IR continuum data is the ISO LWS spectra of the ISO sources. As shown in the sample spectra in Figure 2.3 all ISO source continua have similar spectral energy distributions (SEDs). These SEDs are all consistent with a blackbody distribution.

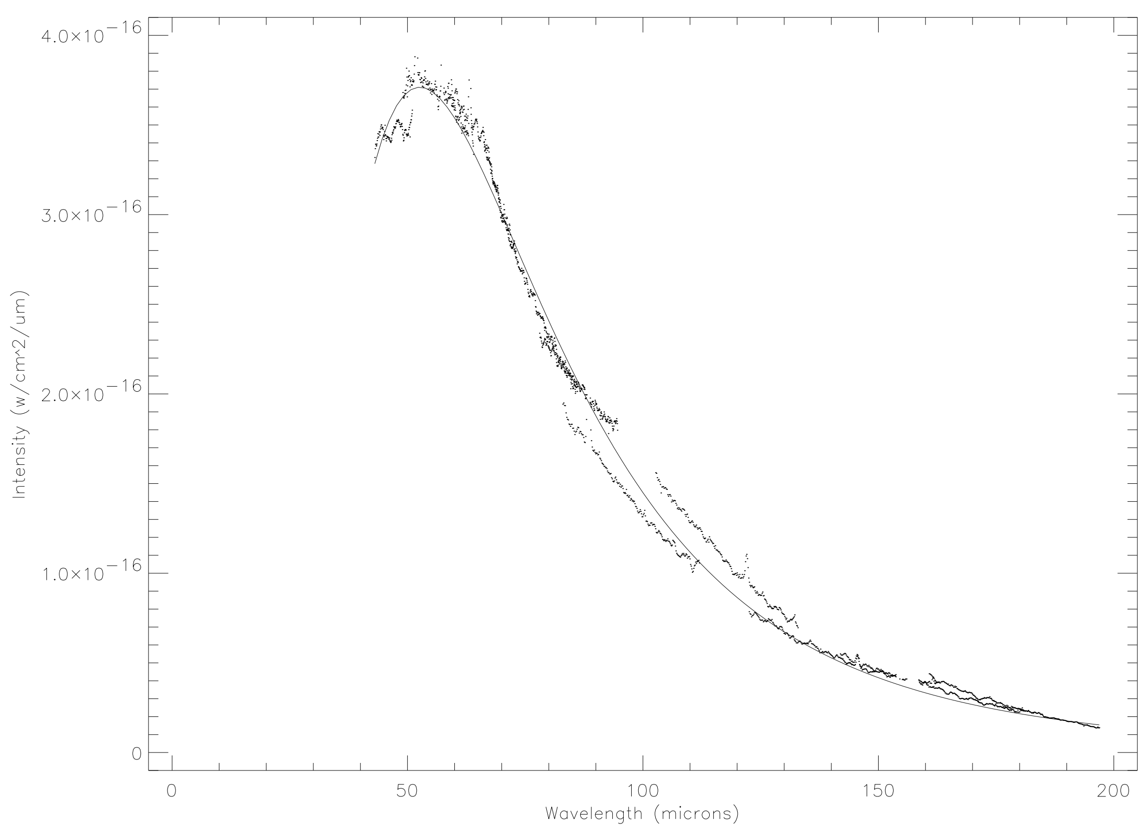

Fig. 2.8.— A typical blackbody fit to the LWS FIR continuum spectrum. The source is G348.71−1.03. The dots show flux data points averaged over multiple scans and different scan directions. The major emission lines have been removed. No attempt was made to connect the sub-spectra of different detectors. The solid curve is the fitting result.

ISAP provides utilities to fit the LWS continuum. Based on previous studies of dust emission properties (e.g., Greenberg & Shah 1971), the fitting function is of the from:

$$I = (1 - e^{-\tau}) \cdot \Omega \cdot B_\lambda(T_{\rm BB}). \tag{2.2}$$

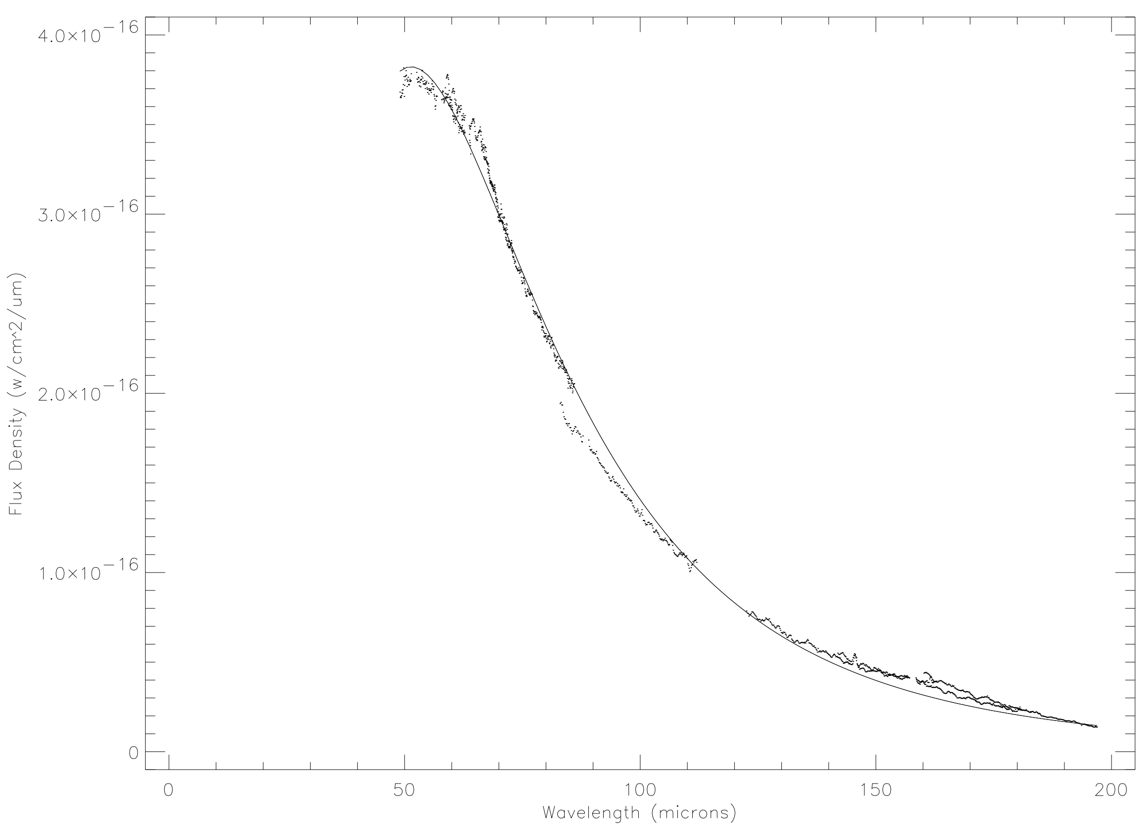

Fig. 2.9.— A blackbody fit to the same source as in Figure 2.8 with out-lying sub-spectra removed. The out-lying spectra are from SW5 and LW2, centered around 85μm and 118μm, respectively. The fitting result is compared in the text.

where τ is the dust emissivity, Ω is the solid angle of the emission area, and the blackbody energy distribution, $B_\lambda(T_{\rm BB})$, is:

$$B_\lambda(T_{\rm BB}) = \frac{2hc^2\lambda^{-5}}{\exp(hc/\lambda k T_{\rm BB}) - 1}, \tag{2.3}$$

where λ is the wavelength, $T_{\rm BB}$ is the blackbody temperature, h is the Planck constant, c is the speed of light, and k is the Boltzmann constant. The dust emissivity, τ, is proportional to dust opacity, and is expressed as:

$$\tau = \tau_{0.55} \left[\frac{0.55}{\lambda}\right]^{\alpha}, \tag{2.4}$$

where $\tau_{0.55}$ is the dust emissivity at visual wavelengths (0.55μm) and α is a spectral index. The unit for wavelength, λ, is μm. The parameters T_{BB}, $\tau_{0.55}$, α, and Ω can be determined by fitting in ISAP. The fitted result also gives 1σ errors for these parameters. Figure 2.8 shows a typical blackbody fit.

The determination of Ω, $\tau_{0.55}$, and α is not robust mostly because they are not independent parameters. In fact when τ is small, the quantity $(1 - e^{-\tau}) \cdot \Omega$ can be approximated as $\tau \cdot \Omega$, rendering these two parameters not independent. As can be seen in the fitting results presented in the next section, τ in the LWS wavelength range is always less than 0.1 for the ISO sources. During the fitting process some of the parameters had to be fixed in order to keep the result from straying too far from sane values. A fixed Ω value of 1.43×10^{-7} ster (the average LWS aperture size) is used when the fitting result is larger than 3 times the aperture area. When the uncontrolled fitting result for α is less than 0.5 a fixed value of 1.0 is used. I have found that forcing α to be 1.0 does not change the fitted curve by more than the relative error stated in §2.2.2 (30%). Therefore the difference between the fitted small α and 1.0 is within the LWS errors. Physically the value of α depends on the dust grain size, composition, optical properties, and details of the spatial distribution. Past investigations have found α to be typically $1 \leq \alpha \leq 2$ for the ISO LWS wavelength ranges (e.g., Cox, Kruegel & Mezger 1986; Duffy, Hawkes & Jones 1987; Helou 1989). I judge it is reasonable to limit α to be greater than 0.5.

Although the fits can produce relatively large uncertainties in Ω, $\tau_{0.55}$, and α, the overall fit still has good quality in terms of determining the dust temperature, which is the main goal of the blackbody fitting. The shape of the fitted curve is predominantly influenced by the blackbody temperature T_{BB}. The fitted values of T_{BB} have relatively small uncertainties (see the errors in Table 2.3 in § 2.3.2). Even when other parameters are artificially varied in a wide range, T_{BB} remains with $\pm$15K.

In order to show that the fitted blackbody temperature is not greatly affected by the unconnected sub-spectra, Figure 2.9 shows the blackbody fit of the same source as in Figure 2.8 with two out-lying sub-spectra (SW5 and LW2) removed. The $T_{\rm BB}$, Ω, $\tau_{0.55}$, and α are 46.5$\pm$2.5K, 2.8$\pm$4.1$\times$10^{-7} ster, 1.0$\pm$1.4, and 0.9$\pm$2.3. Compared with the fit shown in Figure 2.8 (47.4 $\pm$ 1.1K, 2.6 $\pm$ 1.1 $\times$ 10^{-7} ster, 0.6 $\pm$ 0.3, and 0.8 $\pm$ 0.1) the blackbody temperatures agree to within 1σ.

The second source of FIR data is the set of IRAS data products (Beichman *et al.* 1988). As described in §1 the purpose of using IRAS data is to derive the total FIR luminosity of the H II regions. The IRAS Point Source Catalog (PSC) is not used for this purpose because PSC fluxes do not include extended emission associated with the H II regions. Sometimes the PSC sources close to an H II region only represent a relatively small local maximum in flux. The PSC flux can be significantly smaller than the total IR flux of the source. Therefore I use the IRAS image product "FRESCO" (Full REsolution Survey Co-adder) from IPAC to derive the total FIR flux around the H II region. The FRESCO flux intensity maps are constructed using the Maximum Correlation Method from the IRAS scan data (Aumann, Fowler & Melnyk 1990). I obtained a one square degree (240$\times$240 pixels) FITS image for every IRAS band for every ISO source. The angular resolutions are $1^{'} \times 5^{'}$ at 12μm and 25μm, about $2^{'} \times 5^{'}$ at 60μm, and $4^{'} \times 5^{'}$ at 100μm. I wrote a program to integrate the flux within a zone surrounding the source position. Trials of different zone sizes determine a radius that is large enough to cover most of the source emission for each H II region in the sample, but still small enough not to pick up excessive

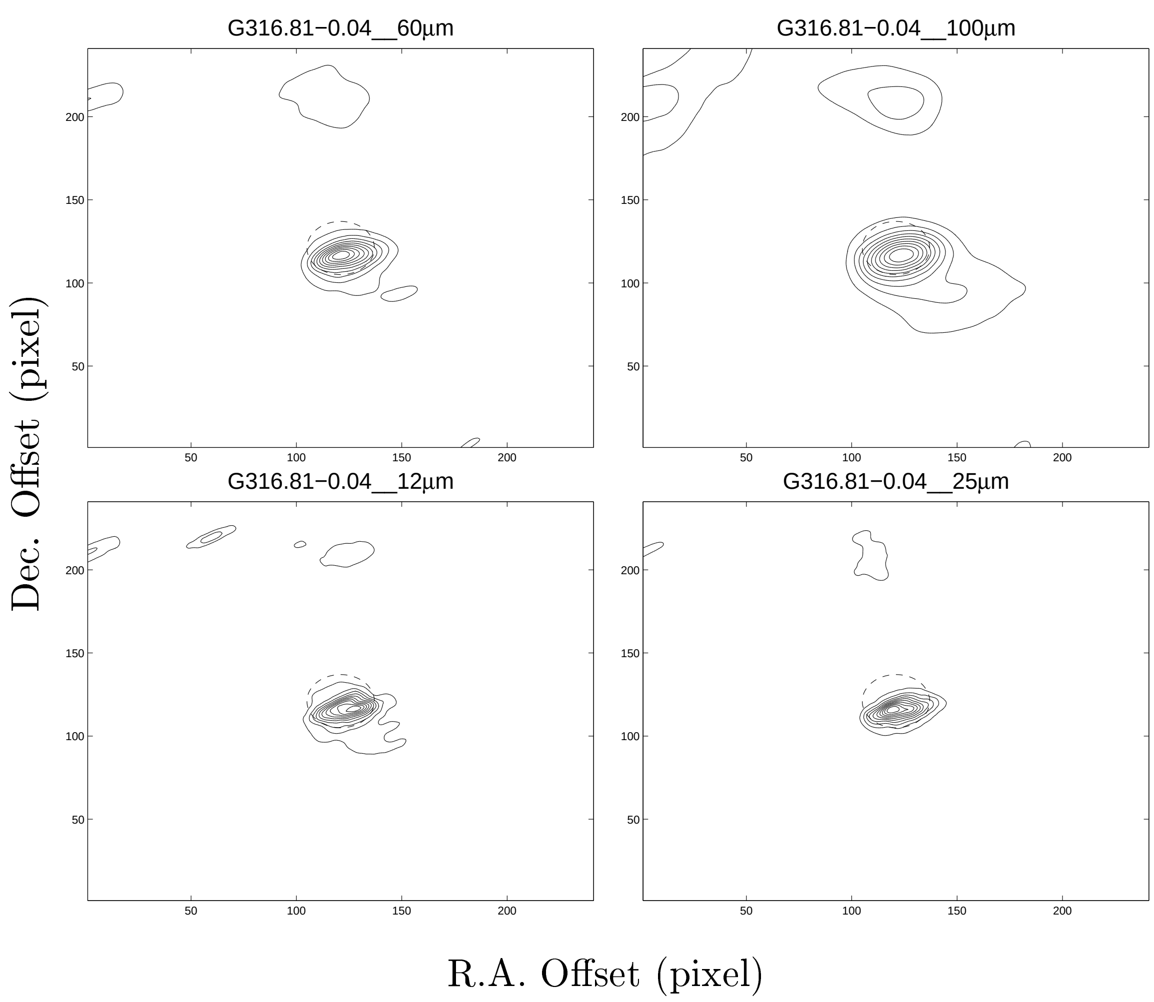

Fig. 2.10.— Example FRESCO flux density map used to calculate total FIR flux of the H II region sources. The figure axes are in units of pixels. There are 240 pixels for each axis, spanning a one degree range on the sky. The dashed circle indicates a $4'$ integration radius around the source used to determine the total flux.

background emission. The result is the total FIR flux of the source in each band. Figure 2.10 shows an example of the FRESCO maps with the circular integration range over-plotted.

2.3.2. Continuum Data, Line-to-continuum Ratios, and G_0

Table 2.3 lists the continuum measurements and analysis results for my ISO LWS observations and the IRAS FRESCO maps. The table gives the blackbody temperature, T_{BB}, the angular size of the emission area, Ω, the emissivity at 0.55μm, $\tau_{0.55}$, and the spectral index, α. (See the descriptions for Equations 2.3 and 2.4.) These parameters are derived from the blackbody fit to the ISO LWS continuum, as discussed in the previous section. The total FIR flux within the LWS aperture, F_{LWS}, is calculated by integrating the fitted blackbody curve over the 20μm to 300μm wavelength range. The error is estimated using the 50% quoted in § 2.2.2. The FIR fluxes, F_{12}, F_{25}, F_{60}, and F_{100}, are calculated by integrating within $4'$ radius from the source using the IRAS FRESCO flux density maps in all the 4 bands: 12μm, 25μm, 60μm, and 100μm.

The overall quality of the fit of the continuum to Equation 2.2 is excellent in the context of achieving the goals of my research: the fits determine the dust blackbody temperatures with relatively small errors and, as shown in Figure 2.8, recover the FIR energy distribution very well. The sometimes large errors of Ω, $\tau_{0.55}$, and α are indications of non-robust fits. The results of a non-robust fit are sensitive to small changes in the input data. The relatively small errors in T_{BB} reflect the fact that the FIR SEDs of the H II regions can be well characterized by a blackbody at temperature T_{BB} with an emissivity proportional to λ^{-1}. This agrees with previous ground-based and airborne observational results (e.g., Thronson &

TABLE 2.3

Analyses of IR Continua of the ISO Sources[a]

Source	$T_{\rm BB}$[b] (K)	Ω[b,c] (10^{-8}ster)	$\tau_{0.55}$	α[c]	$F_{\rm LWS}$[d] 10^{-15}W cm^{-2}	F_{12}[e] 10^3Jy	F_{25}[e] 10^3Jy	F_{60}[e] 10^3Jy	F_{100}[e] 10^3Jy
G291.28−0.72	...	...	...	...	...	2.2 ± 0.4	15.4 ± 3.1	50 ± 10	66 ± 13
G316.81−0.04	48.1 ± 0.8	10 ± 40	0.9 ± 3.1	1.0	6 ± 3	1.2 ± 0.2	5.1 ± 1.0	28 ± 06	37 ± 07
G322.15+0.61	43.0 ± 2.0	41 ± 53	2.2 ± 2.9	1.2 ± 0.2	14 ± 7	0.5 ± 0.1	2.3 ± 0.5	18 ± 04	26 ± 05
G332.66−0.61	49.1 ± 1.1	16 ± 7	0.7 ± 0.3	0.9 ± 0.1	13 ± 6	1.0 ± 0.2	4.1 ± 0.8	26 ± 05	29 ± 06
G333.29−0.37	40.1 ± 0.6	14	5.3 ± 0.4	1.0	20 ± 10	0.8 ± 0.2	6.0 ± 1.2	35 ± 07	45 ± 09
G336.84+0.05	39.2 ± 0.6	26 ± 33	0.9 ± 1.1	1.0	6 ± 3	1.3 ± 0.3	6.2 ± 1.2	67 ± 13	87 ± 17
G337.15−0.18	38.3 ± 0.6	10 ± 14	1.7 ± 2.2	1.0	4 ± 2	0.3 ± 0.1	1.4 ± 0.3	17 ± 03	23 ± 05
G337.95−0.48	46.6 ± 0.8	4 ± 5	1.1 ± 1.4	1.0	2 ± 1	0.8 ± 0.2	4.9 ± 1.0	24 ± 05	28 ± 06
G340.78−1.01	41.7 ± 0.6	14	2.3 ± 0.2	1.0	11 ± 5	0.8 ± 0.2	3.5 ± 0.7	26 ± 05	31 ± 06
G345.31+1.47	46.4 ± 1.0	11 ± 5	1.0 ± 0.4	1.0 ± 0.1	6 ± 3	1.3 ± 0.3	4.8 ± 1.0	33 ± 07	33 ± 07
G348.71−1.03	47.4 ± 1.1	26 ± 12	0.6 ± 0.3	0.8 ± 0.1	25 ± 13	1.8 ± 0.4	11.0 ± 2.2	51 ± 10	64 ± 13
G353.21+0.91	44.3 ± 0.7	14	878 ± 327	2.0 ± 0.1	38 ± 19	8.0 ± 1.6	34.6 ± 6.9	106 ± 21	105 ± 21

[a] ISO data reduction is based on the ISO pipeline OLP6.1 data using ISAP v2.0 and assuming extended sources. IRAS data is based on FRESCO maps.

[b] The fitting results of $T_{\rm BB}$ and Ω are not independent.

[c] The entries without errors are fixed parameters during the blackbody fitting.

[d] Total Flux is derived from integrating the blackbody function over $20\mu{\rm m} \leq \lambda \leq 300\mu{\rm m}$. The error is 50% (see text).

[e] The flux is derived from integrating the IRAS FRESCO flux density map, within $4'$ radius from the source position. The error is 20% (Beichman et al. 1988). $10^3 Jy = 10^{-27}$W cm^{-2} Hz^{-1}

[f] G291.28−0.72 was not observed by ISO. Its IRAS fluxes listed in this table will be used to estimate the luminosity.

Harper 1979; Helou 1989; Chan & Fich 1995). The average value of T_{BB} for the ISO source sample is 44.0 ± 3.6K, which agrees with the result of Kuiper *et al.* (1987) when they investigated IRAS observations of 65 southern molecular clouds and H II regions. They found the median dust temperature to be 42K with 70% of the sources lying within a 5K range.

Since all of the ISO sources have known kinematic distances (see discussion of Table 2.4), the total FIR luminosities can be derived using IRAS fluxes:

$$L_{FIR} = 4\pi d^2 \times F_{total} \tag{2.5}$$

where d is the distance to the source and F_{total} is the total FIR flux seen by the IRAS aperture. The total FIR flux can be derived from the F_{60} and F_{100} IRAS bands (Helou *et al.* 1988; Beichman *et al.* 1988):

$$F_{total} = 1.26 \times 10^{-14}(2.58F_{60} + F_{100}), \tag{2.6}$$

where F_{total} is in units of W m^{-2} and F_{60} and F_{100} are in Jy. This formula was originally defined for point sources (defined to be no larger than $30'$; Beichman *et al.* 1988). An extended source correction should be made to sources that are not point sources. Since all my ISO sources are significantly smaller than $30'$, the above formula is applicable here.

Furthermore, in the spherical configuration of the ISM surrounding the H II regions shown in §1 the incident FUV field (G_o) on the ISM outside the Strömgren sphere can be estimated. Here the term "incident" means the radiation field with respect to the ISM facing the exciting star of the H II region. I assume: 1) all FUV radiation of the exciting star of the H II region is converted to FIR radiation; and 2) the FUV photons from the star are the only source heating the dust. These assumptions mean that the energy in the FIR emission equals that in the incident

TABLE 2.4

Derived FIR Properties of the ISO Sources

Source	d[a] (kpc)	D_{HII}[b] (pc)	L_{FIR}[c] ($10^5 L_\odot$)	G_0[c,d]	$\frac{(I_{63\mu m} + I_{158\mu m})}{I_{LWS}}$[e]
G291.28−0.72	2.6 ±0.3	1.0 ± 0.1	5.3 ± 1.7	4.3 ± 1.6(4)	...
G316.81−0.04	2.5 ±0.5	2.1 ± 0.5	2.6 ± 1.2	4.8 ± 3.2(3)	3.9 ± 1.2(−3)
G322.15+0.61	3.5 ±0.6	1.5 ± 0.2	3.4 ± 1.4	1.2 ± 0.6(4)	4.0 ± 1.2(−3)
G332.66−0.61	3.3 ±0.6	6.0 ± 1.0	4.1 ± 1.6	9.3 ± 4.8(2)	3.8 ± 1.1(−3)
G333.29−0.37	3.5 ±0.6	4.2 ± 0.7	6.3 ± 2.4	2.9 ± 1.5(3)	2.2 ± 0.7(−3)
G336.84+0.05	10.7 ±1.6	41.1 ± 6.2	114.2 ± 41.3	5.5 ± 2.6(2)	6.0 ± 1.8(−3)
G337.15−0.18	10.9 ±1.7	23.4 ± 3.6	30.6 ± 11.1	4.5 ± 2.2(2)	7.5 ± 2.2(−3)
G337.95−0.48	3.1 ±0.6	1.7 ± 0.4	3.4 ± 1.4	9.6 ± 6.0(3)	5.2 ± 1.6(−3)
G340.78−1.01	2.3 ±0.5	3.9 ± 0.9	2.1 ± 1.0	1.1 ± 0.7(3)	3.2 ± 0.9(−3)
G345.31+1.47	1.8 ±0.6	2.8 ± 0.9	1.6 ± 1.0	1.6 ± 1.5(3)	8.4 ± 2.5(−3)
G348.71−1.03	2.0 ±0.7	1.7 ± 0.6	3.0 ± 2.2	8.5 ± 8.6(3)	3.0 ± 0.9(−3)
G353.21+0.91	1.7 ±0.3	5.2 ± 0.9	4.4 ± 1.8	1.3 ± 0.7(3)	3.6 ± 1.1(−3)

[a]Distances are derived from RRL observations and Galactic rotation curve for most sources. See text.

[b]See text for the derivation of the diameter of the ionized hydrogen region.

[c]The errors are derived from the errors of d and the 20% IRAS error.

[d]1 $G_0 \equiv 1.6 \times 10^{-10}$ W cm^{-2} (Habing 1968)

[e]I_{LWS} is converted from F_{LWS} using a nominal aperture size of 84″. The errors in the ratios of ISO measurements are estimated to be 30%.

FUV radiation. In a spherical dust shell outside the Strömgren sphere, G_0 can be easily derived by dividing the FIR luminosity with the surface area of the Strömgren sphere:

$$G_0 = \frac{L_{FIR}}{\pi D_{HII}^2} \tag{2.7}$$

where D_{HII} is the linear size of the ionized hydrogen region.

Table 2.4 lists derived FIR properties of the ISO source sample. The distance, d, is mostly derived from RRL measurements (see below). The Strömgren sphere linear diameter, D_{HII}, is calculated from the source distance as $d \cdot \Theta$, where Θ is the angular size of the 5 GHz radio continuum emission region given by Caswell & Haynes (1987). The FIR luminosity, L_{FIR} (in units of $L_\odot$), is calculated using Equations 2.5 and 2.6. The FUV field, G_0 , is derived using Equation 2.7 and is expressed in units of the ambient interstellar radiation field (1 $G_0 \equiv 1.6 \times 10^{-10}$ W cm^{-2}; Habing 1968). In the last column the FIR fine structure line-to-continuum ratio within the ISO beam is given. Conventionally this ratio is defined as $(I_{63\mu\mathrm{m}} + I_{158\mu\mathrm{m}})/I_{LWS}$ in PDR theory calculations. The continuum intensity is derived from F_{LWS} and an average LWS beam size of $84''$.

All ISO sources have known distances. I have calculated the kinematic distances using the RRL velocities and the Galactic rotation curve of Brand and Blitz (1993). The Galactocentric distance of the Sun is assumed to be 8.5 kpc. Caswell and Haynes (1987) have resolved the near-far distance ambiguities associated with these kinematic distances for all sources except G333.29−0.37 and G336.84+0.05. They used both observational results for the optical counterparts to the radio H II regions and also the H_2CO absorption features observed toward these H II regions. The near-far distance ambiguities of G333.29−0.37 and G336.84+0.05 are resolved elsewhere (e.g., McGee, Newton & Butler 1979; Gardner & Whiteoak 1984).

Therefore, unambiguous kinematic distances are known for all the ISO sources. These are used in Table 2.4 for all sources except G291.28−0.72 and G353.21+0.91. The distances for G291.28−0.72 and G353.21+0.91 are taken from Brand and Blitz (1993) and Neckel (1978). These distances are derived using photometric observations and visual extinction laws. They are considerably more accurate than the kinematic distances.

The error of the kinematic distances has two components. One component is the rotation curve error. It is the systematic error in the rotation curve model, which is estimated to cause 15% uncertainty. The other component is the peculiar motion error. It is caused by the peculiar motion of these H II regions with respect to the theoretical rotation curve model. This error is different from source to source. In order to estimate this error, two new kinematic distances are calculated with nominal LSR velocities of $V_{LSR} \pm 5$ km s^{-1} for each source. The differences between these new distances and the one in Table 2.4 are averaged and used as the peculiar motion error. The errors of d in Table 2.4 are the Gaussian quadrature sum of these two error components.

The source G353.23+0.91 has an unusually large $\tau_{0.55}$. This is caused mainly by its steep SED. A large α ($\sim$2) is needed to fit the shape of the SED. Since the LWS bandwidth is about two orders of magnitude longer in wavelength than 0.55μm, a large nominal $\tau_{0.55}$ is needed to fit the data. Note that $\tau_{0.55}$ is only a parameter for the fit. It is not to be taken as valid at optical wavelengths since observations have shown that the dust emissivity is less than 10 in this H II region (see Neckel 1978).

Some generalizations can be made from the FIR properties given in Table 2.4. The average FIR luminosity is $1.5 \pm 3.0 \times 10^6 L_\odot$. The large dispersion is due to the large luminosities of two distant sources: G336.84+0.05 and G337.15−0.18. Not taking them into account, the average L_{FIR} is $3.6 \pm 1.4 \times 10^5 L_\odot$. The minimum number of stars required to generate a $3.6 \times 10^5 L_\odot$ luminosity is one O6.5 star (Vacca, Garmany, & Shull 1996), assuming all stellar fluxes are converted to FIR emission. In order to account for the luminosity of G336.84+0.05 and G337.15−0.18, more than one O3 star is needed.

There are more than two orders of magnitude difference in the G_0 values for the sources, ranging from 4.5×10^2 to 4.3×10^4. The average G_0 is $7\pm11\times10^3$. Several well studied luminous H II-PDR regions are above this G_0 range, e.g., Orion (1.5×10^5) and M17 (5.6×10^4) (Tielens & Hollenbach 1985a; Stutzki *et al.* 1988; Chokshi *et al.* 1988).

The average line-to-continuum ratio, $(I_{[OI]} + I_{[CII]})/I_{FIR}$ is 0.46%, with a source-to-source dispersion of 0.19%. The [CII]-only line-to-continuum ratio is 0.3±0.2%. Nakagawa *et al.* (1998) used the Balloon-borne Infrared Carbon Explorer to survey the Galactic Plane in [CII]. They found that the [CII] line-to-continuum ratio changes from 0.6% for diffuse [CII] emission to 0.2% for compact sources. My results agree with their conclusions well within the dispersion.

It is difficult to compare the LWS continuum measurements of the ISO sources with IRAS observations for the H II regions I have observed. This is mainly due to the different beam sizes of the two instruments. Kuiper *et al.* (1987) derived the infrared properties of a sample of H II regions using IRAS observational results. I have compared the IRAS continuum intensities at 60μm and 100μm for 9 of the ISO sources studied by Kuiper *et al.* (1987) with the LWS results. The ratios of the IRAS intensity and the LWS intensity are 0.6 ± 0.5 and 0.7 ± 0.6 for 60μm and 100μm, respectively. These ratios are affected mainly by two factors. First, the calibrations of IRAS and LWS may not be consistent. For cross-calibration purposes the ISO team has compared intensity measurements between ISO and IRAS for a sample of extended sources. They have found that the difference is about 10% (§3.5.5 of García-Lario 2000). Since my sources are not extended to IRAS, the calibration consistency could be worse. Second, the large IRAS beams are likely to dilute the intensities of most of the ISO sources, which were chosen to be compact to fit the ISO beam. Therefore most sources have smaller intensities measured by IRAS than by LWS.

2.4. Summary

In this chapter I study the FIR fine structure lines of CII and OI as well as the FIR continuum of the ISO source sample. These intensities and intensity ratios are useful PDR diagnostics.

The Infrared Space Observatory satellite which I used to observe the ISO sample is described. Details of the Medium-Resolution mode (LW01 AOT) of the Long Wavelength Spectrometer of ISO are given. I used the LW01 AOT to obtain my H II region FIR data covering the wavelength range from 43μm to 197 μm. The spectral resolution is about 1500 $\mathrm{km\,s^{-1}}$, so no spectral transitions from Galactic gas are resolved in these data.

The LWS calibration schemes are described in detail. The wavelength and spectral resolution calibrations are sufficient for my requirements. The in-flight flux calibration is based on observing Uranus and using internal illuminator flashes. The Off-Line Processing software attempts to correct an array of instrumental problems. I point out several outstanding problems in the ISO calibration that are still difficult or impossible to solve. Some of these problems such as fringes and problematic beam sizes severely affect my data. The absolute LWS intensity calibration error budget for strong extended sources is 50% and the relative intensity calibration error between adjacent detectors is 30%.

After the observational and data processing details are described, I present observational results for atomic and ionic transitions in the LWS wavelength range for the ISO sample H II regions (§1). The three fine structure lines from [CII] and [OI] are detected in all sources with good signal to noise ratios. Many emission lines from ionic oxygen and nitrogen are also detected. Carbon, oxygen, and nitrogen fine structure line fluxes are presented. They are gotten by fitting Gaussians to the line profiles. The intensities of the PDR diagnostic fine structure lines are derived. The average values of $I_{63\mu m}$, $I_{145\mu m}$, and $I_{158\mu m}$ are $1.6 \pm 2.0 \times 10^{-10}$W cm^{-2}sr^{-1}, $2.8 \pm 2.4 \times 10^{-11}$W cm^{-2}sr^{-1}, and $2.1 \pm 0.7 \times 10^{-10}$W cm^{-2}sr^{-1}, respectively. Three line intensity ratios are also calculated: $I_{63\mu\mathrm{m}}/I_{158\mu\mathrm{m}}$, $I_{145\mu\mathrm{m}}/I_{63\mu\mathrm{m}}$, and $I_{145\mu\mathrm{m}}/I_{158\mu\mathrm{m}}$. Their average values are 0.65 ± 0.60, 0.25 ± 0.12, and 0.12 ± 0.08, respectively. Correlations between $I_{63\mu\mathrm{m}}$ and $I_{145\mu\mathrm{m}}$ and between $I_{63\mu\mathrm{m}}$ and $I_{158\mu\mathrm{m}}$ are found. They will be discussed in §5.

I describe the two data sources for my FIR continuum data: the LWS continuum observations and IRAS data products. The LWS data give total continuum fluxes, accurate dust temperatures, and line-to-continuum data; while the IRAS FRESCO maps spatially cover the emission area so that the global FIR luminosity from the source can be derived.

The blackbody fits to the LWS continuum data have good quality. The continua are well described by a blackbody spectral energy distribution with a dust emissivity proportional to λ^{-1}. The robustness of the fit is discussed. The fitted blackbody temperatures of all the H II regions are nearly identical; the average is 44.0±3.6K, agreeing with previously published studies.

IRAS FRESCO maps are used to calculate the FIR luminosity of the H II regions. Fluxes of the four IRAS bands are calculated by integrating around the source within a determined radius. These results are used to calculate the global FIR flux from the H II region and FIR luminosities. The distances of all ISO sources are known. The error in the distances is discussed. Assuming a spherical geometry, the FUV field intensity G_0 outside the Strömgren sphere is estimated for all sources. The average of the FIR luminosities and G_0 are $1.5 \pm 3.0 \times 10^6 L_\odot$ and $7 \pm 11 \times 10^3$ times the local average FUV field intensity, respectively. The fine structure line to continuum intensity ratios are calculated; the average line-to-continuum ratio is 0.0046 ± 0.0019.

The several PDR models described in §1 can be studied using the observed quantities gotten in this chapter. The intensities and intensity ratios found in this chapter will be used to derive the predicted PDR gas density, n, and G_0 values in §5. These predicted values will be compared with n and G_0 derived from observations (e.g., in this chapter and §3) so that the PDR models that made the prediction can be examined.

Chapter 3

AST/RO CI Observations

3.1. Introduction

Since the first observations of its ground state [$^3P_1 \rightarrow {}^3P_0$] transition, emission from neutral atomic carbon (Phillips *et al*. 1980; Phillips & Huggins 1981), C I, has been observed in a sample of test-bed sources such as the Orion Molecular Cloud, DR21, NGC2024, W3, M17, S140, W51, etc. (Phillips & Huggins 1981; Keene *et al*. 1985; Genzel *et al*. 1988; Stutzki *et al*. 1988; Zmuidzinas *et al*. 1988; White & Padman 1991; Tauber *et al*. 1995). These observations have shown that near the interface between the molecular clouds and the ionizing young OB stars, C I has greater abundance (up to 10^{18} cm^{-2} in column density and $0.1 \sim 1$ in abundance ratio over CO), and is more extensively distributed in the ISM than theoretical models had previous predicted (see Langer 1976). The physical conditions of C I derived by observing these few, very well studied, nearby molecular cloud-H II region complexes are the foundation of current theories of Photodissociation Regions (PDRs) (Tielens & Hollenbach 1985a; Tielens & Hollenbach 1985b; Stutzki 1990; Genzel 1991; Hollenbach & Tielens 1999 and references therein). There have been obvious limitations in the study of carbon properties in the vicinity of H II regions. First, the sample of sources that have been studied is small. The sample may be biased; it may only partially reflect the general properties of the total population. For example most sources that have been closely studied are nearby. Their properties could have been affected by local conditions in the Galaxy. Second, each of the previous studies only samples a small range of density and temperature (see review by Genzel *et al*. 1988). Third, in reality the cloud-star alignment along the line of sight with regard to the observer, the spatial distribution of density and temperature, and the velocity fields in a source are complex. Therefore a particular set of assumptions and simplifications are chosen in a study due to lack of knowledge of details or because of the limitations of the instruments being used. For example, when Keene *et al*. (1985) studied M17, the far ultra-violet (FUV) flux density used to check photo-chemical models was based on a single FIR flux density result. Our understanding of the role of interstellar carbon and PDRs will be more certain if the basic physical conditions are measured for a larger sample of H II regions.

In this chapter I characterize the properties of the C I emission observed toward a large sample of Galactic H II regions. Using the Antarctic Submillimeter Telescope and Remote Observatory (AST/RO, see §1) I collected C I data with excellent signal-to-noise ratios for a large sample of H II regions. These observations have increased the number of H II regions observed in C I by a factor of more than 5. They provide not only the properties of C I emission in each source, but also give a collective picture of C I in H II regions in the Milky Way Galaxy.

I present two sets of observations of the 492.161 GHz fine-structure transition of neutral atomic carbon (C I [$^3P_1 \rightarrow {}^3P_0$]) from Galactic H II regions. The observations were made with AST/RO in August, 1995, and October, 1998. One data set is comprised of single point observations of 49 H II regions in the Wilson *et al*. (1970) H109α radio recombination line (RRL) catalog. Mapping observations for the ISO sources listed in §1, Table 1.2, comprise the other data set. Almost all the mapped H II regions are in the 49-source pointed survey (§ 3.3). Here I: (1) present statistical results to describe the emission properties of C I; (2) propose and verify a method to identify C I spectral components that are associated with H II regions; (3) compare the differences between these two populations of components; (4) conclude that the Galactic C I emission associated with H II regions is dominated by sources of local heating; and (5) calculate C I gas masses and densities.

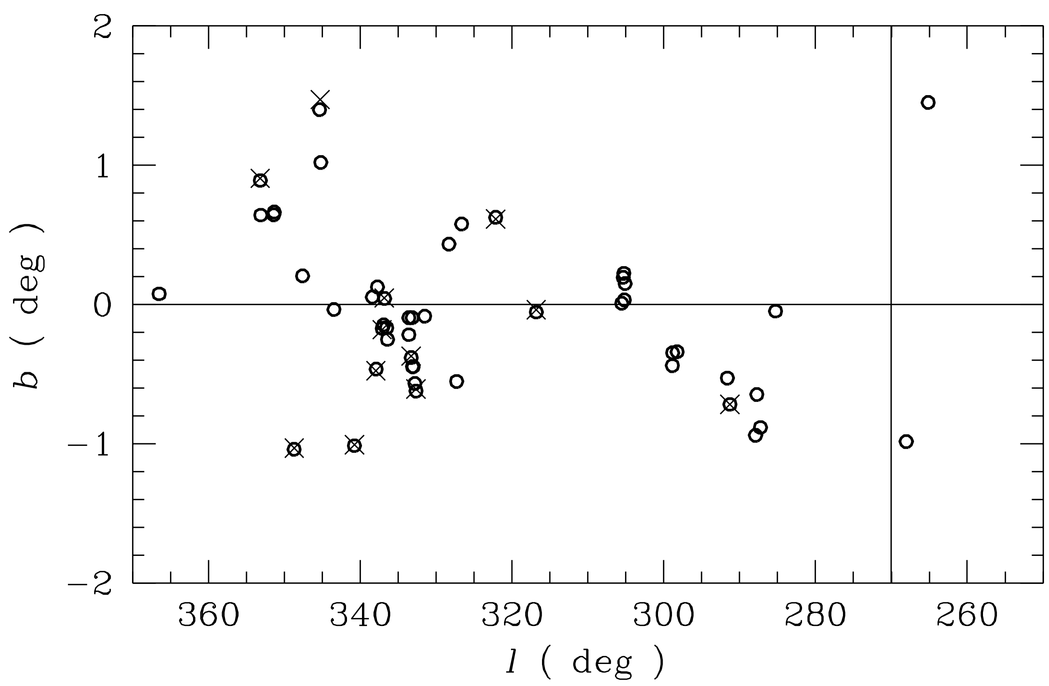

Fig. 3.1.— Galactic position of observed H ii regions. Most sources in this survey are located in the fourth quadrant of Galactic longitude. Sources were selected to be within a declination range of -20° to -65°. The 49 H ii region survey sources are plotted with circles; the ISO sample sources are plotted with crosses.

3.2. C I Observations of 49 Southern H II Regions

I have made a preliminary survey of the emission properties of C I in a sample of 49 Southern Hemisphere H II regions. The sample of H II regions covers a large area of the fourth quadrant of the Galactic plane. These survey observations were made during the commissioning period of AST/RO, however, and were primarily used as pointing sources. Because of this, neither the source sample nor the derived C I properties can be considered comprehensive. The survey data are nonetheless of good quality, since the observations were performed during a short period and are consequently less affected by possible calibration and pointing problems.

This H II region sample was observed during the commissioning of the AST/RO system. Many of these sources were selected primarily to determine the telescope pointing and calibration characteristics. Hence this survey is not a homogeneous sample of objects but rather an assortment of H II regions that are suitable for various equipment tests. These tests required the sources to be bright, isolated, and reasonably compact. The sample sources were chosen from the H109α RRL survey of Wilson *et al*. (1970). Most sources are within the Milky Way's fourth quadrant (see Figure 3.1). Only those sources with both small angular size and 5 GHz continuum flux densities greater than 10 Jy were chosen.

The most important selection criterion was the source 5 GHz intensity because its relation to the C I intensity was unknown. Sources used to determine the telescope pointing had to be smaller than the $\sim$130$''$ beam; these sources comprise one-third of the sample. Moreover, the declination of each source falls between $-25°$ and $-65°$. (At the geographic South Pole, source elevation equals negative declination.) The primary goal of declination selection was to include wide elevation coverage. The lower limit in declination was chosen to reduce the effects of atmospheric attenuation.

3.2.1. Observational Parameters

The observations were made during the 1995 Austral winter with the 1.7 m aperture AST/RO telescope at the United States Amundsen-Scott South Pole Station. The telescope efficiency was measured to be $\eta_{492} \geq 0.75$ (Chamberlin, Lane, & Stark 1997). The telescope beam shape was determined using limb scans of the moon, continuum maps of Jupiter, and spectral line maps of compact sources (Stark *et al*. 1997). For the observations reported here, the telescope half-power beam width (HPBW) at 492 GHz was $\sim$130″. The 492 GHz quasi-optical receiver which has a 165 K DSB noise temperature (Zmuidzinas *et al*. 1993; Engargiola, Zmuidzinas, & Lo 1994) was used. The receiver output was sampled by a 2048-channel acousto-optical spectrometer (AOS). At the C I rest frequency the AOS has a velocity resolution of 0.641 km s^{-1}.

This system configuration gave spectra that sampled a total LSR velocity range of $\sim$500 km s^{-1}. For the observations discussed here the total system noise temperatures were $\sim$3,000 K. For the Austral winter of 1995 the South Pole median 492 GHz atmospheric opacity at zenith was $\tau_{492} = 0.70$ (Chamberlin *et al*. 1997). The bulk of the observations reported here were made on 9 and 11 August 1995. During this period a total of 16 skydip measurements were made. The average zenith opacity was 0.52 ± 0.02, significantly better than the winter median.

A single pointing was made toward each source and position switched spectra were taken. Integration times ranged from 11 minutes to more than an hour. Because these were system test observations, no attempt was made to integrate down to a uniform noise level for the source sample. (The rms noise level for each source is given in Table 3.1) Reference positions were set at $\pm 1^\circ$ in right ascension. An advantage of being at the South Pole is that an offset in right ascension is an offset in azimuth. This switching scheme both eliminates elevation-dependent effects due to changes in atmospheric emission and also gives a switch against two positions fixed in right ascension and declination.

3.2.2. Calibration

The calibration system of the AST/RO telescope is described in Stark *et al.* (1994) and Chamberlin *et al.* (1997). The intensity scale was calibrated by measuring an ambient temperature load and two cooled blackbody loads installed inside a dewar. The cooled blackbody loads are periodically checked against an absorber saturated with liquid nitrogen. Regular skydips and sky temperature measurements were used to correct for atmospheric attenuation and emission. The skydip data were fit to a slab atmospheric model to yield zenith opacity, spill-over, and sky temperatures. In addition, each spectrum was individually calibrated using a sky temperature measurement procedure that compared the sky near the source with one of the blackbody loads (Ingalls 1998). Skydips were usually made several times per day. During the 1995 Austral winter, in good weather the atmospheric opacity over the South Pole was stable for periods of several days (Chamberlin, Lane, & Stark 1997).

The line temperature used through out this chapter is the physically meaningful main beam brightness temperature ($T_{\rm MB}$), which is related to the measured antenna temperature corrected for atmosphere attenuation, T_A^*, by $T_{\rm MB} = \frac{T_A^*}{\eta}$, where η is the antenna efficiency. Detailed discussion of spectral line calibrations for AST/RO are found in Ingalls (1998).

The actual measured line temperature can also be affected by pointing errors if the source has an intensity gradient on a spatial scale that is comparable to the beam size. Even during these commissioning observations the pointing error was less than $\sim 50''$ compared with the $\sim 130''$ HPBW. The effect of mechanical irregularities of the telescope and building structure on pointing was determined by optical measurements. An optical telescope attached to AST/RO was used to observe a set of bright stars distributed throughout the entire visible sky. These measurements were then used to model the telescope pointing. Radio maps of Jupiter and several H II regions, made at all azimuth angles, were then used to determine the radio beam offset with respect to the optical telescope and the precession of the radio beam as a function of azimuth.

Based on repeated observations and an analysis of the skydips, I judge that the overall intensity scale error is about 15%. Because the observations discussed here were conducted during a short period, the relative uncertainty in the antenna temperature scale is expected to be less than 15% within this data sample.

The channel spacing and frequency resolution of the AOS were measured by using a comb signal fed into the AOS and a frequency sweeper. The channel spacing was 0.674 MHz and the effective frequency resolution was 1.05 MHz. The AOS frequency calibration was made using a set of test frequencies spaced at 100 MHz intervals. This gave an AOS center channel frequency calibration of better than 1% of a channel width which corresponds to 4 $\mathrm{m\,s^{-1}}$at the C I rest frequency. The AOS was made at the University of Cologne. Further information about Cologne AOS specifications can be found in Schieder *et al*. (1989).

3.2.3. Properties of C I Emission

Figure 3.2 shows typical C I spectra for a subset of the sources. Both strong and weak C I emission as well as simple and complex line profiles are shown. The

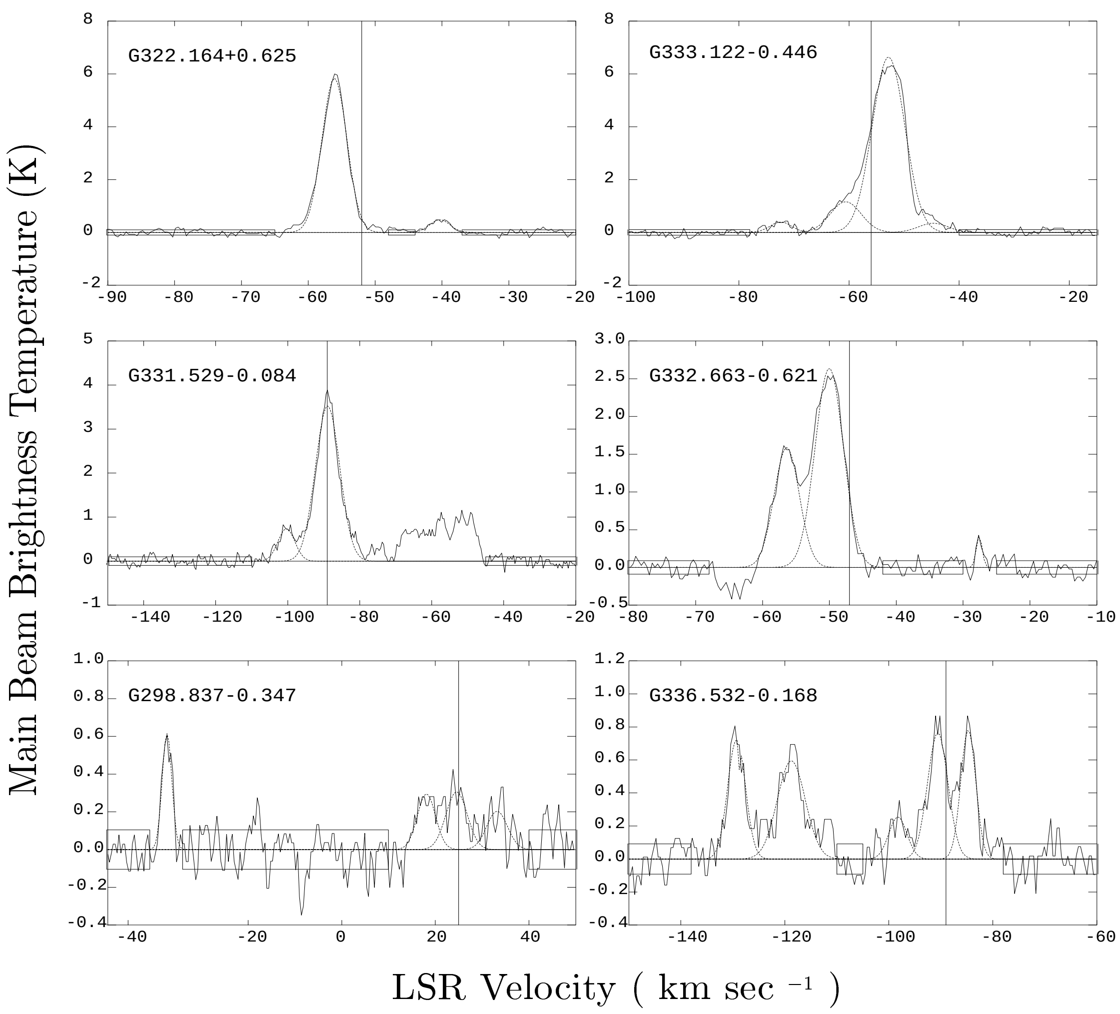

Fig. 3.2.— Typical C I spectra for a subset of the 49 H II region pointed survey sample. The intensity scale is the main beam brightness temperature which is the antenna temperature corrected for both atmospheric attenuation and main beam efficiency. The source name is indicated at the top left corner of each box. The boxes plotted on the baseline span velocity zones where the baseline model is determined and the baseline RMS is calculated. Linear baselines have been removed from most of the survey spectra (see notes in Table 3.1). The dashed curve shows the Gaussian fits to the emission features. The vertical line flags the source H109α RRL LSR velocity.

majority of spectra have had a linear baseline removed. For a number of sources (29%), there is a $\sim$ 30 MHz baseline ripple, likely due to standing waves between mirrors and other structures in the optical path. For these sources a higher order polynomial (typically order 3 or 4) baseline was removed.

The observed parameters of C I emission for the H II region sample are listed in Table 3.1. Gaussian fits were made to significant emission features. Table 3.1 gives the parameters of these fits; listed are the LSR velocity of the component, its peak main beam brightness temperature, linewidth (FWHM), and line area (K $\mathrm{km\,s^{-1}}$), together with the $\pm 1\sigma$ errors of the fits. Also listed are the 1σ root mean square (rms) noise level in the baseline (BRMS) and the residual rms after the Gaussian is subtracted (GRMS). Components that have ideal Gaussian shapes should give equal BRMS and GRMS.

These new observations have increased the number of H II regions with measured C I emission by about a factor of 5. Figure 3.3 shows the (ℓ,v) distribution of C I emission components for the H II region sample. The terminal velocity locus plotted is based on the Clemens (1985) rotation curve which was derived from a survey of the first Galactic quadrant CO gas. Most of the H II region C I components are within this envelope of LSR velocities permitted by Galactic circular rotation. Thus the northern CO gas and this C I emission sample have similar kinematics. There are a few emission components outside this envelope. This could be due to North-South differences in the streaming motions.

TABLE 3.1

C i Emission Properties of H ii Regions

Source	$V_{\rm LSR}$ (km sec^{-1})	$T_{\rm MB}$ (K)	FWHM (km sec^{-1})	Area (K km sec^{-1})	GRMS (K)	BRMS (K)	Note[a]
G6.528+0.076	24.2 ± 0.2	2.87 ± 0.29	4.41 ± 0.58	12.59 ± 1.13	0.36	0.19	B1 n
	38.8 ± 0.1	3.42 ± 0.20	2.58 ± 0.17	9.91 ± 1.02	0.32	0.19	…
G265.144+1.450	6.2 ± 0.0	4.36 ± 0.04	3.59 ± 0.04	17.64 ± 0.27	0.15	0.08	B2 n
G268.034−0.984	3.4 ± 0.3	0.37 ± 0.04	5.86 ± 0.65	2.24 ± 0.24	0.13	0.09	B2 ?
G285.261−0.048	2.1 ± 0.2	0.53 ± 0.08	3.38 ± 0.56	1.55 ± 0.32	0.11	0.10	B3 n
G287.259−0.883	−15.9 ± 0.2	0.45 ± 0.06	2.84 ± 0.43	1.47 ± 0.21	0.09	0.08	B1 n
G287.718−0.646	−26.0 ± 0.1	1.26 ± 0.04	4.91 ± 0.16	6.47 ± 0.24	0.10	0.09	B1 n
G287.906−0.939	−39.3 ± 0.3	0.24 ± 0.06	2.14 ± 0.62	0.52 ± 0.14	0.05	0.09	B1 n
	−22.1 ± 0.1	0.31 ± 0.03	1.83 ± 0.22	0.74 ± 0.08	0.08	0.09	…
G291.276−0.717	−23.9 ± 0.0	2.87 ± 0.02	8.44 ± 0.07	25.33 ± 0.23	0.20	0.07	B1 n
	28.3 ± 1.2	0.16 ± 0.08	4.67 ± 2.83	0.65 ± 0.50	0.06	0.07	…
G291.610−0.528	11.5 ± 0.2	0.42 ± 0.04	5.05 ± 0.60	2.28 ± 0.24	0.07	0.10	B1 n
G298.227−0.340	−36.1 ± 0.4	0.28 ± 0.05	4.94 ± 0.92	1.24 ± 0.30	0.09	0.09	B2 n
	32.7 ± 0.1	0.88 ± 0.03	5.79 ± 0.27	5.83 ± 0.29	0.10	0.09	…
G298.837−0.347	−37.3 ± 0.1	0.61 ± 0.07	2.43 ± 0.33	1.49 ± 0.21	0.07	0.10	B1 o
	18.1 ± 0.3	0.29 ± 0.03	4.58 ± 0.77	1.07 ± 0.13	0.07	0.10	…
	24.6 ± 0.3	0.31 ± 0.03	5.38 ± 0.81	1.48 ± 0.12	0.08	0.10	…
	33.2 ± 0.4	0.20 ± 0.03	5.21 ± 1.01	1.04 ± 0.17	0.10	0.10	…
G298.862−0.438	−37.8 ± 0.3	0.26 ± 0.06	3.15 ± 0.81	0.61 ± 0.26	0.07	0.10	B1 o
	18.6 ± 0.1	0.56 ± 0.04	3.11 ± 0.30	1.52 ± 0.11	0.10	0.10	…
	23.8 ± 0.4	0.28 ± 0.05	3.68 ± 1.05	0.91 ± 0.15	0.07	0.10	…
	30.9 ± 0.2	0.68 ± 0.03	7.69 ± 0.56	5.32 ± 0.27	0.10	0.10	…
G305.096+0.150	−41.3 ± 0.3	0.74 ± 0.03	9.40 ± 0.69	5.63 ± 0.20	0.13	0.09	B1 r
G305.198+0.032	−46.0 ± 0.1	1.35 ± 0.05	4.46 ± 0.18	6.24 ± 0.22	0.11	0.11	B1 r
	−35.7 ± 0.1	1.22 ± 0.04	7.65 ± 0.28	9.47 ± 0.25	0.14	0.11	…
G305.251+0.224	−79.1 ± 0.3	0.30 ± 0.09	2.08 ± 0.69	0.65 ± 0.22	0.08	0.09	B1 r
	−39.4 ± 0.1	1.02 ± 0.02	8.31 ± 0.23	9.18 ± 0.20	0.13	0.09	…
G305.359+0.194	−37.3 ± 0.1	2.98 ± 0.03	8.10 ± 0.11	24.34 ± 0.38	0.21	0.10	B1 r
G305.550+0.009	−39.5 ± 0.0	2.23 ± 0.01	4.46 ± 0.02	11.23 ± 0.35	0.19	0.10	B4 n
	−31.8 ± 0.2	0.58 ± 0.13	1.89 ± 0.51	1.00 ± 0.24	0.15	0.10	…
G316.796−0.055	−38.8 ± 0.0	4.00 ± 0.04	7.50 ± 0.08	33.36 ± 0.37	0.16	0.09	B3 n
	−20.8 ± 1.8	0.27 ± 0.04	13.34 ± 4.71	2.82 ± 0.40	0.09	0.09	…
G322.164+0.625	−56.1 ± 0.0	5.84 ± 0.05	4.39 ± 0.05	27.92 ± 0.37	0.15	0.10	B3 n
	−40.3 ± 0.2	0.48 ± 0.07	3.53 ± 0.60	1.77 ± 0.30	0.05	0.10	…
G326.654+0.578	−40.8 ± 0.1	3.29 ± 0.05	6.60 ± 0.12	24.12 ± 0.41	0.22	0.10	B1 n
	−22.1 ± 0.1	0.82 ± 0.17	1.47 ± 0.35	1.48 ± 0.38	0.13	0.10	…
G327.304−0.552	−47.4 ± 0.0	4.93 ± 0.05	7.32 ± 0.08	39.27 ± 0.46	0.21	0.12	B1 f
G328.312+0.433	−93.5 ± 0.1	2.14 ± 0.05	7.30 ± 0.18	18.04 ± 0.51	0.16	0.10	B1 n
	−102.8 ± 0.4	0.37 ± 0.07	4.59 ± 1.18	1.62 ± 0.28	0.09	0.10	…
	−57.4 ± 0.2	0.40 ± 0.05	2.80 ± 0.39	1.13 ± 0.15	0.06	0.10	…
G331.529−0.084	−88.9 ± 0.1	3.53 ± 0.10	7.96 ± 0.26	34.45 ± 1.11	0.31	0.10	B1 f
	−100.4 ± 0.6	0.74 ± 0.12	5.53 ± 1.50	3.75 ± 0.63	0.09	0.10	…
G332.663−0.621	−56.4 ± 0.2	1.59 ± 0.09	4.44 ± 0.54	5.48 ± 0.35	0.10	0.09	B3 n
	−50.0 ± 0.0	2.64 ± 0.04	4.97 ± 0.09	13.75 ± 0.24	0.10	0.09	…
	−27.6 ± 0.1	0.42 ± 0.09	1.04 ± 0.25	0.53 ± 0.15	0.10	0.09	…

TABLE 3.1—*Continued*

Source	$V_{\rm LSR}$ (km sec^{-1})	$T_{\rm MB}$ (K)	FWHM (km sec^{-1})	Area (K km sec^{-1})	GRMS (K)	BRMS (K)	Note[a]
G332.815−0.567	−57.8 ± 0.0	3.79 ± 0.05	6.13 ± 0.09	26.16 ± 0.38	0.18	0.11	B3 or
	−49.8 ± 0.4	0.37 ± 0.09	3.67 ± 1.02	1.37 ± 0.33	0.11	0.11	...
G333.028−0.447	−72.8 ± 0.3	0.42 ± 0.05	5.61 ± 0.82	2.42 ± 0.32	0.08	0.11	B1 n
	−54.6 ± 0.0	4.69 ± 0.03	6.80 ± 0.04	34.47 ± 0.23	0.26	0.11	...
G333.122−0.446	−72.4 ± 0.4	0.40 ± 0.07	4.58 ± 0.88	1.91 ± 0.31	0.11	0.11	B1 n
	−52.8 ± 0.0	6.65 ± 0.04	7.01 ± 0.08	39.69 ± 0.20	0.45	0.11	...
	−44.7 ± 3.4	0.35 ± 0.18	6.37 ± 8.19	1.57 ± 0.71	0.10	0.11	...
	−60.6 ± 0.1	1.16 ± 0.03	6.59 ± 0.25	7.66 ± 0.22	0.07	0.11	...
G333.167−0.095	−89.3 ± 0.3	1.61 ± 0.10	8.97 ± 0.65	15.94 ± 1.16	0.13	0.11	B1 o
	−69.8 ± 0.2	0.55 ± 0.05	6.09 ± 0.62	3.46 ± 0.29	0.10	0.11	...
	−56.8 ± 1.3	0.23 ± 0.07	8.47 ± 4.21	1.76 ± 0.42	0.07	0.11	...
	−47.9 ± 0.1	1.85 ± 0.04	4.79 ± 0.12	9.02 ± 0.24	0.21	0.11	...
G333.293−0.382	−51.8 ± 0.0	7.09 ± 0.05	7.00 ± 0.10	40.02 ± 0.22	0.09	0.12	B1 o
	−58.4 ± 0.1	0.61 ± 0.04	3.84 ± 0.30	2.38 ± 0.16	0.07	0.12	...
	−43.4 ± 0.1	0.51 ± 0.03	3.59 ± 0.25	1.76 ± 0.14	0.17	0.12	...
G333.605−0.095	−88.7 ± 0.4	0.96 ± 0.08	10.19 ± 0.97	10.42 ± 1.06	0.11	0.09	B1 n
	−69.6 ± 0.3	0.22 ± 0.07	2.29 ± 0.82	0.32 ± 0.23	0.07	0.09	...
	−47.8 ± 0.1	1.61 ± 0.02	12.77 ± 0.16	22.93 ± 0.25	0.18	0.09	...
G333.610−0.217	−88.9 ± 0.3	0.93 ± 0.07	8.70 ± 0.81	8.55 ± 0.65	0.10	0.11	B1 n
	−48.2 ± 0.0	3.32 ± 0.03	9.09 ± 0.10	31.53 ± 0.26	0.18	0.11	...
	−35.5 ± 0.5	0.49 ± 0.06	9.38 ± 1.50	4.27 ± 0.41	0.12	0.11	...
G336.427−0.251	−87.4 ± 0.2	1.45 ± 0.07	7.61 ± 0.44	12.62 ± 0.78	0.17	0.11	B1 n
	−77.8 ± 0.3	0.45 ± 0.09	3.05 ± 0.79	1.35 ± 0.25	0.11	0.11	...
	−24.6 ± 0.1	0.70 ± 0.05	4.17 ± 0.33	3.09 ± 0.27	0.09	0.11	...
G336.532−0.168	−129.3 ± 0.2	0.72 ± 0.09	4.03 ± 0.55	3.36 ± 0.40	0.11	0.09	B1 o
	−118.8 ± 0.2	0.60 ± 0.04	6.32 ± 0.54	4.03 ± 0.25	0.11	0.09	...
	−98.3 ± 0.4	0.26 ± 0.04	4.09 ± 1.09	0.91 ± 0.12	0.06	0.09	...
	−90.6 ± 0.1	0.77 ± 0.05	4.62 ± 0.40	3.43 ± 0.18	0.09	0.09	...
	−84.7 ± 0.1	0.78 ± 0.04	3.40 ± 0.23	2.90 ± 0.16	0.09	0.09	...
G336.807+0.043	−114.7 ± 0.4	0.84 ± 0.08	6.53 ± 0.97	5.52 ± 0.53	0.10	0.10	B1 n
	−122.2 ± 0.1	0.77 ± 0.04	4.95 ± 0.35	3.84 ± 0.20	0.10	0.10	...
	−75.0 ± 0.1	1.50 ± 0.03	12.71 ± 0.26	19.74 ± 0.31	0.12	0.10	...
	−61.2 ± 0.3	0.36 ± 0.05	4.65 ± 0.78	1.84 ± 0.24	0.06	0.10	...
G336.934−0.146	−119.1 ± 0.1	1.36 ± 0.03	7.99 ± 0.21	11.81 ± 0.28	0.13	0.09	B1 o
	−98.3 ± 1.6	0.22 ± 0.11	6.03 ± 3.66	1.37 ± 0.77	0.08	0.09	...
	−81.4 ± 0.4	0.60 ± 0.06	5.78 ± 1.00	3.12 ± 0.33	0.10	0.09	...
	−74.1 ± 0.2	1.59 ± 0.02	11.48 ± 0.42	13.24 ± 0.19	0.16	0.09	...
	−36.8 ± 0.2	0.44 ± 0.06	3.82 ± 0.58	1.96 ± 0.33	0.11	0.09	...
	−19.3 ± 0.1	0.62 ± 0.07	2.26 ± 0.29	1.11 ± 0.26	0.09	0.09	...
G337.122−0.172	−118.6 ± 0.3	1.16 ± 0.10	6.80 ± 0.66	8.39 ± 0.80	0.10	0.09	B3 n
	−74.9 ± 0.1	2.34 ± 0.03	8.42 ± 0.12	21.19 ± 0.34	0.14	0.09	...
	−35.7 ± 0.6	0.19 ± 0.06	3.89 ± 1.48	0.28 ± 0.33	0.10	0.09	...
	−21.8 ± 0.1	0.59 ± 0.06	2.29 ± 0.27	1.03 ± 0.25	0.11	0.09	...
G337.753+0.126	−72.4 ± 0.2	0.89 ± 0.03	8.50 ± 0.53	6.45 ± 0.26	0.09	0.09	B1 o
	−61.5 ± 0.1	0.91 ± 0.03	9.44 ± 0.33	8.69 ± 0.26	0.17	0.09	...
	−50.9 ± 0.5	1.50 ± 0.05	13.10 ± 1.04	13.50 ± 0.43	0.10	0.09	...
	−29.1 ± 0.5	0.25 ± 0.09	2.87 ± 1.21	0.62 ± 0.35	0.08	0.09	...

TABLE 3.1—*Continued*

Source	$V_{\rm LSR}$ (km sec^{-1})	$T_{\rm MB}$ (K)	FWHM (km sec^{-1})	Area (K km sec^{-1})	GRMS (K)	BRMS (K)	Note[a]
G337.920−0.464	−58.3 ± 0.3	0.37 ± 0.05	4.36 ± 0.79	1.79 ± 0.25	0.11	0.13	B1 o
	−40.5 ± 0.0	2.40 ± 0.05	3.98 ± 0.10	10.26 ± 0.28	0.14	0.13	...
	−33.4 ± 0.5	0.36 ± 0.05	5.68 ± 1.21	1.83 ± 0.28	0.10	0.13	...
G338.425+0.053	−117.3 ± 0.2	0.41 ± 0.04	5.37 ± 0.58	2.42 ± 0.28	0.07	0.08	B1 r
	−33.6 ± 0.2	1.11 ± 0.02	17.10 ± 0.44	16.49 ± 0.24	0.12	0.08	...
G340.793−1.014	−28.9 ± 0.1	4.02 ± 0.14	4.47 ± 0.18	18.89 ± 0.96	0.14	0.08	B1 n
G343.475−0.036	−130.1 ± 0.3	0.32 ± 0.08	2.72 ± 0.81	0.40 ± 0.37	0.08	0.11	B1 n
	−29.9 ± 0.0	2.15 ± 0.03	4.60 ± 0.08	10.49 ± 0.22	0.07	0.11	...
	5.1 ± 0.0	1.12 ± 0.06	1.11 ± 0.06	1.57 ± 0.10	0.08	0.11	...
G345.210+1.020	−15.7 ± 0.0	4.62 ± 0.05	3.79 ± 0.05	19.36 ± 0.36	0.15	0.10	B3 o
	−11.8 ± 0.2	0.47 ± 0.12	1.32 ± 0.39	0.67 ± 0.20	0.06	0.10	...
G345.385+1.398	−13.8 ± 0.0	3.43 ± 0.04	3.59 ± 0.05	13.85 ± 0.22	0.12	0.10	B1 n
G347.611+0.205	−95.2 ± 0.1	1.57 ± 0.04	4.89 ± 0.16	8.51 ± 0.33	0.09	0.10	B3 n
G348.719−1.040	−32.3 ± 0.4	0.50 ± 0.07	5.71 ± 0.88	3.20 ± 0.56	0.08	0.10	B1 n
	−13.1 ± 0.0	3.75 ± 0.04	5.60 ± 0.07	22.64 ± 0.29	0.18	0.10	...
G351.347+0.663	−3.6 ± 0.1	2.42 ± 0.04	6.03 ± 0.11	15.27 ± 0.32	0.15	0.09	B3 n
G351.419+0.644	−4.9 ± 0.0	7.01 ± 0.01	7.71 ± 0.02	58.33 ± 0.16	0.28	0.25	B1 n
G353.191+0.890	−4.5 ± 0.1	1.20 ± 0.03	6.23 ± 0.21	7.46 ± 0.27	0.16	0.09	B5 r
G353.122+0.642	−40.2 ± 0.3	0.44 ± 0.07	3.76 ± 0.68	1.67 ± 0.32	0.09	0.10	B1 r
	−4.1 ± 0.2	0.84 ± 0.03	9.03 ± 0.46	7.23 ± 0.26	0.11	0.10	...
	5.2 ± 0.1	0.48 ± 0.09	1.43 ± 0.30	0.64 ± 0.18	0.07	0.10	...

[a]Bn: n-th order polynomial baseline was removed. r: emission at reference position contaminating at least one emission line component;

Association Between C I *Emission and H* II *Regions*

Table 3.1 shows that there are multiple C I emission components found toward 34 of the 49 sources. Apparently, of these 113 emission components, some are associated with the H II regions and others with gas unrelated to the prominent H II region along the line of sight. It is important to identify a sample of C I spectral components that are physically associated with the H II regions. Lacking distance information, such an association can only be made based on coincident positions and velocities. In order to investigate the velocity differences between C I emission components and the source RRLs, define the quantity $\Delta V \equiv V_{CI} - V_{RRL}$. For simplicity, I define

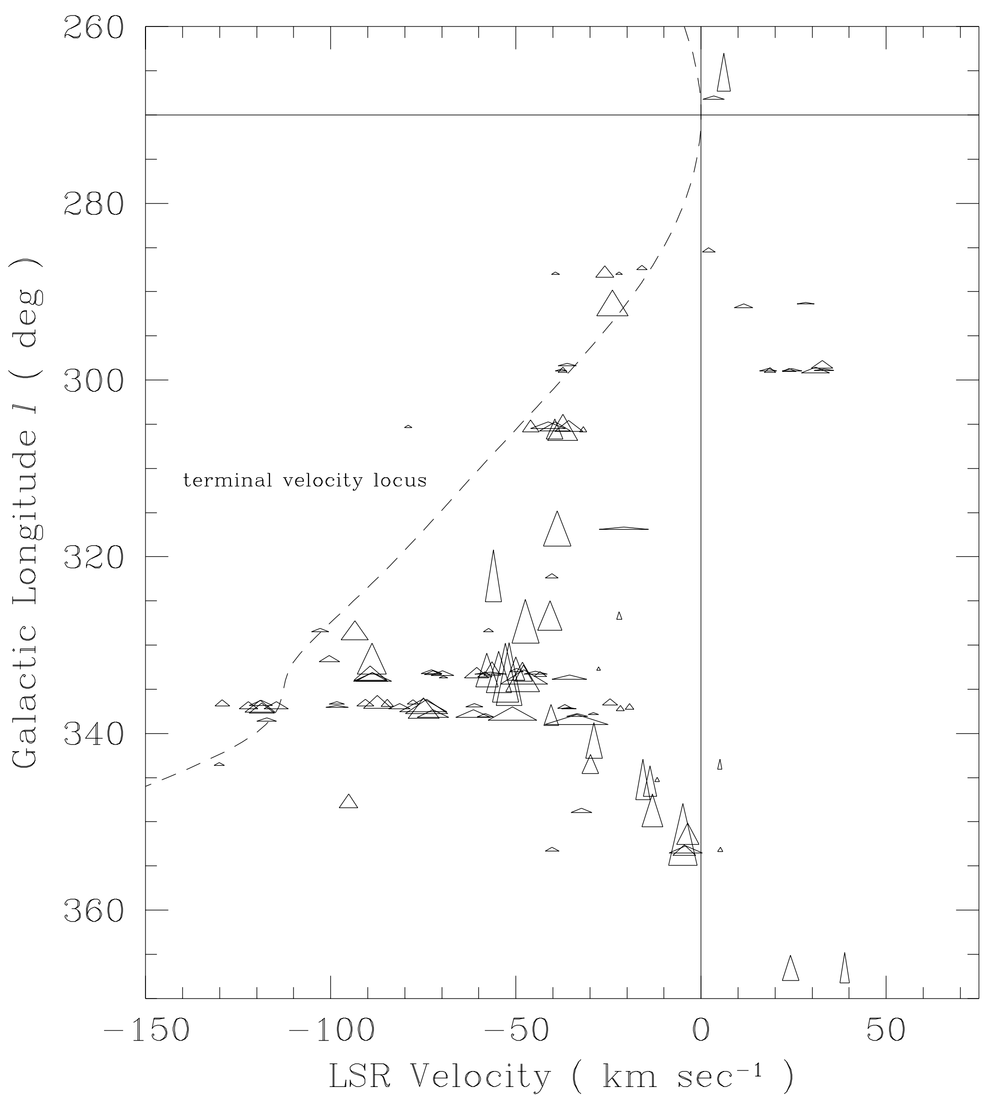

Fig. 3.3.— Every C I spectral line component found toward each of the 49 H II regions is plotted on this (ℓ–v) diagram using a triangle. The base of each triangle shows the FWHM of the line (same scale as the V_{LSR} axis); the height is proportional to the peak line intensity. These emission components are consistent with the observed Galactic rotation: the locus of terminal velocities determined from the Clemens (1985) rotation curve is drawn here as a dashed line.

two groups of spectral components. Group I is comprised of the C I component in each source nearest to the RRL velocity; Group II contains all other C I emission components.

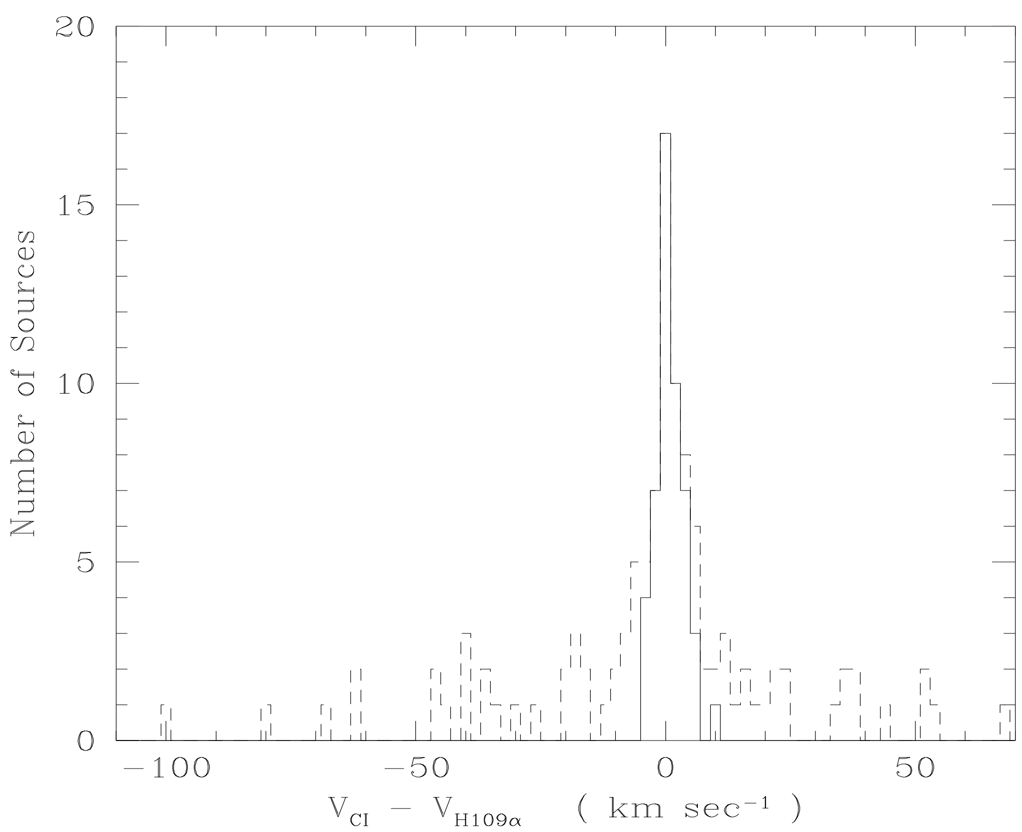

Fig. 3.4.— Histogram showing the LSR velocity difference between C I and H109α RRL emission, ΔV. Each H II region has some C I component nearest to its RRL velocity; the histogram of these components is denoted by solid lines. The histogram of all other velocity components is shown by the dashed lines.

Figure 3.4 shows the histogram of the distribution of all spectral components identified in the source sample as a function of ΔV. There are 49 Group I components; these are denoted by solid lines in Figure 3.4. There are a total of 64 Group II components; these are denoted by dashed lines. The average velocity differences, $\langle \Delta V \rangle$, are 0.8 ± 2.8 km s^{-1} and -4.7 ± 33.6 km s^{-1} for Groups I and II, respectively. The average FWHM line widths are 6.7 ± 3.0 km s^{-1} and 4.8 ± 2.4 km s^{-1}for Groups I and II, respectively. Note that the dispersion of ΔV for Group I is less than the average FWHM linewidth, whereas Group II has a dispersion in ΔV that exceeds its linewidth by a factor of seven.

Note that the Group I components are on average within 1 km s^{-1} of the H II region RRL velocities. This is exact agreement with the RRL velocities since the Wilson *et al*. (1970) H109α RRL catalog has an average LSR velocity error of ± 1 km s^{-1}. For Group I components both the average velocity difference, $\langle \Delta V \rangle$, and its dispersion are comparable to the same quantities evaluated for CO gas associated with Galactic H II regions (Fich, Treffers, & Blitz 1982; Myers *et al*. 1986; Waller *et al*. 1987). I conclude that the Group I C I emission components are physically associated with the H II regions.

It seems possible, however, that this classification procedure conservatively defines C I associated with H II. There may be a bias to label C I emission components as unassociated with the H II gas when they really are. That is, H II regions may have multiple C I components associated with their ambient photodissociation regions. I estimate how many Group II sources are really Group I by assuming that the population of C I components is normally distributed in ΔV. Fitting a Gaussian function to the Figure 3.4 histogram suggests that $\sim$6% of the Group II sources may actually be associated with the H II regions.

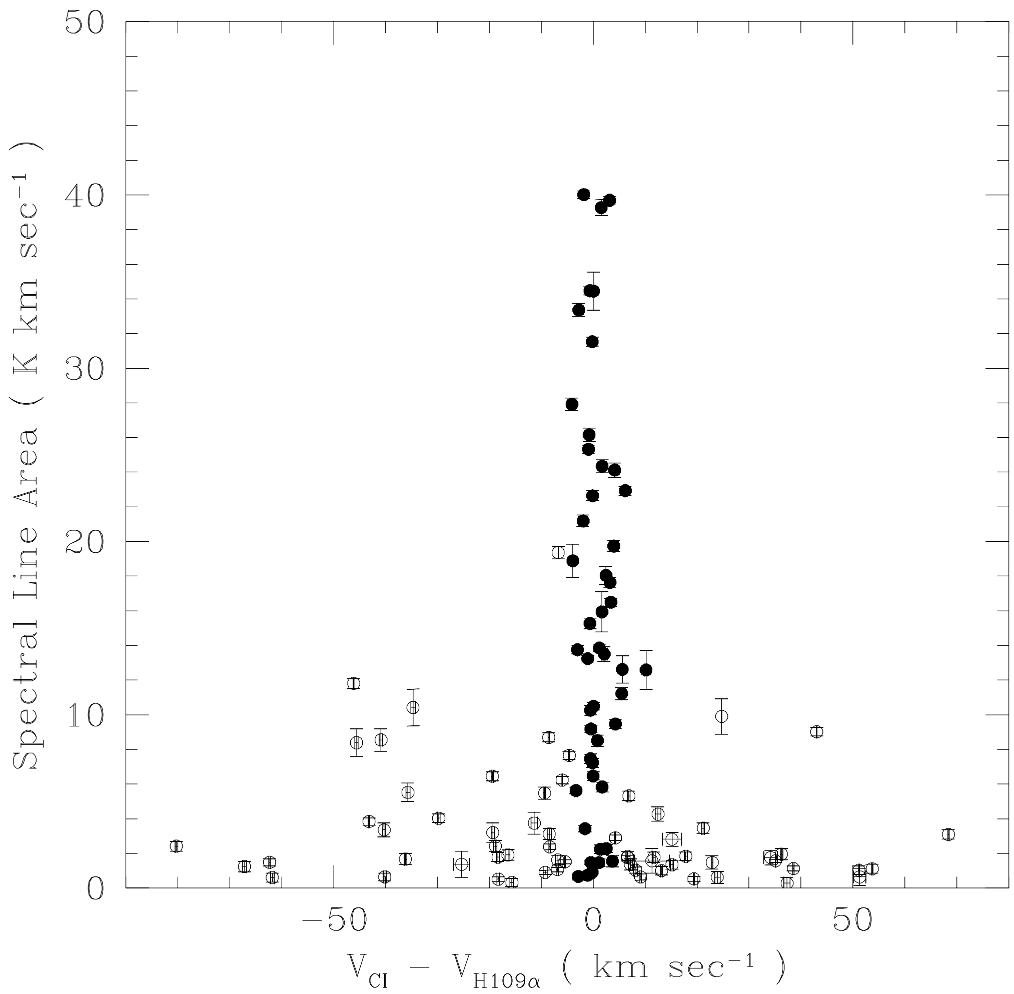

Fig. 3.5.— The C I integrated line intensity plotted as a function of ΔV for all spectral components. Solid symbols denote C I emission components nearest in velocity to the observed hydrogen RRL velocity; open symbols denote all other C I components. The error bars are $\pm$ 1 σ uncertainties from the Gaussian fits. The prominent peak near 0 km s^{-1} indicates that strong C I emission is associated with H II regions.

C I Emission Line Parameters

The C I emission line parameters for this survey are listed in Table 3.1 and summarized in Figure 3.5 and Figure 3.6. In both figures Group I components are plotted as filled circles; Group II components are drawn as open circles. Figure 3.5 shows the C I integrated line intensity plotted as a function of ΔV for all spectral components. Figure 3.6 plots the FWHM linewidth as a function of the peak main beam brightness temperature of each emission component. There is a clear distinction between the Group I and Group II emission parameters. This is best seen in Figure 3.5 which has a prominent integrated intensity peak at 0 $\mathrm{km\,s^{-1}}$ produced by Group I components. Figure 3.6 shows that the average FWHM linewidth for *any* C I component having an intensity greater than 2 K is 6.0 ± 1.8 $\mathrm{km\,s^{-1}}$. Components weaker than 2 K show a much greater dispersion in their FWHM linewidths: $\langle \mathrm{FWHM} \rangle = 5.5 \pm 3.0$ $\mathrm{km\,s^{-1}}$; the poorer signal-to-noise of these components compromises my ability to measure these lines accurately.

Compared with the Group II components, the H II region associated Group I components have brighter C I lines and slightly wider linewidths. The average peak main beam brightness temperatures are 2.4 ± 1.8 K and 0.7 ± 0.7 K for Groups I and II, respectively. This suggests that the Group I components are dominated by local H II region heating. For the Table 3.1 emission components the total line-integrated intensity for the 49 Group I components is 1.6 times as large as that of the total line-integrated emission from the 64 Group II components.

Figure 3.7 shows the histogram of the FWHM linewidths for all C I components. Group I and II components are plotted as solid and dashed lines, respectively. The average FWHM linewidth of Group I components is 6.7 ± 3.0 $\mathrm{km\,s^{-1}}$. Most of the broad lines probably are unresolved blends of multiple components. Note that in

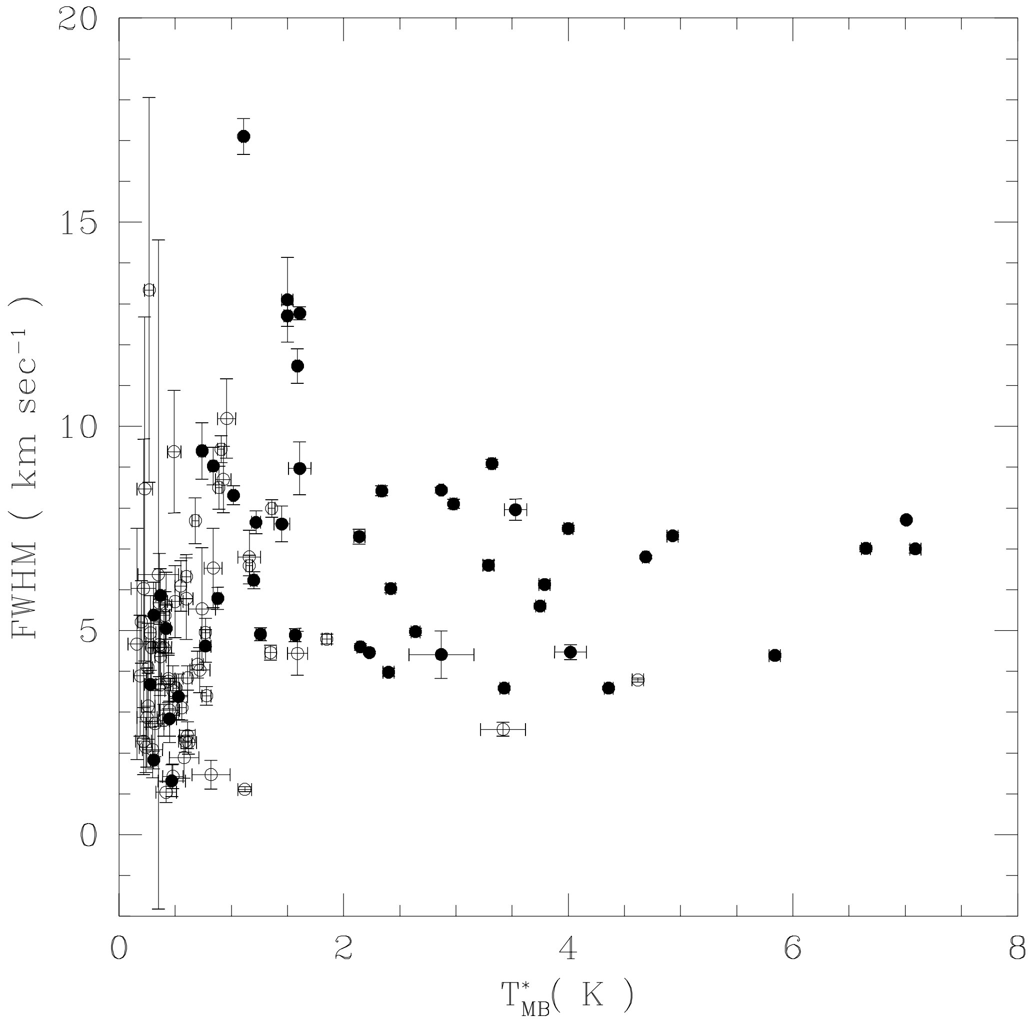

Fig. 3.6.— The C I emission properties for all observed components. Plotted is the component linewidth as a function of its intensity as determined by Gaussian fits. Solid symbols denote C I emission components nearest in velocity to the observed hydrogen RRL velocity; open symbols denote all other C I components. The error bars are $\pm$ 1 σ uncertainties from the Gaussian fits. The 15% uncertainty in the calibration of the absolute intensity scale has not been included here.

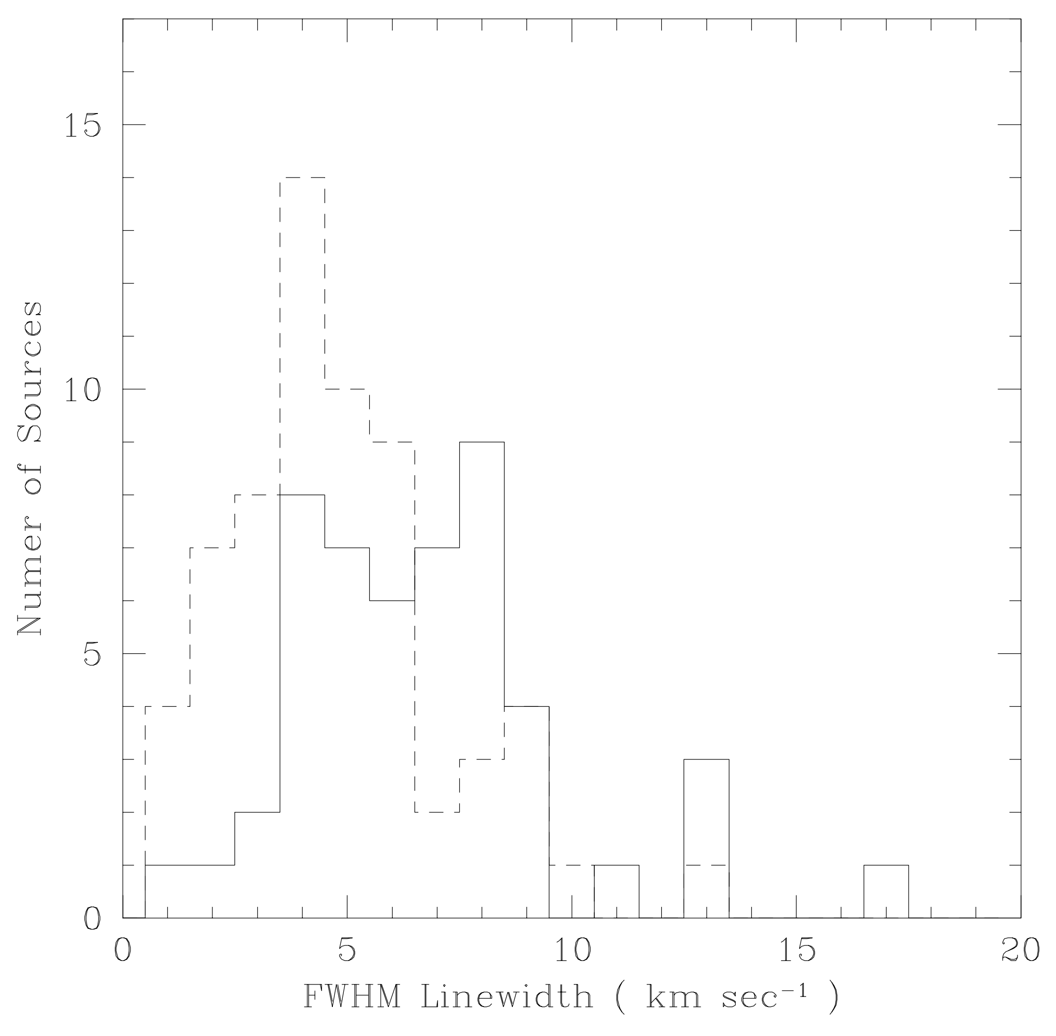

Fig. 3.7.— Histogram of the FWHM linewidths for all C I components as determined by Gaussian fits. Solid lines denote C I emission components nearest in velocity to the observed hydrogen RRL velocity; dashed lines denote all other C I components.

Figure 3.6 the broadest linewidths are all found for weak (< 2 K intensity) emission features. Spectral noise makes the decomposition of these weak features into multiple separate components especially problematic and non-unique.

Whiteoak *et al*. (1982) used CO(1–0) to study 79 southern H II regions with a beam size that is similar to that of AST/RO in C I. They defined CO within 5 $\mathrm{km\,s^{-1}}$ of the H II region RRL velocity to be associated with the nebula. For these emission components they find that the FWHM linewidth is 9.5 ± 3.1 $\mathrm{km\,s^{-1}}$. Note that this is marginally greater than the C I FWHM linewidth found for my Group I components (6.7 ± 3.0 $\mathrm{km\,s^{-1}}$). Both C I and CO H II region associated gas have apparent superthermal linewidths, presumably due to turbulent motions.

3.3. H II Regions Mapped in C I

I have mapped 11 H II regions that were also observed using the Long Wavelength Spectrometer (LWS) on the ISO satellite. I refer hereafter to the survey of 49 H II regions as the "pointed survey" and the survey of the ISO sources as the "mapped survey". In this section I first discuss the source selection, observation and calibration. Then I compare the emission properties between H II region map center spectra and the pointed survey spectra. Next I show that Group I components have a stronger spatial correlation with H II regions than Group II components. Finally, after I calculate C I column densities, I estimate the total C I masses and volume densities of the sample H II regions, analyze various results, and find support for the spherical PDR model.

Detailed source selection criteria are discussed in §1. Since the sources for the two C I surveys are selected from different catalogs, source position differences were compared to find out how many sources are common between the two samples. The parameter "$P_{\rm diff}$" in Table 3.2 shows how far each of the mapped survey sources is from the nearest source in the pointed survey sample. The catalog positions of both samples were determined by the peak of the 5 GHz radio continuum. All mapped sources except G345.31+1.47 have counterparts in the pointed survey. The Wilson *et al.* catalog has a source that is 1.5$'$ away from G345.31+1.47. But that source was not in the pointed survey. Not including G345.31+1.47, the average $P_{\rm diff}$ is 1.2 $\pm$ 0.5$'$. Since the Wilson *et al.* catalog has an estimated position accuracy of 1$'$, and the Caswell and Haynes catalog has a position uncertainty of 30$''$, the combined position uncertainty, $(1^2 + 0.5^2)^{1/2} = 1.1'$, suggests that except for G345.31+1.47 all mapped survey sources are also in the pointed survey sample. This overlap of sample sources allows me to examine the consistency of the results derived from the two surveys in § 3.3.2.

3.3.1. Observation and Calibration

The observations were made from October 7, 1998 to October 8, 1998. Fully sampled 7×7 maps were made toward each of the sources. The standard AST/RO test source H18 (G291.28−0.72) was mapped before the ISO sources were observed to confirm telescope pointing and calibration. According to the beam-precession measurements, the telescope pointing was better than 1$'$. The map grid spacing was 1.1$'$, which is half of the beam size. At each grid position, a position switched observation was made with a 30 second on-source integration. The reference position for each source was a relatively emission-free nearby position on the 100μm IRAS map. After every 14 integrations, a calibration and a sky measurement were made. At the end of the mapping observations of these ISO sources, the two ISO reference positions were observed in single-pointing mode using position switching. The on-source integration time was 4 minutes for each ISO reference source. The reference positions for them were $\pm 30'$away in Right Ascention.

Most of the detailed telescope setups and calibration procedures were the same as for the pointed survey. The average receiver temperature during the observing period was measured to be 220 K DSB. The typical system temperature was 1500K. The telescope beam at 492 GHz in the 1998 Austral winter season was about $230''$. Telescope efficiency (η_{492}) was $\sim$0.7. The zenith opacity during the observing period was 0.78 $\pm$ 0.004 according to skydip measurements. The channel spacing of the AOS was 0.675 MHz. After the observations were made the local frequency standard was found to cause an error in the IF. Comparisons show that this IF error caused a 2.5 $\pm$ 0.6 $\mathrm{km\,s^{-1}}$ velocity shift in the mapped spectra relative to the pointed survey. Therefore the velocities of all mapped survey spectra have been reduced by a constant 2.5 $\mathrm{km\,s^{-1}}$to correct this error.

3.3.2. Properties of C I Emission at Map Centers Compared with the Pointed Survey

C I Detections and the Map Center Spectra

C I emission is found in all the mapped H II regions. Figure 3.8 shows map averaged emission profiles for four of the sample sources. Figures 3.9 and 3.10 show maps of line integrated C I intensity toward a subset of the mapped H II region sample.

Table 3.2 lists the C I emission parameters of the map center spectra. The emission parameters, $\mathrm{V_{LSR}}$, T_{peak}, FWHM linewidth, Area, GRMS, and BRMS, are

TABLE 3.2

C I Emission Properties of Mapped H II Regions: the Map Center Spectrum

Source	$V_{\rm LSR}$ (km sec^{-1})	$T_{\rm MB}$ (K)	FWHM (km sec^{-1})	Area (K km sec^{-1})	GRMS (K)	BRMS (K)	Note[a]	P$_{\rm diff}$[b] ($'$)	$\frac{A_{\rm ctr}}{A_{\rm pnt}}$[c]
G291.28−0.72	−24.2 ± 0.2	4.6 ± 0.2	8.3 ± 0.5	41.0 ± 1.9	0.7	0.8	B1 n	0.5	1.6
G316.81−0.04	−39.6 ± 0.1	3.8 ± 0.1	7.6 ± 0.3	30.0 ± 1.1	0.5	0.5	B2 n	1.3	0.9
G322.15+0.61	−56.2 ± 0.2	2.3 ± 0.2	3.8 ± 0.4	8.5 ± 0.8	0.3	0.5	B3 n	1.0	0.3
G332.66−0.61	−50.4 ± 0.2	3.0 ± 0.2	6.3 ± 0.4	21.4 ± 1.0	0.5	0.5	B1 r	0.8	1.6
	−57.9 ± 0.6	1.2 ± 0.2	5.7 ± 1.6	1.3 ± 1.2	0.6	0.5	...	...	...
G333.29−0.37	−51.5 ± 0.1	5.0 ± 0.1	7.7 ± 0.3	41.0 ± 1.1	0.5	0.5	B1 n	0.7	1.0
G336.84+0.05	−77.5 ± 0.5	1.3 ± 0.1	9.9 ± 1.3	13.3 ± 1.3	0.5	0.6	B1 o	2.0[e]	0.7
	−117.6 ± 0.7	0.9 ± 0.1	10.2 ± 1.8	0.8 ± 1.4	0.5	0.6	...	...	...
G337.15−0.18	−71.9 ± 0.7	1.1 ± 0.1	14.0 ± 1.6	16.0 ± 1.5	0.5	0.5	B1 n	1.6	0.8
	−118.9 ± 0.5	1.2 ± 0.2	7.2 ± 1.2	0.0 ± 1.2	0.7	0.5	...	...	...
G337.95−0.48	−39.5 ± 0.4	1.2 ± 0.1	7.1 ± 1.0	7.1 ± 1.1	0.5	0.5	B1 r	1.9[e]	0.7
G340.78−1.01	−29.0 ± 0.2	2.9 ± 0.2	5.0 ± 0.4	14.2 ± 0.9	0.6	0.5	B1 r	1.0	0.8
G345.31+1.47	−12.3 ± 0.3	1.5 ± 0.3	3.0 ± 0.7	0.7 ± 0.8	0.5	0.7	B1 o	...[d]	...[d]
G348.71−1.03	−13.5 ± 0.1	3.9 ± 0.2	6.0 ± 0.4	24.9 ± 1.2	0.6	0.7	B1 n	0.6	1.1
G353.21+0.91	−5.3 ± 0.4	1.9 ± 0.2	7.9 ± 0.9	15.0 ± 1.6	0.8	0.8	B1 r	1.3	2.0

[a]Bn: n-th order polynomial baseline was removed. o: blended lines make Gaussian fits non-unique; r: emission at reference position contaminating at least one emission line component.

[b]Position difference between the catalog values in Caswell & Haynes (1987) and the counterparts in the Wilson et al. (1970) catalog.

[c]Group I line area ratios between the mapped source and its counterpart in the pointed survey.

[d]The nearest H II region to G345.31+1.47 was not observed in the pointed survey

[e] This source has a complex morphology.

calculated using Gaussian fits to the map center spectra using the same method as for the emission parameters derived in § 3.3.2. The comments made in the "Note" column have the same meaning as in Table 3.1.

There are 12 H II regions in Table 3.2. The first source G291.28−0.72 is the AST/RO standard source for checking pointing and calibration. No C I emission was detected from the two ISO reference positions. The RMS noise is 0.16 K and 0.20 K respectively for G322R (l=322.153, b=3.113) and G337.9R (l=337.949, b=−2.976). The statistics below include G291.28−0.72, but not the two ISO reference positions.

Quantitatively the emission properties of C I averaged over the entire map are not easily compared with the pointed survey results due to the different angular sizes of the sampled areas. Since the spectrum at the map center was observed at the peak of the 5 GHz radio continuum, these spectra were taken in the same way as were the pointed survey observations. Below I compare the properties of these map center spectra with those of the pointed survey.

Comparison of the Results of the Two Surveys

As an example of the repeatability of the observations, Figure 3.11 shows the map averaged spectrum of G332.66-0.61 and the spectrum taken in the pointed survey. Careful comparisons have been made between the pointed survey spectra and mapped survey spectra, which include the map center spectrum, the map averaged spectrum, and the interpolated spectra at the maximum intensity position. Within the signal to noise ratios, the same emission components are found to exist in both surveys. Also, 8 of the 11 H II regions have emission peaks that lie within the AST/RO FWHM beamsize of the map center; these sources show comparable line temperatures for both surveys. The remaining three have comparable line temperatures if the spectrum at the map peak is compared with the pointed survey spectrum.

TABLE 3.3
Comparison of C I Properties between Two Surveys

	Pointed Survey		Mapped Survey[a]	
	Group I	Group II	Group I[b]	Group II
Sample size	49	64	11	4
ΔV ($\mathrm{km\,s^{-1}}$)	0.8 ± 2.8	−4.7 ± 33.6	−1.2 ± 2.1	−20.4 ± 20.0
T_{peak} (K)	2.4 ± 1.8	0.7 ± 0.7	2.8 ± 1.3	1.2 ± 0.2
FWHM ($\mathrm{km\,s^{-1}}$)	6.7 ± 3.0	4.8 ± 2.4	7.6 ± 2.6	6.5 ± 2.6

[a]Statistics are based on the data from the map center scans.
[b]Group I component of G345.31+1.47 is too weak at the center position to fit a Gaussian.

Emission properties derived from both data samples are summarized in Table 3.3. The average of ΔV ($\equiv V_{CI} - V_{RRL}$) for the Group I line components of the mapped survey sources is -1.2 ± 2.1 $\mathrm{km\,s^{-1}}$. This agrees with the 0.8 ± 2.8 $\mathrm{km\,s^{-1}}$ value of the pointed survey within the uncertainty. The average line temperature of Group I emission components is 2.8 ± 1.3 K, compared with 2.4 ± 1.8 K of the pointed survey. There are four sources that have detected Group II components. The average line temperature of these Group II components is 1.2 ± 0.2 K, significantly weaker than the Group I average temperature. This is consistent with the pointed survey result. The average FWHM of the Group I components is 7.6 ± 2.6 $\mathrm{km\,s^{-1}}$. Within the error it agrees with the 6.7 ± 3.0 $\mathrm{km\,s^{-1}}$ value for the pointed survey. The slightly larger value may be a result of the lower signal to noise ratio in the mapped data set, since it is more difficult to tell whether an emission component actually is a blend of two overlapping components.

Figure 3.12 compares the line areas of map center spectra Group I components with those in the pointed survey. The large scatter is shown quantitatively in the area ratios, $A_{\mathrm{ctr}}/A_{\mathrm{pnt}}$, which are listed in the last column of Table 3.2. There is a fluctuation of up to a factor of two in this ratio. Only 15% of this could be due to the calibration. There is, however, a *statistical* agreement between these two samples. The line ratios shown in Table 3.2 have an average value of 1.0 ± 0.5.

Calibration and pointing are possible causes to explain the line areas difference. Since the mapped sources were observed in the order they are shown in Table 3.2, the erratic changes of line area ratios from source to source suggest that the fluctuation was unlikely to have been caused by calibration errors. Within each observing run, the system is relatively stable. For example, in the mapped sample, G333.29−0.37 was mapped twice consecutively by mistake. The center position spectra for the two maps show less than an 8% difference in line temperature. Because the H II regions were chosen to be compact, there can be a large C I brightness temperature change if the pointing error is comparable to the size of the C I peak. For AST/RO pointing is affected by both beam precession and errors which result from inaccuracies in the mechanical pointing model. Since the beam precession correction was not applied in the first year of AST/RO operation, the pointed survey was certainly affected. Within pointing and beam-precession uncertainties, the fact that both the Group I component map peaks are near map centers (the average separation is $2.1 \pm 1.1'$) *and* also that the center spectra match the pointed survey spectrum in 8 of the 11 cases suggest that the overall AST/RO pointing is about $1.6'$, which is less than half of the AST/RO beam. As I argue below in § 3.3.3, these data indicate that the 5 GHz radio continuum and C I peaks are spatially coincident within the pointing uncertainty.

Overall the two data sets have good agreement in emission properties. Although individual pointed measurements are still subject to relatively large discrepancies (up to a factor of 2 in line area ratios), I have shown here that consistent statistical results can nevertheless be obtained from even a small subset of the H II region sample.

The agreement suggests four points: 1) the two surveys are consistent insofar as the statistics of measured parameters are concerned; 2) the mapped sample is an accurate representation of the larger pointed survey sample; 3) the two catalogs from which the source lists were generated agree reasonably with each other; and 4) the results are consistent with AST/RO performing well and uniformly over more than three years.

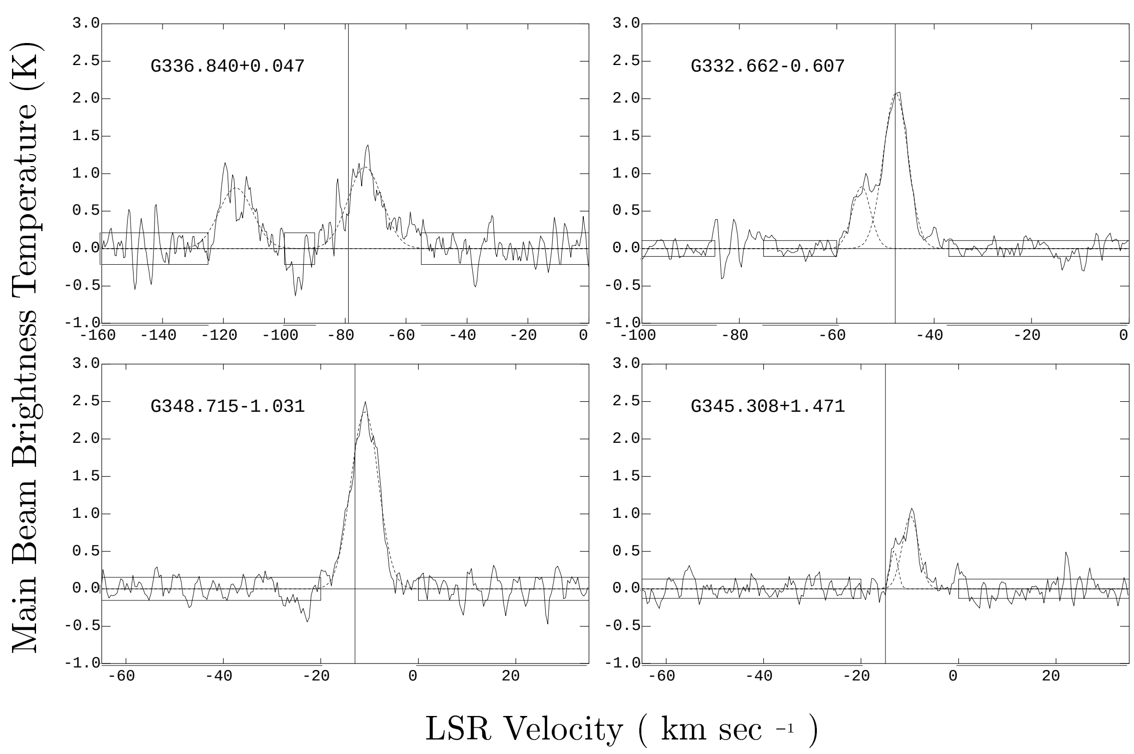

Fig. 3.8.— Typical C I spectra for a subset of the mapped H II region sample are shown similarly as in Figure 3.2. These spectra are averaged over the map to show general properties of the C I emission. The dashed curve is the Gaussian fit to the emission features. The vertical line flags the source H109α RRL LSR velocity.

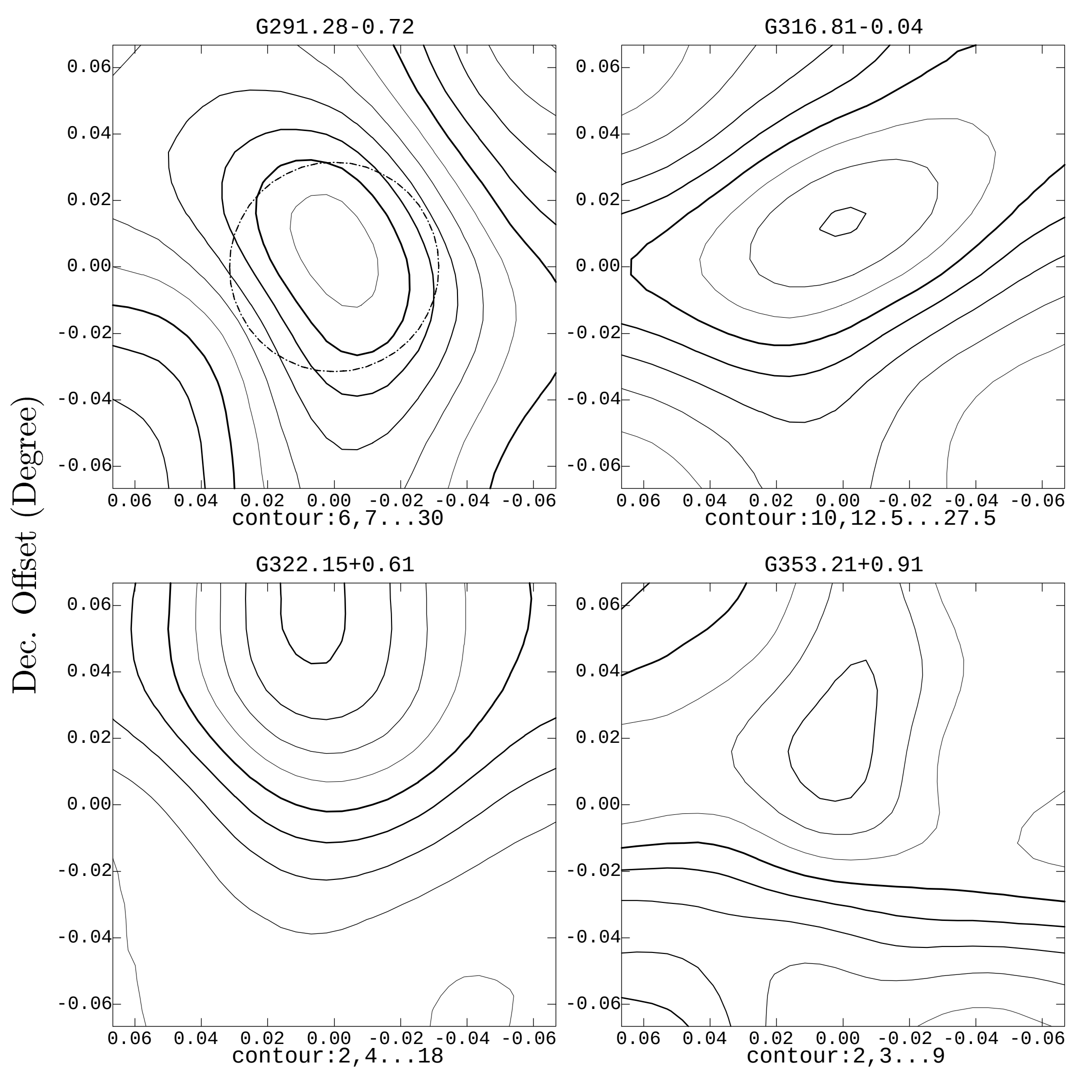

Fig. 3.9.— Maps of C I line integrated intensities (K km s^{-1}) for 4 H II regions that have a single spectral component. Gaussian fits are made to the map averaged spectra to yield the center velocity and FWHM for each line component. The C I integrated intensity at each map point is calculated between ±FWHM around the Gaussian center velocity for every spectral component. The interpolation radius used is 3.1′ and a Gaussian pattern of 2.5′ is used to weight the scans at nearby grid points. Source names are given at the top of each panel; contour levels are labeled at the bottom. The circle drawn as a dashed line in the G291.28−0.72 source map is the size of AST/RO beam.

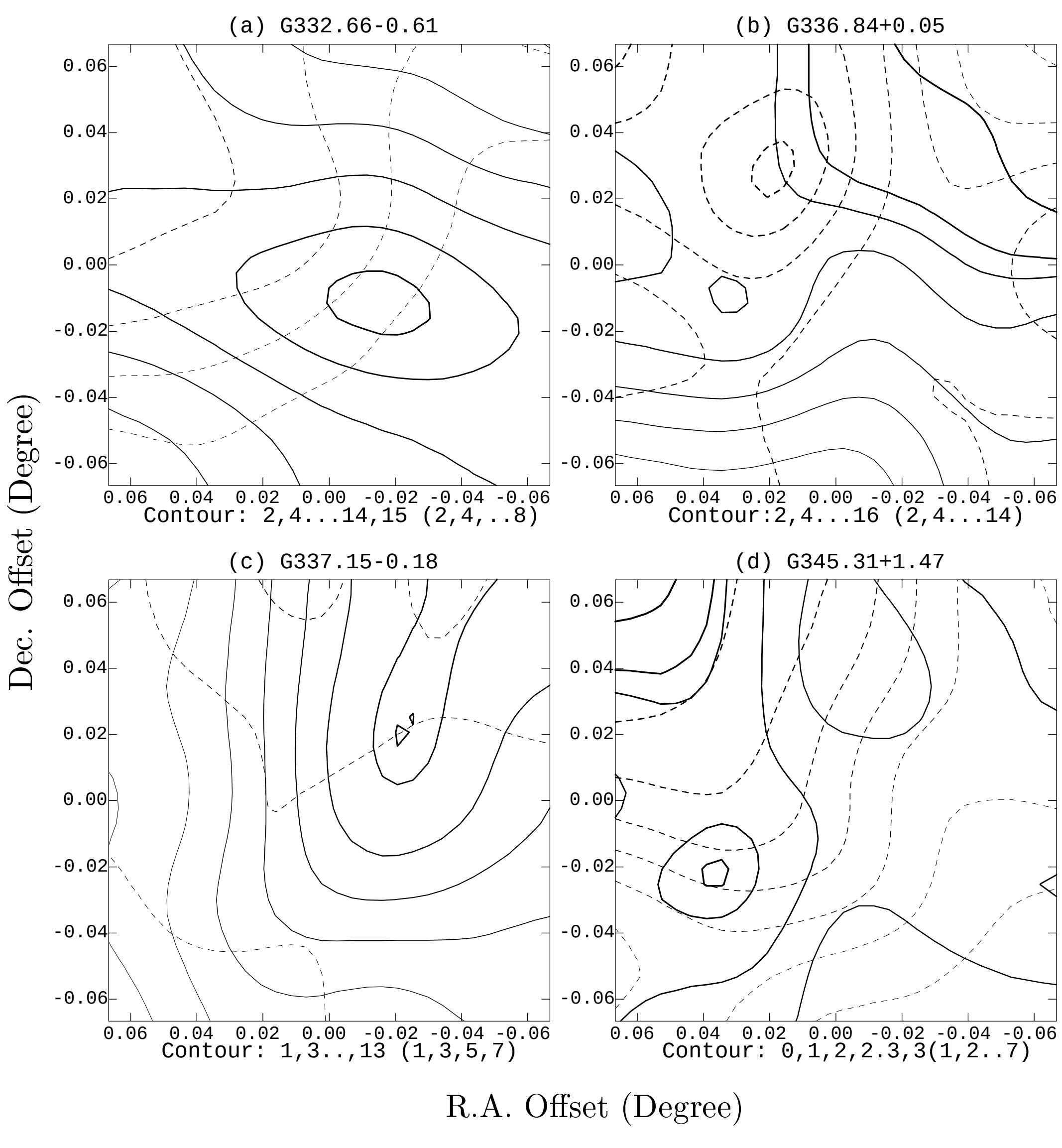

Fig. 3.10.— Maps of C I integrated intensities (K $\mathrm{km\,s^{-1}}$) for H II regions that have multiple spectral components. Source names are given at the top of each panel; contour levels are labeled at the bottom. The Group I component emission is plotted with solid lines. Dashed lines are used for Group II components. Map averaged spectra of G332.66−0.61, G336.84+0.05, and G345.31+1.47 are shown in Figure 3.8.

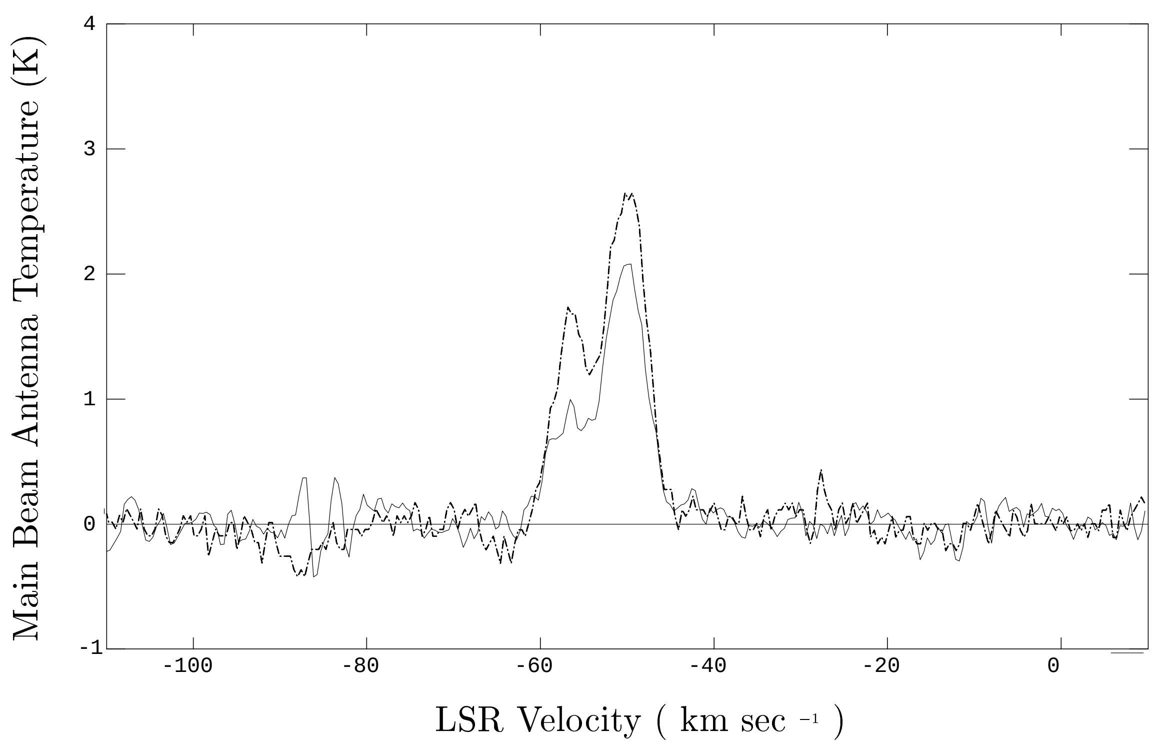

Fig. 3.11.— Map averaged spectrum of G332.66−0.61 is plotted with the pointed survey spectrum overlayed as a dashed line. This shows the agreement between the two surveys. Since most of the emission is confined to within the AST/RO beam, the map averaged spectrum is expected to be less intense than the pointed spectrum which is nearly at the map peak emission (see Figure 3.10).

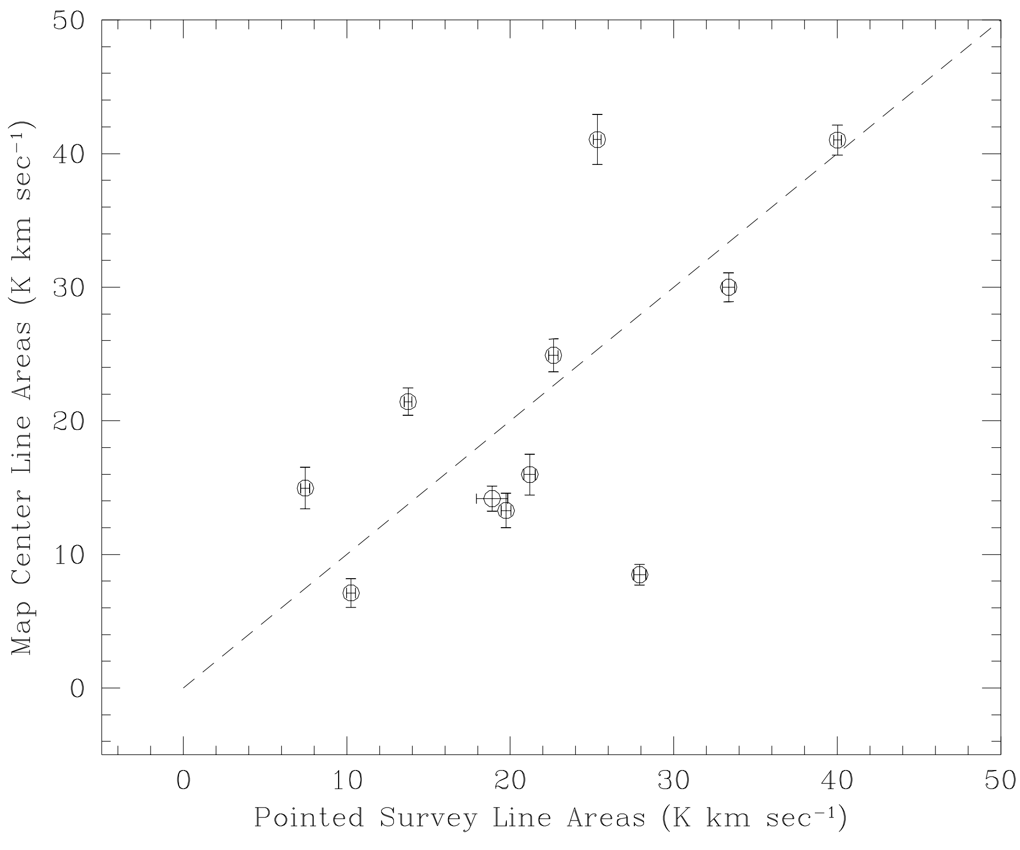

Fig. 3.12.— Group I component line areas of the map center scans are shown as a function of their counterparts in the pointed survey. Only 11 sources are plotted since G345.31+1.47 was not in the Pointed survey. The dashed line represents a perfect correlation. It is not a fit to the data.

3.3.3. Association between C I Spectral Components and H II Regions

In order to study C I properties around H II regions one must identify C I spectral components that are associated with the H II regions with great confidence. In § 3.2.3, I used ΔV to identify which C I emission components are associated with the H II regions when there are multiple line components in the spectrum. With the spatial distribution information available from the mapped sample, I have found more support for the identification method proposed in §3.2.3.

First, the Group I components for all 12 H II regions have single isolated emission peaks in the source map. As an example Figure 3.9 shows 4 H II regions that have a single spectral component. Figure 3.10 shows all 4 regions that have multiple components. Of the 12 H II regions, 10 (83%) have Group I intensities that reach their maxima at isolated peaks. The remainder have a Group I maximum intensity at the map edge, indicating that the real maximum is outside the map.

Secondly, the proximity of Group I C I emission peaks and the peak of the 5 GHz radio continuum supports the association between Group I components and the H II region. The second column of Table 3.5 lists the separations between the mapped survey C I emission peaks and the 5 GHz radio continuum emission peak which is always at the nominal map center. The average offset of the isolated Group I emission peaks is $2.1 \pm 1.1'$. The Caswell and Haynes (1987) catalog has a position accuracy of $0.5'$. The average C I-continuum offset thus implies a residual position offset of $(2.1^2 - 0.5^2)^{1/2} = 2.0'$. Note that the $2.0'$ residual position offset is well within the $3.8'$ AST/RO C I beam. I conclude that there is no evidence in my data for any significant physical offset between the Group I components and the 5 GHz radio continuum peaks.

Thirdly, comparing the spatial morphology of the Group I and II emission components in the maps shows that the Group I components have a much clearer association with the H II region than all the other components. Two spectral components are found in each of the 4 multiple-component sources. (The signal to noise ratio of the data precludes any further spectral decomposition.) Further examination of maps of these sources reveals a spatial distribution difference between Group I and Group II components. Figure 3.10 plots the Group II components as dashed contours. For the sources G332.66−0.61, G345.31+1.47, and G337.15−0.18, the integrated line intensity of the Group I component has a peak near the 5 GHz radio continuum peak (the map center). The other component does not show any localized aggregation in emission. For these sources the different spatial distributions strongly suggest that the Group I components are associated with the H II regions while the others are not. The H II region G336.84+0.05 has a peak for the Group I component but also a peak for the Group II component. The Group II component has a C I velocity of -116.4 km s^{-1} which is close to the -112 km s^{-1} RRL velocity of the H II region G336.732+0.072, which lies 6.5$'$ away. So it is very likely that the Group II component of G336.84+0.05 is associated with G336.732+0.072.

I conclude that: 1) for both H II region samples Group I C I emission components are spatially and kinematically associated with the H II region 5 GHz radio continuum and the 5 GHz H109α radio recombination line emission; 2) the peaks of associated C I emission coincide with the 5 GHz radio continuum peaks within the measurement uncertainties; and 3) Group II components are generally not associated with known H II regions.

3.3.4. C I Densities and Masses

The temperature and density of gas phase carbon near H II regions are important physical parameters of the ISM. It is essential to determine these parameters so that observations can be compared with detailed PDR models. In this section C I column densities, volume densities, and masses are derived for the H II region sample.

Derivation of C I Column Density

In radio astronomy the main beam brightness temperature $T_{\rm MB}$ is defined as:

$$\frac{kT_{\rm MB}}{h\nu} = \frac{c^2}{2h\nu^3} B_\nu(T_{\rm ex})[1 - e^{-\tau_\nu}] \tag{3.1}$$

where $B_\nu(T_{\rm ex})$ is the Planck function, $T_{\rm ex}$ the excitation temperature, and τ_ν the opacity at frequency ν. At the C I frequency 2.7K cosmic background radiation contributes to $T_{\rm MB}$ at the mK level, and is therefore ignored here. Optical depth can be calculated from:

$$\exp(-\tau_\nu) = 1 - \frac{kT_{\rm MB}}{h\nu}(e^{h\nu/kT_{\rm ex}} - 1). \tag{3.2}$$

Note that $T_{\rm ex}$ is not known *a priori*. At the end of this subsection I estimate $T_{\rm ex}$ and argue that the optically thin condition is a sound assumption for C I emission regions around H II regions.

For the ground state transition of C I, the optical depth and the population of ground state atoms, N_0, are connected by

$$\tau_\nu = N_0 S \phi(\Delta\nu) \tag{3.3}$$

where S and $\phi(\Delta\nu)$ are the line strength and the line profile, respectively. S is given by

$$S = \frac{c^2}{8\pi\nu^2}\frac{g_1}{g_0}A_{10}\left[1 - \exp(-\frac{h\nu}{kT_{\rm ex}})\right], \tag{3.4}$$

where A_{10} is the Einstein spontaneous emission coefficient ($= 7.9 \times 10^{-8}$ s^{-1}; Nussbaumer 1971), and $g_0(= 1)$ and $g_1(= 3)$ are the degeneracies of the ground state and the first level. For a Maxwellian velocity distribution, the profile at the line center is:

$$\phi(0) = \frac{c}{\nu \Delta V_i} D \tag{3.5}$$

where the factor $D = (4 \ln 2/\pi)^{\frac{1}{2}} \approx 1$, and ΔV_i is the intrinsic FWHM of the velocity distribution. The observed line FWHM approaches ΔV_i when the line center optical depth is $\tau_0 \ll 1$. With finite optical depth τ_0, the linewidth becomes:

$$\Delta V = \Delta V_i F(\tau_0) \tag{3.6}$$

where the factor $F(\tau_0)$ is:

$$F(\tau_0) = \left\{ \frac{1}{\ln 2} \ln \left[\frac{\tau_0}{\ln\{2/[\exp(-\tau_0) + 1]\}} \right] \right\}^{\frac{1}{2}} \tag{3.7}$$

(see Phillips *et al*. 1979).

There are only three states (J=0,1,2) for the ground level C I atoms to populate. Assuming thermal equilibrium for the ground state C I atoms as a result of collisional excitation, then any two population levels N_u and N_l are related by:

$$\frac{N_u}{N_l} = \frac{g_u}{g_l} e^{-h\nu/kT_{\rm ex}} \tag{3.8}$$

Thus the total population of C I atoms is:

$$N_{\rm total} = N_0 \frac{f}{g_0}. \tag{3.9}$$

The partition function, f, for the C I ground state fine structure transition is given by

$$f = 1 + 3e^{-E_{10}/T_{\rm ex}} + 5e^{-E_{20}/T_{\rm ex}} \tag{3.10}$$

where $E_{10} \approx 23.5$K and $E_{20} \approx 62.5$K.

From the above equations, the total C I population $N_{\rm total}$ can be expressed as:

$$N_{\rm total} = \tau_0 \Delta V f \frac{8\pi\nu^3}{3c^3 A_{10}} \left[\exp(-\frac{E_{10}}{T_{\rm ex}})\right]^{-1} F(\tau_0)^{-1} \tag{3.11}$$

In the optically thin case, $\tau_0 \ll 1$, the relation between the brightness temperature and the total column density of C I atoms can be given as :

$$N_{\rm total} = \frac{8\pi k\nu^2}{3hc^3 A_{10}} \frac{\Delta V T_{\rm MB}}{e^{-E_{10}/kT_{\rm ex}}} f = \frac{8\pi k\nu^2}{3hc^3 A_{10}} \frac{W_{\rm CI}}{e^{-E_{10}/kT_{\rm ex}}} f \tag{3.12}$$

where $W_{\rm CI}$(K km s^{-1}) is the integrated line intensity. This equation will be used to estimate the total mass of the C I emitting region in § 3.3.4, where a two dimensional Gaussian fit to the C I map yields the integrated line intensity. When $T_{\rm ex}$ = 50K, Equation 3.12 is reduced to:

$$N_{\rm total}[{\rm cm}^{-2}] = 1.36 \times 10^{16}\ {\rm W_{CI}}[{\rm K\ km\,s^{-1}}]. \tag{3.13}$$

The accuracy of the $N_{\rm total}$ values derived here for my sample depends most critically on whether the gas is in fact optically thin. Optical depth, as given by Equation 3.2, is a function of excitation temperature, $T_{\rm ex}$. Previous studies (e.g., Keene *et al*. 1985; Tauber *et al*. 1995) have shown that near H II regions the C I excitation temperature can vary from just under 20 K to up to 100 K. C I column densities and excitation conditions near several H II regions have been obtained using more accurate methods. Zmuidzinas *et al*. (1988) have studied a sample of H II regions using C I [^{3}P$_1$ $\rightarrow$ ^{3}P$_0$] and [^{3}P$_2$ $\rightarrow$ ^{3}P$_1$] transition data to measure the excitation temperature and opacity directly. They reported that typically $T_{\rm ex}$ is between 30-80 K, and $\tau_{10} < 1$ for the [^{3}P$_1$ $\rightarrow$ ^{3}P$_0$] transition of C I. I show in Table 3.4 that within the range of measured C I intensities, C I is mostly optically thin when $T_{\rm ex}$ changes from 15 K to 100K. At $T_{\rm ex}$ = 15K, the C I opacity for the pointed survey H II regions reaches moderate values, τ =0.3±0.2. For my pointed survey sources $\tau < 0.1$ holds if $T_{\rm ex} > 90$K.

TABLE 3.4

C I Optical Depth and C I Column Densities (10^{16} cm^{-2}) for Different $T_{\rm ex}$

Source	$T_{\rm ex}$ = 15 K				$T_{\rm ex}$ = 50 K				$T_{\rm ex}$ = 100 K			
	$\tau \pm 1\sigma$		$N_{CI} \pm 1\sigma$		$\tau \pm 1\sigma$		$N_{CI} \pm 1\sigma$		$\tau \pm 1\sigma$		$N_{CI} \pm 1\sigma$	
G291.28−0.72	0.57	0.01	37.1	0.5	0.07	0.00	26.2	0.3	0.03	0.00	28.5	0.3
G316.81−0.04	0.50	0.01	30.5	0.3	0.06	0.00	21.9	0.2	0.03	0.00	23.9	0.2
G322.15+0.61	0.30	0.01	12.5	0.3	0.04	0.00	9.4	0.2	0.02	0.00	10.3	0.2
G332.66−0.61	0.40	0.00	22.7	0.3	0.05	0.00	16.8	0.2	0.02	0.00	18.3	0.2
	0.13	0.01	6.0	0.5	0.02	0.00	4.8	0.4	0.01	0.00	5.2	0.4
G333.29−0.37	0.87	0.01	59.7	0.5	0.10	0.00	39.1	0.2	0.04	0.00	42.3	0.2
G336.84+0.05	0.19	0.00	22.8	0.5	0.03	0.00	17.8	0.3	0.01	0.00	19.5	0.4
	0.13	0.01	16.3	0.9	0.02	0.00	12.9	0.7	0.01	0.00	14.2	0.7
G337.15−0.18	0.14	0.00	13.9	0.4	0.02	0.00	11.0	0.3	0.01	0.00	12.0	0.3
	0.11	0.01	8.2	0.9	0.02	0.00	6.5	0.7	0.01	0.00	7.2	0.7
G337.95−0.48	0.23	0.01	10.8	0.3	0.03	0.00	8.3	0.2	0.01	0.00	9.1	0.2
G340.78−1.01	0.52	0.01	22.0	0.3	0.07	0.00	15.8	0.2	0.03	0.00	17.1	0.2
G345.31+1.47	0.09	0.01	1.5	0.2	0.01	0.00	1.2	0.2	0.01	0.00	1.3	0.2
	0.17	0.01	6.4	0.3	0.03	0.00	5.0	0.2	0.01	0.00	5.5	0.2
G348.71−1.03	0.48	0.01	29.1	0.4	0.06	0.00	21.0	0.3	0.03	0.00	22.9	0.3
G353.21+0.91	0.13	0.01	10.9	0.5	0.02	0.00	8.7	0.3	0.01	0.00	9.5	0.4
Column Average	0.31	0.22	19.4	14.2	0.04	0.02	14.2	9.3	0.02	0.01	15.4	10.1

The derivation in this section does not consider the case when the source under-fills the telescope beam. Although the fitting results in Table 3.5 show that all but one of my sources have angular sizes larger than the AST/RO beam, there could be small areas that have high $T_{\rm MB}$ but which are diluted by the beam. If there is indeed clumping within the AST/RO beam, the clump optical depths could reach high values. Because the column densities increase proportionally to τ, the column density could be underestimated by the diluted brightness temperature. Because I cannot resolve the clumps, neither their opacity nor their filling fraction of the beam is known. Values of $N_{\rm total}$ calculated here thus are lower limits.

Finally, since all of the 12 mapped H II regions have known distances (see §2), the mass of C I in each nebula can be derived if the angular area is also known:

$$M[M_\odot] = 8.1 \times 10^{-5} A[\mathrm{arcmin}^2]\mathrm{d}^2[\mathrm{kpc}^2]\mathrm{N}_{\mathrm{total}}[\,\mathrm{cm}^{-2}]. \tag{3.14}$$

Here d is the source distance and A is the angular area of the C I emission region.

Densities and Masses

Two Dimensional Gaussian Fits to the Maps

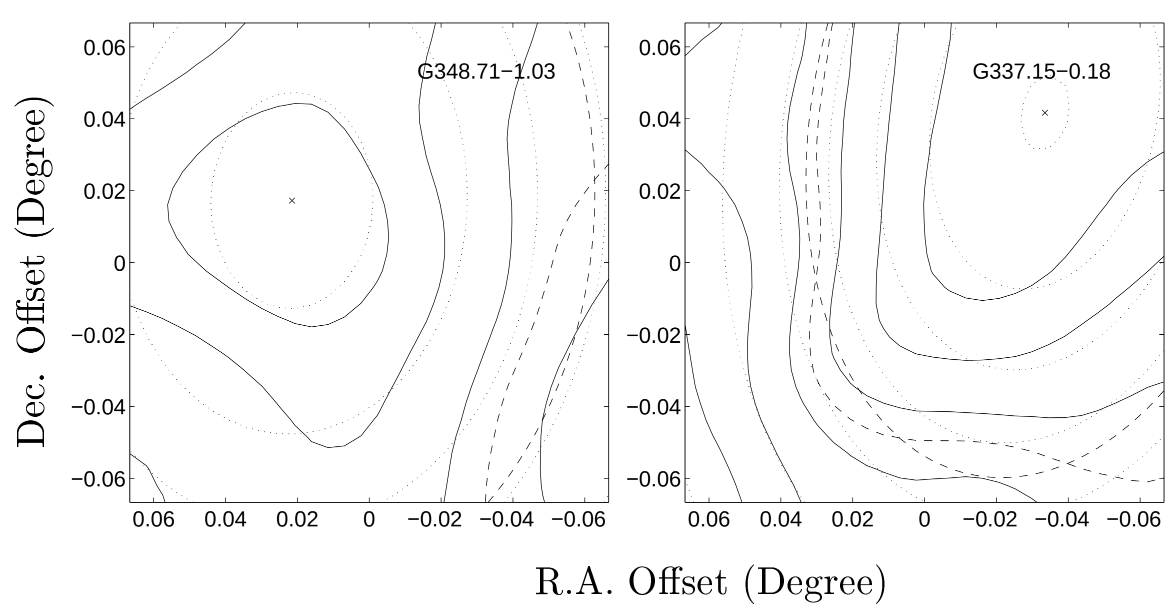

Fig. 3.13.— Two of the H II regions maps superimposed by their two-dimensional Gaussian fit are shown here. Solid and dotted lines are used to plot the measured line intensity contours and the Gaussians, respectively. The dashed lines delineate the half-maximum of the measured and Gaussian contours. The Gaussian fits follow reasonably well with measured contours.

The formalism of the preceding section can be used together with C I emission line parameters to calculate the properties of the C I gas in the H II regions. From Figure 3.9 and Figure 3.10 it is apparent that the C I emitting regions extend beyond the mapped areas. To estimate the total C I content of the H II region associated (Group I) gas, a two dimensional Gaussian function is fitted to the Group I C I intensity peak in every map. C I emission parameters are derived using these Gaussian fits. Figure 3.13 shows 2 examples of the Gaussian fitting results. The Gaussian fits agree reasonably well with the measured contours, indicating that the Gaussian fits recover most of the C I emission around the H II region. As is shown later in this section some sources have a better fit than others because of their simple morphology.

The C I intensity integrated over the Gaussian is

$$\int_{\text{Gaussian}} W_{\text{CI}} d\Omega = \frac{\pi}{\ln 2} R_x R_y W_{\text{CI}}^{\text{peak}} \tag{3.15}$$

where $W_{\text{CI}}^{\text{peak}}$ is the peak integrated line intensity and the quantities R_x and R_y are the angular Gaussian half width half maxima (HWHM) along the major and minor axes. The average C I integrated intensity $\langle W_{\text{CI}} \rangle$ is:

$$\langle W_{\text{CI}} \rangle = \frac{\int_{\text{Gaussian}} W_{\text{CI}} d\Omega}{\pi \theta_x \theta_y} = \frac{1}{\ln 2} \frac{R_x R_y}{\theta_x \theta_y} W_{\text{CI}}^{\text{peak}} \tag{3.16}$$

where θ_x and θ_y are the angular HWHM of the two dimensional Gaussians after correction for the beam size $\Theta_B = 3.8'$: $\theta_x^2 = R_x^2 - (\Theta_B/2)^2$ and $\theta_y^2 = R_y^2 - (\Theta_B/2)^2$.

Assuming optically thin gas, the average C I column density can be calculated from Equation 3.13 using $\langle W_{\text{CI}} \rangle$. Given the known distance of the H II region and the Gaussian angular area, the total mass of C I can be gotten from Equation 3.14.

The C I volume density can also be estimated by:

$$n_{\text{CI}} = \frac{N_{\text{total}}}{L} \tag{3.17}$$

where L is the scale of the C I emission region given by:

$$L = 2\sqrt{\theta_x \theta_y} d \tag{3.18}$$

Observational Results from the Mapped C I Survey

Observed and derived properties of the mapped H II region survey are compiled in Table 3.5. Listed as the "peak offset" is the angular distance between the C I maximum position and the 5 GHz radio continuum peak (the map center). The determination of the source distance, d, and its error are discussed in §2. The angular size of the C I emitting region, θ, is the average of the two dimensional Gaussian FWHM angular size along each axis, corrected for the telescope beam size. The error of the angular size determined by Gaussian fit is assumed to be 10%. The errors of the rest of the quantities in Table 3.5 described below are propagated from the errors of d and θ and the 15% calibration error of AST/RO. The linear size of the H II region, $D_{\rm HII}$, is derived from the angular size of the 5 GHz radio continuum and the distance. The size of the C I emitting region, $D_{\rm CI}$, is similarly derived from d and θ. The total C I column density, $N_{\rm CI}$, is calculated from Equation 3.13 assuming the gas is optically thin with $T_{\rm ex} = 50$K. The total atomic carbon mass, M_{CI}, in the entire Gaussian shaped C I emitting region is estimated using Equation 3.14. The volume density, $n_{\rm CI}$, is derived using Equation 3.17. Finally, the emergent integrated line intensity of the C I emission, $I_{\rm em}$, is listed in units of 10^{-6} erg s^{-1} cm^{-2} sr^{-1} in order to make comparison with theoretical models convenient.

From Table 3.5 the following results can be obtained immediately: (1) the scale of the C I emission regions for the mapped sample is $D_{CI} = 10 \pm 7$ pc; (2) all the C I emission regions are larger than their associated H II regions, except for G345.31+1.47 which is unresolved; (3) the average $D_{\rm CI}/D_{\rm HII}$ ratio is 4.1 ± 2.3; (4) the average C I column density is $3.7 \pm 2.2 \times 10^{17}$ cm^{-2}; (5) the derived C I masses

TABLE 3.5

H II REGION PARAMTERS AND DERIVED C I PARAMETERS FROM GAUSSIAN FITS[a]

Source	peak offset ($'$)	d (kpc)	θ[b] ($'$)	$D_{\rm HII}$ (pc)	$D_{\rm CI}$ (pc)	$N_{\rm CI}$[c] (10^{16}cm^{-2})	M_{CI} ($M_\odot$)	$n_{\rm CI}$ (cm^{-3})	$I_{\rm em}$[d]
G291.28−0.72	0.5	2.6 ± 0.3	8.1 ± 0.8	0.7 ± 0.1	6.3 ± 1.0	62 ± 16	1.8±0.6 (0)	3.2±0.9 (-2)	5.6 ± 1.4
G316.81−0.04	1.1	2.5 ± 0.5	8.3 ± 0.8	1.4 ± 0.3	6.0 ± 1.4	54 ± 14	1.5±0.7 (0)	2.9±1.0 (-2)	4.9 ± 1.2
G322.15+0.61	4.1	3.5 ± 0.6	6.6 ± 0.7	1.0 ± 0.1	6.7 ± 1.4	50 ± 13	1.7±0.7 (0)	2.4±0.8 (-2)	4.5 ± 1.1
G332.66−0.61	0.6	3.3 ± 0.6	13.5 ± 1.3	4.1 ± 0.7	13.0 ± 2.6	30 ± 8	3.9±1.6 (0)	7.6±2.4 (-3)	2.7 ± 0.7
G333.29−0.37	2.7	3.5 ± 0.6	12.3 ± 1.2	2.9 ± 0.5	12.4 ± 2.4	81 ± 20	9.3±3.9 (0)	2.1±0.7 (-2)	7.3 ± 1.8
G336.84+0.05[e]	...	10.7 ± 1.6	...	28.0 ± 4.2	...	18 ± 5	...	...	1.7 ± 0.4
G337.15−0.18	3.2	10.9 ± 1.7	8.9 ± 0.9	15.9 ± 2.4	28.4 ± 5.1	38 ± 10	2.3±0.9 (1)	4.3±1.3 (-3)	3.4 ± 0.9
G337.95−0.48[e]	...	3.1 ± 0.6	...	1.2 ± 0.3	...	7 ± 2	...	...	0.6 ± 0.2
G340.78−1.01	2.6	2.3 ± 0.5	13.5 ± 1.3	2.7 ± 0.6	9.2 ± 2.2	36 ± 9	2.3±1.2 (0)	1.3±0.4 (-2)	3.2 ± 0.8
G345.31+1.47[f]	2.8	1.8 ± 0.6	4.1 ± 0.4	1.9 ± 0.6	2.2 ± 0.7	4 ± 1	2.0±1.0 (-2)	6.6±2.7 (-3)	0.4 ± 0.1
G348.71−1.03	1.7	2.0 ± 0.7	11.0 ± 1.1	1.2 ± 0.4	6.4 ± 2.3	42 ± 10	1.3±1.0 (0)	2.1±0.9 (-2)	3.8 ± 0.9
G353.21+0.91	1.6	1.7 ± 0.3	10.2 ± 1.0	3.5 ± 0.6	5.1 ± 1.1	17 ± 4	0.3±0.1 (0)	1.1±0.3 (-2)	1.5 ± 0.4

[a] Errors of quantities are explained in the text.

[b] Geometric average of FWHM Gaussian angular widths. Values have been corrected for the beamsize.

[c] Assuming $T_{\rm ex} = 50$K.

[d] Emergent C I intensity (10^{-6} erg sec^{-1} cm^{-2} sr $^{-1}$).

[e] The morphology of this source is too complex to allow Gaussian fit. Map-averaged quantities are used in places of Gaussian-averaged ones.

[f] This source is unresolved. The sources size given is not corrected for the beam size. See text.

span three orders of magnitude for the sample; and (6) the average C I intensity is $I_{\rm em} = 3.3 \pm 2.0 \times 10^{-6}\,{\rm erg}s^{-1}\,{\rm cm}^{-2}{\rm sr}^{-1}$. Comparison between these observational results and PDR models will be made in §5.

Column Densities of the Pointed Survey Sources

For pointed survey sources I cannot do such an analysis as above. But the column densities can be studied. Assuming the same 50K excitation temperature, the column densities for the line components in the pointed survey can be calculated using Equation 3.11. The column densities span two orders of magnitude. The mean value is $\langle N_{CI} \rangle = 12 \times 10^{16}\,{\rm cm}^{-2}$, with a dispersion of $15 \times 10^{16}\,{\rm cm}^{-2}$ for this sample. The mean optical depth of the Group I components is $\langle \tau \rangle = 0.06 \pm 0.05$.

Figure 3.14 shows the histograms of the column density distribution for both Group I and Group II components. The mean column density is $22 \pm 17 \times 10^{16}\,{\rm cm}^{-2}$ for Group I and $4.3 \pm 4.3 \times 10^{16}\,{\rm cm}^{-2}$ for Group II. The average uncertainties of the column densities for both groups are $0.4 \pm 0.3 \times 10^{16}\,{\rm cm}^{-2}$, corresponding to 4% and 15% in $\langle \Delta N_{CI}/N_{CI} \rangle$ for Group I and II, respectively.

The mean column density for Group I of the pointed survey is less than that of the mapped survey ($39 \pm 22 \times 10^{16}\,{\rm cm}^{-2}$) by 44%. The column density is proportional to the integrated line intensity in the optically thin condition. Since the integrated intensities of the center scan of the mapped survey agree with the pointed survey (see § 3.3.2), the $\langle N_{CI} \rangle$ difference is possibly explained by calibration and pointing uncertainties. Furthermore, I am able to correct for the beam size when calculating $\langle W_{CI} \rangle$ in the mapped survey and this yields larger values for $\langle W_{CI} \rangle$.

Using the $\sim$10 pc average scale size of the C I emission regions found in the mapped survey, the pointed survey column densities imply an average volume density

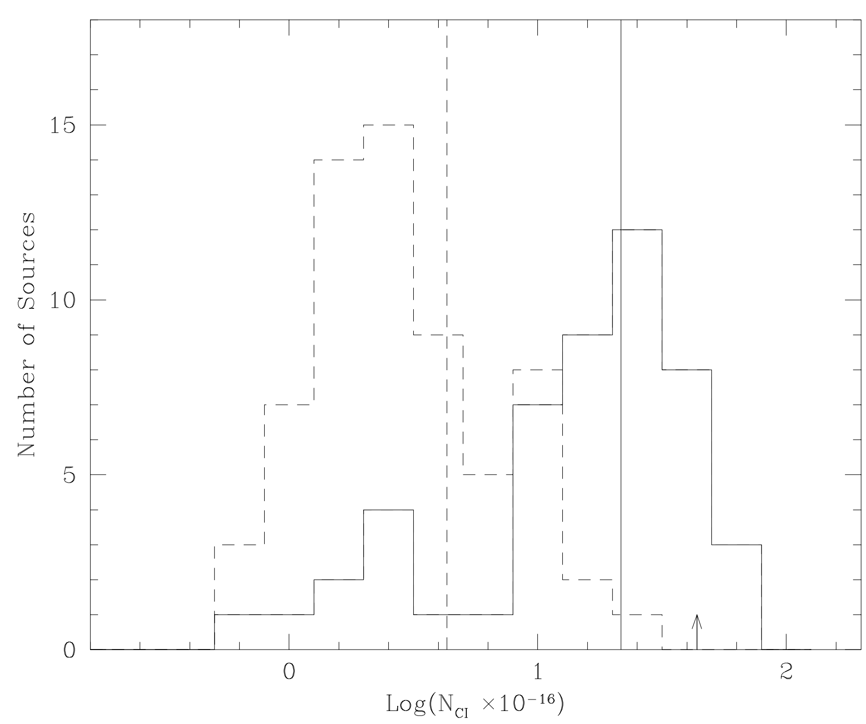

Fig. 3.14.— The histograms of the C I column density distributions for the pointed H II region C I survey. The histograms for Group I and Group II components are plotted in solid and dashed lines, respectively. The two vertical lines mark the mean column density values, $22 \pm 17 \times 10^{16}\,\mathrm{cm}^{-2}$ for Group I and $4.3 \pm 4.3 \times 10^{16}\,\mathrm{cm}^{-2}$ for Group II. The arrow on the $\log(N_{CI})$ axis marks the mean column density of the mapped survey. The average uncertainty in the N_{CI} determination is $0.4 \pm 0.3 \times 10^{16}\,\mathrm{cm}^{-2}$ for both groups. The small peak in the Group I histogram at $\log(N_{CI}) = 0.4$ is not caused by confusion with Group II components of the same source, because all but one of the 9 Group I components to the left of $\log(N_{CI}) = 0.8$ are the strongest C I emission component of their corresponding sources.

of carbon ($n_{\mathrm{CI}} \approx 1.1 \pm 0.8 \times 10^{-2}\,\mathrm{cm}^{-3}$), which agrees with the mapped survey results ($1.7 \pm 0.9 \times 10^{-2}\,\mathrm{cm}^{-3}$ on average) within 1σ errors.

3.3.5. Support for the Spherical Model

Spatial and Kinematic Coincidences

The spatial and kinematic associations between C I emission and H II regions found in this chapter support the spherical PDR configuration described in §1. This model makes several predictions. 1) The PDR is formed around the central OB stars in spherical symmetry, so a single maximum is seen in C I. 2) The radiation from the central OB stars is both the ionization source of the H II region and the photodissociation source of the PDR. The center of the spherical C I region therefore coincides spatially with the peak of the 5 GHz radio continuum emission of the ionized region. 3) If the C I gas is optically thin, the observer sees C I on both the near and the far sides of the ionized region at the center of the spherical PDR. Since any global movement of ionized and neutral gases is also symmetric with respect to the central stars, there should be no systematic velocity difference between the C I and H II gas.

I find support for all three predictions in this Chapter. Point 1 is supported by the result described in § 3.3.3. Each of the 12 mapped sources has an isolated C I emission peak in the map. The isolated peaks of 10 of the 12 sources (83%) are also at the location of the maximum emission intensity. Only 2 of the sources have the maximum intensity on the edge of the map.

The spatial association between the C I emission and the 5 GHz radio continuum also described in § 3.3.3 supports Point 2. I find that the average offset ($2.1 \pm$

$1.1'$) between the C I emission peak and the 5 GHz continuum peak is insignificant compared with the AST/RO C I beam ($3.8'$) and AST/RO's pointing error. This offset is, moreover, very much smaller than the average angular size of the C I emission peaks ($10 \pm 3'$).

The support for Point 3 is the kinematic association established in the pointed survey (see §3.2.3) and the mapped survey (see § 3.3.2). The C I emission velocities are found to be in exact agreement with the H109α radio recombination line velocities within the measurement uncertainties.

The Morphologies of the C I Emission Regions

In general, observed PDR morphologies ought to be complex because what one sees is a combination of the intrinsic source morphology and its orientation with respect to the observer. There ought to be a range of PDR morphologies with configurations spanning all possibilities from simple spherical symmetry, to slab geometries, to extremely complex structures. The slab H II region and PDR complexes such as M17 are the obvious examples. The complex morphologies of some of the mapped survey sources (G336.84+0.05, G345.31+1.47, and G353.21+0.91. see figures 3.9 and 3.10) indicate that the spherical PDR configuration is relatively less suitable to describe them than other sources. In these complex sources the photodissociating UV radiation from the OB stars intersects with the border of molecular clouds where a large gas density gradient exists. In this situation even if a C I emission peak can be found near the 5 GHz radio continuum peak, part of the FUV radiation from the OB stars may not intersect any molecular clouds to generate detectable C I emission, and part of the radiation may reach clouds beyond the border of the maps. In this case the true extent of the H II region associated C I emission is entirely unknown.

It is striking that the bulk of my mapped sample sources can be adequately described by a spherical PDR morphology. In the mapped survey sample 8 out of 12 sources have simple morphologies. Their maps exhibit well defined, single, symmetric maxima near the 5 GHz radio continuum peak. This suggest that the spherical model can be used to explain many of the PDRs.

3.4. Summary

I report observations of atomic carbon (C I [$^3P_1 \rightarrow {}^3P_0$]) emission for two samples of sources using the Antarctic Submillimeter Telescope and Remote Observatory (AST/RO). The first sample is comprised of 49 southern hemisphere H II regions selected as compact and isolated members of the Wilson *et al.* (1970) H109α RRL catalog. The fourth Galactic quadrant is well-covered by the sample. Pointed observations were made with AST/RO. Atomic carbon emission is detected toward all of the regions, with multiple C I emission components found toward most sources. The RRL velocity is used to identify the C I emission associated with the H II region. The mean velocity difference between the C I and RRL emission is 0.8 $\pm$ 2.8 km s^{-1}. Within the measurement errors this is exact agreement in velocity; I conclude that all H II regions have associated C I emission. The FWHM linewidth of C I gas associated with H II regions is marginally greater than that found for unassociated gas (6.7 $\pm$ 3.0 km s^{-1} compared with 4.8 $\pm$2.4 km s^{-1}). The total integrated line intensity for the associated spectral components for all 49 sources is 1.6 times greater than that of the unassociated components. The mean C I line temperature of associated components is 2.4 $\pm$ 1.8 K, compared with 0.7 $\pm$ 0.7 K for the C I emission components not associated with the H II region. This suggests that the C I intensity is dominated by local heating.

The second sample of sources was selected from the Caswell & Haynes (1987) H109α RRL catalog. These sources were also chosen to be compact and isolated compared with the 100$''$ aperture of the LWS on the ISO satellite. All but one source also appears in the pointed survey sample. All of these H II regions have known distances. Mapped observations were made of these sources with AST/RO. C I emission is found in all the sources.

The comparisons between spectra taken in the two surveys show that the two surveys have excellent agreement. Using the mapped survey results, I confirm that Group I C I spectral components are spatially and kinematically associated with the H II regions. The C I emission peaks coincide with the 5 GHz radio continuum peaks within measurement errors.

I make two-dimensional Gaussian fits to the maps to estimate the total C I emission around the H II regions, and to derive C I densities and masses. I have found it is reasonable to assume that C I emission is optically thin. The C I atomic column densities derived from the mapped data are $3.7 \pm 2.2 \times 10^{17}$ cm^{-2} on average. Using available distances for H II regions in the mapped sample, I estimate the linear sizes and total masses of C I in the mapped areas. The sizes of the C I emission regions are 10 ± 7 parsecs on average, and they are 4.1 ± 2.3 times the H II region size defined by the 5 GHz radio continuum emission. The masses range from 0.02 to 23M$_\odot$, spanning three orders of magnitude. The average source emergent C I intensity is $3.3 \pm 2.0 \times 10^{-6}$ erg s^{-1} cm^{-2} sr^{-1}.

I also calculate C I column densities for the pointed survey. The C I column densities span two orders of magnitude. For Group I, $\langle N_{CI} \rangle = 2.2 \pm 1.7 \times 10^{17}\,\mathrm{cm}^{-2}$, and $4.3 \pm 4.3 \times 10^{16}\,\mathrm{cm}^{-2}$ for Groups II. Group I $\langle N_{CI} \rangle$ is 44% lower than the mapped survey result, possibly caused by calibration and pointing errors, and beam size correction made in the mapped survey.

In sum, my analysis of the C I properties of the mapped H II region sample provides strong support for the spherically symmetric PDR model described in §1. The spherical PDR model explains the single isolated C I peaks found in the C I maps and the strong spatial and kinematic coincidences between the C I and the RRL emission. While acknowledging that there are more complex PDR configurations I argue that the spherical model can be used to describe many PDRs.

Chapter 4

CO Observations

4.1. Introduction

When studying the environs of H II regions it is impossible to ignore the ambient molecular clouds typically revealed by the ubiquitous CO molecular tracer of the H_2 distribution. The association between H II regions and molecular clouds is by now well established. In fact interstellar CO was first observed in a sample of H II regions (e.g., Wilson, Jefferts & Penzias 1970). CO observations have been one of the foundations to our understanding of the ISM, the GMC population, and the kinematics, dynamics and evolution of the Galaxy.

I mapped the ISO H II region sources in the $(J = 4 \rightarrow 3)$ transition of CO with AST/RO. The $CO(J = 4 \rightarrow 3)$ transition (461.041 GHz) rotational excitation energy is 22K above the ground state, very close to that of [C I] (23K). The critical density is 8×10^4 cm^{-3} (Schulz *et al.* 1995), two orders of magnitude higher than C I and one order of magnitude higher than $CO(J = 1 \rightarrow 0)$. Therefore comparing the properties of $CO(J = 4 \rightarrow 3)$ and C I emission can help us understand the physical conditions of these sources. This information can be used to examine PDR theoretical predictions.

In this chapter I first report my AST/RO observations of $CO(J = 4 \rightarrow 3)$ emission in the ISO sample of H II regions (see §1). Then I present $CO(J = 1 \rightarrow 0)$ data collected from the published literature. I also compare relevant emission parameters of [C I] from §3 with the CO results described here.

4.2. AST/RO Observations of the CO(J=4→3) Transition

4.2.1. Observations and Calibration

I observed the ISO sources in the ($J = 4 \rightarrow 3$) transition of CO with AST/RO on November 15, 1998. Source selection details and source positions of the ISO sources are given in §1. Most of the detailed telescope setups and calibration procedures were intentionally kept the same as for the mapped survey of C I described in §3. The average receiver temperature during the observing period was measured to be about 300K DSB with a fluctuation of only several Kelvins. The typical system temperature was 2,700K, and was roughly constant due to the stable sky conditions. The telescope beam at 461 GHz is estimated to be $240''$, close to that at 492 GHz in the 1998 Austral winter season. Telescope efficiency was $\sim$0.7. The channel spacing of the AOS was 0.675 MHz. At the CO($J = 4 \rightarrow 3$) rest frequency the AOS has a velocity resolution of 0.601 $\mathrm{km\,s^{-1}}$.

The calibration procedures are the same as in the mapped C I observations described in §3 except that the post-observation re-calibration using the most recent skydip is not performed. This is because at 461 GHz the sky is much more stable and less opaque than at the C I frequency. Therefore the change of sky zenith opacity during a normal observation does not affect the intensity calibration significantly.

The CO($J = 4 \rightarrow 3$) maps were made in identical fashion as the mapped survey of C I described in §3. Fully sampled 7×7 maps were made toward each of the ISO sample sources. A position-switched observation was made at each grid point for a total time of 20 seconds. The standard AST/RO test source G291.28−0.72 was one of the sample H II regions. It was mapped routinely during the observations to confirm telescope pointing and calibration.

There are three problems with the observations. The first is that due to equipment failure, the observations were interrupted and never completed. More observations were requested and were made in the 1999 season. Unfortunately these 1999 observations cannot be used due to major problems with pointing, telescope focusing, and an unexplained frequency shift. These problems could not be solved during the 1999 winter season. Therefore CO($J = 4 \rightarrow 3$) data for only 6 sources are available in this thesis. The second problem is that an unexplained spectral line velocity shift was discovered in the data set. The test source G291.28−0.72 had an apparent -3.5 km s^{-1} shift in its LSR velocity. This was possibly caused by an instability in the IF chain. It is not known when this shift happened. It is likely that the next source, G336.84+0.05, was also affected. The third problem is that the LSR velocity error found in C I observations (see §3) is also found in these CO observations. Therefore a -2.5 km s^{-1} correction is made to the velocity measurement results.

4.2.2. Observational Results

Results

The CO($J = 4 \rightarrow 3$) transition is detected in emission in all sources with excellent signal to noise ratios. Some of the sources have multiple spectral components. Figure 4.1 shows the spectra of all 6 observed ISO sources. Despite the fact that not all ISO sources are observed, the spectra obtained are of good quality. Figure 4.2 shows the maps of all the sources in the sample. For 5/6 of the sources the morphological similarity between the CO($J = 4 \rightarrow 3$) and C I (shown in §3) distributions is evident in the maps. This similarity will be studied quantitatively below in § 4.2.2.

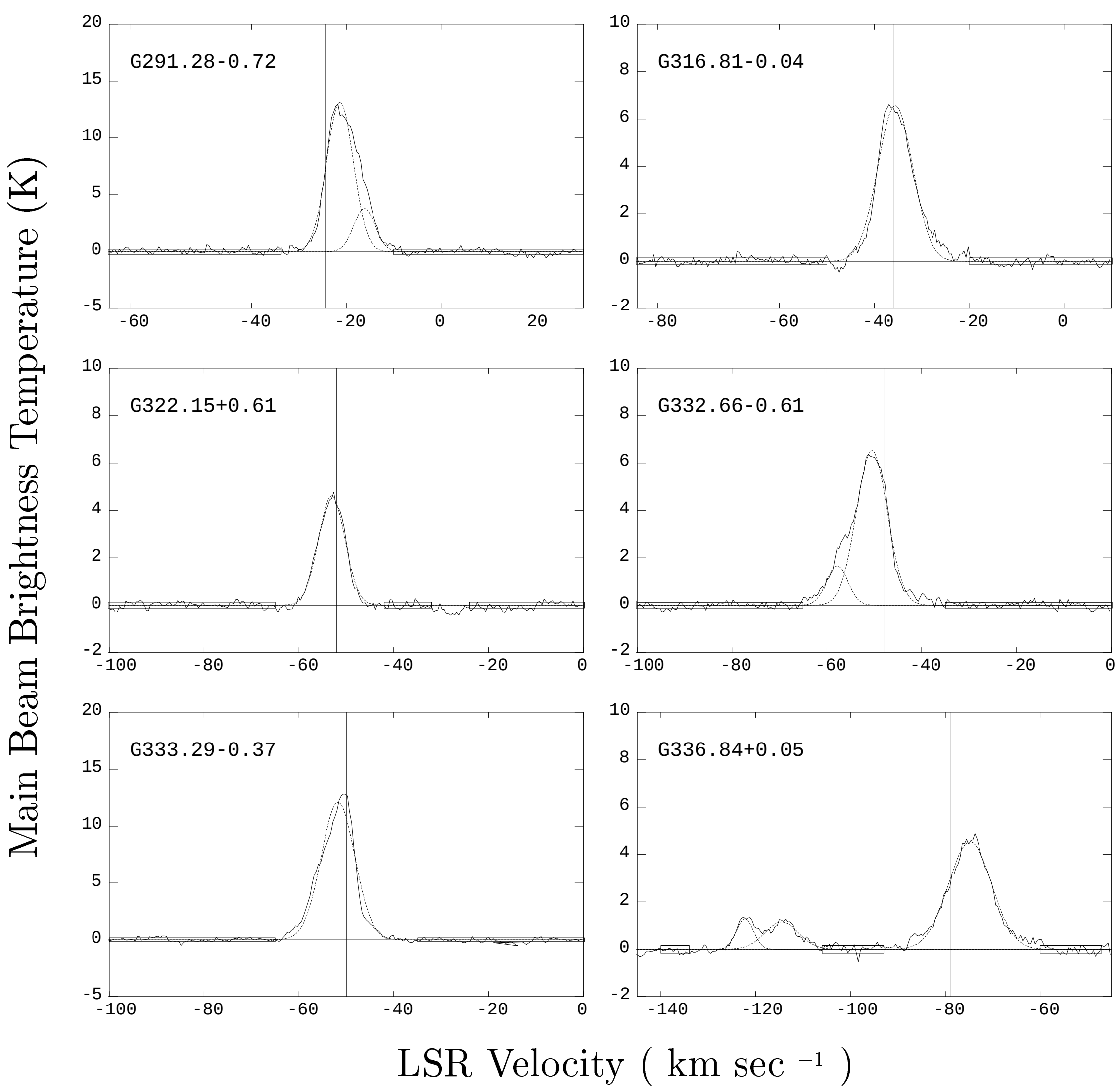

Fig. 4.1.— The CO(J $= 4 \rightarrow 3$) spectra for every observed H II region in the ISO source sample. The spectra shown are the average spectrum of each map. The intensity scale is the main beam brightness temperature which is the antenna temperature corrected for both atmospheric attenuation and main beam efficiency. The boxes plotted on the baseline indicate velocity zones where the baseline model is determined and the baseline RMS calculated. Linear baselines have been removed. The dashed curves show the Gaussian fits to the emission features. The vertical line plotted over each spectrum marks the RRL velocity as listed in Table 1.2.

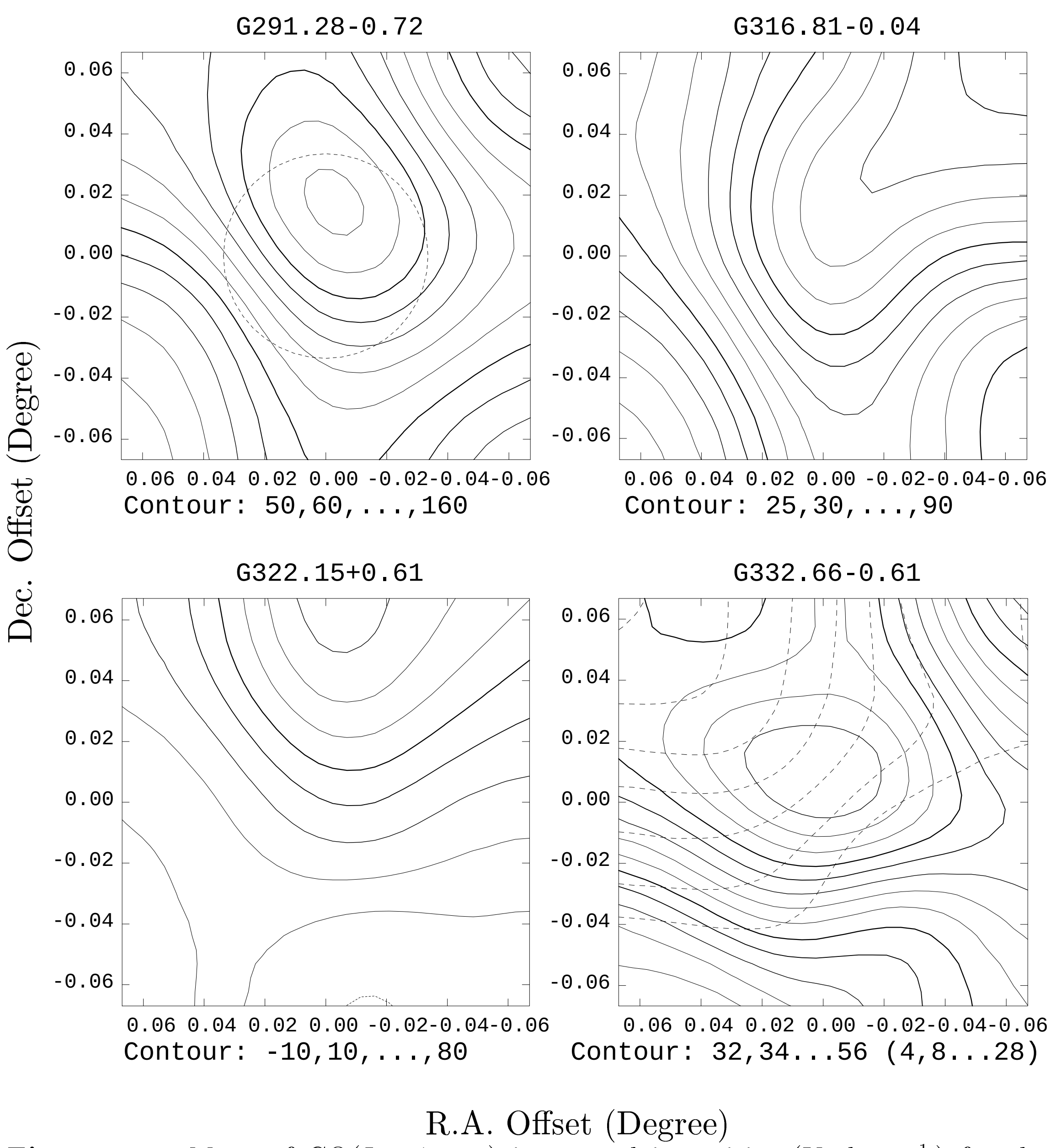

Fig. 4.2.— Maps of CO(J $= 4 \rightarrow 3$) integrated intensities (K $\mathrm{km\,s^{-1}}$) for the ISO sample H II regions. The maps are made in the same manner as in §3. The interpolation radius is also $3.1'$ with a Gaussian radius of $2.5'$. The contour levels are labeled at the bottom. The circle drawn in a dashed line in the G291.28$-$0.72 map shows the size of AST/RO beam. The dashed contour lines are for Group II sources. (continuing to the next page)

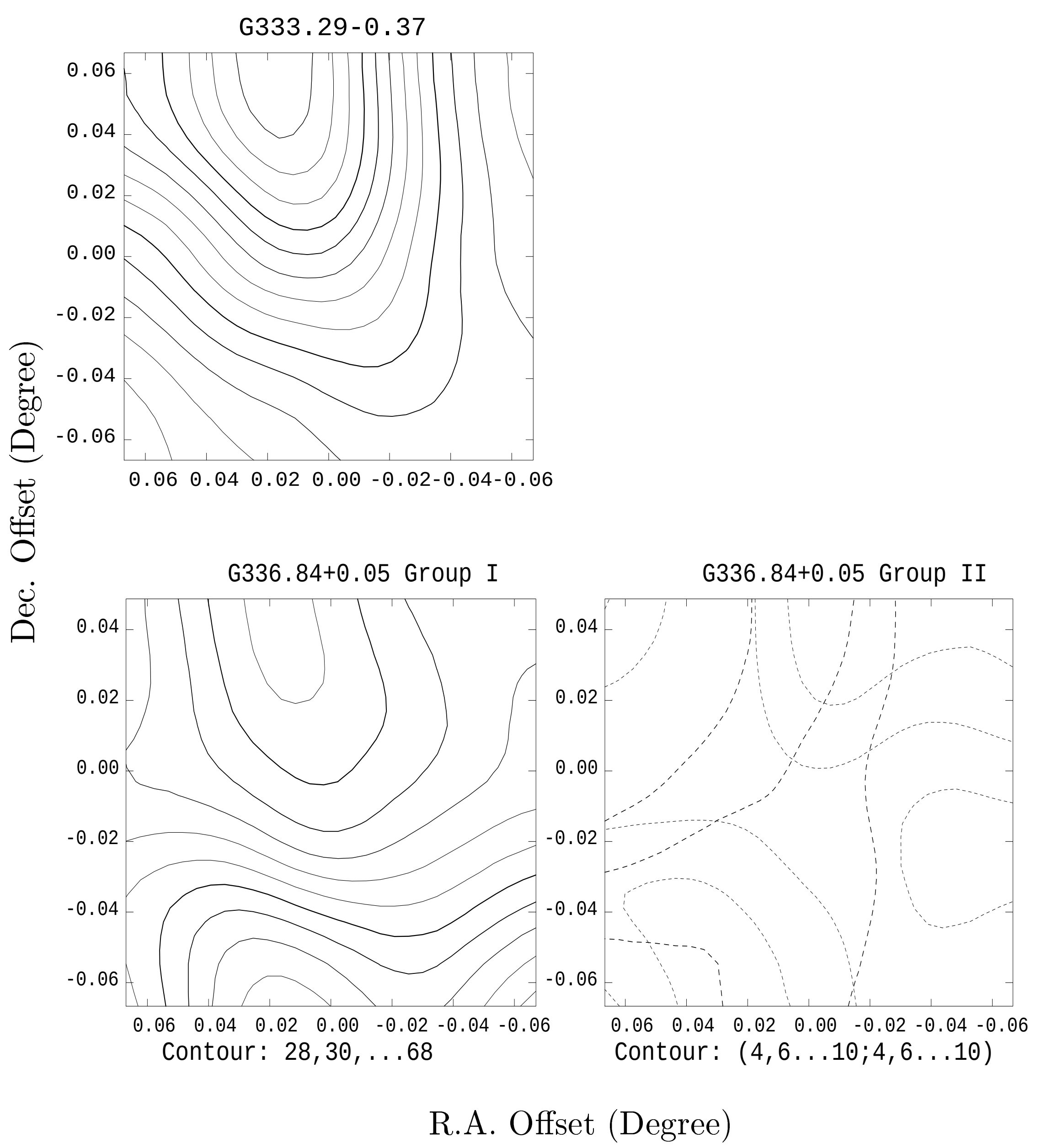

Fig. 4.2.— (continued) The source G336.84+0.05 has two Group II components. They are plotted in a separate panel from the Group I component.

TABLE 4.1

CO(4→3) Emission Properties: Map Center Positions

Source[a]	$V_{\rm LSR}$ (km sec^{-1})	$T_{\rm MB}$ (K)	FWHM (km sec^{-1})	Area (K km sec^{-1})	GRMS (K)	BRMS (K)
G291.28−0.72	−22.8 ± 0.1	18.4 ± 0.5	9.3 ± 0.3	168 ± 4	1.6	1.5
G316.81−0.04	−37.9 ± 0.1	8.5 ± 0.2	10.1 ± 0.3	91 ± 2	0.8	0.8
G322.15+0.61	−54.7 ± 0.1	7.1 ± 0.3	5.2 ± 0.3	39 ± 2	0.9	0.8
G332.66−0.61	−52.8 ± 0.1	8.6 ± 0.3	7.6 ± 0.4	62 ± 2	0.8	0.8
	−60.3 ± 0.4	2.0 ± 0.3	5.9 ± 1.0	15 ± 2	0.9	0.8
G333.29−0.37	−54.4 ± 0.1	14.1 ± 0.3	8.6 ± 0.2	132 ± 3	1.5	0.8
G336.84+0.05	−77.3 ± 0.2	5.3 ± 0.1	10.5 ± 0.3	63 ± 4	0.8	0.9
	−116.2 ± 0.9	1.3 ± 0.3	8.9 ± 2.6	11 ± 2	0.6	0.9
	−124.8 ± 0.3	1.8 ± 0.3	4.4 ± 0.8	7 ± 1	0.7	0.9

[a]Only 6 ISO sources were observed in CO(4-3) due to equipment failure. See text.
[b]The velocity scale of G336.84+0.05 is likely to have been affected by instrumental error.

TABLE 4.2

CO(4→3) Emission Properties: Map Averaged Spectra[a]

Source	$V_{\rm LSR}$ (km sec^{-1})	$T_{\rm MB}$ (K)	FWHM (km sec^{-1})	Area (K km sec^{-1})	GRMS (K)	BRMS (K)
G291.28−0.72	−23.10 ± 0.02	12.72 ± 0.07	8.30 ± 0.05	112.36 ± 0.77	0.7	0.2
G316.81−0.04	−38.10 ± 0.02	6.56 ± 0.04	8.69 ± 0.06	59.21 ± 0.33	0.4	0.1
G322.15+0.61	−55.60 ± 0.03	4.62 ± 0.04	6.55 ± 0.07	31.05 ± 0.28	0.2	0.1
G332.66−0.61	−53.00 ± 0.03	6.53 ± 0.04	7.68 ± 0.08	51.56 ± 0.31	0.3	0.1
	−60.30 ± 0.16	1.67 ± 0.11	5.29 ± 0.39	-0.38 ± 0.55	0.2	0.1
G333.29−0.37	−54.20 ± 0.01	12.10 ± 0.04	8.34 ± 0.03	109.00 ± 0.40	0.9	0.2
G336.84+0.05	−77.30 ± 0.04	4.53 ± 0.04	10.73 ± 0.10	48.79 ± 0.40	0.2	0.2
	−117.00 ± 0.27	1.14 ± 0.07	8.32 ± 0.71	1.17 ± 0.54	0.1	0.2
	−124.80 ± 0.10	1.28 ± 0.06	4.21 ± 0.23	-0.50 ± 0.25	0.1	0.2

[a]For table notes see Table 4.1.

Tables 4.1 and 4.2 give the CO(J $= 4 \rightarrow 3$) line emission properties at the map center position and averaged over the map, respectively, obtained from Gaussian fits to the line profiles. These tables use a similar format as that of Tables 3.1 and 3.2, so the detailed explanation of symbols and nomenclature can be found in the relevant text there.

To recap briefly, the source names are the same as in Table 1.2; the LSR velocity, V_{LSR}, is the Gaussian center velocity; the peak main beam brightness temperature, T_{MB}, and the full line width at half maximum, FWHM, are the height and width of the Gaussian; the line area under the Gaussian is calculated from T_{MB} and the FWHM; BRMS and GRMS are, respectively, the baseline RMS noise and the RMS of the residual when the fitted Gaussian is subtracted from the line.

There are multiple emission components in the spectra of G332.66−0.61 and G336.84+0.05. The Group I components are stronger than their respective Group II components (see §3). A Group II component is also found in C I in G332.66−0.61 at a nearly identical LSR velocity as that of the CO counterpart (0.1 km s^{-1}difference). For G336.84+0.05, the noise level in its C I spectrum blends the two Group II components found in CO together.

For these sources, the CO(J $= 4 \rightarrow 3$) line temperature at the map center increases with C I temperature for the Group I components. Figure 4.3 shows the C I main beam brightness temperature plotted against that of the CO(J $= 4 \rightarrow 3$) for all 6 observed sources. A linear fit to the data yields the relation: $T_{CI} = (0.33 \pm 0.05)T_{CO} - (0.2 \pm 0.4)$, with a correlation coefficient of 0.90. This correlation will be discussed at the end of §4.4 after the kinematic properties of CO have been presented. The average temperature ratio for the Group I components is 3.2 ± 0.7. This ratio will be used in §5 to derive predicted densities using PDR theories (see

Figure 1.8).

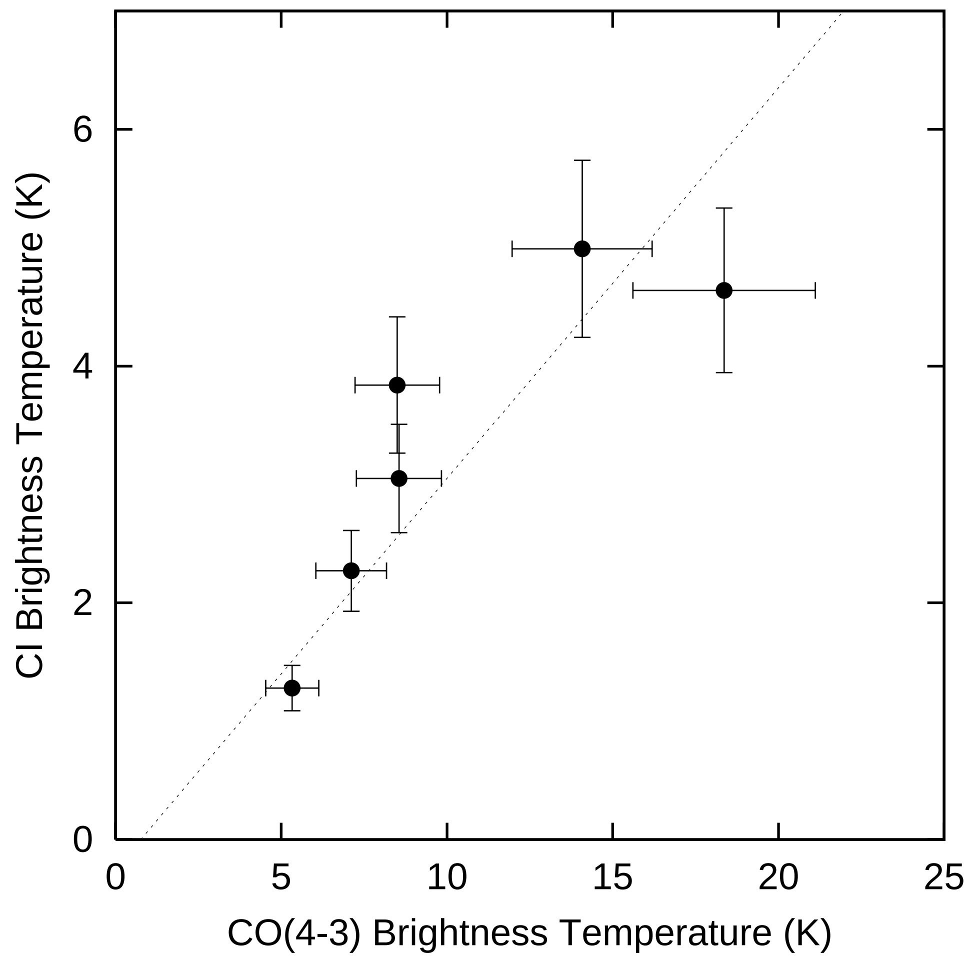

Fig. 4.3.— The main beam brightness temperatures of C I and CO(J = 4 $\rightarrow$ 3) at the map centers. The error is chosen to be the larger one of either the 15% systematic calibration error or the statistical RMS error from the fit. The dotted line is a linear fit to the data: $T_{CI} = (0.33 \pm 0.05)T_{CO} - (0.2 \pm 0.4)$.

TABLE 4.3

CO(4→3) Map Parameters and Comparisons with C I

Source[a]	$\Delta\alpha_{\rm CO}, \Delta\delta_{\rm CO}$ ($'$, $'$)	$\Delta\alpha_{\rm CI}, \Delta\delta_{\rm CI}$ ($'$, $'$)	peak offset ($'$)	$P_{CI\to CO}$ ($'$)	$\theta_{\rm CO}$ ($'$)	$\frac{\theta_{\rm CO}}{\theta_{\rm CI}}$
G291.28−0.72	0.2, 1.7	0.4, 0.3	1.7	1.4	9.5	1.2
G316.81−0.04	−2.0, 3.4	−0.4, 1.1	3.9	2.8	12.0	1.5
G322.15+0.61	−0.9, 4.2	−0.0, 4.1	4.3	0.9	6.3	1.0
G332.66−0.61	0.7, 1.4	−0.3, −0.5	1.5	2.1	14.6	1.1
G333.29−0.37	1.6, 4.9	0.5, 2.7	5.2	2.5	14.0	1.1
G336.84+0.05[b]	0.3, 2.2	. . . , . . .	2.2	. . .	14.0	. . .

[a]Only 6 ISO sources were observed the CO(4-3) due to equipment failure. See text.
[b]The spatial distribution in C I is too complex to fit a Gaussian. Therefore CO results cannot be compared.

Sizes and Positions of CO Emission Regions

The size and peak position of the CO($J = 4 \rightarrow 3$) emission region can be derived using two dimensional Gaussian fits to the maps. The fitting techniques are identical to those in §3. Table 4.3 gives the parameters obtained using two dimensional Gaussian fits to the emission peaks found in the CO($J = 4 \rightarrow 3$) maps of the ISO sources. The Right Ascension and Declination offsets, $\Delta\alpha_{\rm CO}$ and $\Delta\delta_{\rm CO}$ (in arcmin), are the Gaussian peak positions with respect to the nominal source position (the map center, which is the centroid of the radio continuum emission). The same offsets for the C I fit, $\Delta\alpha_{\rm CI}$ and $\Delta\delta_{\rm CI}$, are also given as a reference. They are used below for calculating $P_{CI\to CO}$. The angular offset distance (arcmin) of the CO emission peak from the nominal source position, denoted as "peak offset" in Table 4.3, is defined as $(\Delta\alpha_{\rm CO}^2 + \Delta\delta_{\rm CO}^2)^{1/2}$. The angular distance (arcmin) between the CO emission peak and the C I emission peak for the same source, $P_{CI\to CO}$, is calculated by $[(\Delta\alpha_{\rm CO} - \Delta\alpha_{\rm CI})^2 + (\Delta\delta_{\rm CO} - \Delta\delta_{\rm CI})^2]^{1/2}$. The angular size of the CO($J = 4 \rightarrow 3$)

emission area, θ_{CO}, is calculated by geometrically averaging the major and minor FWHM widths of the Gaussian, corrected for the telescope beam size: the corrected $\theta_{CO} = (\mathrm{FWHM}^2_{fitted} - \phi^2)^{1/2}$, where ϕ is the AST/RO telescope beam size. Although my maps are smaller ($8' \times 8'$) compared with most of the angular sizes of the emission regions, these parameters still give quantitative measures of the scale of the emission features. This is because 2-D Gaussian fits allow one to estimate the size and position by extrapolation. The last column of Table 4.3 lists the ratio of CO(J $= 4 \rightarrow 3$) angular size and that of C I found in §3.

Note that because the C I spatial distribution is too complex to fit a Gaussian for G336.84+0.05, the comparison of morphological properties with CO cannot be made for this source.

How closely the radio continuum, the CO(J $= 4 \rightarrow 3$), and the C I emission features are spatially associated can be studied statistically using qualities shown in Table 4.3. The average CO(J $= 4 \rightarrow 3$) emission peak offset is $3.1 \pm 1.4'$. This means the peaks are separated by less than a beam size ($4'$) from the radio continuum peak at the map center. Calculated similarly, the average angular distance between the emission peaks of CO and C I is $1.9 \pm 0.7'$, less than half of the beam. Considering the random telescope pointing error and receiver beam precession error ($\sim 1'$ total), the actual average residual offsets should be even less. This means that the data are consistent with *all* CO emission centroids being coincident with C I.

The above average angular offsets can be compared with the size of the radio continuum emission region located at the map center. The average angular radius of the Strömgren sphere is $1.6 \pm 0.9'$ for the sample of H II regions (§3). The average C I offset is $1.8 \pm 1.4'$ (§3), comparable to the average Strömgren sphere radius. The average CO offset is $3.1 \pm 1.4'$, twice as large as the Strömgren sphere radius.

The atomic regions statistically are located at the borders of the ionized regions. The molecular regions are found farther away from the ionizing sources than the atomic regions. Although a provoccative result, note that these differences are not statistically significant compared with the measurement errors and source-to-source dispersions. More insight into the emission peak displacements can be gained when they are compared with the size of the emission regions, as is shown in § 4.5.

Besides the relative positions of the C I and CO emission regions, the sizes of these zones can be compared from the data in Table 4.3. The average angular size of the emission region is $12 \pm 3'$ for CO(J $= 4 \rightarrow 3$) and $10 \pm 3'$ for C I (Note that these sizes are large with respect to the offsets from RRL emission controid.) The average ratio of the angular sizes between CO(J $= 4 \rightarrow 3$) and C I is 1.2 ± 0.1. On average the CO(J $= 4 \rightarrow 3$) emission regions are larger than the C I emission regions by a statistically significant factor. When examined individually, there is not one source (except G336.84+0.05 which cannot be fit to a Gaussian) among the observed sources that has a larger C I emission region than CO(J $= 4 \rightarrow 3$).

Although the maps I use are relatively small and the number of available CO(J $= 4 \rightarrow 3$) maps is scant for statistical studies (the $N^{-1/2}$ error is 45% for 5 samples), nevertheless based on my measurements I conclude that: 1) The 5 GHz radio continuum, CO(J $= 4 \rightarrow 3$), and C I emission regions spatially coincide statistically. The offset, if any, is no more than 30% of the size of the neutral and molecular emission regions; 2) The sizes of the CO(J $= 4 \rightarrow 3$) and the C I emission region are comparable, with the CO size being slightly larger; and 3) there is some evidence that the neutral component of carbon peak is just outside the ionized regions, while the molecular emission peak is at a greater distance. The peak offsets of C I and CO are not significant compared with the size of their respective emission regions. These results will be related to the spherical PDR models in § 4.5 where the velocity coincidence of these tracers is described.

4.3. Single Point CO(1→0) Data

In order to complement the AST/RO $CO(J = 4 \rightarrow 3)$ observations, measurements of $CO(J = 1 \rightarrow 0)$ emission from the published literature are compiled for all 12 ISO sources. The observational details are reported in Whiteoak, Robina & Rennie (1982). They used the 4-m radio telescope of the CSIRO Division of Radiophysics at Epping, Australia to conduct a survey of CO in the $(J = 1 \rightarrow 0)$ transition. The reported sources are bright southern H II regions, selected on the basis of high 4.8 GHz continuum and high H_2CO line to continuum ratios. The telescope beamwidth was $2.8'$, comparable to the actual AST/RO C I and $CO(J = 4 \rightarrow 3)$ beams. The estimated pointing accuracy was $30'' \sim 40''$. The cooled mixer receiver temperature was about 500K DSB. The AOS backend covers 244 $km\,s^{-1}$ with a 0.6 $km\,s^{-1}$ spectral resolution, also comparable to AST/RO at the C I and $CO(J = 4 \rightarrow 3)$ rest frequencies. The typical on-source integration time was 4 minutes. The observed antenna temperature was corrected for a mean atmosphere absorption for the two sidebands. The source OMC1 was observed at different elevations to calibrate the atmosphere attenuation. A corrected temperature of 65K for OMC1 in CO emission is assumed. On this scale the final spectra have a RMS noise of about 1 K. The effective limit of detection is 2K.

4.3.1. Emission Line Parameters

I tabulate the $CO(J = 1 \rightarrow 0)$ spectral line parameters and the line temperature ratios between C I and $CO(J = 1 \rightarrow 0)$ in Table 4.4. The absorption velocity of

TABLE 4.4

CO(1→0) SINGLE POINT DATA[a]

Source	T_{MB}[b] (K)	V_{LSR}[c] (km sec^{-1})	FWHM[c] (km sec^{-1})	$\frac{T_{CI}}{T_{CO}}$
G291.28−0.72	18.1	−24.3	9.0	0.26 ± 0.02
G316.81−0.04	20.0	−39.3	8.8	0.19 ± 0.01
G322.15+0.61	27.0	−56.0	5.5	0.08 ± 0.01
G332.66−0.61	13.1	−51.6	13.3	0.23 ± 0.02
G333.29−0.37	28.3	−52.4	9.0	0.18 ± 0.01
G336.84+0.05	9.2	−74.3	11.4	0.14 ± 0.02
G337.15−0.18	13.2	−73.8	10.1	0.08 ± 0.01
G337.95−0.48	8.6	−42.1	5.2	0.14 ± 0.02
G340.78−1.01	22.0	−30.8	5.9	0.12 ± 0.01
G345.31+1.47	20.0	−14.0	5.8	0.07 ± 0.01
G348.71−1.03	34.8	−13.0	6.6	0.11 ± 0.01
G353.21+0.91	13.6	− 4.3	4.8	0.14 ± 0.02

[a]Data compiled from Whiteoak, Robina, & Rennie (1982).
[b]The RMS error for temperature is 1K.
[c]The errors in velocities and FWHM linewidths are not given in the original paper. The velocity resolution is 0.6 km sec^{-1}.

H_2CO is also given in Whiteoak, Robina & Rennie (1982). This information is used in Caswell & Haynes (1987) to resolve the near-far kinematic distance ambiguity for the H II regions (see §2). The average C I to CO(J = 1 → 0) brightness temperature ratio at the map center is 0.15 ± 0.06. The temperature ratios of CO(J = 1 → 0)/C I is 6.7 ± 2.7 compared with 3.2 ± 2.7 for CO(J = 4 → 3)/C I. Figure 4.4 plots the main beam brightness temperature in CO(J = 1 → 0) and C I at the map center. A weak linear relation can be fitted to the data: $T_{CI} = (0.11 \pm 0.04)T_{CO1-0} + (0.7 \pm 0.9)$. The correlation coefficient is 0.62. Comparing Figure 4.3 and Figure 4.4 the line temperature of C I has a stronger correlation with CO(J = 4 → 3) than it does with CO(J = 1 → 0). The correlation between CO(J = 4 → 3) and CO(J = 1 → 0) is weak with a linear correlation factor of 0.5, as shown in Figure 4.5. These correlation differences will be discussed in § 4.4 and in the context of PDR theory in §5.

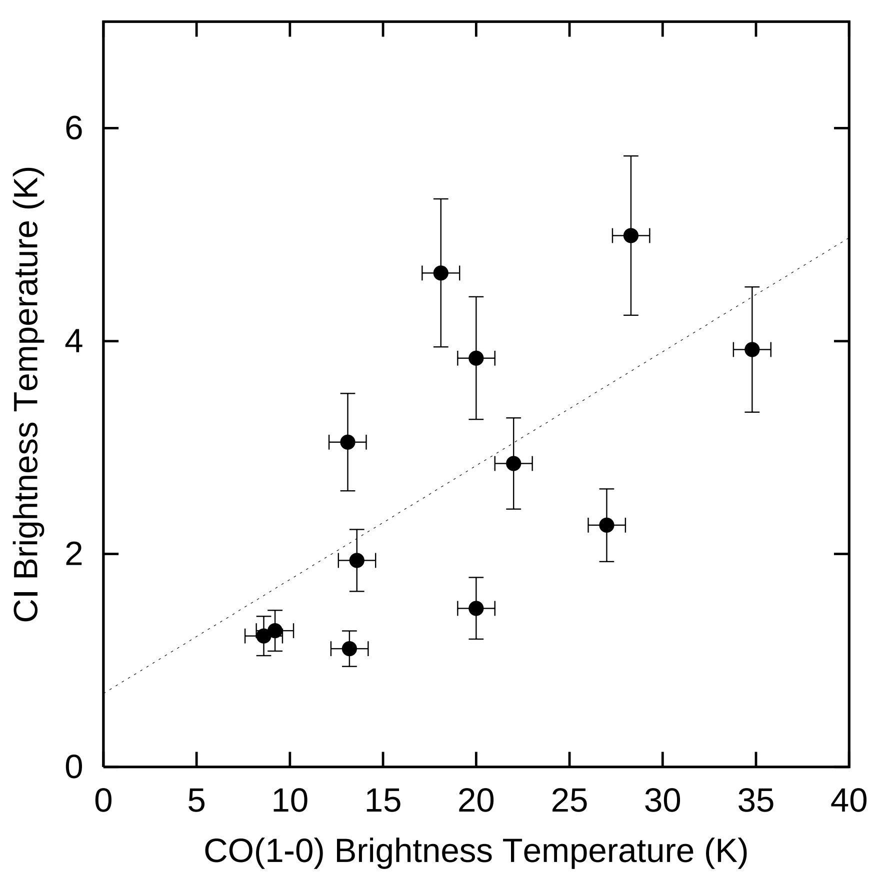

Fig. 4.4.— The main beam brightness temperatures of C I and CO(J = 1 → 0) at the C I map center. The error of C I is chosen to be the larger one of either the 15% systematic calibration error or the statistical RMS error from the fit. The error used in CO(J = 1 → 0) (Whiteoak *et al*. 1982) is the 1K RMS noise. The dotted line is a linear fit: $T_{CI} = (0.11 \pm 0.04)T_{CO1-0} + (0.7 \pm 0.9)$.

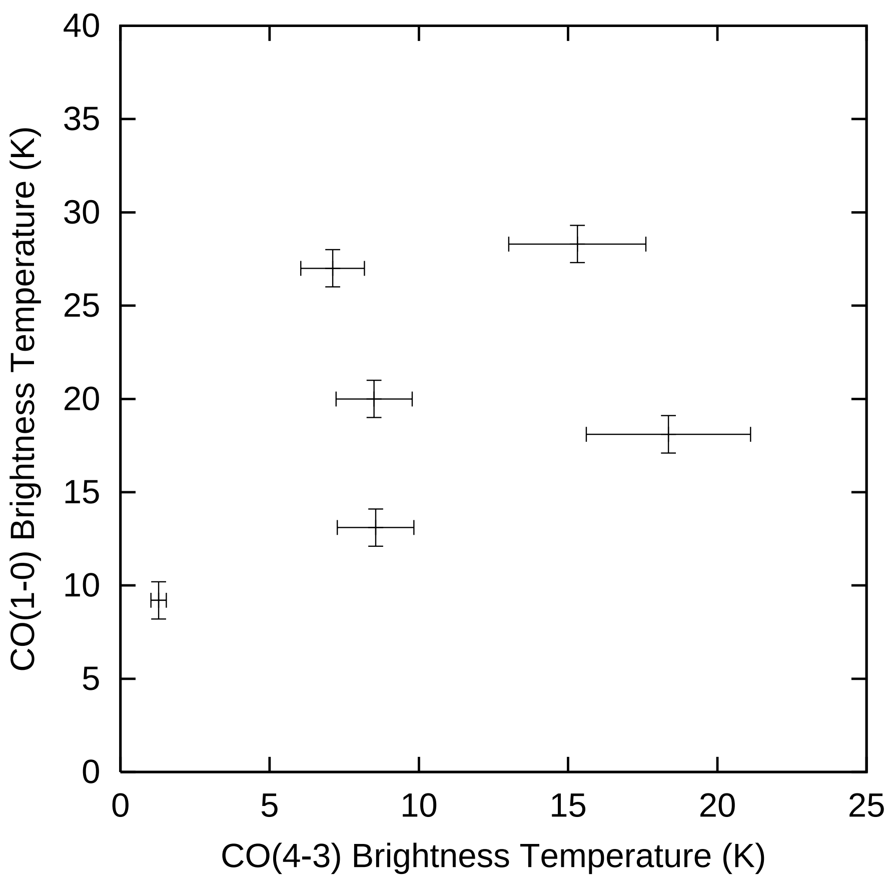

Fig. 4.5.— The main beam brightness temperatures of CO(J $= 1 \rightarrow 0$) and CO(J $= 4 \rightarrow 3$) at the CO(J $= 4 \rightarrow 3$) map center. The error of CO(J $= 4 \rightarrow 3$) is chosen to be the larger one of either the 15% systematic calibration error or the statistical RMS error from the fit. The error used in CO(1-0) (Whiteoak *et al*. 1982) is the 1K RMS noise.

4.4. Kinematics of C I, CO(4-3), and CO(1-0)

I compare the kinematic properties of C I, CO(J $= 4 \rightarrow 3$), and CO(J $= 1 \rightarrow 0$) based on their emission line properties in this section. The reliability of the emission line velocities and linewidths is greater than the brightness temperatures for the data I use in this thesis. This is because there are fewer steps and uncertainties in the calibration of velocity scales. Further analysis and discussion of line temperatures can be found in §5.

4.4.1. LSR Velocities

Figure 4.6 shows the LSR velocity difference between CO(J $= 1 \rightarrow 0$) and C I emission components for all ISO sources. The mean LSR velocity difference between the C I and CO(J $= 1 \rightarrow 0$) components is found to be $\langle V_{CO} - V_{CI} \rangle = -0.4$ km s^{-1}, with a dispersion of 1.5 km s^{-1}. Both species have the same AOS velocity resolution (0.6 km s^{-1}). The systematic error in V_{LSR} is estimated to be no more than the velocity resolution. Thus within the errors and the dispersion, the CO(J $= 1 \rightarrow 0$) and C I velocities are identical. No systematic relative motion between the C I gas and the CO gas is found. The average LSR velocity difference between CO(J $= 4 \rightarrow 3$) and C I is -0.1 km s^{-1}. There is a relatively large RMS dispersion of 1.9 km s^{-1}. The average difference between the LSR velocities of CO(J $= 1 \rightarrow 0$) and CO(J $= 4 \rightarrow 3$) is 0.3 ± 1.8 km s^{-1}. I discuss the implication of the results found in this section in §5.

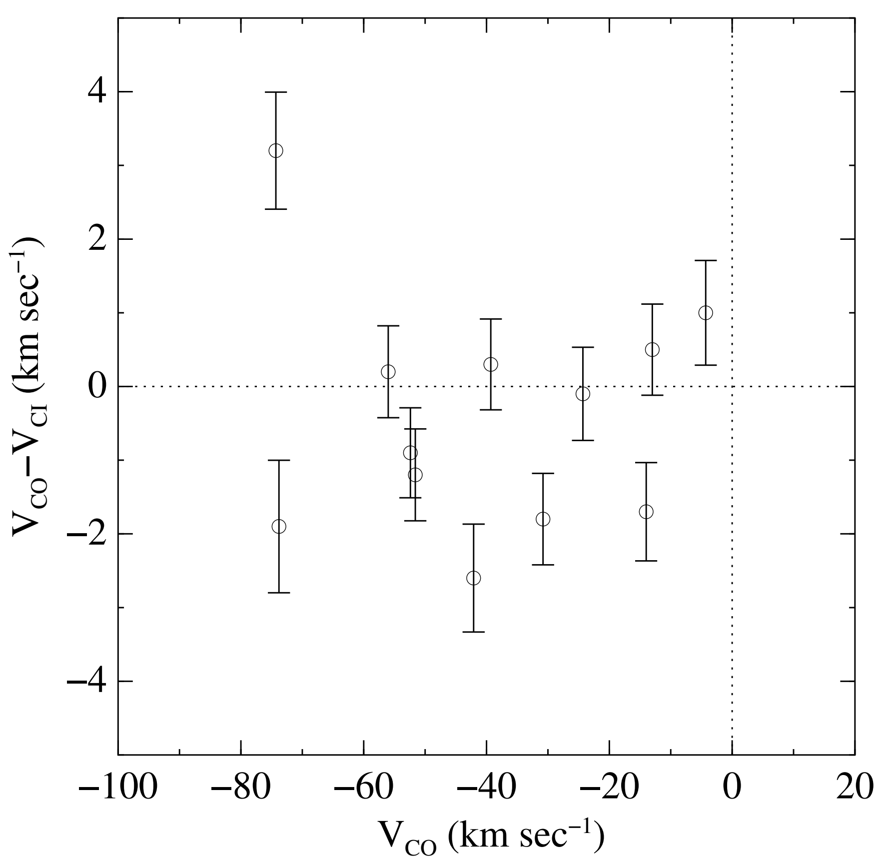

Fig. 4.6.— The V_{LSR} difference between CO($J = 1 \rightarrow 0$) and C I emission components (Group I only) is plotted against the CO V_{LSR}. The error bar at each point shows the 1σ error from the Gaussian fit when the C I V_{LSR} is measured. The error in CO V_{LSR} is estimated to be less than the velocity resolution (0.6 km s^{-1}), and is not shown. This result is consistent with $V_{CO} = V_{CI}$.

4.4.2. Linewidths

On average the linewidth (FWHM) ratio of CO to C I is 1.2 ± 0.1 for CO($J = 4 \rightarrow 3$) and 1.4 ± 0.4 for CO($J = 1 \rightarrow 0$). I find that the C I linewidth has a strong correlation with CO($J = 4 \rightarrow 3$) as shown in Figure 4.7. The same correlation

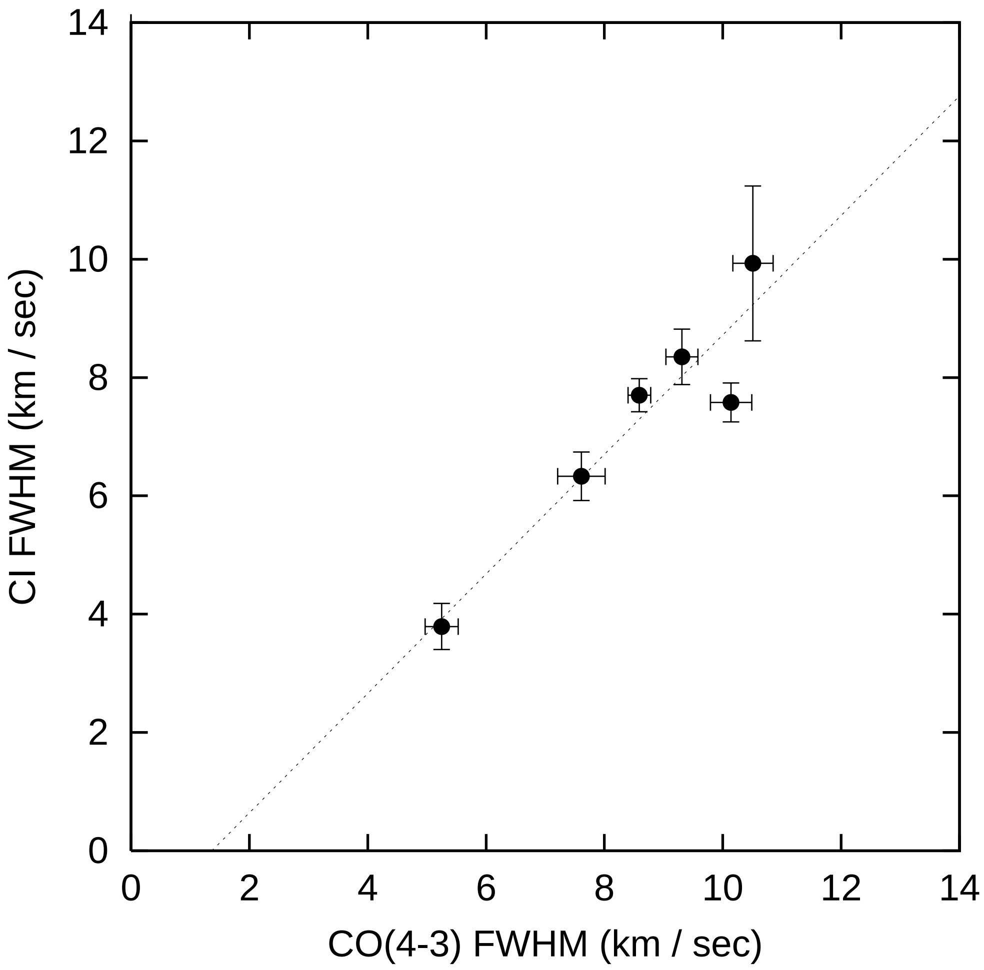

Fig. 4.7.— The linewidths of Group I components of C I and CO($J = 4 \rightarrow 3$) emission. The spectra are taken at the map center which is also the radio continuum peak. The error bar at each point shows the 1σ error from the Gaussian fit when the linewidth is calculated. The dashed line is a linear fit to the data: $\mathrm{FWHM_{CI}} = (1.0 \pm 0.2) \cdot \mathrm{FWHM_{CO4-3}} - (1.4 \pm 1.6)$.

between C I and CO($J = 1 \rightarrow 0$) is much weaker as can be seen in Figure 4.8. The correlation shown in Figure 4.7 is $\mathrm{FWHM_{CI}} = (1.0 \pm 0.2) \cdot \mathrm{FWHM_{CO4-3}} - (1.4 \pm 1.6)$, with a correlation coefficient of 0.94. The above relation shows that the gas traced by the atomic and molecular species have similar linewidths. Since the linewidths are superthermal, they are mainly determined by the gas internal motions and

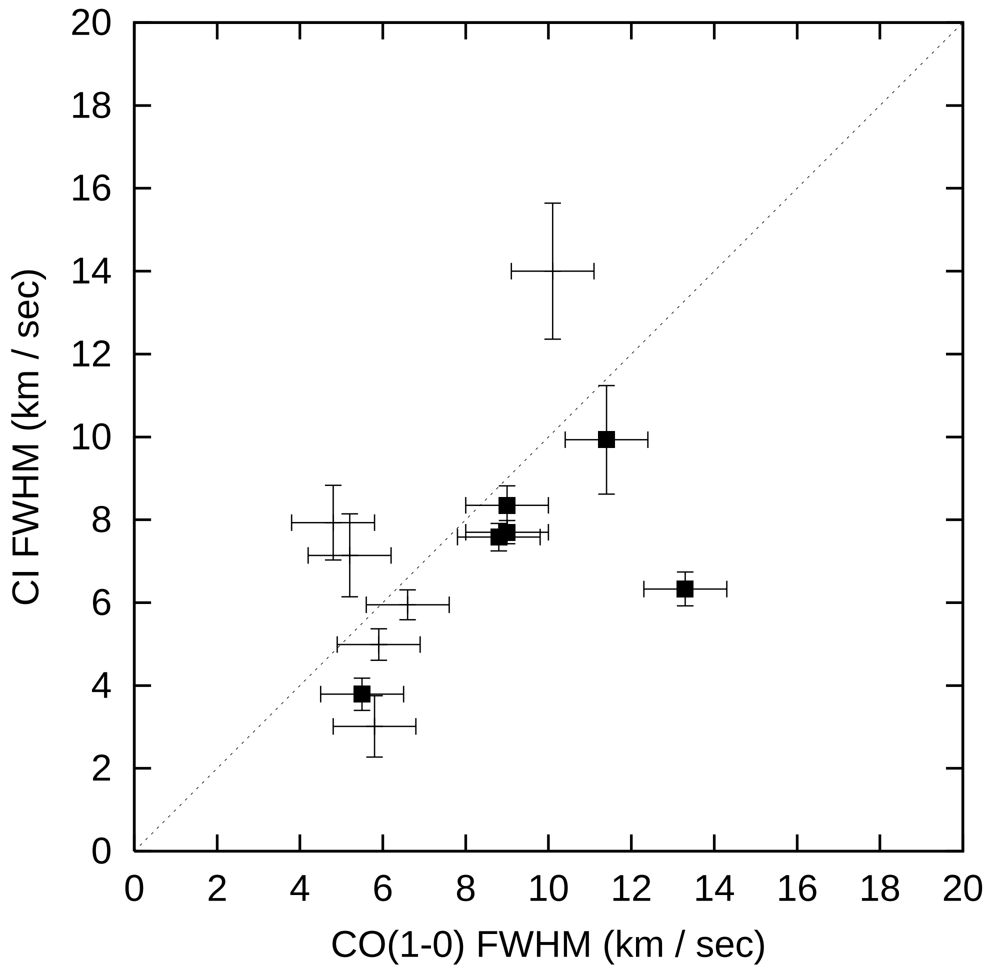

Fig. 4.8.— The linewidths of C I and CO($J = 1 \rightarrow 0$) emission components. The error bar at each point shows the 1σ error from the Gaussian fit when the C I linewidth is calculated. The dashed line bisects the quadrant. The six sources that have been observed in CO($J = 4 \rightarrow 3$) are identified by filled circles. There is only a weak correlation between the linewidth of C I and CO($J = 1 \rightarrow 0$).

line optical depth. The strong positive correlation between C I linewidths and CO($J = 4 \rightarrow 3$) linewidths suggests that the properties of the H II region and the exciting star predominantly determine the line broadening of both the atomic and the molecular ISM gases surrounding the H II regions. This point is further discussed below. Assuming that the CO($J = 4 \rightarrow 3$) lines are wider than the C I lines because of optical depth effects, then the optical depth of CO($J = 4 \rightarrow 3$) can be calculated using the curve of growth method, as shown in Equation 3.7. Equation 3.7 gives a monotonous relation between the line-groadening factor and the line optical depth. The range of CO($J = 4 \rightarrow 3$) and C I linewidth ratios is 1.06 to 1.39. Assuming CO($J = 4 \rightarrow 3$)to be optically thick and C I to be optically thin, Equation 3.7 gives CO($J = 4 \rightarrow 3$) line-center optical depths ranging from 0.3 to 2.5. These are are reasonable optical depth values for these sources, therefore an optical depth effect could explain the larger linewidths of CO($J = 4 \rightarrow 3$) than C I.

The relationships between C I and CO linewidths and the excitation parameter (U; see §1 and §3) are shown in Figure 4.9. A linear fit to the C I data gives the relation: FWHM = (0.045 ± 0.007) U + (2.3 ± 0.7), where FWHM is the linewidth in units of $\mathrm{km\,s^{-1}}$ and U is in units of $\mathrm{cm^{-2}}$ pc. The correlation coefficient is 0.91. CO($J = 4 \rightarrow 3$) and CO($J = 1 \rightarrow 0$) points are also plotted in Figure 4.9 for comparison. They show various degrees of agreement with the fitted linear relation.

The above results indicate that the excitation source influences the kinematics of PDR gas. If U is set to 0, the above correlation gives a linewidth of 2.3 ± 0.7 km $\mathrm{s^{-1}}$. This gives an extrapolated ISM gas velocity dispersion if it was not disturbed by the H II regions. This result agrees with the average CO($J = 1 \rightarrow 0$) linewidths of 2.2 ± 1.0 $\mathrm{km\,s^{-1}}$ found in the dark clouds by Dickman (1975). This result, combined with the correlation between the C I and CO linewidths, indicates that part of the mechanical energy in the surrounding ISM is from the H II regions. Since the linewidths of ISM gas in general are between those of the dark clouds and those of the H II regions (~ 9 $\mathrm{km\,s^{-1}}$ in CO), the above result confirms the well known fact that H II regions are a major source of mechanical energy input to the Galactic ISM. This will be discussed further in §5.

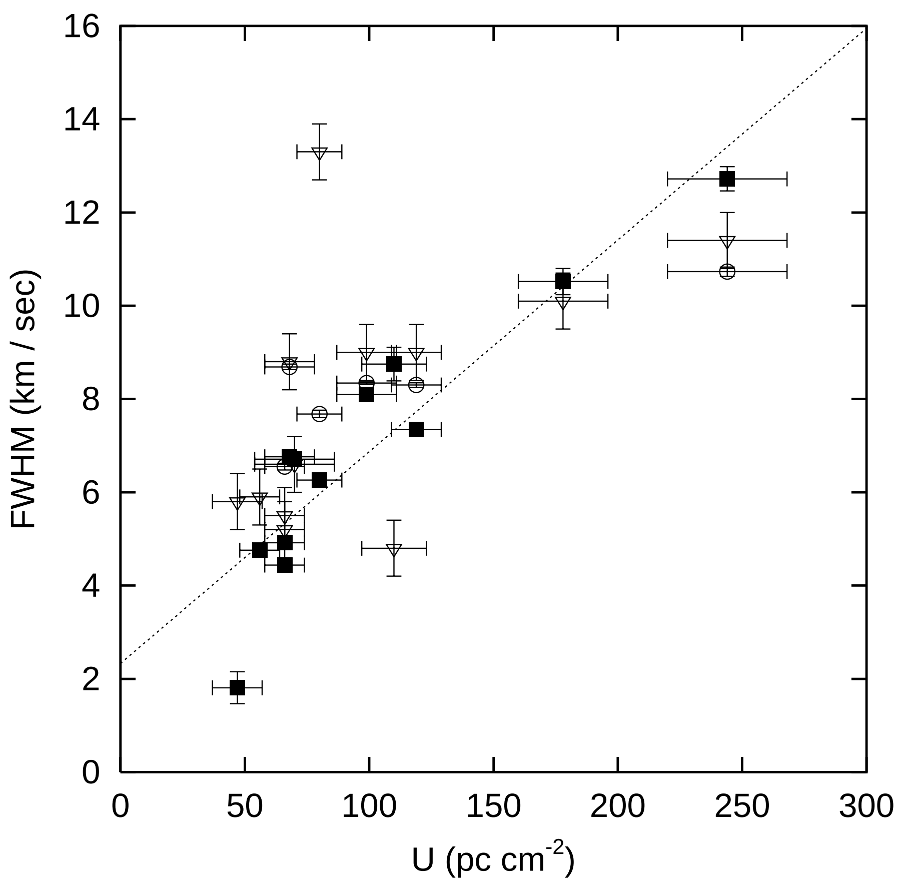

Fig. 4.9.— The linewidths of C I, CO(J = 4 → 3), and CO(J = 1 → 0) as functions of the excitation parameter, U, in units of cm $^{-2}$ pc. The symbols for C I, CO(J = 4 → 3), and CO(J = 1 → 0) are filled squares, open circles, and open triangles, respectively. The dashed line is a linear fit to the C I data only. The error bar at each point shows the 1σ error from the Gaussian fit when the linewidth is calculated. The highest point in the figure (a CO(1-0) measurement) is likely to be the result of fitting two blended components of G322.66−0.61 with one Gaussian in Whiteoak, Robina & Rennie (1982). The lowest point (in C I) is the Group I component of G345.31+1.47. Its Group II component has a greater linewidth at 4.0 $\mathrm{km\,s^{-1}}$ and is likely to be associated with the H II region as well (the difference in LSR velocity is only 3.3 $\mathrm{km\,s^{-1}}$; See Figure 3.7.).

The discussion and analyses of this chapter show that CO(J = 4 → 3) emission has a stronger correlation with C I in line temperature and width than does CO(J = 1 → 0) emission (see § 4.2.2, § 4.3.1, and § 4.4.2). This can be understood by the following argument. Basically, the C I and CO(J = 4 → 3) emission traces the same PDR gas close to the H II regions, and so these species have well correlated properties. The CO(J = 1 → 0) emission does not originate in the same gas, and is probably optically thick, so its correlations with C I and CO(J = 4 → 3) are not strong. Because of its high critical density, CO(J = 4 → 3) traces the warm and dense gas around H II regions. Atomic carbon, C I, is created in the PDR around H II regions, so therefore C I also traces the gas around H II regions. On the other hand, the CO(J = 1 → 0) gas has a low excitation energy (5.5K) and therefore its emission stems from gas located not only in the warm H II region environs, but also in the molecular clouds along the line of sight. The optical depth of CO(J = 1 → 0) emission is generally large enough to cause self-absorption. So the properties of CO(J = 1 → 0) emission are likely to have been affected by the molecular clouds that are on the line of sight of, but unrelated to, the H II regions.

4.5. Support for the Spherical PDR Model

In this chapter the results found in § 4.2.2 and § 4.4 support the spherical PDR model described in §1. The spherical PDR model predicts that the PDR tracer emission coincides with the radio continuum emission in spatial position and in line velocity. The predictions of a spherical PDR model have been confirmed by findings in this chapter: 1) the C I, CO, and radio continuum emission regions are found statistically to be spatially coincident to within 30% of the size of the neutral and molecular emission regions; 2) the CO(J = 4 → 3) region is slightly larger than but comparable to, the C I region size; and 3) the gas velocities of the ionized, neutral, and molecular gas are identical within the errors.

In regard to point (1), an ideal spherical PDR model does not allow there to be offsets between emission peaks of different tracers. The offsets found among the emission peaks of radio continuum, C I, and CO($J = 4 \rightarrow 3$) in § 4.2.2 indicate that the conditions required by the spherical model may not always be strictly satisfied. (For example the distributions of gas and densities may not be homogeneous.) Therefore offsets may exit among emission peaks of species that trace different physical conditions. These offsets, as has also been shown, are not significant compared with the emission region sizes of C I and CO($J = 4 \rightarrow 3$). That these are minor exceptions suggests that the spherical model is a good description of the PDR around H II regions. How prevalent the spherical PDRs are in the Galaxy is discussed in § 5.

In regard to point (2), the relative size of the CO($J = 4 \rightarrow 3$) emission region compared with the C I emission region depends on the clumpiness of the PDR model. A homogeneous spherical model predicts the CO($J = 4 \rightarrow 3$) region to form farther away from the ionizing star than the C I; whereas a clumpy model predicts them to be more mixed. The CO emission region size of very source in the sample is larger than the C I one. This is consistent with either the homogeneous or the clumpy PDR models.

4.6. Summary

I report the results of AST/RO CO($J = 4 \rightarrow 3$) observations of the ISO source H II regions. The observational set up, calibration scheme, and relevant data parameters are described. The CO observations are incomplete because of equipment failure and telescope conditions that were beyond my control. Nevertheless the quality of the available data is excellent. CO($J = 4 \rightarrow 3$) emission is detected in all sources, with some sources having multiple spectral components. I show CO($J = 4 \rightarrow 3$) emission line profiles and sample maps. The spectral line parameters derived from Gaussian fits are presented. I find that the CO($J = 4 \rightarrow 3$) and C I line temperatures are correlated. The average CO($J = 4 \rightarrow 3$) brightness temperature is 3.2 ± 0.7 times brighter than the C I emission at the same LSR velocity.

I fit the CO($J = 4 \rightarrow 3$) maps with two-dimensional Gaussians to yield emission peak positions and emission region sizes. The average CO($J = 4 \rightarrow 3$) emission peak offset with respect to the radio continuum emission peak is found to be $3.1 \pm 1.4'$, comparable to the telescope beam size. Recalling the C I mapping results in §3, I conclude that the atomic, molecular, and radio continuum emission regions spatially coincide to within 30% of the size of the neutral and molecular emission regions. I compare CO($J = 4 \rightarrow 3$) and C I offsets with the average size of the radio continuum emission regions.

I compile CO($J = 1 \rightarrow 0$) observational results from Whiteoak, Robina & Rennie (1982). Their observations and calibration are briefly described. I find the average C I to CO($J = 1 \rightarrow 0$) brightness temperature ratio to be 0.15 ± 0.06. The temperature ratios of CO($J = 1 \rightarrow 0$)/C I is 6.7 ± 2.7 compared with 3.2 ± 2.7 for CO($J = 4 \rightarrow 3$)/C I. The $T_{\rm MB}$ correlation between CO($J = 1 \rightarrow 0$) and C I is weaker than that between CO($J = 4 \rightarrow 3$) and C I, probably due to optical depth effects in CO($J = 1 \rightarrow 0$).

I investigate and compare the kinematic properties of C I and CO emission. I find no systematic relative motion between the C I gas and the CO gas for my sample of H II regions. The same is true for CO($J = 4 \rightarrow 3$) and CO($J = 1 \rightarrow 0$)

emission. A strong correlation between the linewidth of CO($J = 4 \rightarrow 3$) and C I is found. The linewidth correlation between CO($J = 1 \rightarrow 0$) and C I is much weaker. I show a positive correlation between the C I linewidth and the excitation parameter of the H II region. A linear fit can be made where FWHM linewidth = (0.045 ± 0.07) U + (2.3 ± 0.7), where the linewidth, FWHM, is in units of $\mathrm{km\,s^{-1}}$ and U is in $\mathrm{cm^{-2}}$ pc. From this I derive an extrapolated linewidth of 2.3 ± 0.7 $\mathrm{km\,s^{-1}}$ for ISM gas that is not disturbed by an H II region. This linewidth agrees with published results for quiescent dark clouds. Considering the linewidth correlation between CO($J = 4 \rightarrow 3$) and C I gas, the FWHM-U correlation indicates that the H II region is one source for the mechanical energy of the ISM.

CO($J = 4 \rightarrow 3$) shows better correlations in derived parameters with C I than CO($J = 1 \rightarrow 0$) does. This indicates that CO($J = 4 \rightarrow 3$) and C I emission traces the same PDR gas around H II regions whereas CO($J = 1 \rightarrow 0$) emission is likely to be affected by optical depth effects in the CO($J = 1 \rightarrow 0$) transition.

I conclude that results found in this chapter about the CO spatial distribution and line velocities support the spherical PDR models described in §1. Specifically, the C I, CO, and radio continuum emission regions are found statistically to be spatially coincident to within 30% of the size of the neutral and molecular emission region; the CO($J = 4 \rightarrow 3$) region is slightly larger than but comparable to, the C I region size; and the gas velocities of the ionized, neutral, and molecular gas are identical within the errors.

Chapter 5

Comparing Observations with PDR Theories

5.1. Introduction

5.1.1. Data

In previous chapters I have presented the observational results of five species (C^+, OI, dust, C I, and CO) in seven types of emission (C^+, [OI] at 63μm, [OI] at 145μm, FIR continuum emission of dust, C I, CO(J $= 4 \rightarrow 3$), and CO(J $= 1 \rightarrow 0$) for the sample of 12 ISO sources. These results are the first of their kind because the sources were chosen to span a wide range of excitation conditions and were observed in the emission of ionized, neutral, and molecular carbon species. These data come from instruments having similar beam sizes.

The observational results are given in Table 2.2 (for FIR line emission and emission ratios) and in Table 5.1 (for all other emission). Table 5.1 compiles the intensities in previous chapters and presents them in units of ergs cm^{-2} sec^{-1} which are the units used in the PDR models. All intensities are in these units hereafter unless specified. In the table the FIR continuum intensity, I_{FIR}, is derived from the flux of the FIR emission measured by the ISO LWS (F_{FIR} as given in Table 2.3) using an LWS aperture size of 84$''$. The FIR line-to-continuum ratio, $([I_{OI} + I_{CII}])/I_{FIR}$, is the same as in Table 2.4. The C I intensities at the map center, CI$_{ctr}$, and those averaged over the two dimensional Gaussian, CI$_{map}$, are given in the next two columns. The CO(J $= 4 \rightarrow 3$) intensities are given similarly as CO(4-3)$_{ctr}$ and CO(4-3)$_{map}$. The last column gives the CO(J $= 1 \rightarrow 0$) intensity at the map center, CO(1-0)$_{ctr}$.

TABLE 5.1

DERIVED PDR DIAGNOSTICS[a]

Source	I_{FIR}	$([I_{OI}+I_{CII}])/I_{FIR}$	CI_{ctr}	CI_{map}	$CO(4\text{-}3)_{ctr}$	$CO(4\text{-}3)_{map}$	$CO(1\text{-}0)_{ctr}$
G291.28−0.71	...	...	5.0±0.4(−6)	5.6±1.4(−6)	1.8±0.1(−5)	2.7±0.0(−5)	2.7±0.2(−7)
G316.81−0.04	0.5±0.2	3.9±1.2(−3)	3.8±0.2(−6)	4.9±1.2(−6)	9.2±0.4(−6)	1.4±0.0(−5)	2.9±0.2(−7)
G322.15+0.61	1.1±0.5	4.0±1.2(−3)	1.1±0.2(−6)	4.5±1.1(−6)	4.0±0.3(−6)	1.7±0.0(−5)	2.5±0.3(−7)
G332.66−0.61	1.0±0.5	3.8±1.1(−3)	2.5±0.2(−6)	2.7±0.7(−6)	7.0±0.4(−6)	8.7±0.0(−6)	2.9±0.3(−7)
G333.29−0.37	1.5±0.8	2.2±0.7(−3)	5.0±0.2(−6)	7.3±1.8(−6)	1.3±0.0(−5)	2.6±0.0(−5)	4.3±0.3(−7)
G336.84+0.05	0.4±0.2	6.0±1.8(−3)	1.7±0.3(−6)	1.7±0.4(−6)	6.0±0.3(−6)	1.0±0.0(−5)	1.8±0.2(−7)
G337.15−0.18	0.3±0.1	7.5±2.2(−3)	2.0±0.3(−6)	3.4±0.9(−6)	...	...	2.2±0.2(−7)
G337.95−0.48	0.2±0.1	5.2±1.6(−3)	1.1±0.2(−6)	6.0±2.0(−7)	...	...	7.5±1.2(−8)
G340.78−1.01	0.8±0.4	3.1±0.9(−3)	1.9±0.2(−6)	3.2±0.8(−6)	...	...	2.2±0.2(−7)
G345.31+1.47	0.5±0.2	8.4±2.5(−3)	5.8±1.8(−7)	4.0±1.0(−7)	...	...	1.9±0.2(−7)
G348.71−1.03	1.9±1.0	3.0±0.9(−3)	3.0±0.2(−6)	3.8±0.9(−6)	...	...	3.8±0.4(−7)
G353.21+0.91	2.9±1.5	3.6±1.1(−3)	2.0±0.3(−6)	1.5±0.4(−6)	...	...	1.1±0.2(−7)

[a]FIR line emission intensities and intensity ratios measured by ISO are in Table 2.2. Intensities in this table are in units of erg cm^{-2} sec^{-1} sr^{-1}

5.1.2. Models

One important question that this thesis attempts to answer is: *Can the PDR models self-consistently explain the PDR conditions found for a large sample of H II regions with a wide range of excitation conditions?* In this chapter I examine PDR models by comparing observational results with model predictions. I will examine whether the models can self-consistently explain my data, and examine if the model prediction of the physical conditions of the PDR around H II regions agrees with PDR properties derived by other methods.

As described in § 1, PDR models calculate radiation emission intensities and intensity ratios of species in the PDRs based on given conditions. The most important physical parameters are the incident FUV flux density at the surface of the PDR and the gas density of the PDR. Other conditions that can influence the physical processes of the PDR, and hence influence the predictions of the PDR models, include the geometry and density distribution of the PDR, the gas composition and element abundances, the dust and PAH abundances, the kinetic properties (e.g., gas turbulent velocity), etc. To limit the scope of my study, in this thesis I focus on testing three kinds of simplified PDR models: 1) the published homogeneous slab models (Tielens & Hollenbach 1985a; Hollenbach, Takahashi, & Tielens 1991; Wolfire, Tielens & Hollenbach 1990; Kaufman *et al*. 1999) which have the simplest PDR geometry and density distribution; 2) the spherical PDR models which vary the geometry of the PDR compared with the slab models; and 3) the clumpy PDR models which preserve the slab geometry of case (1) but have clumpy density distributions. These models have been described in detail in § 1.

First in § 5.2 I derive the FUV flux, G_0, which is produced on the interface between the H II region and the neutral ISM by the exciting star(s) in the H II region.

Then in § 5.3 I estimate the density of hydrogen nuclei, n, using the observed C I and C^+ intensities. After G_0 and n are obtained using these methods, I first examine the homogeneous one-dimensional PDR models in § 5.4. I select a set of diagnostic, observed quantities of the sources and use them to calculate model-predicted G_0 and n values. I examine whether the models give consistent G_0 and n values using different sets of diagnostic quantities, and whether the model-predicted G_0 and n values agree with those calculated using other methods. I show that these models agree with the observational results derived using the FIR tracers. The C I and CO tracers, however, do not yield the values of G_0 and n predicted by the model. In § 5.5 I show that the spherical PDR model can help explain the observational results in G_0 that cannot be explained by the homogeneous slab PDR model, and in § 5.6 I show that the clumpy PDR models are helpful in solving the discrepancy in n. In the end I summarize the results, make conclusions of this thesis, and discuss the direction of future work.

5.2. Determination of G_0 Using Radio and FIR Data

In this section I estimate the incident FUV intensity on the interface between the ionized gas in the H II region and the neutral gas in the PDRs. I use the RRL and the 5 GHz radio continuum observations reported by Caswell and Haynes (1987) and the infrared observational results of IRAS (see §2). In this chapter the FUV flux is always expressed in terms of the average interstellar radiation field ($1G_0 = 1.6 \times 10^{-3}$ ergs cm^{-2} s^{-1}; Habing 1968). The gas number density is always in cm^{-3}.

5.2.1. Assumptions and Method

I assume that the FUV radiation received by the PDRs surrounding my sample of H II regions comes only from the ionizing star or stars in the H II region. Possible other sources of FUV radiation include the Galactic background radiation and the FUV field from near-by stars. The Galactic background FUV field is 2 to 6 orders of magnitude weaker than that near an H II region, and therefore is neglected here. All my sources are selected to be compact in the radio continuum and isolated on IRAS maps. The angular sizes of these sources are small compared with the angular distances to the nearest other ionizing sources. Therefore the sources selected in my sample are unlikely to be influenced significantly by the FUV field from nearby H II regions.

The basic method for deriving the incident FUV flux density on the surface of the PDR surrounding an H II region has been described in § 1. To recap briefly, the steps are: 1) assume the FIR luminosity derived in § 4 using IRAS FRESCO maps is the total luminosity from the exciting star in the H II region; 2) estimate the stellar contents in the H II region to find out the spectral type and effective temperature of the star or stars; 3) assume the spectral energy distribution of the star is that of a blackbody at the effective temperature and calculate the intensity of the FUV (6eV$<h\nu<$13.6eV) radiation flux density at the surface of the star; and 4) the FUV flux density at the surface of the Strömgren sphere is calculated by geometrically diluting the flux at the star surface. I regard this as the incident FUV field flux density on the surface of the surrounding PDR. More details are described in the following sections.

5.2.2. The Stellar Contents and the Effective Temperatures

In § 4 I estimated the G_0 strength using the total FIR luminosity, assuming the FIR emission comes only from the heating of FUV photons. This estimate in fact gives only an upper limit to G_0 because basically the entire spectrum of the central star can contribute to the heating of surrounding gas and dust. In order to calculate the FUV portion of the total luminosity of a star's radiation, the stellar content of the H II region and the stars' spectral types are needed. I have derived the excitation parameters (U) and the total FIR luminosity of the sources. I will show that from these parameters it is possible to derive the spectral type and effective temperature of the exciting stars for the H II region.

H II Region Luminosities: L and L_c

As described in § 1, U^3 is proportional to the Lyman photon flux, L_c, which is defined as:

$$L_c = 4\pi R_*^2 \int_{13.6eV}^{\infty} \frac{\pi F_\nu(R_*)}{h\nu} d\nu, \tag{5.1}$$

where R_* is the radius of the ionizing star, and $F_\nu(R_*)$ is the flux density from the ionizing star as the function of the frequency, ν, at the surface of the star. The proportional relation is explicitly expressed as:

$$L_c = \frac{4\pi}{3} r_s^3 n_e \alpha_{(2)} = \frac{4\pi}{3} U^3 \alpha_{(2)}, \tag{5.2}$$

where n_e is the electron density, r_s is the Strömgren sphere radius (see §1 for definitions and their relation to U), and $\alpha_{(2)}$, the recombination rate, is a slowly varying function of the electron temperature in the H II region (Osterbrock 1989; see § 1). When the electron temperature is near its typical value of 7000K, the recombination rate is $\alpha_{(2)} = 3.43 \times 10^{-13}\,\mathrm{cm}^3\ \mathrm{s}^{-1}$ (Panagia 1973). So the above relation can be written as:

$$\left[\frac{L_c}{\mathrm{s}^{-1}}\right] = 3.18 \times 10^{43} \left[\frac{U}{\mathrm{pc\,cm}^{-2}}\right]^3. \tag{5.3}$$

Table 5.2 gives derived parameters from RRL and 5 GHz radio continuum observations, and IRAS maps for all sources. The Strömgren sphere radius, r_s, the excitation parameter, U, and the Lyman continuum photon flux, Lc, are based on observations of Haynes and Caswell (1987). The unit of L_c has been normalized to that of a B_0 Class V star ($1.4 \times 10^{48}\ \mathrm{s}^{-1}$; Vacca, Garmany, & Shull 1996; also see below). The IR luminosity, L_{FIR}, and the FUV flux estimated solely from L_{FIR} are reproduced from § 4.

H II Regions and OB Stars

The relation between an OB star's spectral type, the total star luminosity (L), the Lyman continuum photon flux (L_c), the effective temperature (T_{eff}), and the radius (R_*) is calculated in Vacca, Garmany, & Shull (1996). The stellar atmosphere

TABLE 5.2

PROPERTIES DERIVED FROM RADIO AND IR MEASUREMENTS

Source	r_s pc	U pc cm^{-2}	L_c[a]	L_{FIR} $L_{\odot}$	FUV$_{FIR}$ G$_0$
G291.28−0.71	0.5 ± 0.1	1.2±0.1(2)	2.3±0.6(2)	5.3±1.7(5)	4.3±1.6(4)
G316.81−0.04	1.1 ± 0.2	6.8±1.0(1)	4.4±1.9(1)	2.6±1.2(5)	4.8±3.2(3)
G322.15+0.61	0.8 ± 0.1	6.6±0.8(1)	4.0±1.5(1)	3.4±1.4(5)	1.2±0.6(4)
G332.66−0.61	3.0 ± 0.5	8.0±0.9(1)	7.1±2.4(1)	4.1±1.6(5)	9.3±4.8(2)
G333.29−0.37	2.1 ± 0.3	9.9±1.2(1)	1.3±0.5(2)	6.3±2.5(5)	2.9±1.5(3)
G336.84+0.05	20.6 ± 3.1	2.4±0.2(2)	2.0±0.6(3)	1.1±0.4(7)	5.5±2.6(2)
G337.15−0.18	11.7 ± 1.8	1.8±0.2(2)	7.8±2.4(2)	3.1±1.1(6)	4.5±2.2(2)
G337.95−0.48	0.8 ± 0.2	6.6±0.8(1)	4.0±1.5(1)	3.4±1.4(5)	9.6±6.0(3)
G340.78−1.01	1.9 ± 0.5	5.6±0.8(1)	2.4±1.1(1)	2.1±1.0(5)	1.1±0.8(3)
G345.31+1.47	1.4 ± 0.5	4.7±1.0(1)	1.4±0.9(1)	1.6±1.0(5)	1.6±1.5(3)
G348.71−1.03	0.8 ± 0.3	7.0±1.6(1)	4.8±3.3(1)	3.0±2.2(5)	8.5±8.6(3)
G353.21+0.91	2.6 ± 0.5	1.1±0.1(2)	1.8±0.7(2)	4.4±1.8(5)	1.3±0.7(3)

[a]Lyman continuum photon flux is in normalized by that of a B_0 star (1.4×10^{48} s^{-1}; Vacca et al. 1996).

models and spectral type calibrations they use are newer than those in the often-cited calculations by Panagia (1973) published more than twenty years ago.

Figure 5.1 shows the relation between L and L_c (in connected open circles; hereafter referred to as the L-L_c curve) for Class V OB stars (Vacca, Garmany, & Shull 1996). The stellar spectral types from O3 to B0.5 are plotted. In the same figure I plot my H II region sources (plotted as stars) according to their Lyman continuum photon fluxes and their L_{FIR} with the errors. Figure 5.1 shows that the luminosity measurements of 8 of the 12 H II regions in the sample fall on the stellar L-L_c relation curve within the errors. The sources G291.28−0.71, G353.21+0.91, G336.84+0.05 and G337.95−0.48 do not. Many factors can affect the position of an H II region in L-L_c space. The arrows in the lower right corner of Figure 5.1 indicate

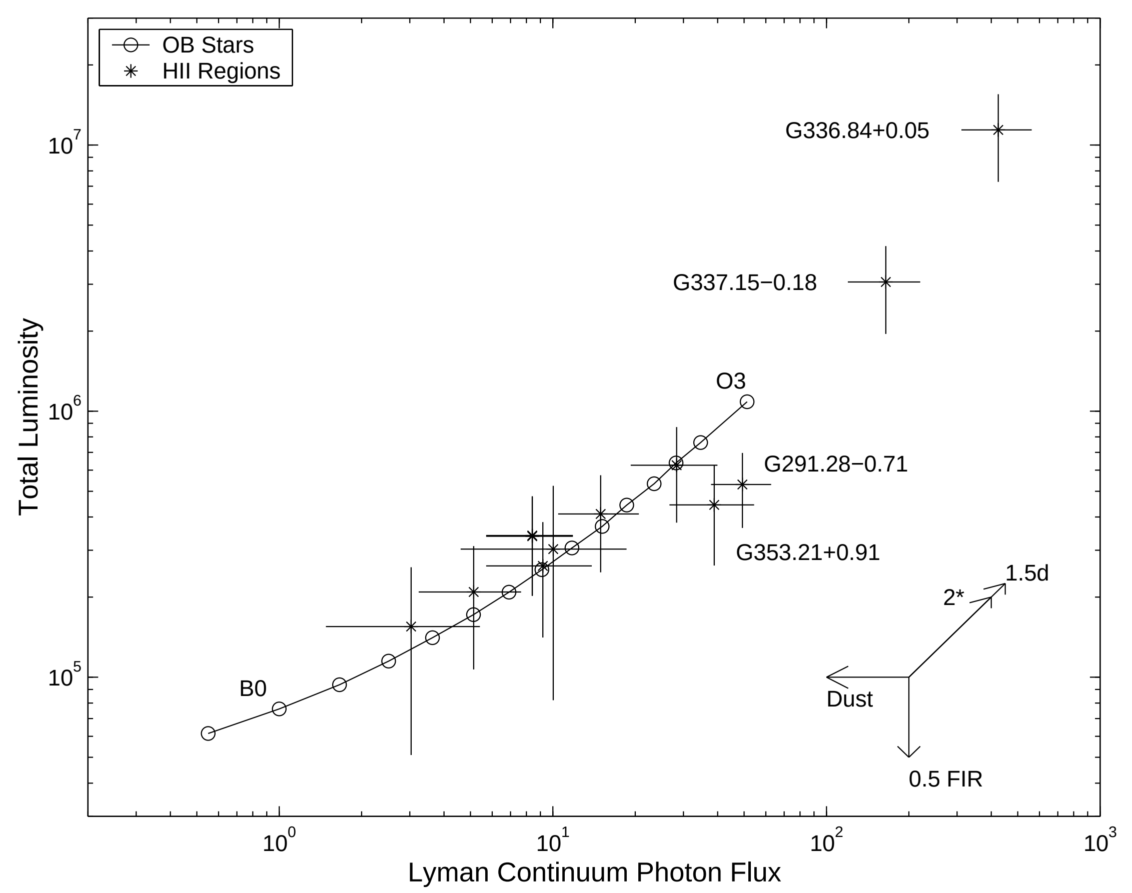

Fig. 5.1.— Comparison of the total luminosity, L, and the Lyman continuum photon flux, L_c. The total luminosity and Lyman continuum photon flux of OB stars (Vacca *et al*. 1996) are plotted as connected open circles. The spectral types, from right to left, are O3, O4, O5, O5.5, O6, O6.5, O7, O7.5, O8, O8.5, O9, O9.5, B0, B0.5. The stars mark the H II region sample using their Lyman continuum photon flux, derived from RRL and 5 GHz radio continuum observations, and their FIR luminosity, derived from IRAS maps (§4). The arrows drawn in the lower right indicate the magnitude and direction that several uncertainty factors could move the H II region position in the figure (see text for details).

the direction and magnitude of the position shifts produced by effects which are discussed below in later sections.

Determination of Stellar Contents

Given a pair of L and L_c luminosities of an H II region, one can usually select a number of stars, each of a certain spectral type, such that the stars' total L and L_c can match the observations within the errors. This set of stars is referred to as a "valid" combination of stellar contents. Generally, a valid combination of stellar contents is not a unique fit. The arrow in Figure 5.1 marked with "2*" illustrates where the position of the representative star of an H II region would move if the number of stars in the H II region were doubled. All H II regions plotted in the figure could be the result of many different combinations.

In order to simplify the process, for each H II region I look for a combination of valid stellar content that requires *the smallest number of stars*. This choice does not affect the estimation of the FUV flux output of the H II region significantly if the stellar content is in fact a cluster of a few stars of later spectral types. This is mainly because when the number of star(s) in the combination increases, the FUV fraction of the total luminosity does not vary significantly. The ratio of FUV flux and the total stellar luminosity varies from 34% to 52% for stars of spectral type from O4 to B3 (a 20% change from the median value; Kraemer 1998a). Consequently the ratio of the total FUV output of a cluster compared with the total luminosity of the cluster also remains almost constant. Since the total luminosity remains constant for all valid choices of stellar content, the total FUV output does not change significantly either. The G_0 values found in this section are to be compared with those fitted by PDR models (§ 5.4). (The above variation in the FUV fraction of the total stellar luminosity is relatively small compared with that found for the § 5.4 model-fitted G_0 values.)

A straightforward analysis gives the stellar contents for those H II regions that fall on the L-L_c curve. Figure 5.1 shows that 8 sources (all sources except G291.28−0.71, G353.21+0.91, G336.84+0.05 and G337.95−0.48) can by fitted to the L-L_c curve within the errors. As explained above I assume these H II regions are excited by a single O star. I choose a point on the L-L_c curve closest to an H II region to represent this star. This star comprises the stellar content of this H II region. The total luminosity and total Lyman continuum photon flux of the central exciting star of the H II region are then determined.

Assessing the stellar content in G336.84+0.05 and G337.95−0.48 is more complicated. The position of these sources in Figure 5.1 with respect to the L-L_c curve suggests that a number of O stars in the H II region could explain the total L and L_c. I assume there are multiple O3 stars in each of these H II regions and calculate the number of stars according to the total L_c and its error. The total FUV flux is the sum of all O3 stars in the cluster, assuming they all are located at the center of the H II region. Although the choice of the stars' spectral type (O3) is somewhat arbitrary, choosing other OB spectral types would alter the total luminosity by only about 20%, as I argued in earlier part of this section. This change is insignificant.

The sources G291.28−0.71 and G353.21+0.91 in Figure 5.1 have less total luminosity than an O star with the same L_c would have. This discrepancy cannot be solved by having a small number of O stars in these H II regions, as indicated by their positions relative to the L-L_c curve and the direction of the "2*" arrow. I assume there are only a small number of stars in these H II regions because of their compact sizes. Then there are two likely scenarios that can explain the observation: 1) There is dust in the H II region that competes with the hydrogen ionization process by absorbing Lyman continuum photons (Spitzer 1978). This process will not decrease the total luminosity because the energy of a Lyman photon absorbed by dust is eventually re-radiated, contributing to the H II region total luminosity. The absorption of Lyman photons only changes the spectral distribution of the radiation field in the H II region. The arrow marked "dust" in Figure 5.1 indicates where the position of the star representing an H II region would move if half of the Lyman continuum photons are absorbed by dust. 2) The molecular cloud outside the H II region does not entirely encompass the H II region. Only part of the total luminosity of the exciting star is absorbed by dust and radiated in FIR in the molecular cloud. Most or all Lyman continuum photons are absorbed by the ubiquitous hydrogen gas, however, and contribute to RRL and radio thermal continuum emission at 5 GHz just as would happen if the H II region is entirely surrounded by the molecular cloud. The observed L_c is therefore unchanged. This effect is shown by the arrow labeled with "0.5FIR" in Figure 5.1. The length and direction of the arrow show how an H II region would move in L-L_c space if half of the total stellar luminosity is not observed at FIR wavelengths.

Scenario 2) is a more plausible scenario if the H II region is located at the edge of a molecular cloud and forms a "blister" type of PDR on the surface of the cloud. Examination of the sample (see § 1) shows that G291.28−0.71 and G353.21+0.91 are the only two bright visible sources in the sample, and are identified as NGC3574 and NGC6357, respectively. Deep H_α surveys and the summary presented by Georgelin *et al*. (2000) show that G291.28−0.71 is optically bright, with a visual extinction at about only 1. The evidence strongly suggests that G291.28−0.71 is a face-on H II-PDR complex. For G353.21+0.91, past observations have shown that it is an

H II region eroding into a molecular cloud, with an ionization front seen side-on (Massi, Brand & Felli 1997; Persi *et al*. 1994). The presence of a sharp edge to the south of the emission peak in my C I map of G353.21+0.91 (Figure 3.9) supports their conclusions. The visual extinction of this H II region is found to be less than 2 mag by Massi *et al*. (1997). Some part of the visual extinction for both of the H II regions could also come from the unrelated ISM along the line of sight. The dust absorption effect in these sources is likely to be weak because of the low visual extinction, so therefore I conclude that the argument in (2) is the likely cause of the low total luminosity observed. Thus in order to derive the total luminosity, L, I will use the L_c values of these H II regions to determine a single O star using the L-L_c curve.

Table 5.3 lists derived properties of the exciting stars for all sources. The spectral type, star total luminosity, L, star effective temperature, T_{eff}, and star radius, R_*, are found using the L-L_c relation with the Lyman continuum photon flux given by Vacca *et al*. (1996). The FUV/L ratio and the FUV flux, G_0, are discussed in the next section.

5.2.3. Determination of FUV Flux, G_0

As discussed in § 1, assuming that: 1) the border of the Strömgren sphere is the boundary between the ionized gas in the H II region and the neutral ISM in the PDR; and 2) the exciting star is the only source of incident FUV radiation on the PDR, I calculate the incident FUV flux using Equation 1.9. The FUV fraction of the total stellar flux is calculated using the star's effective temperature, T_{eff}. It is listed in Table 5.3 as FUV/L. The G_0 values in Table 5.3 are calculated using Equation 1.9. Note that, as discussed in § 1, the source sample proposed for ISO observations had

TABLE 5.3

Derived Properties of the Exciting Stars and FUV Flux

Source	Spec. Type[a]	L $L_\odot$	T_{eff} 10^4K	R_* $R_\odot$	FUV/L %	FUV flux G_0
G291.28−0.71	O3.1	1.0±0.3(6)	5.1±0.2	13.1±0.5	100	8.4±2.7(4)
G316.81−0.04	O7.0	2.6±0.5(5)	4.1±0.1	10.0±0.4	100	4.8±2.5(3)
G322.15+0.61	O7.2	2.7±0.5(5)	4.1±0.1	10.1±0.3	100	9.8±3.1(3)
G332.66−0.61	O6.0	3.9±0.7(5)	4.4±0.1	10.8±0.3	100	8.7±3.2(2)
G333.29−0.37	O4.5	6.3±1.2(5)	4.7±0.1	11.8±0.5	100	2.9±1.1(3)
G336.84+0.05	O3 $\times 8^{+3}_{-2}$ [b]	8.7±2.7(6)	5.1±0.0	13.2±2.1	100	4.2±2.6(2)
G337.15−0.18	O3 $\times 3^{+1}_{-1}$ [b]	3.2±1.1(6)	5.1±0.0	13.2±1.6	100	4.8±3.1(2)
G337.95−0.48	O7.2	2.7±0.5(5)	4.2±0.1	10.1±0.3	100	7.6±3.8(3)
G340.78−1.01	O8.0	1.8±0.4(5)	3.9±0.1	9.4±0.3	100	9.6±4.8(2)
G345.31+1.47	O8.7	1.3±0.4(5)	3.7±0.2	8.9±0.4	100	1.4±1.0(3)
G348.71−1.03	O6.8	2.8±0.9(5)	4.2±0.2	10.2±0.6	100	7.9±6.2(3)
G353.21+0.91	O3.7	8.3±2.8(5)	4.9±0.2	12.6±0.8	100	2.5±1.2(3)

[a]Spectral type is determined by the calibration in Vacca et al. (1996).

[b]The symbol "O3 $\times 8^{+3}_{-2}$" means there are 8^{+3}_{-2} O3 stars existing in the H II region.

a wider G_0 range. ISO only observed a subset of the sample so the G_0 range is more limited.

Except for G291.28−0.71, which has a G_0 of 7400, all sources have G_0 values less than 3300. The average G_0 of these sources is $1.2 \pm 1.1 \times 10^3$, which is 40% of the average G_0 estimated in § 4 using the total source luminosity. This is understandable from the FUV/L values listed in Table 5.3, which shows this ratio to be about 40% on average. The FUV/L ratio should be smaller than 1 since in § 4 G_0 was estimated assuming that the total FIR luminosity is emitted in FUV photons.

The average FUV flux of the ISO sample H II regions, as shown in Table 5.3, is about one order of magnitude less than the PDR "test bed" sources: Orion (G_0 $=10^5$; Tielens & Hollenbach 1985b), M17 (5.6×10^4; Meixner *et al*. 1992), the Galactic Center and the nucleus of starburst Galaxy (M82) ($G_0 = 10^4 \sim 10^5$; Wolfire, Tielens & Hollenbach 1990). Although the PDR theories have been tested on H II regions that have less intense FUV field (e.g., Chokshi *et al*. 1988), the G_0 values of the ISO sample show that typical compact Galactic H II regions produce FUV fields in the 10^3 to 10^4 range. For the H II regions that are more extended than my compact H II regions, the FUV field is likely to be weaker. The strong FUV fields of 10^4 to 10^5, which are often cited in the literature to discuss PDRs near H II regions, are not typical of normal Galactic H II regions.

5.3. Determination of Gas Density Using Emission Line Intensities

In addition to the FUV radiation field one needs to know the density of the hydrogen nuclei, n, in order to specify the physical state of a PDR. I determine n of the PDR using the observed emission line intensity of carbon species. I will derive the gas density in the C^+/C I zone. I assume that there is not a large gradient in gas density between the C^+/C I zone of the PDR and the zones where CO dominates. This is true for the homogeneous slab PDR models by definition. The gas density derived in the C^+/C I zone is then regarded as an appropriate estimate of the PDR gas density.

I have estimated column densities of C I for the ISO sources in § 3 where I argue that C I emission is optically thin. The results are in Table 3.5 where the PDR gas temperature is assumed to be 50K. A higher temperature would decrease the optical depth.

The relation between the 158μm emission intensity, I_{158}, and the C^+ column density, N_{c+}, is given by Crawford *et al*. (1985) and Kraemer (1998a). When the gas temperature is much higher than $h\nu_{158}/k = 91$K and the gas density greater than the critical density of C^+ (4×10^3cm^{-3}; colliding with hydrogen) the equation is:

$$\left[\frac{I_{158}}{\text{ergs s}^{-1}\text{cm}^{-2}\text{sr}^{-1}}\right] = 1.7 \times 10^{-21}\left[\frac{N_{c+}}{\text{cm}^{-2}}\right]. \tag{5.4}$$

The above relation also assumes that the optical depth of C^+ emission is small and that the beam filling factor is unity. When the gas temperature is not well above 91K and the gas density is well below 3×10^3cm^{-3}, the constant on the right side of the equation will decrease only by a factor of several (e.g., by a factor of 3 when the gas temperature is 50K). Since the bulk of C^+ gas is found in an environment that is typically several hundred K (Crawford *et al*. 1985), the relation in Equation 5.4 is used below to derive the C^+ column density.

Molecular carbon is negligible in regions where C I and C^+ are abundant. In § 4 I showed that C I and CO(J = 4 $\rightarrow$ 3) emission regions have the same location and comparable sizes, and have similar kinematic properties. I argued that this evidence suggests that these two species are likely to be coexistent. I assume the excitation temperatures of the two species to be equal, and show in Appendix B that in CO(J = 4 $\rightarrow$ 3) emission regions the CO abundance is an order of magnitude less than C I. Because CO(J = 4 $\rightarrow$ 3) and C I are assumed to be coexistent, this implies that the CO column density estimated in Appendix B reflects the total CO column density in the C I region. The fractional abundance of any other carbon-bearing molecule must be even smaller than that of CO. So therefore I conclude that the contribution of molecular carbon species to n_c is negligible compared with C I and C^+ in regions where C^+ and C I are abundant.

Because of its high ionization potential, C^{++} is formed in a relatively small fraction of the Strömgren sphere. Since the C I region is found to be about 4 times the size of the Strömgren sphere in § 3, assuming the volume density of C^{++} is no more than that of C I, the total C^{++} column density should be negligible compared with that of C^+ plus C I.

Based on the above calculations and estimates, the carbon nuclei column number density, N_c, is the sum of the C^+ column density, $N_{\rm CII}$, and the C I column density, $N_{\rm CI}$. I reported measurements of the C^+ intensities at positions away from the ISO sources in § 2 and found them to be about 0.2% of the the average C^+ intensity from the ISO sources. Large scale diffuse C^+ emission measurements (Shibai *et al.* 1991; Nakagawa *et al.* 1998) found the diffuse C^+ emission component on the Galactic plane to be about a 10% of the intensity of my ISO sources. Based on these results I further assume that the bulk of the C^+ emission only comes from inside the C I emission region, then N_c reflects the total carbon nuclei column density *within* the C I emission region. So the assumption that C^+ is mostly from inside the C I region is a reasonable. The carbon nuclei volume density is then derived by dividing N_c by the C I emission region linear size, as expressed in Equation 3.17. The hydrogen nucleus volume density is derived using a carbon to hydrogen abundance ratio of

TABLE 5.4

Column and Volume Densities

Source	N_{CI} cm^{-2}	N_{CII} cm^{-2}	$\frac{N_{\mathrm{CII}}}{N_{\mathrm{CI}}}$	N_c[a] cm^{-2}	n_c[a] cm^{-3}	n_H[a] cm^{-3}
G291.28−0.71	6.2±1.6(17)	...	...	6.2±1.6(17)	4.7±1.4(-2)	3.4±1.0(2)
G316.81−0.04	5.4±1.4(17)	8.0±4.0(17)	1.5±0.8	1.3±0.4(18)	1.1±0.4(-1)	7.6±3.0(2)
G322.15+0.61	5.0±1.3(17)	1.2±0.6(18)	2.5±1.4	1.7±0.6(18)	1.2±0.5(-1)	8.8±3.7(2)
G332.66−0.61	3.0±0.8(17)	1.5±0.8(18)	5.0±2.8	1.8±0.8(18)	6.6±3.1(-2)	4.7±2.2(2)
G333.29−0.37	8.1±2.0(17)	1.4±0.7(18)	1.7±0.9	2.2±0.7(18)	8.3±3.2(-2)	6.0±2.3(2)
G336.84+0.05[b]	1.9±0.5(17)	1.4±0.7(18)	7.4±4.2	1.6±0.7(18)	...	...
G337.15−0.18	3.8±0.9(17)	1.1±0.5(18)	2.8±1.6	1.5±0.5(18)	2.5±1.0(-2)	1.8±0.7(2)
G337.95−0.48[b]	7.0±1.8(16)	5.0±2.5(17)	7.1±4.0	5.7±2.5(17)	...	...
G340.78−1.01	3.6±0.9(17)	8.6±4.3(17)	2.4±1.3	1.2±0.4(18)	6.3±2.7(-2)	4.5±1.9(2)
G345.31+1.47	4.4±1.1(16)	1.3±0.7(18)	29.8±16.7	1.4±0.7(18)	2.9±1.7(-1)	2.1±1.2(3)
G348.71−1.03	4.2±1.1(17)	2.0±1.0(18)	4.7±2.6	2.4±1.0(18)	1.8±1.0(-1)	1.3±0.7(3)
G353.21+0.91	1.7±0.4(17)	1.9±0.9(18)	10.8±6.0	2.0±0.9(18)	1.9±1.0(-1)	1.4±0.7(3)
Average	3.7±2.2(17)	1.3±0.4(18)	6.9±7.8	1.5±0.5(18)	1.2±0.8(-1)	8.4±5.5(2)

[a]Densities include both CI and C^+. G291.28−0.71 is not observed by ISO so the densities only include CI.

[b]The volume density for this source cannot be calculated because the morphology is too complex to fit a Gaussian (see § 3).

1.4×10^{-4} (gas phase abundance; Kaufman *et al*. 1999; also see Table 5.5 below).

Table 5.4 gives densities derived from C I and C^{+} observations. The neutral carbon column density, N_{CI}, is derived in § 3. The ionized carbon density, N_{CII}, is calculated using Equation 5.4. The ratio of these two column densities is calculated without any correction for the effect of different beam sizes. The carbon nuclei column density and volume density, N_c and n_c, respectively are derived as discussed in the above paragraph. The hydrogen nucleus volume density, n_H, is given in the last column.

Some observations can be made from the results listed in Table 5.4 and from discussion in this section. Firstly the C^{+} column density in the vicinity of the H II region is many times higher (by a factor of 7 ± 8) than the C I column density. Secondly the molecular (CO) component of the gas in C I emission regions is one order of magnitude less than C I. Using the CO(J = $1 \rightarrow 0$) intensities, the average CO column density along the line of sight is estimated (Scoville & Sanders 1987) to be $\langle N_{CO}^{\mathrm{total}} \rangle = 1.4 \pm 0.5 \times 10^{19}\,\mathrm{cm}^{-2}$ for all sources, which is one order of magnitude higher than $\langle N_{CI} + N_{CII} \rangle$ ($1.7 \pm 0.4 \times 10^{18}\,\mathrm{cm}^{-2}$; see Table 5.4). The contrast between the lack of CO in the close environs of the H II regions and the abundance along the line of sight clearly shows that H II regions are dissociating molecular gas into neutral and ionic species. Thirdly the gas hydrogen nuclei volume density is about 1000 cm^{-3} on average.

5.4. The Homogeneous Slab PDR Model

In their landmark papers Tielens and Hollenbach described the concept, physics, and chemistry of PDRs, and constructed homogeneous one-dimensional PDR models (Tielens & Hollenbach 1985a; Tielens & Hollenbach 1985b). They successfully explained many observational results for the Orion molecular cloud using one of their models. These PDR models have been used successfully in numerous studies of star forming regions, the Galactic Center, galaxies, and galactic nuclei (e.g., Genzel *et al*. 1988; Phillips & Mampaso 1989; Wolfire, Tielens & Hollenbach 1990; Tauber *et al*. 1995). More details of the model have been described in § 1.

In this section I determine the incident FUV fluxes, G_0, and the gas hydrogen nuclei densities, n, of the ISO sources using my observational results and the homogeneous slab PDR models. I then compare these model G_0 and n values gotten from different sets of observed species with G_0 and n derived previously in this thesis. (If you don't like the word *gotten*, talk to Bania.)

Note that all line and continuum intensities calculated in the one-dimensional PDR models refer to the exit intensity from the side of PDR that faces the FUV source (See Figure 1.1). This is what an observer would see when the PDR is viewed face-on. There is no comprehensive treatment of the radiative transfer to calculate the emission intensities seen side-on. In the literature, authors use the face-on intensities predicted by the PDR models (given the G_0 and n) even when the geometry is decidedly side-on (e.g., Meixner *et al*. 1992; Meixner & Tielens 1993). When discussing PDR diagnostic quantities in this thesis, I will ignore the difference caused by the face-on or the side-on point of view of the observer, following this perhaps too optimistic astrophysical tradition.

5.4.1. Derived Gas Densities and FUV Fluxes

In this section I use the existing homogeneous one-dimensional PDR models to derive the gas densities, n, and incident FUV fluxes, G_0, from various combinations of the C I, CO(1-0), CO(4-3), C^+, [OI], and FIR continuum data for all the ISO sources. The determination method is described below in detail.

Method to Determine G_0 *and* n

TABLE 5.5

STANDARD MODEL PARAMETERS OF THE HOMOGENEOUS SLAB PDR MODELS[a]

Parameter	Symbol	Value
Turbulent Doppler Velocity	$[\delta v_D]$	1.5 km sec^{-1}
Carbon abundance[b]	X_C	1.4×10^{-4}
Oxygen abundance[b]	X_O	3.0×10^{-4}
Silicon abundance[b]	X_{Si}	1.7×10^{-6}
Sulfer abundance[b]	X_S	2.8×10^{-5}
Iron abundance[b]	X_{Fe}	1.7×10^{-7}
Magnesium abundance[b]	X_{Mg}	1.1×10^{-6}
Dust abundance relative to diffuse ISM	δ_d	1
FUV Dust absorption/visual extinction	δ_{UV}	1.8
Dust visual cross section per H	$\sigma_{\rm V}$	$5 \times 10^{-22}\,{\rm cm}^2$
Formation rate of H_2 on dust[c]	R_{form}	$3 \times 10^{-17}\,{\rm s}^{-1}$
PAH abundance	$X_{\rm PAH} = n_{\rm PAH}/n$	4×10^{-7}
Cloud density	n	$10^1\,{\rm cm}^{-3} \le n \le 10^7\,{\rm cm}^{-3}$
Incident FUV flux	G_0	$10^{-0.5} \le G_0 \le 10^{6.5}$

[a]Reproduced from Kaufman et al. (1999).
[b]Gas phase abundances relative to H nuclei from Savage & Sembach (1996).
[c]Rate (cm^{-3} s^{-1}) given by $R_{form}n$

The numerical results of the homogeneous slab PDR models that are used in this thesis are calculated by Kaufman *et al.* (1999; see § 1). The PDR is assumed to be homogeneous, static, and semi-infinite. The Standard Model parameters of Kaufman *et al.* (1999) are reproduced in Table 5.5, including the elemental abundances, gas turbulent velocity, dust-to-gas ratio, etc. The meanings of the parameters are explained in the first column. The detailed parameter explanations and how these parameters are selected are discussed in the original paper and will not be repeated here. In later sections in this chapter the selections of some of the parameters will be discussed.

When the incident FUV intensity, G_0, and the column density of hydrogen nuclei, n, are given, the model calculates spectral line intensities for any PDR species or the FIR continuum intensity. These intensities and the intensity ratios thereof are hereafter referred to as the *diagnostic quantities* of the PDR. The models calculate diagnostic quantities in the range of G_0 spanning from $10^{-0.5}$ to 10^7 and of n from 10^1 to 10^7. These results are published in the form of PDR diagnostic quantities as functions of G_0 and n. The major results of model calculations are presented in Figures 1.4 to 1.11.

A pair of known PDR diagnostic quantities is needed to determine the values of model-predicted G_0 and n combinations. Each one of the two diagnostic quantities corresponds to a contour in one model plot (see Figure 5.2). When the two sets of contour plots are overlayed the contours generally have a intersecting point, and predicted values of G_0 and n are obtained by reading the coordinates of the intersection point. The errors in G_0 and n can be estimated from the 1σ errors of the observational results using this pair of diagnostic quantities.

The ensemble of possible permutations of diagnostic pairs also gives an estimate of systematic errors and the internal consistency of the data and the model. I will show in the next section that because of limitations on usable diagnostic quantities, available ones are limited to one pair of species traced by IR emissions and one pair of those traced by the millimeter and sub-millimeter emissions. I will compare the G_0 and n values predicted based on these two pairs in § 5.4.2 to check the internal consistency of the data and the model.

The actual operation to overlay the two contour plots and to determine G_0 and n is made by a computer program I wrote. The program reads the FITS format files

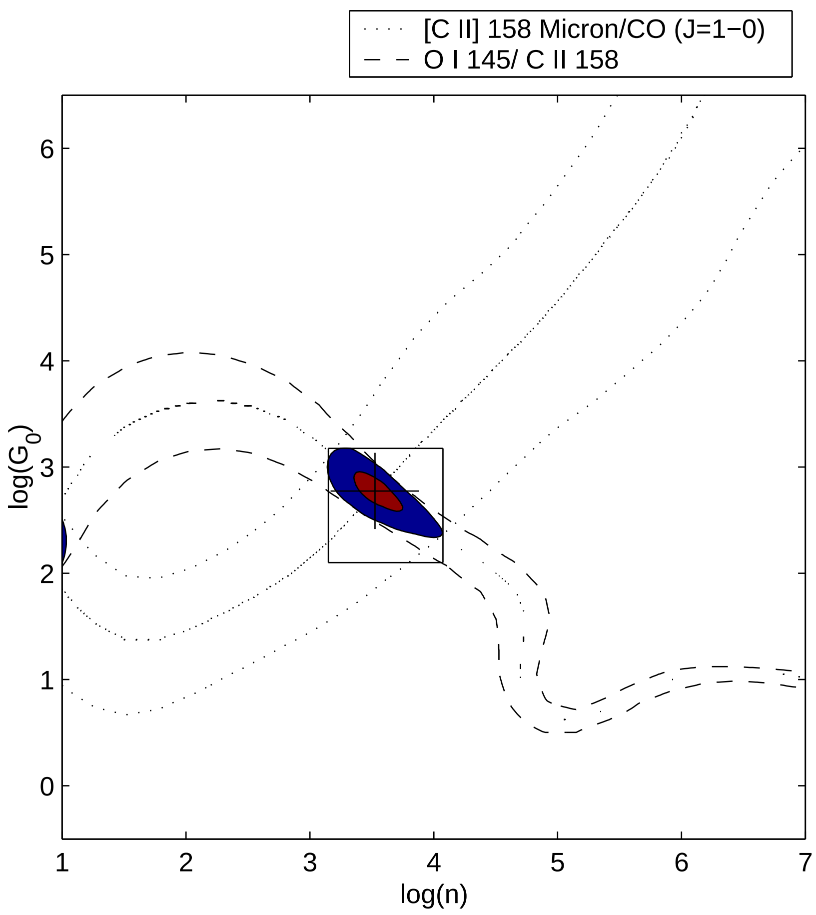

Fig. 5.2.— An example of the determination of G_0 and n using a pair of PDR diagnostic quantities. This plot shows the results using the [C II]/CO($J = 1 \rightarrow 0$) and the 145μm[OI]/[C II] intensity ratios of the source G316.81−0.04. The dotted contours show the likelihood that a point in the G_0-n space agrees with the measured [C II]/CO($J = 1 \rightarrow 0$) intensity ratio and its error (see Figure 1.10). The outer contours are at the $\pm 1\sigma$ error levels. The center line is for the most likely points. The dashed contours are similarly plotted for the [OI]/[C II] ratio (see Figure 1.11). These two sets of contours intersect. Their product contours are plotted at 60.8% and 90% likelihood in grey colors. The cross marks the maximum likelihood point, where the associated G_0 and n values are the fitting results. The rectangle shows the $\pm 1\sigma$ error of the fitting.

of the model contours and calculates G_0 and n values and their errors. The algorithm used is a maximum likelihood method based on the given diagnostic quantities and their errors. The procedure is fundamentally a parameter fitting process. Figure 5.2 shows an example of the fitting results and briefly explains the procedure. I have compared my calculation with a web-based calculation program released by the *PDR Toolbox*[1] group after my program was written. The results agree within the quantization errors of the parameter grid of the models.

Diagnostic Quantity Selection

The observational results shown in § 5.1 allow many possible combinations of intensities and intensity ratios that could be used by the overlay method described above to determine G_0 and n from PDR models. Not all diagnostic quantities listed in Table 5.1, however, are suitable to be used for finding G_0 and n. Figure 5.3 shows an example for the source G316.81−0.04 with unsuitable diagnostic quantities plotted. There are two zones plotted in dark color in the Figure. The one to the left is for all the allowable points in G_0-n space based on the C I intensity measurement and its 1σ error; the one to the right is similarly plotted for the $CO(J = 1 \rightarrow 0)$ data. These two zones do not intersect within the ranges of G_0 and n, therefore this pair of diagnostic quantities is not suitable for predicting G_0 and n. Below I discuss why turbulent Doppler velocity differences, beamsize differences, and self-absorption in foreground gas can compromise the utility of some potential diagnostic quantities.

The observed intensities alone are unsuitable for comparison with the models because the gas Doppler velocity used by the models is incompatible with those in

[1]See `http://dustem.astro.umd.edu` for details

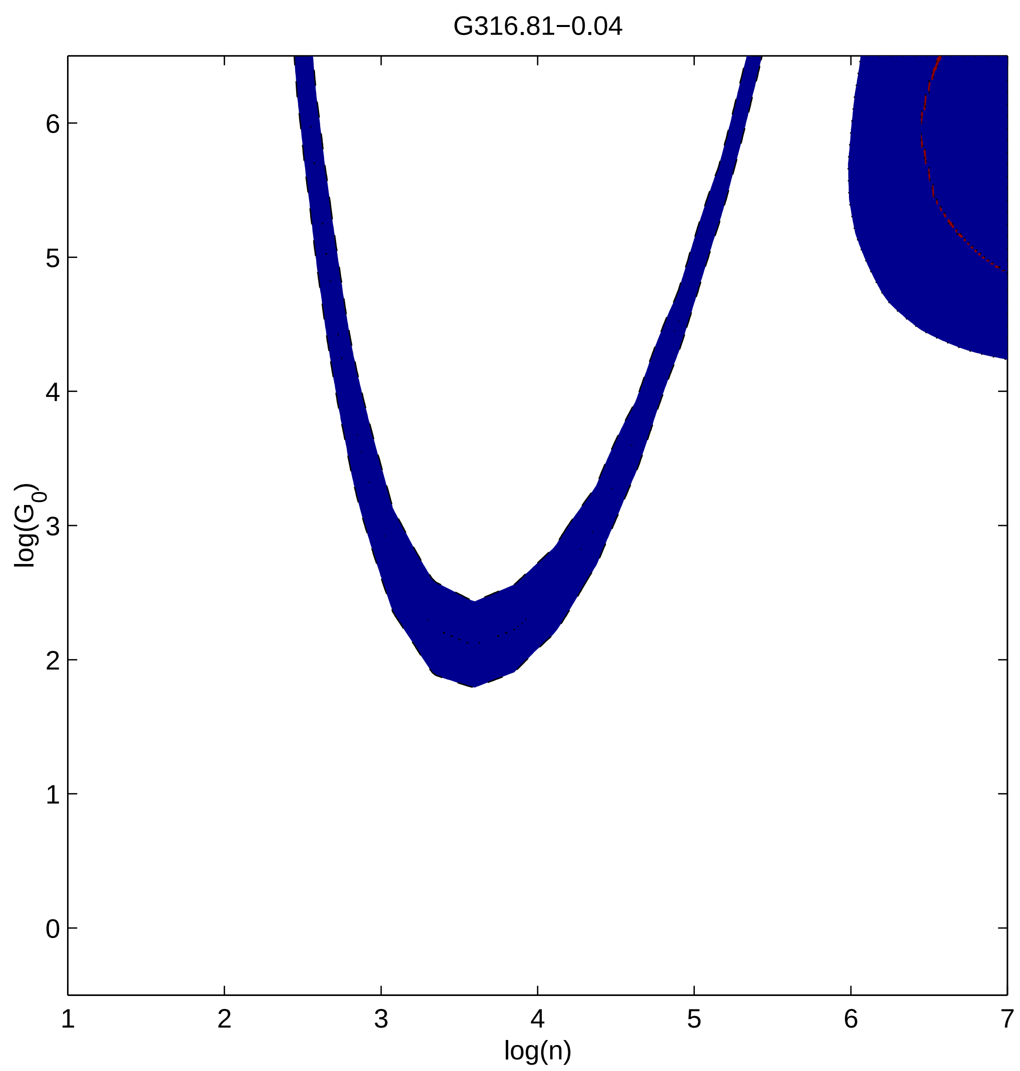

Fig. 5.3.— Not all potential diagnostic quantities are suitable estimators of G_0 and n. See text for details.

my sources, as will be further explained in the next paragraph. An example of the effect of this problem is that 6 of the 12 sources have $\mathrm{CO}(\mathrm{J} = 1 \rightarrow 0)$ intensities greater than 2×10^{-7}, which would indicate that the PDR gas density is greater than $2 \times 10^5\,\mathrm{cm}^{-3}$ (see Figure 1.6). Two of these sources would have $n > 10^6\,\mathrm{cm}^{-3}$. The gas density is a beam averaged quantity. If these densities were real, they would require the gas to fill a region corresponding to the $2.8'$ beam size. At a typical distance of 3 kpc, such a region would have comparable size and mass of the central region of a globular cluster, which is highly unlikely for the ISM near H II regions.

Another example of an inappropriate diagnostic quantity is that the C^+ intensities of all but one of the 11 sources would indicate that the FUV fields are stronger than 2×10^5. Eight of these sources would have $G_0 > 10^6$. These fields are significantly higher than *any* known star formation regions that have strong FUV field such as Orion ($G_0 \approx 10^{4.2}$; Tielens & Hollenbach 1985b) and the inner 5 pc of the Galactic Center ($G_0 \approx 10^{4.9}$; Wolfire, Tielens & Hollenbach 1990). Although these high FUV fields are not impossible to reach in the very close environs of the most luminous young stars, they are about two orders of magnitude too strong given the observed FIR luminosities and H II region sizes (§ 4 and § 5.2).

Using line intensity ratios instead of line intensities as the diagnostic quantities is less problematic. The main cause of the unrealistic values of predicted G_0 and n for line intensities above is that the turbulent velocity of the PDR gas, δv_D, is assumed in the models to be 1.5 $\mathrm{km\,s^{-1}}$ in the Standard Parameters. This is too small for the PDR gas of the H II regions I study. My observations of the linewidths of the optically thin C I emission show that the gas Doppler velocities are on average 6.7 ± 3.0 $\mathrm{km\,s^{-1}}$. If a wider linewidth is used in the PDR model, the intensities tend to increase for all lines that have finite optical depth, for a given pair of G_0 and n (Wolfire 2000). Conversely the predicted G_0 and n will change if the linewidth implemented in the model does not agree with that of the input diagnostic quantities. As diagnostic quantities, line ratios tend to be less affected from such problems. Also note that as observed quantities, intensity ratios are usually less prone to systematic calibration errors between different receivers or detectors and between data taken at different times. So therefore I will use line ratios instead of line intensities for deriving the model predictions of G_0 and n.

Furthermore different instrumental beamsizes make it impossible to calculate appropriate line ratios using ISO and AST/RO data. As described in § 1, one consideration I had when I planned to use AST/RO and ISO to observe the ISO sample of H II regions was that the theoretical beam sizes of the two instruments should match well. The beamsize of AST/RO unfortunately is about $3.8'$ at the C I frequency and $4'$ at the CO($J = 4 \rightarrow 3$) frequency because of problems in the optics. (These beam sizes are about 2.5 times that of the diffraction limits, $\sim 1.5'$). The ISO LWS aperture size at the theoretical diffraction limit is $1.8'$($110''$; see § 2). The actual aperture size is even smaller, at only $1.3'$($80''$). Because the ISO data are taken by single point observations, and the LWS aperture is smaller than the AST/RO beam, it is therefore not possible to match the beams using data processing techniques.

The different beam sizes have caused serious problems in making a diagnostic quantity using the intensity ratios between intensities measured by these two instruments. This problem is exacerbated by the fact that all ISO sources are chosen to be compact. The dilution effect of the AST/RO beam also has a serious impact on the measured intensities of these sources. For example the average C I and C^+ intensity ratio of the sources is $(1.1 \pm 0.7) \times 10^{-3}$. The model prediction of Kaufman *et al*. (1999) would give $G_0 > 10^6$ and $n > 10^6$ cm^{-3}. Both parameters are too large to make astrophysical sense. The standard PDR model calculation of the C I/C^+ ratio as a function of G_0 and n shows that, if the observed ratio could be reduced by a factor of a few from the current values, the G_0 allowed by the model could be smaller than 10^3 and the allowed n could span the entire range (10 to 10^7). These ranges would be close to that found in typical PDRs. An error of a factor of a few introduced by different beam sizes makes this line ratio useless. All other combinations of line ratios which compare ISO and AST/RO data have similar problems. Consequently

I will not select diagnostic quantities from intensity ratios between the data taken by ISO and the data taken by AST/RO or the CO(J $= 1 \rightarrow 0$) data set described in § 4.

Another problem in diagnostic quantity selection is that the [OI] emission line at 63μm is not a good diagnostic quantity to probe the PDR because of the effect of self-absorption. The intensity ratios of [OI] at 145μm and [OI] at 63μm (R_{63}^{145} hereafter) are outside the model range for all but one source. The average ratio for the ISO sources, 2.5 ± 1.1, is more than two times higher than the highest contour (ratio=0.09) in the model. According to the model, all ISO sources would have G_0 stronger than at least $10^{5.5}$, which is again too high. Kraemer, Jackson & Lane (1998) have shown that there is strong evidence for the 63μm[OI] line to be self-absorbed in the foreground molecular clouds in NGC6334. My results are consistent with their conclusion. Because it is impossible to estimate the self-absorption in the 63μm emission without knowing the details of the foreground molecular clouds, I do not use this emission line in my study of PDRs in this thesis.

After considering the above restrictions, the usable diagnostic quantities are the [OI] 145μm line and the [CII] 158μm line ($I_{148\mu}/I_{158\mu}$; hereafter referred to as R_{158}^{145}), the [CII] line-to-continuum ratio ($I_{158\mu}/I_{FIR}$; R_{FIR}^{158} hereafter), and two independent combinations of C I, CO(J $= 4 \rightarrow 3$), and CO(J $= 1 \rightarrow 0$) intensities. This leaves one pair of FIR diagnostic quantities and two pairs of millimeter and submillimeter diagnostic quantities to derive G_0 and n.

Predicted G_0 and n Values from PDR Models

The incident FUV fluxes and hydrogen nuclei volume densities (hereafter n_{ir}) are determined using the FIR emission intensity ratios listed in Table 5.6, with their

TABLE 5.6

PREDICTED G_0 AND n USING FIR EMISSION[a]

source	$I_{[OI]148\mu m}/I_{[CII]158\mu m}$ and $I_{[CII]158\mu m}/I_{FIR}$	
	$\log(G_{ir})$	$\log(n_{ir})$
G291.28−0.71	...	...
G316.81−0.04	2.83 (+0.55,−0.35)	3.48 (+0.50,−0.62)
G322.15+0.61	3.00 (+0.40,−0.25)	3.10 (+0.38,−0.75)
G332.66−0.61	2.83 (+0.42,−0.25)	3.15 (+0.40,−0.77)
G333.29−0.37	3.25 (+0.57,−0.32)	3.65 (+0.37,−0.48)
G336.84+0.05	2.23 (+0.23,−0.40)	2.77 (+0.53,−1.00)
G337.15−0.18	2.20 (+0.27,−0.30)	3.00 (+0.65,−1.00)
G337.95−0.48	2.40 (+0.27,−0.23)	2.93 (+0.50,−1.00)
G340.78−1.01	3.17 (+0.62,−0.40)	3.88 (+0.52,−0.50)
G345.31+1.47	2.53 (+0.50,−1.50)	3.53 (+1.15,−0.50)
G348.71−1.03	3.12 (+0.52,−0.27)	3.38 (+0.35,−0.57)
G353.21+0.91	3.45 (+0.60,−0.30)	3.80 (+0.35,−0.43)

[a] G_0 and n units are 1.6×10^{-3} erg s^{-1} cm^{-2} and cm^{-3}, respectively. Numbers in parenthesis are 1σ errors.

1σ errors. The intensity ratios used are given in the table-heading. The FUV flux and density determined using the C I and CO emission ratios are given in Table 5.7 in a similar format as that of Table 5.6. I will use G_{ir} and n_{ir} to denote the G_0 and n values gotten using the FIR emission tracers, and G_{cc} and n_{cc} for those using the C I and CO tracers. The line ratios used to determine the first pair of G_{cc} and n_{cc} values are $I_{CI}/I_{CO(4-3)}$ (R_{43}^{CI} hereafter) and $I_{CI}/I_{CO(1-0)}$ (R_{10}^{CI} hereafter). The C I and CO(J $= 4 \rightarrow 3$) intensities are those of the map-center spectra. (The meaning of the second pair of G_{cc} and n_{cc} values listed in Table 5.7 is described below in § 5.4.2).

5.4.2. Comparing PDR Models with Other Methods

In this section I compare the FUV flux, G_0, and hydrogen nuclei density, n, predicted by the PDR models with the values for these quantities derived using

TABLE 5.7

Predicted G_0 and n Using Microwave Emission[a]

source	$I_{CI}/I_{CO(4-3)}$ and $I_{CI}/I_{CO(1-0)}$[b]		$I_{CI}/I_{CO(4-3)}$ and $0.5\times I_{CI}/I_{CO(1-0)}$[b,c]	
	$\log(G_{cc})$	$\log(n_{cc})$	$\log(G_{cc})$	$\log(n_{cc})$
G291.28−0.71	3.05 (+1.05,−1.10)	4.70 (+0.10,−0.05)	1.40 (+0.35,−0.28)	5.50 (+0.10,−0.12)
G316.81−0.04	0.55 (+0.15,−0.12)	5.08 (+0.07,−0.10)	0.48 (+0.10,−0.10)	5.62 (+0.03,−0.03)
G322.15+0.61	−0.05 (+0.17,−0.17)	5.60 (+0.05,−0.05)	−0.12 (+0.17,−0.20)	5.92 (+0.05,−0.05)
G332.66−0.61	0.28 (+0.12,−0.12)	5.35 (+0.05,−0.05)	0.25 (+0.12,−0.13)	5.78 (+0.02,−0.05)
G333.29−0.37	0.48 (+0.13,−0.05)	5.17 (+0.05,−0.08)	0.45 (+0.07,−0.10)	5.65 (+0.02,−0.05)
G336.84+0.05	0.58 (+0.28,−0.25)	5.38 (+0.12,−0.12)	0.55 (+0.25,−0.25)	5.83 (+0.05,−0.05)

[a] G_0 and n units are 1.6×10^{-3} erg s^{-1} cm^{-2} and cm^{-3}, respectively. Numbers in parenthesis are 1σ errors.

[b] C I and CO(4-3) intensities are taken from the map center spectra.

[c] C I intensities are multiplied by 0.5. See text for details.

other methods in § 5.2 and § 5.3.

G_0 Comparison

In Figure 5.4 the two sets of G_0 values given in Table 5.6 and Table 5.7 (G_{ir} and G_{cc} respectively) are plotted against those found in § 5.2 (see Table 5.3). All 11 sources observed by ISO and all 6 sources observed in C I and CO emission are plotted. There are only five sources observed both by ISO and by AST/RO in CO($J = 4 \rightarrow 3$) which allow for comparison of G_0 values of the same source.

Several observations and conclusions can be made by studying Figure 5.4. First the dotted line which bisects the quadrant shows that the FUV intensities predicted by the PDR model using the FIR emission ratios generally agree with those found using the L-L_c method. The average difference in $\log(G_0)$ is 0.0 ± 0.5. This is a direct support of the effectiveness of the homogeneous slab PDR theory when it is applied to FIR emission line ratios to find out G_0. Because the PDR models are constructed based on past observations of known PDR regions, the above agreement also suggests that using the L-L_c relation to find out the incident FUV flux on the PDR around H II regions can produce results that are in agreement with past observations of well known PDRs. Secondly, the models are not consistent with the G_{cc} values derived here. In fact, $\log(G_{cc})$ is 2.5 ± 0.5 smaller than $\log(G_{ir})$ on average. This will be discussed in § 5.5 in the context of the spherical PDRs.

n Comparison

Figure 5.5 compares the hydrogen nuclei volume densities n. Plotted are densities derived using the PDR models (n_{ir} and n_{cc}; data taken from Table 5.6

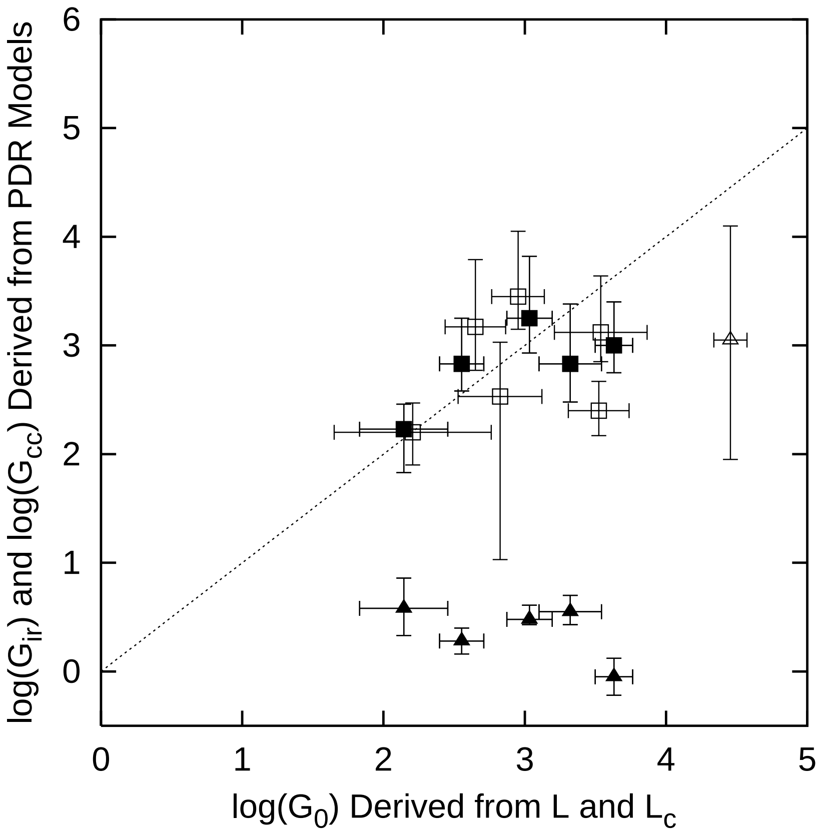

Fig. 5.4.— The G_0 values gotten using PDR models are compared with those derived from the FIR luminosities and Lyman continuum flux. The squares show $\log(G_{ir})$ derived using FIR emission intensity ratios of [OI], [CII], and FIR continuum, as given in Table 5.6. The triangles show $\log(G_{cc})$ derived from C I, CO($J = 4 \rightarrow 3$), and CO($J = 1 \rightarrow 0$) intensity ratios, as given in Table 5.7. There are five sources that have been observed in all tracers. Their square and triangle symbols are filled. The remaining sources use open symbols. The dotted line bisects the quadrant and shows that the FUV intensity predicted by the PDR model using the FIR emission generally agrees with that found using the L-L_c method.

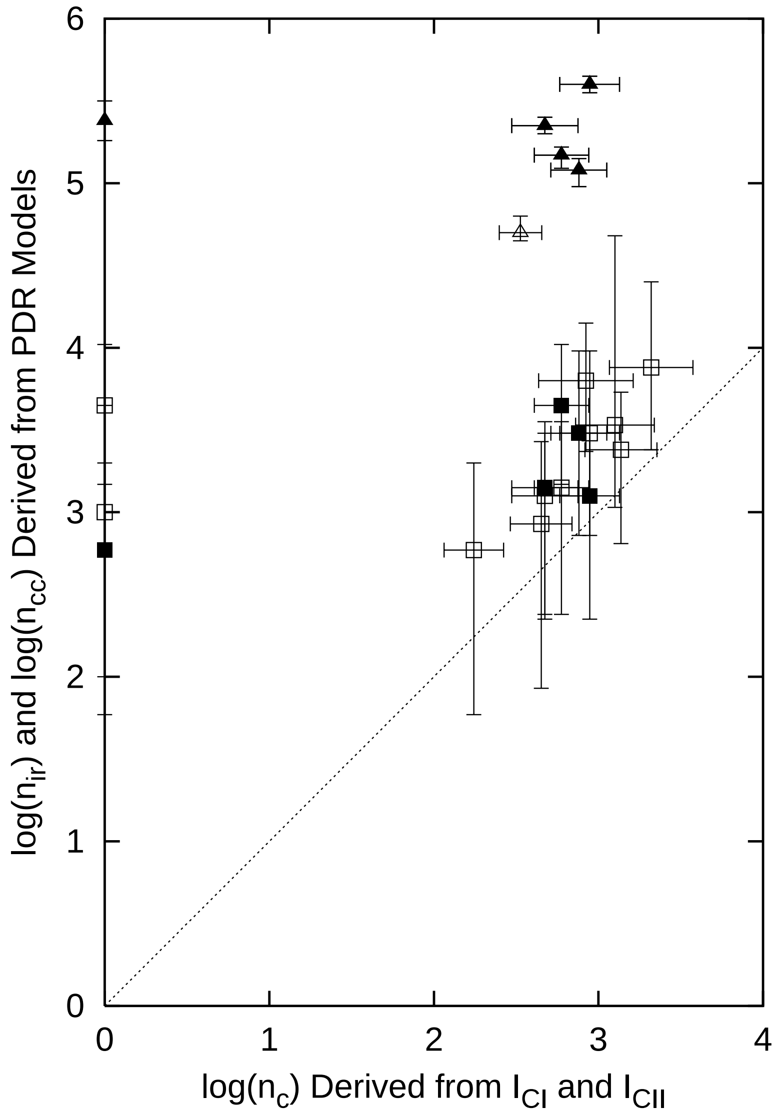

Fig. 5.5.— Volume number densities derived using PDR models ($n_{\rm ir}$ and $n_{\rm cc}$) are compared with that gotten from § 5.3 (n_c). Plotting symbol usage is identical to that in Figure 5.4. The volume densities of C I for G336.84+0.05 and G337.95−0.48 are unavailable due to the complex morphology of their C I distributions. Their densities gotten from PDR models are plotted on the vertical axis. The dotted line bisects the quadrant.

and Table 5.7, respectively) as a function of the density derived using C I and C^+ intensities in § 5.3 (n_c).

Figure 5.5 shows that the average $n_{\rm ir}$ is about two orders of magnitude lower than the average $n_{\rm cc}$: $\log\langle n_{\rm ir}\rangle = 3.3 \pm 0.4$ and $\log\langle n_{\rm cc}\rangle = 5.2 \pm 0.3$. This is very surprising since $n_{\rm cc}$ determinations are for a big beam. One possible explanation is the effect of the different optical depths of C I, CO(J $= 4 \rightarrow 3$), and CO(J $= 1 \rightarrow 0$). It is likely that C I emission is optically thin while the CO(J $= 1 \rightarrow 0$) emission lines are optically thick. If this is the case, assuming that the molecular gas surrounds the H II region so that there are PDRs on both the foreground side and the background side of the H II region, the observer can see C I emission from PDRs on both sides of the H II region. Only the foreground CO emission can be seen, however, because the CO emission coming from the background side is self-absorbed. A factor of 0.5 has been applied to R_{10}^{CI} in Table 5.7 in an attempt to estimate the magnitude of this effect. The fitting results show that after this correction the average $\log(n_{\rm cc})$ is increased by 0.5 ± 0.1. This correction factor is in the wrong direction to account for the two orders of magnitude difference in $n_{\rm ir}$ and $n_{\rm cc}$ cited above. The above can be seen from Figures 1.8 and 1.9: when the line ratios decease, the corresponding n increases. This discrepancy is even greater when considering that the CO(J $= 1 \rightarrow 0$) line is likely to be optically thick (see discussions in § 5.3). As a result it is highly likely that the CO lines have been self-absorbed when they propagate through different parts of the PDR. The observed CO intensities should be stronger if they are not self-absorbed. A correction for CO self-absorption, if applied, would decrease R_{10}^{CI} and R_{43}^{CI}, and make the difference between $n_{\rm ir}$ and $n_{\rm cc}$ even greater. This discrepancy in $n_{\rm ir}$ and $n_{\rm cc}$ will be investigated in § 5.6 where the clumpy PDR models are discussed.

Figure 5.5 also shows that there is an apparent correlation between $n_{\rm ir}$ and n_c: $n_{\rm ir} = (1.0 \pm 0.2) n_c + (0.4 \pm 0.6)$. The correlation shows that except for being too large by a constant offset factor ($10^{0.4\pm0.6} = 2.5$, ranging from 1.6 to 10 within 1σ error), the predictions of PDR models for hydrogen volume density based on the [CII], [OII], and FIR continuum agree with the § 5.3 results. The constant offset factor in the correlation is very likely due to a combination of the difference in the IR and AST/RO beam sizes and under-estimation of hydrogen density in the analysis in § 5.3. The large AST/RO beam in C I is likely to dilute the C I intensity measurement, resulting in an underestimation of N_{CI}, and therefore under-estimation of N_H. Note that this offset factor is relatively small compared with the errors of $n_{\rm ir}$ for the sources. The relatively large uncertainty of this factor could be reduced if the ISO line intensity ratio errors are reduced below their current values of 30%. I conclude that the PDR homogeneous slab models are consistent with the densities calculated using FIR lines, FIR continuum, and AST/RO C I measurements.

5.4.3. About the Published Models

The published PDR models of Tielens and Hollenbach (1985a), Wolfire *et al.* (1990), and Kaufman *et al.* (1999) should be used with caution. These models are used to observations to interpret observational results (e.g., Chokshi *et al.* 1988; Jaffe *et al.* 1994; Steiman-Cameron *et al.* 1997). Usually, satisfactory comparisons between observations and PDR models are obtained when the details of the geometries and physical conditions have been obtained from independent analyses. The homogeneous slab PDR models considered above explained my observational results of the ISO sample of sources with mixed results. They successfully explain the incident FUV fluxes and number densities traced by some of the FIR, [CII], [OI], and continuum tracers. The PDR models do not explain the incident FUV fluxes and number densities traced by C I, CO($J = 4 \rightarrow 3$), and CO($J = 1 \rightarrow 0$) emission very well. The models also fail to explain the oxygen line ratio ($I_{145\mu\mathrm{m}}/I_{63\mu\mathrm{m}}$). Based on my investigation I find that there are particular issues that should be taken care of carefully in order to apply the published PDR models to data: 1) the model is sensitive to the selection of diagnostic quantities because of differences in gas Doppler velocity; 2) the beam sizes of different detectors should match since the input and output of PDR models are beam averaged quantities; and 3) the optical depths of diagnostic quantities should be small.

5.5. Homogeneous Spherical PDR Model

5.5.1. Method to Verify the Spherical PDR Model

In previous chapters (§ 3 and § 4) I showed that both C I and CO(J = 4 → 3) mapping of my sample of H II regions supported spherical PDR model geometries. The support comes from the spatial correlation and LSR velocity coincidence among C I, CO(J = 4 → 3), RRL, and radio continuum observations.

Numerical models that describe a spherical PDR illuminated from a central exciting star (see § 1) do not exsit. Current numerical models have so far basically been limited to treating a homogeneous slab geometry or to embedding spherical "clumps" in ambient FUV radiation (e.g., Stutzki *et al*. 1988; Bolatto, Jackson, & Ingalls 1999). A quantitative model of a spherical PDR has never been constructed or compared with slab PDR models. Such a model requires that one solve for the radiative transfer, ionization and excitation population of all species, chemical networks, and thermal balance simultaneously in a spherical configuration. Constructing such a model is beyond the scope of this thesis.

Even a simplified spherical PDR model that calculates the spatial distribution of

PDR diagnostic quantities could only be schematically verified because of the quality of the observational data available here. The observational results required to verify the spatial distribution accurately need to have high spatial resolution with respect to the size of the PDR. Unfortunately the beamsizes of the AST/RO telescope at the C I and CO($J = 4 \rightarrow 3$) frequencies are $3.8'$ to $4'$, respectively, 2.5 times larger than the $1.5'$ diffraction limit. For the sources I selected for my research the C I beam size is about 1/3 of the average angular size of the C I emission region size. Another factor that hinders precise comparison between models and my data is that the signal to noise ratio at each map point is low (only a few for some sources) due to high receiver noise and limited observing time (both originated from unexpected equipment problems). Data of such angular resolution and signal to noise ratio can only be used to study general trends of the geometry of the PDR.

In this section I will make calculations using a very simplified two-layer model and show that the spherical PDR helps to interpret the observational results unexplained by the homogeneous slab PDR in § 5.4.2.

5.5.2. The Geometrical Dilution Effect

In § 5.4.2 I find that the observationally derived FUV flux is larger than what the homogeneous slab PDR models can explain by 2.5 ± 0.5 in logarithmic scale. Some of this discrepency can be explained by dilution of FUV radiation in a spherical geometry.

My observations allow me to estimate the geometrical dilution factor at the outside border of the C I region. When the FUV radiation leaves the Strömgren sphere and starts to penetrate the PDR, its flux is subjected to the geometrical dilution effect. In § 3 I find that the linear sizes of the C I emitting regions are larger than the size of the H II regions by a factor of 4.1 ± 2.3 on average (see illustration in Figure 1.13). This implies that by the time the FUV radiation reaches the outside border of the C I region the FUV flux would be geometrically diluted by a factor of $(4.1 \pm 2.3)^2 = 18 \pm 5$ on average. In the PDR the C^+/C I/CO transition takes place as the FUV flux decreases. If the outside border of the C I region is taken as the zone where the CO emission reaches its maximum intensity then the bulk of the CO gas would receive 18 times less FUV flux than would the C^+ gas near the surface of the Strömgren sphere. Note that although CO($J = 4 \rightarrow 3$) emission regions have almost the same size compared with C I regions (§ 4), bulk of the CO gas is not traced by CO($J = 4 \rightarrow 3$) emission (see Appendix B), and is expected to exist outside the C I zone.

I assume a "two-layer" model of the spherical PDR to calculate the geometrical dilution effect. The ionized carbon and atomic oxygen emission lines are generally from the warm gas near the exciting star because of their formation and excitation conditions. I assume the FUV flux they receive equals that at the outside border of the Strömgren sphere of the H II region. This FUV flux is calculated in § 5.2. The C I and CO layers of the PDR are found further away from the exciting star, with the CO layer being more distant. I assume that the FUV flux that these species receive has been geometrically diluted. In the previous sections I derived the FUV fluxes predicted by the homogeneous slab PDRs using the FIR dust, C^+, and oxygen tracers (G_{ir}) and that using C I and CO tracers (G_{cc}). I assume the homogeneous slab PDR model applies in each of the two layers described above. Therefore I can examine the effectiveness of my model by comparing G_{ir} with G_{cc} corrected by a geometrical dilution factor of $(D_{CI}/D_{HII})^2$, where D_{CI} and D_{HII} are the sizes of the C I emission region and the Strömgren sphere as given in Table 3.5.

I find that the geometrical dilution effect can help explain part of the discrepancies between G_{ir} and the FUV field derived from the L-L_c relation. Figure 5.6 compares the uncorrected G_{ir} (open circles) and the corrected ones (solid circles) for the sources. It can be seen that the corrected FUV strengths are closer to those calculated from the L-L_c relation (as shown by the dotted line). The difference between $\log(G_{ir})$ and the $\log(G_{cc})$ corrected by the geometrical dilution factors is 1.4 ± 0.2, a definite improvement when compared with the uncorrected difference which is 2.5 ± 0.5. Although the geometrical dilution effect cannot account for all the difference, the improvement is a support for the spherical PDR geometry in this sample of sources. Note that on average the D_{CI}/D_{HII} ratio would need to be 4.3 times larger than the observed value to account for all the difference. This is unlikely given the errors of the observations. Larger C I maps and smaller radio continuum beams, however, can certainly help determine the D_{CI}/D_{HII} ratio more reliably.

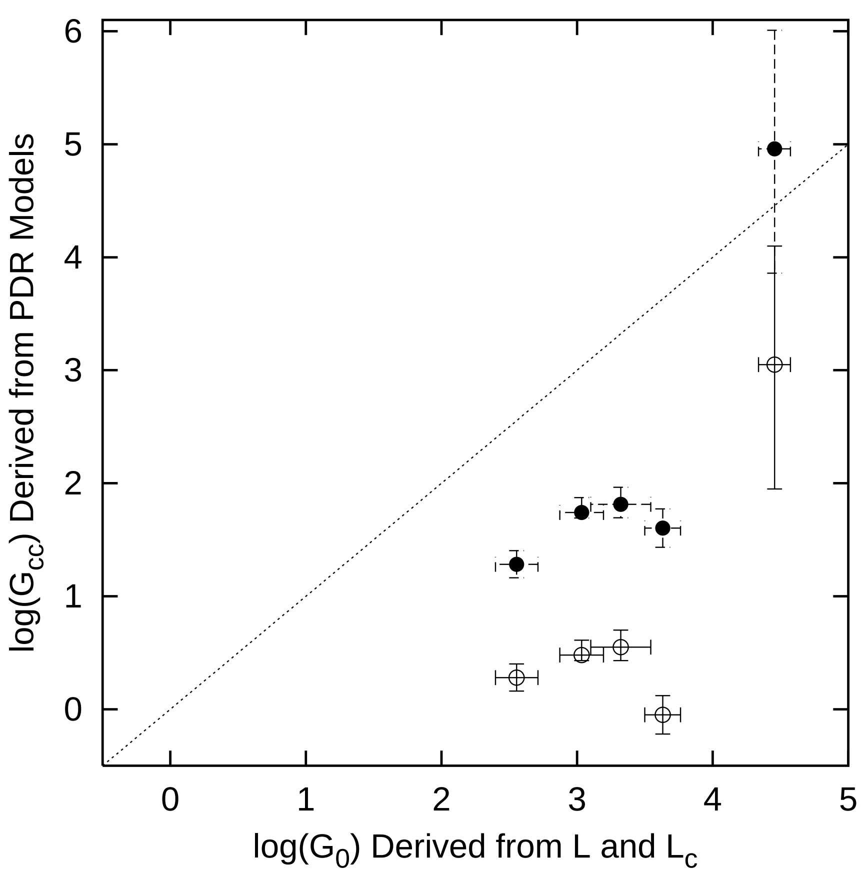

Fig. 5.6.— The FUV fluxes (G_{cc}) are plotted against those derived from the luminosities in § 5.2. Plotted points include the FUV fluxes corrected for the geometrical dilution effect (filled circles) and those uncorrected (open circles). The details of the correction are discussed in the text. Only five of the six sources observed in CO($J = 4 \rightarrow 3$) are plotted. This is because the morphology of the C I map of G336.84+0.05 is too complex to fit a Gaussian. As a consequence the correction factor cannot be calculated. The dotted line bisects the quadrant.

5.6. Clumpy PDRs

In this section I will show that the clumpiness of PDRs can help explain the observational results of the hydrogen nuclei density, n, which cannot be explained by the homogeneous slab PDRs found in § 5.4.

5.6.1. Previous Evidence for Clumpiness

Clumpiness has been studied in PDRs by various authors (e.g., Stutzki *et al.* 1988; Stutzki 1990; Meixner *et al.* 1992; Meixner & Tielens 1993). In § 4 I concluded that C I and CO($J = 4 \rightarrow 3$) emission regions are likely to be clumpy. This is supported by several pieces of evidence. First, in § 3 I find that the sizes of the C I emission regions are on the scale of 10 pc, about 4 times larger than the sizes of the ionized hydrogen regions. This extensive distribution of C I over many parsecs into the PDR is in agreement with past observational results and corresponding conclusions that the PDRs are clumpy (Keene *et al.* 1985; Genzel *et al.* 1988). Secondly, in § 4 I find that the emission region sizes of C I and CO are nearly identical. The average ratio of C I and CO($J = 4 \rightarrow 3$) emission region sizes is 1.2 ± 0.1 for the observed sources. This small size difference between the C I and CO($J = 4 \rightarrow 3$) regions is small compared with that between the C I region and the ionized region. Since the homogeneous slab PDR models predict that the CO emission region extends further away from the FUV source, the CO emission regions should be in a shell outside the C I region (see Figures 1.1 and 1.13). The identical sizes of CO($J = 4 \rightarrow 3$) and C I gives a strong support for the clumpy PDR theory. Furthermore my observations of the kinematics of C I and CO($J = 4 \rightarrow 3$) show that the LSR velocities of the two species are identical and that their linewidths are highly correlated. Altogether, these results suggest that neutral and molecular carbon species are mixed together. These results agree with the notion that the PDRs are clumpy in my source sample.

5.6.2. Density in the PDR

In § 5.4.2 I find that the density predicted traced by the FIR tracers ($n_{\rm ir}$) is about two orders of magnitude lower than that predicted from C I and CO observations ($n_{\rm cc}$) on average: $\log\langle n_{\rm ir} \rangle = 3.3 \pm 0.4$ and $\log\langle n_{\rm cc} \rangle = 5.2 \pm 0.3$. In the following I argue that clumpiness of the PDR can help explain this discrepancy. Meixner & Tielens (1993; also see § 1 and Figure 1.12) investigated clumpy PDR models which were tailored for the M17SW H II region. The FUV flux is fixed at 5.6×10^4. Therefore it is not possible to predict G_0 and n quantitatively as in § 5.4.

In a clumpy PDR dense clumps exist in a more tenuous inter-clump medium. For example Meixner *et al*. (1992) have modeled the M17SW PDR region and found that the data can be explained by a clumpy PDR that has a clumpy core submerged in a molecular cloud. The clumpy core has clumps of density of $5 \times 10^5\,\mathrm{cm}^{-3}$ and an inter-clump medium with a density of $3000\,\mathrm{cm}^{-3}$. The ambient molecular cloud has a density of $300\,\mathrm{cm}^{-3}$. In the clumped PDR where the C^+, C I, and CO are mixed, CO exists mostly in the dense clumps where dust opacity and CO self-shielding is so strong that they prevent FUV radiation from dissociating CO. Since the critical density of CO($J = 4 \rightarrow 3$) is $8 \times 10^4\,\mathrm{cm}^{-3}$ (Schulz *et al*. 1995), it is sensitive to dense gas found in the clumps. As a result the density predicted by C I and CO, particularly CO($J = 4 \rightarrow 3$), tends to reflect the high density of the clumps. In Appendix B the CO($J = 4 \rightarrow 3$) emission is found to be optically thin within the beam. This does not contradict the fact the CO($J = 4 \rightarrow 3$) is optically thick within the clumps. This is because in clumpy CO gas the optically thick CO($J = 4 \rightarrow 3$) emission is mainly from the surface of the clumps, and therefore will not fill the telescope beam. The apparent low optical depth of CO($J = 4 \rightarrow 3$) is a result of low beam filling factors.

Assuming that the CO($J = 4 \rightarrow 3$) emission is optically thick in the clumps, the lower limit of the clump volume filling factor can be estimated. From the average optical depth found in Appendix B (0.12 ± 0.07, assuming 50K excitation temperature), the beam filling factor is 0.12. If the mean free path for photons in the optically thin inter-clump media is larger than the PDR size along the line of sight (i.e., the opaque clumps do not block each other along the line of sight), the lower limit of the clump volume filling factor can be estimated by assuming there are m identical clumps in the beam, then the volume filling factor is $m(0.12/m)^{1.5}$. For the values of m to be from 10 to 1000, the dense CO gas would only occupy a tiny fraction, 1% to 0.1%, of the volume. The size of the clumps would range from 10% to 1% of the beam size. Given a typical distance of 3 kpc for the H II regions sample, this size corresponds to about 0.2pc to 0.02pc ($10^{18\sim17}$ cm). In order for CO to survive in such small clumps, the optical depth of the clump should be at least 4 to 5. This minimum optical depth translates into $10^{22}\,\mathrm{cm}^{-2}$ minimum hydrogen nuclei column density inside the clumps. This minimum gas volume density in the clumps needs to be $10^{4\sim5}$ cm^{-3}, given the $10^{18\sim17}$ cm clump size. From Figure 5.5, it can be seen that these densities are one to two orders of magnitude higher than n_c on average. Compared with the average n_{cc} ($\sim 10^5\,\mathrm{cm}^{-3}$). This clumpiness correction is in the right direction and comparable magnitude. Therefore I conclude clumpiness of the PDR can help reconcile the discrepancy found in applying the homogeneous slab models to my observational data.

5.7. PDRs in Reality

High resolution images of optical H II regions show that the morphologies of dust and gas clouds near the ionized regions are very complex. Filaments, arches, "fingers", clumps, globules, and other fractal shaped aggregations abound.

In previous sections I show that all three kinds of PDR models are needed to explain all the aspects of my observational data: the homogeneous slab models, the spherical models, and the clumpy models. The homogeneous slab models are shown to be able to explain the FIR data. The difficulty in applying the spherical and the clumpy PDR models to my data is mainly in the lack of full fledged numerical models and in the observational data taken with a beam that is not much smaller than the size of the PDR. Even with the lack of accurate treatment, the discussion in § 5.4 has shown that the spherical and the clumpy models need to be invoked and give improvement over the simple homogeneous one dimensional slab model.

The above observations suggest that: 1) the PDRs around the H II regions are generally spherical in global structure, as shown in § 5.5 using the tracers that exist relatively deeper in the PDR or at large optical depths; 2) the global structure does not necessarily mean all physical processes need to be treated in a spherical geometry. The FIR tracers can be well described by the homogeneous slab PDR model of Kaufman *et al*. (1999). This implies that these tracers are found in layers close to the ionized region with small optical depths, so the physical state of this gas is close to that found in a homogeneous slab. Hence the observed emission characteristics of these FIR emitters is well described by a geometry of semi-infinite slabs; and 3) the global geometry may not be strictly layered or spherical as suggested in Figures 1.1 and 1.13. Clumps and other isolated, denser gas components may exist throughout the PDR, as suggested in § 5.6. The C^+/C I/CO interfaces are neiher smoothly planar nor concentrically spherical structures. The local structure of PDR gas is much more complex than the global structure.

These conclusions are illustrated in Figure 5.7, which shows a schematic diagram of such a PDR: it is globally spherical, appears "flat" or slabby when observed in FIR tracers, but has an abundance of clumpiness in the entire region.

5.8. Summary

In this chapter I first compile observational results from the studies of previous chapters. Then I derive for the ISO sample the FUV flux, G_0, using the FIR total luminosities and the Lyman continuum photon fluxes obtained from RRL and radio continuum observations (Caswell & Haynes 1987). The major assumptions are: 1) incident FUV fluxes on the PDR surrounding the H II regions are solely produced by the central exciting star(s); 2) the boundary between the ionized gas and the PDR gas is the surface of the Strömgren sphere; 3) the stellar spectrum can be described by a blackbody; and 4) a minimum number of O stars exist in the H II region to account for the observed total luminosities and the Lyman continuum photon fluxes. The first assumption is strongly supported by the correlation between the H II regions' luminosities and the OB stars' L-L_c relation. This is the first time that the total luminosity and the Lyman photon flux of a sample of H II regions is compared with the stellar properties (calculated by Vacca *et al.* 1996). I point out that the "test bed" sources used to establish the major PDR models are too strong in FUV flux density when compared with those found in typical Galactic H II regions.

I estimate the density of hydrogen nuclei, n, for the ISO source sample using the observed carbon species intensities. I show that CO, C^{++}, and other carbon-bearing species do not contribute to the carbon nuclei column density, N_c. The column

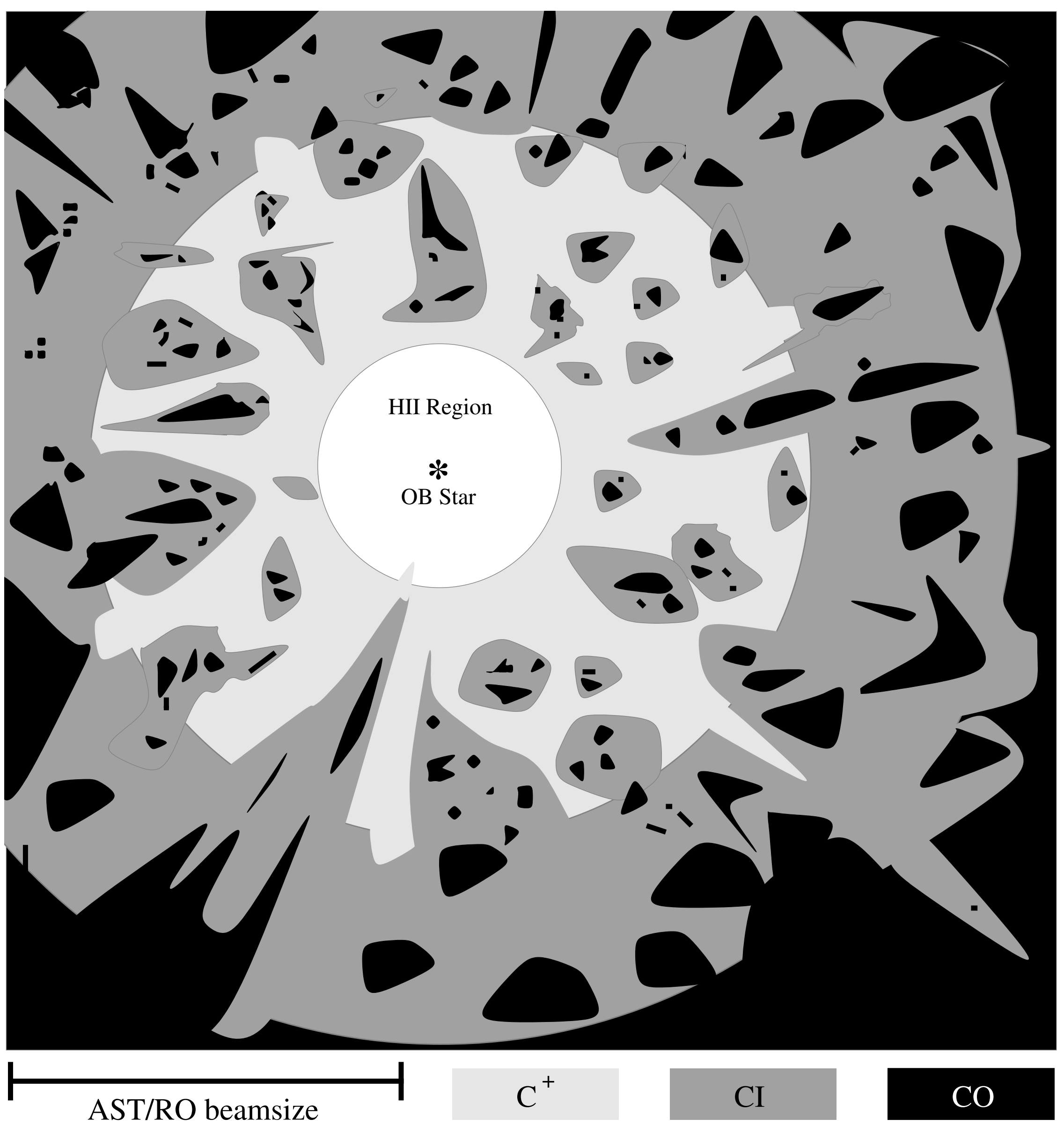

Fig. 5.7.— Schematic diagram for a spherical clumpy PDR. Compared with Figure 1.13, clump cores of dense C I and CO gas are found in the C^+ regions. The borders of the C^+/C I/CO transition zones are no longer strictly spherical. "Fingers", filaments and clump cores of different sizes add irregularities to these zones. In most clump cores there are dense molecular clumps and less dense atomic inter-clump media.

density of CO is an order of magnitude less than that of C I. I estimate gas density for the PDRs based on N_c ($\langle N_c \rangle \approx 1000\,\mathrm{cm}^{-3}$), which appears to be lower than many "test bed" sources.

I select a set of diagnostic, observed quantities of the sources and use them to calculate model-predicted G_0 and n values. I examine the homogeneous one-dimensional PDR models by comparing the model predicted G_0 and n values with those obtained using other methods described previously in the chapter. The models do not give consistent G_0 and n values using different sets of quantities. I find the predicted G_0 and n values agree with those found using the FIR tracers within the errors. The difference for G_0 is 0.0 ± 0.5 in log scale on average, and 0.4 ± 0.6 for n. The predicted values of G_0 and n both deviate from those gotten using other methods by more than two orders of magnitude. I give comments on the reliability of the published PDR models and point out factors which can compromise an analysis of physical properties of PDRs.

I use a two-layer simplified model to show that the spherical PDR model can help resolve the discrepancy in G_0 which cannot be explained by the homogeneous slab PDR model. The average difference is reduced from 2.5 ± 0.5 to 1.4 ± 0.2 in logarithmic scale. The published clumpy PDR models by Meixner & Tielens (1993) are not helpful in my study because their models have a fixed FUV flux. I argue that clumpy PDR models would be helpful in solving the discrepancy in n. I show that my observational data allow clumps with gas densities of at least $10^{4\sim5}$ to exist. The PDR prediction made using C I and CO tracers may reflect mainly the denser clump gas.

Based on my investigations I describe a general picture of PDR around H II regions. The typical H II region PDR must: 1) be globally spherical; 2) appear "flat" or slabby when observed in FIR tracers; and 3) possess an abundance of clumpiness which exists throughout the entire PDR zone.

5.9. Conclusions, Astrophysical Context, and Future Work

5.9.1. Conclusions

In this section I summarize the major conclusions in the 5 chapters of this thesis.

In chapter one I summarize important concepts and theories about H II regions and PDRs. I identify the limitations of current PDR studies, and point out that a sample of H II regions with a wide range of excitation conditions could help overcome these limitations. I discuss how I intend to compare my observations with PDR models. I describe the two source samples for my thesis. Both are samples of relatively isolated compact sources selected from RRL catalogs. I then describe the AST/RO telescope system. My contributions to building AST/RO constitute a significant part of my dissertation research.

In chapter two I present my results of observations using the Long Wavelength Spectrometer (LWS) on-board the ISO satellite. After describing the fundamentals of the satellite and LWS, I discuss in detail the problems in calibration and post-pipeline data reduction. I present the measurement results of the intensity of C^+ and [OI] emission lines as well as the FIR continuum. I calculate important intensity ratios and use IRAS FRESCO maps to derive the total luminosities of the H II region sample. I calculate the upper limit to the FUV flux and the line-to-continuum ratios. On average they are $1.5 \pm 3.0 \times 10^6$ G_0 and 0.0046 ± 0.0019, respectively. I find the dust temperatures do not vary significantly within the sample (44 ± 4K).

In chapter three I present the results of observing C I in the two samples of

H II region sources using AST/RO. The first sample is comprised of 49 southern hemisphere H II regions. They are observed in single-point mode. This is by far the largest sample of H II regions observed in C I. C I emission is detected in all sources. The high quality spectra show that the mean LSR velocity difference between the C I and RRL emission is 0.8 ± 2.8 km s^{-1}. Within the measurement errors this is exact agreement in velocity. I identify C I emission components that associated with the H II region, and conclude that all H II regions have associated C I emission. The basic C I spectral parameters are obtained: the mean linewidth and line temperature are 6.7 ± 3.0 km s^{-1} and 2.4 ± 1.8K, respectively. Comparison of emission properties of the C I components associated with the H II regions with those unassociated shows that the C I intensity is dominated by local heating. The second sample of H II regions, the ISO sources, are mapped in C I. After checking the consistency between the observational results of the two samples, I find that both the spatial distribution and LSR velocity of C I gas coincides with the 5 GHz radio continuum peaks. I argue that this is support for a spherical PDR geometry. Using the maps, I derive the size of the C I emission region to be 10 ± 7 parsecs, 4.1 ± 2.3 times the H II region size. I argue that C I emission is optically thin and calculate the C I column density to be $\langle N_{CI} \rangle = 2.2 \pm 1.7 \times 10^{17}\,\mathrm{cm}^{-2}$.

In chapter four I report AST/RO CO mapping observations of the ISO sources. Although the observations were not complete, data analyses still show some useful results. For example, the average CO(J $= 4 \rightarrow 3$) brightness temperature is 3.2 ± 0.7 times brighter than the C I emission. Furthermore, the spatial distribution and line velocities of CO(J $= 4 \rightarrow 3$) emission coincide with those of C I and H II within the errors, again lending strong support to a PDR spherical geometry. I compile CO(J $= 1 \rightarrow 0$) observational results from Whiteoak, Robina & Rennie (1982). A strong correlation in linewidth between CO(J $= 4 \rightarrow 3$) and C I emission is found.

Overall, the correlation between CO($J = 1 \rightarrow 0$) and C I is weaker than that between CO($J = 4 \rightarrow 3$) and C I, probably due to optical depth effects in CO($J = 1 \rightarrow 0$). The linewidths of all C I and CO emission are found to be correlated with the excitation parameter, U, of the H II regions: FWHM linewidth = (0.045 ± 0.07) U + (2.3 ± 0.7), where the linewidth, FWHM, is in units of $\mathrm{km\,s^{-1}}$ and U is in $\mathrm{cm^{-2}}$ pc. From this I derive an extrapolated linewidth of 2.3 ± 0.7 $\mathrm{km\,s^{-1}}$ for ISM gas that is not disturbed by an H II region.

In chapter 5 I investigate the FIR total luminosities and the Lyman continuum photon fluxes of the H II regions and compare them to the OB star models of Vacca *et al*. (1996). I derive the stellar contents of the H II regions and calculate the incident FUV flux on their ambient PDRs. Then I calculate the gas density in the PDR. I conclude that within the C I emission regions C^+ gas is more abundant than C I, which is in turn one order of magnitude more abundant than CO. I point out that the current PDR models are based on H II region samples that are not typical in their FUV fluxes and densities, when these quantities are compared to the values found for most Galactic H II regions. After selecting a set of PDR diagnostic quantities, I calculate predicted FUV flux, G_0, and gas density, n. I find the homogeneous slab PDR models explain well the data gotten using FIR tracers. These models do not explain the results based on C I and CO observations very well. I show that the discrepacies in G_0 can be partly explained by a spherical PDR geometry, and the clumpy PDRs can help to interpret the discrepancies in n. Based on my comparisons of models and data, I describe a general picture of the PDR that is globally spherical, clumpy, and can appear "slabby" when observed in FIR tracers.

5.9.2. Astrophysical Context and Future Work

Astrophysical Context

This thesis attempts to answer these questions: what are the properties of ionic (C^{+}), atomic (C I), and molecular (CO) carbon in photodissociation regions (PDRs) near H II regions? How do young OB stars and the H II regions they create influence the properties of the PDR? Can the PDR models self-consistently explain the PDR conditions found for a large sample of H II regions that has a wide range of excitation conditions? To answer these questions, I summarize theoretical groundwork, describe my observations, process the data, analyze, and discuss the results in 5 chapters. The findings in these chapters are summarized in the previous section.

First of all, most of the conclusions found in this thesis are based on studying a sample of H II regions that has a wide span of excitation. This is the first time that the properties of ISM near H II regions are studied using such a source sample, and using all the ionic, neutral, and molecular carbon species. Furthermore all observations are carried out uniformly (or attempted to be). Past studies focussed on individual sources. Even if some results found in this thesis were found in previous studies of individual sources, my results are a significant step forward because they provide a more complete general description of the ISM influenced by H II regions.

I find that for my H II region source sample the gas densities are $1000\,\mathrm{cm}^{-3}$ and the FUV fluxes a few times 10^{3} stronger than the local average FUV flux. Both the spatial distributions and kinematic properties of all the carbon species center around those of the ionized gas in H II regions. This result is best explained by a spherical PDR geometry. This distribution of gas properties shows the influence of H II regions on the ambient ISM. In the C I region the abundance of the ionized carbon is greater than that of the neutral carbon, which in turn is more abundant than CO by an order of magnitude. This clearly shows that H II regions dissociate surrounding molecular gas into neutral and ionic species. The influence of the H II region also manifests itself in the thermal and mechanical energy it injects into the surrounding ISM. This is shown by the correlation between the emission linewidths and the excitation strength (U) of the H II regions.

The widely used homogeneous slab PDR models (Tielens & Hollenbach 1985a; Hollenbach, Takahashi, & Tielens 1991; Wolfire, Tielens & Hollenbach 1990; Kaufman *et al*. 1999) do not produce self-consistent results for all species I have observed. They appear to work for the FIR tracers which tend to exist close to the H II regions. Both the geometric dilution effect on the FUV radiation field as well as the clumpy density distribution of the neutral and molecular species need to be considered when interpreting the observational results.

Past Lessons and Future Work

This research has been plagued by instruments that fail to work as promised. A large amount of time and a significant part of the uncertainty in the research results are due to this unfortunate fact. Future studies should on one hand make every effort to obtain data of good quality, and on the other hand be conservative in using new instruments. Specifically, the beam sizes, pointing, calibration, etc. of most of the instruments used in my study could be improved. Observational results for the originally proposed ISO source list would allow for a more convincing analysis of the relationship between H II region excitation conditions and the properties of the PDRs.

Fully self-consistent numerical models of the PDR gas that employ spherical geometry and clumpiness are needed to study "real life" PDRs. The current slab models are good for studying:

1. sources of well known slab geometry;
2. a small part of the PDR with small beams so that the area being studied can be treated as if in a homogeneous geometry; and
3. use only FIR tracers, as shown in this thesis.

Conversely, if a source that is little known is to be studied using the published homogeneous slab PDR modles, it is best to choose tracers that are optically thin and at FIR wavelengths. The CO($J = 1 \rightarrow 0$) transition, although widely used for Galactic and extra-galactic studies, is not a suitable tracer for studying individual sources due to its high optical depth and low critical density.

The connections between the properties of the H II regions and those of the PDRs are only weakly made here. The G_0 value estimates based on the assumptions listed in § 5.2 appear crude and may contain some unkown systematic errors. This in fact is a problem with most current PDR model studies. Detailed treatment of the FUV field can be calculated in the CLOUDY package (Ferland 2000; also see `http://www.pa.uky.edu/~gary/cloudy`) using the ISO atomic and ionic data including that of oxygen and nitrogen. A unified model that incorporates the frameworks of CLOUDY and the basics of the homogeneous slab PDR models, a range of Doppler turbulent velocities, customized geometry, and a semi-analytical treatment of the clumpiness (Stutzki *et al*. 1988; Bolatto, Jackson, & Ingalls 1999) appears to be a reasonable next step in the evolution of PDR models.

Chapter 6

Appendix

A. Software for Telescope Servo System

AST/RO Technical Memorandum #32 v1.3

May 2000

Software for Telescope Servo System

Maohai Huang
Department of Astronomy
725 Commonwealth Ave.
Boston, MA 02215

Abstract

This memorandum describes the software servo system used on AST/RO. The tracking program `tracker` controls the movement of the telescope. The form and parameters of the Ramp Function are described and discussed. The user can change these parameters to fine-tune the responsiveness and stability of the telescope. The optical telescope and the `rc` command can be used to observe the dynamic properties of the telescope.

A.1. The Drive System for AST/RO

The AST/RO drive system controls the motion of the telescope. Several levels of servo loops keep the telescope pointing and tracking accurately and smoothly. The block diagram in Figure A.1 shows the structure of the servo loop that includes the computer, the Drive Box, the motor, and the encoders (*loop 1* here after) and the servo loop comprises the amplifier, the Servo Circuits, the motor, and the tachometer (*loop 2* here after).

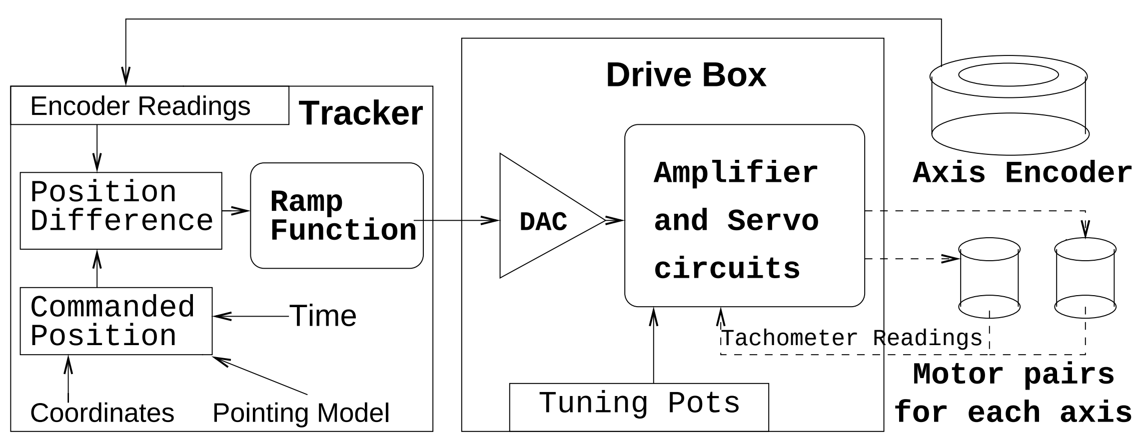

Fig. A.1.— Block diagram of the servo loops of AST/RO. The servo loop that comprises the amplifier, the Servo Circuits, the motor, and the tachometer (*loop 2*)is drawn in dashed lines. The servo loop structures are shown only for one axis.

For *loop 1*, the program `tracker` running on the AST/RO control computer reads the axis encoders to obtain the position of the telescope and sends angular velocity commands to the Drive Box. The Drive Box translates the command to the amount of current that powers the axial motor pairs for each of the azimuth and elevation axis.

The hardware servo circuits in *loop 2* keep the motor following to the angular velocity commanded by the computer as closely as possible. Tuning of the hardware servo using the potentiometers on the Drive Box circuit-boards can be crucial to the telescope pointing and tracking performance. Details of this hardware servo loop fall beyond the scope of this memorandum and hence will not be discussed here. The behavior of this loop is hereby simplified to be: A) when the telescope is slewing at a steady speed, the speed of the telescope rotation is proportional to the angular velocity command the computer sends to the Servo Box; B) when the telescope is accelerating or decelerating, there exists a difference between the real angular velocity of the telescope and the computer's angular velocity command. This angular velocity difference (hereafter referred as ω_{diff}), when fed into the hardware servo loop, results in a proportional amount of current flowing through the drive motors. The sign of this current is chosen such that ω_{diff} will be decreased. Assuming the torque generated by the motors is proportional to the current flowing through them, point B implies that ω_{diff} is proportional to the acceleration of the telescope rotation:

$$\frac{d\omega}{dt} = -A\omega_{diff} \tag{A1}$$

where A is a positive constant. This relation will be used in §A.3 to develop the Ramp Function in `tracker`.

A.2. The `tracker` program

The telescope motion control software, `tracker` (named as `ntracker` for AST/RO), controls the pointing and tracking of the telescope. Most of `tracker` runs in a perpetual loop that repeats every 10 milliseconds. In every cycle, `tracker` calculates the difference between the current telescope position and the commanded telescope position and then sends out an angular velocity command to the telescope drive system in order to minimize this difference. `Tracker` runs as a separate process from the program *OBS*, communicating with *OBS* using the *shared memory* mechanism provided by the operating system.

In every cycle `tracker` calculates the commanded telescope position using the current time, the coordinates of the object, and the pointing model. Then `tracker` reads the telescope axis encoders to obtain the current position of the telescope for both the azimuth and elevation axes. The encoder positions are compared with the commanded position to derive a *position difference* for each axis. In addition, `tracker` also uses the current telescope position and the positions in a number of previous cycles to calculate a *measured angular velocity* (Ω_m) of the telescope.

The *position difference* and the *measured angular velocity* of the telescope are used to calculate the *angular velocity command* using the Ramp Function. The Ramp Function is described in the next section. The *angular velocity command* is in the format of the input to a 16-bit Digital-Analog Convertor (DAC) used in the motor Drive Box. The output of this DAC is amplified in the Drive Box and then sent to the drive motors of the telescope.

A.3. The Ramp Function

In order to keep the telescope movement smooth, responsive, and stable, a function is developed to calculate the commanded velocity for the telescope according to the telescope status. This function is implemented in the Ramp Function.

Two pieces of information are provided by `tracker` to the Ramp Function for each axis. One is the current Ω_m. The other is the current *position difference*, i.e. how much difference there is between where the telescope is pointing (denoted by p), and where the computer wants the telescope to point (denoted by p_{cmd}).

The Formula

The formula to calculate the angular velocity command is:

$$\omega_{cmd} = \mathtt{sign}(p_{cmd} - p) \cdot M \cdot S \cdot |p_{cmd} - p|^{\gamma} + D \tag{A2}$$

where ω_{cmd} is the angular velocity command, the sign function $\mathtt{sign}(p_{cmd} - p)$ takes the sign of $(p_{cmd} - p)$, p_{cmd} is the position to which the computer wants the telescope to point to, p is the real position of the telescope provided by the telescope encoder, M is the maximum input that the DAC in the Drive Box accepts (M=`0x7fff`), S is a scaling factor, and D is a damping term.

The exponent, γ, in Equation A2 allows for fine-tuning of how steeply the commanded velocity increases as a function of $(p_{cmd} - p)$. This power-law form of the Ramp Function allows the commanded velocity to be small when the position difference is small and accelerates the telescope quickly when the destination is far from the current position. It can be shown that if a constant torque is to be maintained throughout the acceleration period γ should be 0.5. In practice the value of γ is usually determined by tracking stability considerations (see §A.3).

The value of ω_{cmd} remains at the maximum, M, when the position difference is larger than a maximum ramp-up distance. This maximum ramp-up distance, denoted by R_m, is pre-selected and is used to calculate the value of S:

$$S = \frac{1}{R_m^{\gamma}} \tag{A3}$$

For the azimuth axis $R_m \approx 6\,^{\circ}$. The elevation axis has a smaller rotational inertia so $R_m \approx 4\,^{\circ}$. When the destination point is farther than R_m, the velocity command is $\pm M$. The sign of M is determined by the desired rotation direction.

Servo Stability

For each axis, there is the relation described in Equation A1:

$$\frac{d\omega}{dt} = -A\omega_{diff} = -A(\omega - \omega_{cmd}), \tag{A4}$$

where ω is the angular velocity at which the telescope rotates. If a linear relation is used to approximate the behavior of the Ramp Function when $(p_{cmd} - p)$ changes from 0 to a certain small number p_s, then the software servo can be seen as if it were providing the telescope a torque proportional to negative p_s. This can be expressed as:

$$\omega_{cmd} = B(\gamma)(p_{cmd} - p), \tag{A5}$$

where $B(\gamma)$ is a positive value:

$$B(\gamma) = \frac{M \cdot S \cdot p_s^{\gamma}}{p_s} = \frac{M \cdot p_s^{\gamma}}{R_m^{\gamma} \cdot p_s}. \tag{A6}$$

Note that when p_s is small compared with R_m, $B(\gamma)$ decreases as γ increases.

Given that:

$$\frac{dp}{dt} = \omega \tag{A7}$$

and

$$\frac{d^2p}{dt^2} = \frac{d\omega}{dt}, \tag{A8}$$

then from Equations A4 and A5 we have:

$$\frac{d^2p}{dt^2} + A\frac{dp}{dt} + AB(\gamma)p = AB(\gamma)p_{cmd}. \tag{A9}$$

The above equation has oscillatory solutions when $A < 4B$. Since A is related to the amplification of the hardware servo and the rotational inertia of the telescope, it is basically not affected by the changes in S and γ. Therefore $B(\gamma)$ is critical in determining the stability of the solution. From Equation A6 it can be concluded that *if either γ or R_m is too small, the telescope will become unstable.*

A rigid servo loop (i.e. large B) means that the telescope has a quicker response to tracking errors and new commanded positions. But the response of the AST/RO telescope and the hardware servo could become unstable with a servo loop that is too rigid. This instability shows in the form of an oscillatory behavior when the telescope is instructed to move to a new position. The telescope would vibrate before settling down to a new position, or in severe cases, never stop vibrating. Sometimes the vibration can be so strong that it could be felt in the control room, or it can be as subtle as an elusive intermittent oscillation which is difficult to track down.

The oscillation can be observed in several ways: 1) the RMS of position differences displayed on the `namon` screen has a value that is larger than several millidegrees. This RMS value is calculated using $(p - p_{cmd})$ sampled in the past two seconds. These RMS values for azimuth and elevation can also be accessed by the two dot variables: `.prmsa` and `.prmse`; 2) the stellar images on the monitor screen of the CCD camera of the optical guide-scope appear as streaks rather than points; 3) the encoder display on the red LED panel of the Servo Box rack shows varying numbers when the telescope is supposed to be motionless, or the azimuth encoder reading is not decreasing smoothly during tracking; 4) data integration will take longer to finish because *OBS* will not record the taken when the telescope is not in position.

Whether an object is "in position" is determined by `tracker`. In every 10 ms cycle, `tracker` considers the pointing to be good when $(p - p_{cmd})$ is smaller than a preset error criterion. The error criterion is stored in the *shared memory* as `sm.sv.errorCriterion` in units of turns (i.e. 0.001 means 0.36 degrees) and can be accessed at the *OBS* command line using the variable `.trcr`. The criterion is usually set in the start-up macro `strt` in the *OBS* global macro `.nGMACROS`. The variable `sm.sv.servoError` in the shared memory will be set or reset accordingly by `tracker` every cycle. So during an integration, `tracker` will discard the scan if the telescope is not in position. Whenever this occurs, the bad data sample count, *Nbad*, in the scan header is incremented. If the telescope vibrates, it is possible that the telescope is not in position most of the time. A high value of *Nbad* is displayed on the `namon` screen and recorded in the scan file.

Stabilizing and Damping

In order to eliminate the spurious oscillatory behavior, $B(\gamma)$ should remain small (i.e. γ and R_m should be kept large). On the other hand when $B(\gamma)$ is too small the telescope will respond sluggishly to new position commands. In order for the telescope to have efficient movement, small tracking errors, and be resistant to wind gusts, the telescope should react quickly to any change of $(p - p_{cmd})$. The servo system that has the fastest settle time during a slew usually has a slight overshoot and quickly diminishing ringing after reaching the new position. This means the system is oscillatory but has damping factors.

Damping factors that exist in the AST/RO drive system include the mechanical friction in the bearings on the telescope and the negative differential feedback in the hardware servo loop in the Drive Box. Because of the variation of the mechanical friction and difficulty in tuning the hardware servo, the Ramp Function has a built-in damping term D to influence the damping of the telescope motion explicitly.

The damping term D emulates a "viscosity effect". The viscosity effect is a deceleration proportional to the current telescope speed. In §1 it is assumed that, in a transient state, in a first order approximation, the hardware servo system will accelerate the telescope at a rate that is proportional to the difference between ω_{cmd} and the telescope angular velocity measured by the tachometer. So by modifying the commanded angular velocity, `tracker` can command extra acceleration as is desired. The term D is constructed to be proportional to the measured angular velocity of the telescope but in the opposite direction:

$$D = -d \cdot \Omega_m \tag{A10}$$

where d is a positive damping factor and Ω_m is the measured angular velocity. The effect of the term D on the telescope is a viscous deceleration.

In the 1997 Austral winter, a spurious oscillation caused by a servo hardware problem occurred. The damping term was used to reduce the RMS of the oscillation amplitude by a factor of 5 so that it was within half a telescope beam.

Note that the damping terms have their limitations. For example, the assumptions about the hardware servo (see §1) are not always good ones; the 10 ms cycle of `tracker` is not always fast enough for all conditions. In order to reduce the system complexity the damping term in the Ramp Function is usually set to 0. Well tuned hardware damping is preferable than software damping.

Code for the Ramp Function and Software Tuning Parameters

The Ramp Function (Equation A11) has three coefficients S, γ, and d. They can be used to change the responsive character of the telescope. By default d is set to 0. These coefficients can be accessed in *OBS* by the user via a set of dot variables. For the azimuth axis they are `.faz1` for S, `.faz2` for γ, `.faz3` for d. Similarly `.fel1`, `.fel2`, and `.fel3` are for the elevation axis. These variables will be referred to as the *tuning parameters*.

The tuning parameters have counterparts in the *shared memory*. The initialization of the tuning parameters has been discussed above. It is carried out when `tracker` is started and these lines of C code are run:

```
svp->faz3 = 0.;
```

```
    svp->faz2 = 1.0;
    svp->faz1 = 1.0/pow(6.5/360,svp->faz2);
    svp->fel3 = 0.0;
    svp->fel2 = 1.0;
    svp->fel1 = 1.0/pow(4/360,svp->fel2);
```

where the pointer `svp` points to the `sm.sv` structure in the *shared memory.*

The Ramp Function:

$$\omega_{cmd} = \mathtt{sign}(p_{cmd} - p) \cdot M \cdot S \cdot |p_{cmd} - p|^{\gamma} - d \cdot \Omega_m \tag{A11}$$

is implemented in `tracker` as two simple C functions: `azSpeed()` and `elSpeed()`. This is the code for `azSpeed()`:

```
int azSpeed(diff, encV)
double diff;
short int encV;
{
    register int v, max;

    max = (int) (MAXVP * sm->sv.faz1);
    /* objective velocity according to a certain curve at this spot */
    v = max * pow(fabs(diff),sm->sv.faz2);
    /* servo quirk. goes to "-" when sending "+"*/
    if ( diff > 0 ) v = -v;
    /* velocity feed back. */
    /* damping */
    v = v - sm->sv.faz3*encV;
    /* cut at the limit */
```

```
    if (abs(v) > MAXVP) v = (v>=0) ? MAXVP : -MAXVP;
    return v;
}
```

where `MAXVP` is M in the Ramp Function (M=`0x7fff`).

In the next section, some useful techniques for tuning the telescope servo responsiveness will be discussed.

A.4. Telescope Servo Tuning Using Software Parameters

Changing the Servo Parameters

As described in §A.3, S, γ, and d have been preset to their initial values during the *OBS* start-up process and are accessible as dot variables. Inspecting and changing these parameters can be done easily at the *OBS* command line. For example, this command prints out γ for the azimuth axis:

```
-> p .faz2
1
```

The following command will increase the S value for the azimuth axis servo by 20%:

```
-> p .faz1=.faz1*1.2
66.4615
```

By changing these variables, one can tune the performance of the telescope. But the question remains as what values should these variables have?

A responsive telescope with good tuning will result in short moving time between one telescope position and another. This efficiency of movement certainly benefits position-switched observations where the telescope keeps moving back and forth between the fixed source and reference positions.

The movement of the telescope depends on the transfer function. The transfer function translates the computer angular velocity commands into real telescope velocities. The transfer function of the telescope depends not only on the rotational inertia of the telescope at different elevations, but also on the settings of the Drive Box circuits. These factors have made it practically impossible to obtain a rigorous analytical form of the transfer function.

Without going into a full-blown transfer function analysis, one can tune the telescope servo to a very good point by experimenting. Experience shows that the minimum moving time between two positions is obtained when the telescope overshoots a little and quickly settles down to the target position. Note that the optimum setting of the tuning parameters can depend on many other factors such as how far apart the most often used source-reference angular separations are, which elevations are most commonly observed, as well as the balance of the elevation axis. Small R_m and small γ (i.e. large B) usually result in faster acceleration and make the telescope more prone to overshoot. When B is too large, the telescope tracking becomes unstable and prone to oscillation when small perturbations occur. The damping term can be used to stabilize the telescope in this situation.

When tuning the telescope servo, it is essential to be able to observe the dynamic characteristics of the telescope. Two methods which can be used to examine the transient movement behavior of the telescope are described in the following sections. One involves using the optical pointing telescope, the other involves using the `rc` command to record the encoder readings of the telescope.

Using the Optical Telescope

Using the optical guide-scope that is installed for optical pointing, one can see the telescope movement from the shifting of the star image on the display of the CCD camera. This method can give a quick visual presentation of the telescope servo performance when the servo parameters are changed.

Set the CCD display software at a high refresh rate (e.g. 200 ms), and select a star that is bright enough to see on the computer monitor screen easily, but not so bright as to produce strong saturation trails. When the telescope is moved to the position of the star from a different position, one can see on the CCD screen whether the image of the star shows behavior such as overshooting, ringing, or persistent oscillation (sign of large B), or whether the telescope is inching toward the final position too slowly (small B).

Using the `rc` *Command*

Although the optical telescope can give a quick visual examination of the telescope behavior, often a quantitative description of the telescope movement during a long period of time is needed.

The `rc` command in OBS is able to log the encoder readings of the telescope in a *shared buffer* data structure in the computer memory and record these data in a file when needed. The on-line documentation of the `rc` command describes how to start and stop recording and how to write the recorded result to a file.

Since the recording can be made when *OBS* is running any commands that do not use the *shared buffer*, `rc` can be used to catch intermittent drive problems even when the telescope is observing.

Figure A.2 shows an example recording of the azimuth encoder reading using the `rc` command.

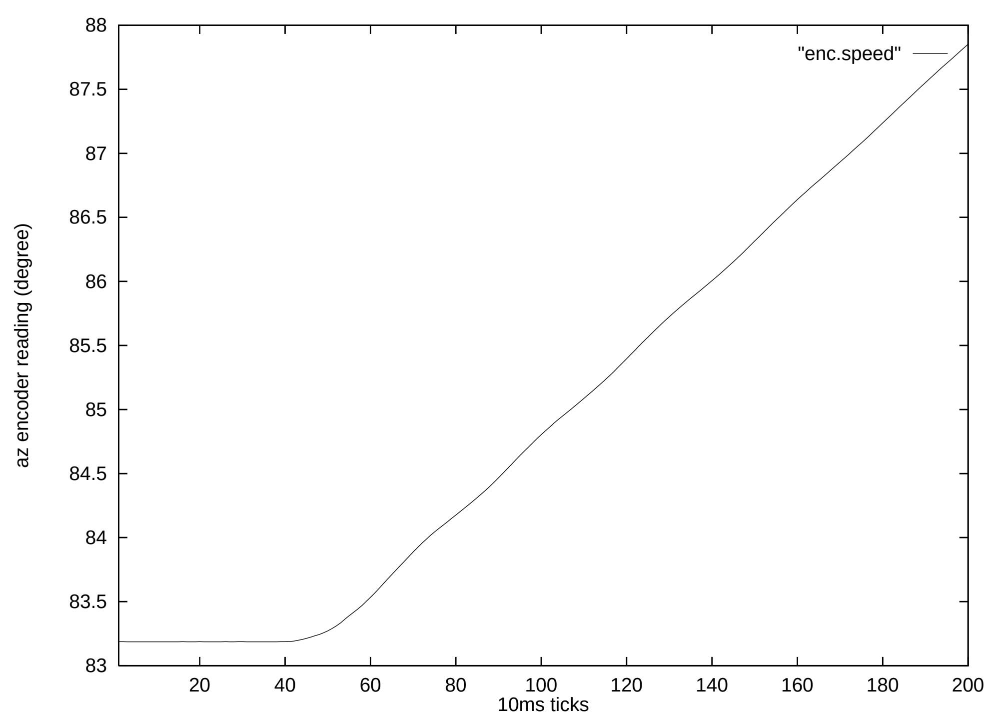

Fig. A.2.— The encoder readings of the azimuth axis during acceleration. The units of the vertical axis in have been converted from 23-bit binary to degrees. The horizontal axis shows time in units of 10 ms ticks. See text for more detail.

The OBS commands used to generate this measurement are in the form of:

```
-> az 0; pa tr: // wait for the telescope to stop
-> rc enc:30
-> az 100 // telescope will start to slew
...
-> rc en:-1 f:"enc"
```

Figure A.2 only shows the azimuth encoder reading during the acceleration period. Since the target azimuth is farther than the maximum ramp-up distance (usually about 6 degrees), the maximum velocity command allowed by the Ramp Function is sent to the Drive Box when the `az 100` command is entered. So the angular velocity command sent to the DAC resembles a step function with respect to time.

With quantitative measurement of the telescope movement recorded, more sophisticated analysis can be conducted to calculate the properties of the telescope and the status of the servo system. Adjustment of the servo system can be made based on the result of these analyses.

The Figure A.3 shows the telescope speed calculated from the encoder readings shown in Figure A.2. In principle the transfer function can be derived from these readings.

These tools discussed in §4.2 and §4.3 together with experiment are usually sufficient to refine the servo tuning without elaborate numerical analysis.

A.5. Discussion

There are many other factors to consider when tuning the telescope besides the movement efficiency and stability of the servo. For example, when the telescope accelerates or decelerates, the telescope will shake the base structure and the optical table holding the receivers. The receivers and optics working at submillimeter wavelengths could be affected by residual vibration, possibly causing a baseline problem in the spectra.

The tuning of the hardware servo, which is not being discussed in this memo, can greatly affect the dynamical properties of the telescope. For example, a simple non-zero offset in the op-amp used with the DAC can cause a puzzling behavior. This offset can produce a slow drifting of the telescope when the angular velocity

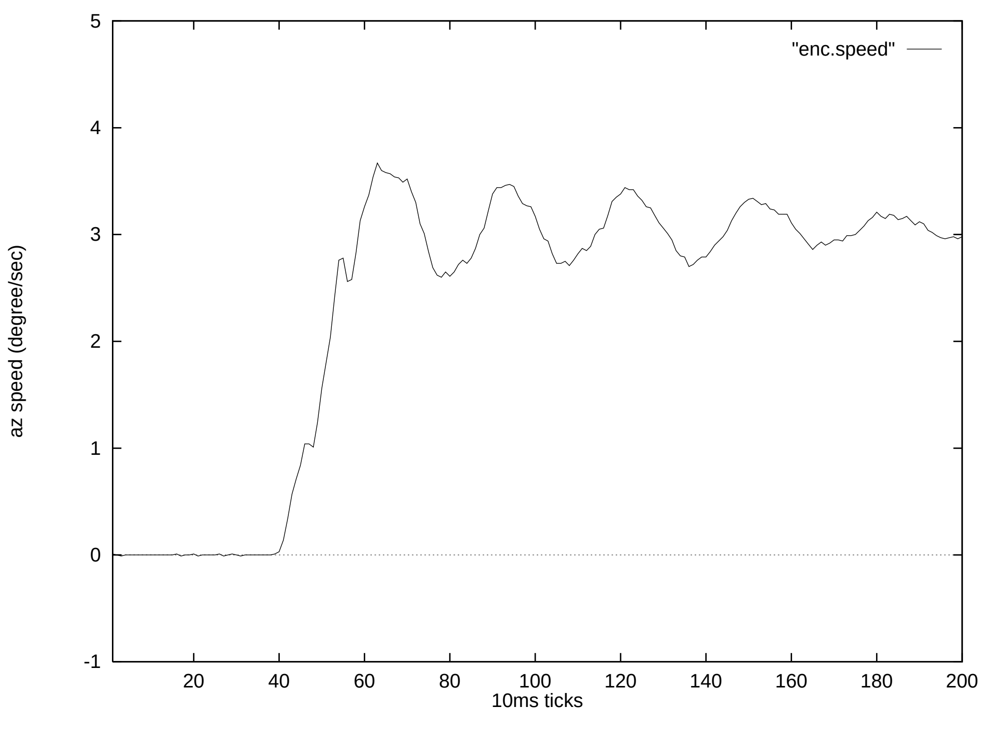

Fig. A.3.— The telescope speed calculated from the encoder readings shown in Figure A.2. The units of the vertical axis are degrees per second.

command from the computer is 0 and when the brake is released. The puzzling part of this problem is that when `tracker` is off, the telescope brake usually is applied so the operator does not see the drifting. When the problem does show, it is a mysterious constant pointing error when `tracker` is on. This is because `tracker`, through the Ramp Function, has to maintain a pointing error to compensate for the velocity drift caused by the non-zero op-amp offset. A naive observer is usually tricked into looking for software reasons to solve the pointing error problem.

Apparently, more refined tuning and Ramp Function can be developed based on more rigorous analyses of the transfer function of the telescope. The Submillimeter Array project is going down this path. It can be tempting to add more and more sophistication and complexity to the Ramp Function. So far on AST/RO the system development has been trying to follow the “Keep It Simple and Stupid” philosophy.

B. Optical Depth and Column Density of CO(4-3) Compared with CI

B.1. Optical Depth of CO(4-3) Transition Emission

In this section I show that the CO(J $= 4 \rightarrow 3$) transition emission is optically thin. I assume the emission region to be a homogeneous slab. First I derive the relation between the observed main beam antenna temperature and the optical depth for both CO(J $= 4 \rightarrow 3$) and C I, then I show that the CO(J $= 4 \rightarrow 3$) emission of the ISO sample of sources is optically thicker than C I by a factor of a few.

When observing a species in a homogeneous cloud, according to the theory of radiative transfer, the line intensity observed at I_ν frequency ν is:

$$I_\nu = I(T_{bg})e^{-\tau_\nu} + S_\nu(T_{\rm ex})(1 - e^{-\tau_\nu}), \tag{B1}$$

where $I(T_{bg})$ is the intensity of the radiation from the background that has a temperature of T_{bg}, τ_ν is the optical depth of the emission from the source at frequency ν, $T_{\rm ex}$ is the excitation temperature of the transition, and $S_\nu(T_{\rm ex})$ is the source function at $T_{\rm ex}$. Assuming local thermal equilibrium (LTE), $S_\nu(T_{\rm ex})$ is simply the Planck function $B_\nu(T_{\rm ex})$.

The brightness temperature, T_B, which is used in radioastronomy to measure the intensity, is defined as:

$$T_B \equiv \frac{c^2}{2k\nu^2} I_\nu, \tag{B2}$$

where k and c are the Planck constant and the speed of light, respectively. In millimeter and submillimeter wavelengths, the specific intensity expressed in temperature units, J_ν, is:

$$J_\nu(T_B) = \frac{h\nu}{k}(e^{h\nu/kT_B} - 1)^{-1}. \tag{B3}$$

Note that for the C I and the CO(J $= 4 \rightarrow 3$) transitions, the values of $h\nu/k$ are 23.7K and 22.2K, respectively. Using this expression, Equation B1 can be re-written as:

$$J_\nu(T_B) = J_\nu(T_{bg})e^{-\tau_\nu} + J_\nu(T_{\rm ex})(1 - e^{-\tau_\nu}). \tag{B4}$$

Assuming that the cloud fills the beam of the antenna, the emission intensity emitted from the source, $J_\nu^{\rm source}$, is the intensity observed toward the cloud, $J_\nu^{\rm cloud}$, minus that toward the background, $J_\nu^{\rm background}$. Using Equation B4, we have:

$$J_\nu^{\rm source} = J_\nu^{\rm cloud} - J_\nu^{\rm background} = \left[J_\nu(T_{\rm ex}) - J_\nu(T_{bg})\right](1 - e^{-\tau_\nu}). \tag{B5}$$

The background is the 3K cosmic background radiation. At C I and CO(J = 4 $\rightarrow$ 3) frequencies $J_\nu(3K)$ is about 0.01K, much weaker than that of the source, and is therefore ignored. The left hand side of the Equation, $J_\nu^{\rm source}$, expressed in temperature units, will be denoted with the customary T_{MB}, to emphasize that it is the main beam antenna temperature of the source:

$$T_{MB} = J_\nu(T_{\rm ex})(1 - e^{-\tau_\nu}). \tag{B6}$$

Equation B6 applies for both C I and CO(J = 4 $\rightarrow$ 3) transition emission. In § 4 I find that for the ISO sample of H II regions the C I and CO(J = 4 $\rightarrow$ 3) emission areas coincide and have nearly the same size. I therefore assume that these species spatially co-exist and that their excitation temperatures are equal. This means that their beam filling factors are also equal. With these assumptions the ratio of the main beam antenna temperatures of CO(J = 4 $\rightarrow$ 3) and C I (denoted by T_{MB}^{CO} and T_{MB}^{CI}, respectively) is:

$$\frac{T_{MB}^{CO}}{T_{MB}^{CI}} = \frac{J_\nu^{CO}(T_{\rm ex})}{J_\nu^{CI}(T_{\rm ex})} \cdot \frac{1 - e^{-\tau_\nu^{CO}}}{1 - e^{-\tau_\nu^{CI}}}. \tag{B7}$$

The factor $J_\nu^{CO}(T_{\rm ex})/J_\nu^{CI}(T_{\rm ex})$ is greater than 0.9 when $T_{\rm ex} > 23K$, and approaches unity for even larger $T_{\rm ex}$ values. Assuming this factor to be 1 and using the optically thin limit approximation that $1 - e^{-\tau_\nu} \approx \tau_\nu$, the above relation becomes:

$$\frac{T_{MB}^{CO}}{T_{MB}^{CI}} = \frac{\tau_\nu^{CO}}{\tau_\nu^{CI}}. \tag{B8}$$

I have argued in § 3 that C I emission is optically thin. I showed that if $T_{\rm ex}$ is greater than 50K, τ_ν^{CI} is 0.04 ± 0.02 on average (see Table 3.4), and that τ_ν^{CI} will decrease for higher $T_{\rm ex}$. In § 4 I find the average ratio of T_{MB}^{CO} and T_{MB}^{CI} to be 3.2 ± 0.7, which implies that the optical depth of CO(J $= 4 \to 3$) is a few times greater than that of C I, with an average of 0.12 ± 0.07. So therefore I conclude CO(J $= 4 \to 3$) emission is optically thin.

B.2. CO Column Density Compared with CI

In this section I show that CO total column density, N_{CO}, traced by CO(J $= 4 \to 3$) emission is small compared with the C I column density, N_{CI}.

The optical depth of CO(J $= 4 \to 3$) emission is related to the transition's spontaneous emission coefficient, A, the line strength and shape $\phi(\Delta\nu)$, and the column density of CO molecules occupying the upper (J_u=4) transition level, N_u, by the following equation:

$$\tau_\nu = \frac{c^2}{8\pi\nu^2} A(e^{h\nu/kT_{\rm ex}} - 1) N_u \phi(\Delta\nu), \tag{B9}$$

where the meanings of τ_ν, c, ν, h, k, and $T_{\rm ex}$ have been explained in previous equations. The spontaneous emission coefficient is also known as the Einstein A coefficient. It can be calculated by:

$$A = \frac{64\pi^4\nu^3}{3hc^3}\mu^2 \frac{J_u}{g_u}, \tag{B10}$$

where μ is the electric dipole moment of CO (about 0.11 Debyes), rotational quantum number J_u equals 4, and statistical g_u equals $2J_u + 1$. The line strength $\phi(\Delta\nu)$ can be approximated as $\Delta\nu^{-1}$, and is related to the FWHM linewidth, Δv by:

$$\phi(\Delta\nu) \approx \Delta\nu^{-1} = \frac{c}{\nu\Delta v}. \tag{B11}$$

Thus the optical depth of the CO(J $= 4 \rightarrow 3$) transition can be written as:

$$\tau_\nu = \frac{8\pi^3}{3h}\mu^2\frac{J_u}{g_u}(e^{h\nu/kT_{\mathrm{ex}}} - 1)\frac{N_u}{\Delta v}. \tag{B12}$$

Assuming LTE, the total CO column density is related to N_u by (Townes & Schawlow 1955):

$$N_u = N_{CO} g_u e^{-hBJ_u(J_u+1)/kT_{\mathrm{ex}}}\frac{hB}{kT_{\mathrm{ex}}}, \tag{B13}$$

where B is the CO molecule rotational constant in the absence of zero-point vibrations. For $T_{\mathrm{ex}} = 50K$, $hB/kT_{\mathrm{ex}} \approx 0.055$. For the upper level of the CO(J $= 4 \rightarrow 3$) transition, at $T_{\mathrm{ex}} = 50K$, Equation B13 is approximately $N_u \approx 0.16 N_{CO}$. From Equations B12 and B13, using the average CO(J $= 4 \rightarrow 3$) optical depth of 0.12 ± 0.07, N_{CO} is $(1.3 \pm 0.8) \times 10^{16}\,\mathrm{cm}^{-2}$, which is one order of magnitude lower than $N_{CI} = (1.4 \pm 0.9) \times 10^{17}\,\mathrm{cm}^{-2}$.

If the excitation temperature of the gas is much lower than 50K, which is unlikely given the excitation conditions of C I and CO(J $= 4 \rightarrow 3$), the column density of CO would still be smaller than that of C I. For example if T_{ex} is as low as 15K, approaching the temperature deep inside Giant Molecular Clouds, then CO(J $= 4 \rightarrow 3$) would just reach a moderate optical depth (1.0 ± 0.7), and the column density of CO would be $(0.7 \pm 0.5) \times 10^{17}\,\mathrm{cm}^{-2}$, which still smaller than N_{CI}.

I conclude that if CO and C I are coexistant as has been shown in § 4, then CO must be a negligible contribution to the density of carbon nuclei calculated in § 5.

Journal Names

A&A	Astronomy and Astrophysics
ApJ	Astrophysical Journal
ApJS	Astrophysical Journal Supplement Series
ApL	Astrophysical Letters
AJ	Astronomical Journal
ARA&A	Annual Review of Astronomy and Astrophysics
MNRAS	Monthly Notices of the Royal Astronomical Society

REFERENCES

Afflerbach, A., Churchwell, E. & Werner, M. W. 1997, ApJ, 478, 190

Auer, L. H., & Mihalas, D. 1970, ApJ, 160, 233

Auer, L. H., & Mihalas, D. 1972, ApJS, 24, 193

Aumann, H. H., Fowler, J. W. & Melnyk, M. 1990, AJ, 99, 1674

Beichman, C. A., Neugebauer, G., Habing, H. J., Clegg, P. E. & Chester, T. J. 1985, Infrared Astronomical Satellite (IRAS) Catalogs and Atlases, Vol. 1 Explanatory Supplement, NASA RP-1190, (US Government Printing Office: Washinton, DC)

Bergin, E. A., Snell, R. L., and Goldsmith, P. F. 1996, ApJ, 460, 343

Black, J. H., & Dalgarno, A. 1977, ApJS, 34, 405

Bolatto, A. D., Jackson, J. M., & Ingalls, J. G. 1999, ApJ, 513, 275

Brand, J., & Wouterloot, J. G. A. 1998, A&A, 337, 539

Cardelli, J. A., Clayton, G. C. & Mathis, J. S. 1989, ApJ, 345, 245

Caswell, J. L., & Haynes, R. F. 1987, A&A, 171, 261

Chamberlin, R. A., Lane, A. P., & Stark, A. A. 1997, ApJ, 476, 428

Chan, G. & Fich, M. 1995, AJ, 109, 2611

Chokshi, A., Tielens, A. G. G. M., Werner, M. W. & Castelaz, M. W. 1988, ApJ, 334, 803

Clegg, P. E. & 62 colleagues 1996, A&A, 315, L38

Clemens, D. P. 1985, ApJ, 295, 422

Code, A. D., Bless, R. C., Davis, J., & Brown, R. H. 1976, ApJ, 203, 417

Cooksy, A. L., Saykally, R. J., Brown, J. M., & Evenson, K. M. 1986, ApJ, 309, 828

Cox, P., Kruegel, E. & Mezger, P. G. 1986, A&A, 155, 380

Crawford, M. K., Genzel, R., Townes, C. H. & Watson, D. M. 1985, ApJ, 291, 755

Dickman, R. L. 1975, ApJ, 202, 50

Dupree, A. K., & Goldberg, L. 1970, ARA&A, 8, 231

Duffy, A. G., Hawkes, R. L. & Jones, J. 1987, MNRAS, 228, 55

Eggel, H., Schaap, H., & Bagnasco, G. 1990, ESA Bulletin No. 61 (February 1990)

Emery, R. *et al*. 1996, A&A, 315, L285

Engargiola, G., Zmuidzinas, J., & Lo, K.-Y. 1994, Rev. Sci. Instr., 65, 1833

Felli, M., Persi, P., Roth, M., Tapia, M., Ferrari-Toniolo, M. & Cervelli, A. 1990, A&A, 232, 477

Ferland, G. J., 2000, Hazy, a brief introduction to Cloudy 94.01a

Fischer, M. L. *et al*. 1995, ApJ, 444, 226

Forster, J. R., Whiteoak, J. B., Kesteven, M. J., Manchester, R. N., Rayner, P. T., Ables, J. G. & Peters, W. L. 1987, MNRAS, 226, 173

García-Lario, P. 2000, 3rd Post-Operation Cross-Calibration Status Report, v1.0, SAI/2000-029/Rp

Gardner, F. F. & Whiteoak, J. B. 1984, MNRAS, 210, 23

Genzel, R., Harris, A. I., Stutzki, J., & Jaffe, D. T. 1988, ApJ, 332, 1049

Genzel, R. 1991, in Physics of Star Formation and Early Stellar Evolution, C. Lada & N. Kylafis (eds.), (Kluwer: Dordrecht), p. 155

Georgelin, Y. M., Lortet-Zuckermann, M. C., & Monnet, G. 1975, A&A, 42, 273

Georgelin, Y. M., Russeil, D., Amram, P., Georgelin, Y. P., Marcelin, M., Parker, Q. A. & Viale, A. 2000, A&A, 357, 308

Glassgold, A. E., & Langer, W. D. 1976, ApJ, 206, 85

Greenberg, J. M. & Shah, G. A. 1971, A&A, 12, 250

Gry, C. 2000, The ISO Handbook, Vol. IV, LWS - The Long-Wavelength Spectrometer, SAI/99-077/Dc v1.0

Frerking, M. A., Langer, W. D., & Wilson, R. W. 1982, ApJ, 262, 590

Fich, M., Treffers, R. R., & Blitz L., 1982, in Regions of Recent Star Formation, R. S. Roger & P. E. Dewdney (eds.), (Dordrecht: Reidel), p.201

Habing, H. J. 1968, Bull. Astron. Inst. Netherlands, 19, 421

Harper, D. A. 1974, ApJ, 192, 557

Haynes, R. F., Caswell, J. L., & Simons, L. W. J. 1978, Australian Journal of Physics Astrophysical Supplement, 45, 1

Helou, G., Khan, I. R., Malek, L. & Boehmer, L. 1988, ApJS, 68, 151

Helou, G. 1989, in IAU Symp. 135: Interstellar Dust, L. J. Allamandola & A. G. G. M. Tielens (eds), (Dordrecht:Kluwer), p.285

Hjellming, R. M. 1968, ApJ, 154, 533

Hjellming, R. M., Andrews, M. H., & Sejnowski, T. J. 1969, ApJ, 157, 573

Hollenbach, David J., Takahashi, Takamasa, & Tielens, A. G. G. M. 1991, ApJ, 377, 192

Hollenbach, D.J., & Tielens, A.G.G.M. 1999, Rev. of Mod. Phy., 71, 173

Howe, J. E., Jaffe, D. T., Genzel, R., & Stacey, G. J. 1991, ApJ, 373, 158

Hughes, V. A., & Vallee, J. R. 1978, A&A, 69, 445

Ingalls, J. G., Chamberlin, R. A., Bania, T. M., Jackson, J. M., Lane, A. P., & Stark, A. A. 1997, ApJ, 479, 296

Ingalls, J. 1998, Ph.D. Thesis, Boston University

Jaffe, D. T., Zhou, S., Howe, J. E., Herrmann, F., Madden, S. C., Poglitsch, A., van der Werf, P. P. & Stacey, G. J. 1994, ApJ, 436, 203

Neckel, T. 1978, A&A, 69, 51

Neckel, T. & Chini, R. 1981, A&AS, 45, 451

Kaufman, M. J., Wolfire, M. G., Hollenbach, D. J., & Luhman, M. L. 1999, ApJ, 527, 795

Keene, J., Blake, G. A., Phillips, T. G., Huggins, P. J., & Beichman, C. A. 1985, ApJ, 299, 967

Kessler, F., Heske, A., Metcalfe, L., & Salama, A. 1991, ESA Bulletin No. 67 (August 1991)

Kessler, M. F. *et al*. 1996, A&A, 315, L27

Kraemer, K. E. 1998, Ph.D thesis, Boston Univ.

Kraemer, K. E., Jackson, J. M. & Lane, A. P. 1998, ApJ, 509, 931

Kuiper, T. B. H., Whiteoak, J. B., Fowler, J. W. & Rice, W. 1987, MNRAS, 227, 1013

Kurucz, R. L. 1979, ApJS, 40, 1

Lane, A. P. 1998, American Astronomical Society Meeting, 192, 4805

Lane, A. P., Haas, M. R., Hollenbach, D. J. & Erickson, E. F. 1990, ApJ, 361, 132

Langer, W. 1976, ApJ, 206, 699

Massi, F., Brand, J. & Felli, M. 1997, A&A, 320, 972

Mathewson, D. S., Healey, J. R. & Rome, J. M. 1962, Australian Journal of Physics, 15, 354

McGee, R. X., Newton, L. M. & Butler, P. W. 1979, MNRAS, 189, 413

Meixner, M., Haas, M. R., Tielens, A. G. G. M., Erickson, E. F. & Werner, M. 1992, ApJ, 390, 499

Meixner, M., & Tielens, A. G. G. M. 1993, ApJ, 405, 216

Melnick, G., Gull, G. E., & Harwit, M. 1979, ApJ, 227, L29

Mezger, P. G., & Ellis, S. A. Astrophys. Lett., 1, 159

Mezger, P. G., & Henderson, A. P. 1967, ApJ, 147, 471

Mezger, P. G., & Hoglund, B. 1967, ApJ, 147, 490

Mihalas, D., & Auer, L. H. 1970, ApJ, 160, 1161

Morton, D. C. 1969, ApJ, 158, 629

Myers, P. C. 1978, ApJ, 225, 380

Myers, P. C., Linke, R. A. & Benson, P. J. 1983, ApJ, 264, 517

Myers, P. C., *et al*. 1986, ApJ, 301, 398

Nachman, P. 1979, ApJS, 39, 103

Nakagawa, T., Yui, Y. Y., Doi, Y., Okuda, H., Shibai, H., Mochizuki, K., Nishimura, T., & Low, F. J. 1998, ApJS, 115, 259

Natta, A. & Panagia, N. 1976, A&A, 50, 191

Nussbaumer, H. 1971, ApJ, 166, 411

Osborn, W. 1974, MNRAS, 166, 463

Osterbrock, D. E. 1989, in Astrophysics of Gaseous Nebulae and Active Galactice Nuclei, (Mill Valley, CA: USB)

Panagia, N. 1973, AJ, 78, 929

Peimbert, M. 1982, New York Academy Sciences Annals, 395, 24

Persi, P., Ferrari-Toniolo, M., Roth, M. & Tapia, M. 1986, A&A, 170, 97

Persi, P., Roth, M., Tapia, M., Ferrari-Toniolo, M. & Marenzi, A. R. 1994, A&A, 282, 474

Phillips, J. P. & Mampaso, A. 1989, A&A, 218, 24

Phillips, T. G., Wannier, P. G., Scoville, N. Z., & Huggins, P. J. 1979, ApJ, 231, 720

Phillips, T. G., Huggins, P. J., Kuiper, T. B. H., & Miller, R. E. 1980, ApJ, 238, L103

Phillips, T. G., & Huggins, P. J. 1981, ApJ, 251, 533

Reifenstein, E. C., Wilson, T. L., Burke, B. F., Mezger, P. G., & Altenhoff, W. J. 1970, A&A, 4, 357

Rubin, R. H., Simpson, J. P., Lord, S. D., Colgan, S. W. J., Erickson, E. F. & Haas, M. R. 1994, ApJ, 420, 772

Russell, R. W., Melnick, G., Gull, G. E., & Harwit, M. 1980, ApJ, 240, L99

Russell, R. W., Melnick, G., Smyers, S. D., Kurtz, N. T., Gosnell, T. R., Harwit, M., & Werner, M. W. 1981, ApJ, 250, L35

Salama, A. 2000, ISO Beyond Point Sources: Studies of Extended Infrared Emission, September 14-17, 1999, ISO Data Centre, Villafranca del Castillo, Madrid, Spain, R. J. Laureijs, K. Leech & M. F. Kessler (eds.), ESA-SP 455, 2000, p 7., 455, 7

Savage, B. D. & Sembach, K. R. 1996, ASP Conf. Ser. 99: Cosmic Abundances, 315

Schaerer, D., & de Koter, A. 1997, A&A, 322, 598

Schaerer, D., & de Koter, A. 1997, A&A, 322, 614

Schieder, R., *et al*. 1989, Experimental Astronomy, 1, 101S

Schulz, A. and 8 colleagues 1995, A&A, 295, 183

Scoville, N. Z. & Sanders, D. B. 1987, Interstellar Processes, 21

Shibai, H. *et al*. 1991, ApJ, 374, 522

Solomon, P. M., Rivolo, A. R., Barrett, J. & Yahil, A. 1987, ApJ, 319, 730

Spaans, M. and van Dishoeck, E. F. 1997, A&A, 323, 953

Spitzer, L. 1978, in Physical processes in the interstellar medium (New York: Wiley-Interscience)

Stacey, G. J., Geis, N., Genzel, R., Lugten, J. B., Poglitsch, A., Sternberg, A. & Townes, C. H. 1991, ApJ, 373, 423

Staguhn, J., Stutzki, J., Chamberlin, R. A., Balm, S. P., Stark, A. A., Lane, A. P., Schieder, R., & Winnewisser, G. 1997, ApJ, 491, 191

Stark, A. A., *et al*. 1994, Antarctic Journal of the U. S., 29, 344

Stark, A. A., *et al*. 1997, Rev. Sci. Instr., 68, 2200

Stark, A. A., Bolatto, A. D., Chamberlin, R. A., Lane, A. P., Bania, T. M., Jackson, J. M., & Lo, K. -Y. 1997, ApJ, 480, L59

Steiman-Cameron, T. Y., Haas, M. R., Tielens, A. G. G. M. & Burton, M. G. 1997, ApJ, 478, 261

Sternberg, A., & Dalgarno, A. 1995, ApJS, 99, 565

Storey, J. W. V., Watson, D. M., & Townes, C. H. 1979, ApJ, 233, 109

Strömgren, B. 1939, ApJ, 89, 526

Stutzki, J., Stacey, G. J., Genzel, R., Harris, A. I., Jaffe, D. T., & Lugten, J. B. 1988, ApJ, 332, 379

Stutzki, J. 1990, in Atoms, Ions, & Molecules: New Results in Spectral Line Astronomy, A.S.P. Conf. Ser., A. D. Haschick & P. T. Ho (eds.), (San Francisco:BookCrafters), 1991, vol. 88, 115

Swinyard, B. M. & 54 colleagues 1996, A&A, 315, L43

Tauber, J. A., Lis, D. C., Keene, J., Schilke, P., & Buettgenbach, T. H. 1995, A&A, 297, 567

Tielens, A. G. G. M. & de Jong, T. 1979, A&A, 75, 326

Tielens, A. G. G. M. . G., & Hollenbach, D. 1985, ApJ, 291, 747

Tielens, A. G. G. M., & Hollenbach, D. 1985, ApJ, 291, 722

Thronson, H. A. & Harper, D. A. 1979, ApJ, 230, 133

Townes, C. H., & Schawlow, A. L. 1955, in Microwave Spectroscopy (New York, NY: Dover)

Trams, N. 1998, ISO LWS Data Users Manual, Issue 5.0, SAI/95-219/Dc

Vacca, W. D., Garmany, C. D., & Shull, J. M. 1996, ApJ, 460, 914

van der Werf, P. P., Stutzki, J., Sternberg, A. and Krabbe, A. 1996, A&A, 313, 633

Waller, W. H., Clemens, D. P., Sanders, D. B., & Scoville, N. Z. 1987, ApJ, 314, 397

White, G. J., & Padman, R. 1991, Nature, 354, 511

White, G. J., & Sandell, G. 1995, A&A, 299, 179

Whiteoak, J. B. & Gardner, F. F. 1974, A&A, 37, 389

Whiteoak, J. B., Robina, E. O., & Rennie, C. J. 1982, Proc. ASA, 4(4) 434

Wilson, T. L., Mezger, P. G., Gardner, F. F., & Milne, D. K. 1970 A&A, 6, 364

Wilson, R. W., Jefferts, K. B. & Penzias, A. A. 1970, ApJ, 161, L43

Wolfire, M. G., Tielens, A. G. G. M. & Hollenbach, D. 1990, ApJ, 358, 116

Wolfire, M. 2000, private communication

Zmuidzinas, J., Betz, A. L., & Goldhaber, D. M. 1986, ApJ, 307, L75

Zmuidzinas, J., Betz, A. L., Boreiko, R. T., & Goldhaber, D. M. 1988, ApJ, 335, 774

Zmuidzinas, J., & LeDuc, H. G. 1993, IEEE Trans. Microwave Th. & Tech., 40, 1797

Vita

Family Name: Huang	Given Name: Maohai
Place of Birth: Beijing, China	Date of Birth: May 23, 1968

Educational Institutions Attended	Dates
Peking University, Beijing, China	1987 to 1991
Boston University	1992 to present

Degrees Awarded	Dates
B.Sc. in Astrophysics, Peking University	1991
M.A. in Astronomy, Boston University	1999

Research	Dates
A Computerized Pulsar Observation System	1990 to 1992
Molecular Outflows	1992 to 1996
AST/RO Project and C I in PDRs around H II Regions	1992 to present

Selected Publications

"Atomic Carbon Observations of Southern Hemisphere H II Regions" Huang, M., Bania, T. M., Bolatto, A., Chamberlin, R. A., Ingalls, J. G., Jackson, J. M., Lane, A. P., Stark, A. A., Wilson, R. W. & Wright, G. A. 1999, ApJ, 517, 282

"A catalogue of high velocity molecular outflows" Wu, Y., Huang, M. & He, J. 1996, A&AS, 115, 283

"The data acquisition and processing system used for pulsar observations" Huang, M., Jin, S. Z., Wu, H. & Kang, L. S. 1993, Publications of the Beijing Astronomical Observatory, 22, 19